3D Climate Modeling of Earth-like Extrasolar Planets Orbiting Different Types of Central Stars

vorgelegt von
Diplom-Physikerin
Mareike Godolt
aus Berlin

Von der Fakultät II - Mathematik und Naturwissenschaften
der Technischen Universität Berlin
zur Erlangung des akademischen Grades
Doktor der Naturwissenschaften
Dr.rer.nat.

genehmigte Dissertation

Promotionsausschuss:

Vorsitzender: Prof. Dr. rer. nat. Mario Dähne
Berichter/Gutacher: Prof. Dr. rer. nat. Heike Rauer
Berichter/Gutacher: Prof. Dr. rer. nat. Ulrike Langematz

Tag der wissenschaftlichen Aussprache: 17. Oktober 2012

Berlin 2012

D 83

Abstract

The habitability of a terrestrial planet is usually defined by the existence of liquid water on the surface. This is motivated by the fact, that life as we know it, needs liquid water at least during a part of its life cycle. The potential presence of liquid water on a planetary surface depends e.g. on surface temperatures. These are mainly determined by the properties of the planetary atmosphere, dynamical processes and the interaction with the radiative energy provided by the planet's host star.

This work focuses on the importance of dynamical processes for the habitability of terrestrial extrasolar planets. The main scientific questions addressed are: What is the influence of dynamical atmospheric processes on the habitability of a planet? What is the influence of different stellar types on climate feedback cycles and how do they affect the habitability of the planet?

To evaluate the influence of dynamical atmospheric processes and climate feedbacks a state-of-the-art three-dimensional climate model has been adapted and applied to Earth-like extrasolar planets orbiting different types of central stars. The influence of different stars has been accounted for by using stellar spectra of an F and a K-type main-sequence star and by assuming appropriate planetary orbits. The planets have been placed at orbital distances where the total amount of energy received from the host star equals the solar constant. For the first time, such a complex three-dimensional climate model is utilized to study these scenarios. In contrast to one-dimensional radiative-convective climate models, previously applied to determine the atmospheric properties and surface temperatures of Earth-like extrasolar planets around different types of central stars, the three-dimensional climate model used in this work accounts for complex dynamical processes, such as atmospheric dynamics, the hydrological cycle, as well as changes in surface albedo due to melting of sea ice.

Dynamical processes exhibit the largest impact for the planet around the K-type star. For this scenario, the spectral distribution of the stellar energy flux leads to a warming of the planetary surface and the lower atmosphere, which is in agreement with previous one-dimensional modeling studies. However, a larger increase in temperature is obtained here, because of the interaction of the stellar irradiation and the atmospheric water vapor. The corresponding temperature increase yields a massive build-up of water vapor and clouds in the atmosphere. Consequently, this increases the absorption of stellar radiation and the greenhouse effect, which leads to a further rise in temperature. A comparison of this result to those of a cloud-free one-dimensional radiative-convective climate model reveals that this strong increase in water vapor and temperature can be reproduced by such a simplified model by assuming a completely saturated lower atmosphere. For the planet around the F-type star no large impact of the dynamical processes on the climate is found, despite the increase in surface albedo due to the build-up of sea ice. Furthermore, the influence of the orbital periods (length of the year) on the global mean climatic conditions is small for the extrasolar planets studied in this work.

Despite the changes in the dynamical processes all planetary scenarios studied in this work result in habitable surface conditions. A strong coupling of the water vapor feedback cycle with the stellar near infrared radiation is identified.

Zusammenfassung

Die Habitabilität terrestrischer extrasolarer Planeten wird üblicherweise über die Existenz von flüssigem Wasser auf der planetaren Oberfläche definiert, da Leben, wie wir es kennen, flüssiges Wasser zumindest während eines Teils seiner Lebenszeit benötigt. Ob flüssiges Wasser vorhanden sein kann, wird unter anderem durch die Oberflächentemperatur bestimmt. Diese hängt wiederum stark von der planetaren Atmosphäre, dynamischen Prozessen und deren Wechselwirkung mit der stellaren Einstrahlung ab.

In dieser Arbeit werden folgende Fragestellung zur Auswirkung dynamischer Prozesse untersucht. Welchen Einfluss haben dynamische atmosphärische Prozesse auf die Habitabilität eines Planeten? Wie beeinflussen verschiedene Sternentypen Klima-Rückkopplungen und welche Auswirkungen haben diese auf die Habitabilität eines Planeten?
Um den Einfluss dynamischer Prozesse und Klima-Rückkopplungen zu untersuchen, wird ein modernes, dreidimensionales Erdklimamodell erweitert, um Studien erdähnlicher Planeten um sonnenähnliche Sterne zu ermöglichen. Mit diesem Modell wird untersucht, wie sich das Klima dieser Planeten ändert, wenn diese um Hauptreihensterne der Spektralklassen F und K kreisen. Hierzu wird neben der Spektralverteilung des einfallenden Sternenlichts auch jeweils die Orbitperiode des Planeten und damit die Jahreslänge angepasst. Diese wird so gewählt, dass der Planet dieselbe stellare Gesamtenergie erhält wie die Erde von der Sonne. Diese Szenarien werden hier zum ersten Mal mit einem solch komplexen dreidimensionalen Klimamodell untersucht. Im Gegensatz zu eindimensionalen Klimamodellen, mit denen der Einfluss verschiedener Sternentypen auf erdähnliche Planeten bereits untersucht worden ist, berücksichtigt das hier verwendete Modell komplexe dynamische atmosphärische Prozesse, wie z.B. die atmosphärische Zirkulation, den hydrologischen Zyklus, sowie Änderungen der Oberflächenalbedo aufgrund der Ausbildung von Meereseis. Für einen erdähnlichen Planeten um einen K-Stern ergeben sich die größten Änderungen in den dynamischen Prozessen. In diesem Szenario führt die spektrale Energieverteilung zu einer Erwärmung der Planetenoberfläche und der unteren Atmosphäre. Dieses Ergebnis stimmt qualitativ mit Ergebnissen vorangegangener Klimastudien mit eindimensionalen Atmosphärenmodellen in der Literatur überein. Quantitativ zeigen die hier durchgeführten Modellstudien jedoch eine stärkere Erwärmung, die sich aufgrund der Wechselwirkung des hohen Wasserdampfgehalts in der Atmosphäre mit der stellaren Einstrahlung ergibt. Der hohe Wasserdampfgehalt und die Ausbildung von Wassereiswolken führen zu einer verstärkten Absorption der stellaren Einstrahlung und zu einem stärkeren Treibhauseffekt, welche wiederum eine weitere Erhöhung der Temperatur verursachen. Der Vergleich mit einem eindimensionalen radiativ-konvektiven Klimamodell zeigt, dass ähnlich hohe Temperaturen und Wasserdampfkonzentrationen unter der Annahme einer vollständig gesättigten unteren Atmosphäre mit solch einem vereinfachten Modell reproduziert werden können. Die Modellstudien eines Planeten um einen F-Stern zeigen einen vergleichsweise geringen Einfluss der dynamischen Prozesse trotz einer stärkeren Ausbildung von Meereseis. Außerdem wird gezeigt, dass für die untersuchten Szenarien die Orbitperiode im Mittel keinen deutlichen Einfluss auf das Klima aufzeigt.

Trotz teils großer Änderungen in den dynamischen Prozessen ergeben die untersuchten Modellrechnungen habitable Oberflächenbedingungen. Des Weiteren kann eine starke Wechselwirkung des Wasserdampf-Rückkopplungsprozesses mit der stellaren Einstrahlung im nah infraroten Wellenlängenbereich ausgemacht werden.

TABLE OF CONTENTS

List of Figures

List of Tables

Part I

Introduction

CHAPTER 1

Motivation and aim of this thesis

From early on in the history of mankind people have argued for the existence of other worlds, as e.g. Epicurus (341-270 BC), who stated that "... there are infinite worlds both like and unlike this world of ours". With the first detections of extrasolar planets in the early 1990s, testing the theoretical arguments for or against the existence of planets like ours seemed to be in reach. Despite the fact that many extrasolar planets have been found, little is known about their detailed properties, since observations are challenging for these faint objects.
The first step towards finding life on other planets is to detect a planet which could in principle be habitable. Since all life on Earth needs liquid water at least temporarily during its life cycle, liquid water has been chosen as the main prerequisite for life on other planets. For extrasolar planets it is difficult, if not impossible, to determine whether a planet may have subsurface water. Therefore, the search for habitable extrasolar planets focuses on planets which may have liquid water on their surface, hence rocky extrasolar planets.

Whether or not a terrestrial planet may posses surface conditions that allow for liquid water, depends strongly on the energy input by the star and the atmospheric composition and mass. Additionally to the stellar irradiation and atmospheric processes, which determine the climate of a planet, other processes may also influence planetary habitability, as discussed in sec. 2.2. However, this work focuses on the factors which influence the planetary climate and thereby surface habitability.

Introduction to factors influencing planetary climate and habitability

Longterm planetary habitability is believed to be the result of a complex interplay of various processes. Fig. 1.1 shows a sketch of some of the important processes, mostly related to the atmosphere, hence planetary climate. The interaction of the various processes leading or influencing planetary habitability is studied in the framework of the Research Alliance *Planetary Evolution and Life* of the Helmholtz Association, which started in 2008. This thesis is a contribution to this research alliance.

The main energy source for terrestrial planets is usually stellar radiation, but it might also be possible, that heating from the interior via radioactive decay, tidal forces or during accretion in the early stages could cause temperatures allowing for liquid water.

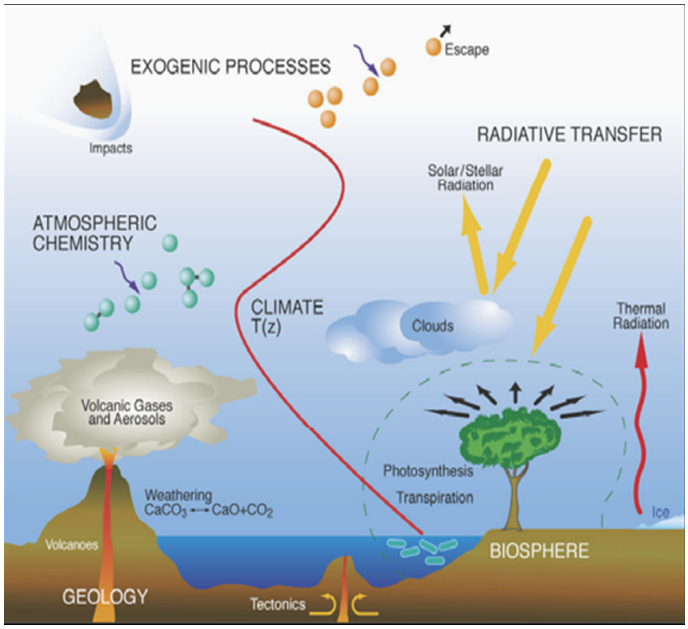

Figure 1.1: Illustration of important processes influencing the planetary habitability, taken from the Helmholtz Research Alliance *Planetary evolution and life*

For the most probable case of heating of the planet by stellar light, it is important to understand the interaction of the stellar light with the atmosphere and the planetary surface. Absorption and scattering of stellar light by atmospheric gases and particles as well as at the planetary surface determine a great part of the heating of the atmosphere. This heat is reradiated by the surface and the atmosphere. This thermal emission is partly lost to space and partly trapped by the atmosphere, via the greenhouse effect. The greenhouse effect depends on the composition and temperatures of the planetary atmosphere. The atmospheric composition is influenced by atmospheric chemistry and condensation or evaporation of constituents.
The surface temperature, hence habitability, and the temperature structure of a planetary atmosphere is determined by various processes, such as radiative heating, convection and atmospheric dynamics. Atmospheric circulation critically depends on the radiative heating, planetary parameters such as gravity, rotation period, and land mass distribution, but also on orbital parameters such as obliquity. It reduces temperature gradients caused by the locally and temporarily varying stellar insolation and transports atmospheric constituents.

Atmospheric processes are complex and highly non-linear. For example, climatic feedback processes may lead to an amplification of small disturbances of the climate state. Some important climate feedback cycles are shortly described in the following.

Albedo feedback For lower surface temperatures the surface albedo increases by the build-up of sea ice and snow which lead to more reflection, hence less heating of the surface. For higher surface temperatures the albedo decreases due to melting of snow and ice, which leads to enhanced warming of the surface by increased absorption.

Water vapor feedback High surface temperatures lead to an increase in the evaporation of water vapor. This causes a stronger greenhouse effect by absorption of planetary thermal radiation by the water vapor in the atmosphere, which further increases

the surface temperature. For low surface temperatures the evaporation is weaker, leading to less water in the atmosphere, thereby to a smaller greenhouse effect by water, hence lower surface temperatures.

Cloud feedback Clouds can have a warming or a cooling effect depending on the cloud particles and height. Kitzmann et al. (2010) studied the influence of clouds on the habitability of extrasolar planets and found that high level ice clouds have a net greenhouse effect by absorbing planetary thermal radiation, while low level ice clouds lead to cooling by reflecting the stellar light. Whether clouds enhance the atmospheric response by a positive feedback or dampen the response via a negative feedback therefore depends on the types of clouds which build up.

The impact of these feedback cycles upon the planetary climate, and hence planetary habitability, depends on the interaction of various processes and boundary conditions. Climate modeling is a valuable method to determine which processes and boundary conditions play a crucial role for planetary habitability. The influence of the stellar irradiation upon the atmospheres of terrestrial extrasolar planets has been studied in detail by one-dimensional (1D) models, see sec. 4.1, showing that the stellar irradiation can effectively alter the global mean temperature structure of a terrestrial atmosphere, even for the same atmospheric composition.

A change in radiative heating of the atmosphere also influences the atmospheric circulation. Atmospheric modeling studies including atmospheric dynamics and surface interactions, see Chapter 4, showed that the hydrological cycle plays an important role for the habitability of planets. The hydrological cycle cannot easily be taken into account by 1D models since processes like convection, cloud formation and precipitation depend on local planetary conditions, which are hard to capture in a 1D model.

The interaction of stellar irradiation different from the Sun with dynamical atmospheric processes, such as atmospheric dynamics and the hydrological cycle has not been studies in detail, except for the special case of the potentially habitable extrasolar planet Gl 581d (Wordsworth et al., 2011).

Aim of this thesis

Little is known about the properties of terrestrial extrasolar planets, besides mass, radius and orbit parameters, see sec. 2.1. However, it is known that planets exist around different types of stars. Therefore, it is necessary to understand the impact of the different planet host stars on the climate, hence habitability of the planet. Different stellar irradiations may cause different temperature structures and thereby influence the atmospheric processes. Since their influence on dynamical processes has not been studied in detail for the atmospheres of terrestrial extrasolar planets the following main scientific question are addressed in this thesis.

- What is the influence of dynamical atmospheric processes on the habitability of a planet?
- What is the influence of different stellar types on climate feedback cycles and how do they affect the habitability of the planet?

These questions will be addressed by investigating the climatic response of Earth-like planets around main-sequence F and K-type stars, which receive the same total amount of energy from the star as the Earth receives by the Sun. A state-of-the art three-dimensional (3D) climate model for the Earth, which can resolve the differences in the stellar irradiances, has been adapted in order to allow for the calculation of the climate for these scenarios.

F and K-type main-sequence stars have been chosen as planet host stars, since these stars are not too different from our Sun. Planets around such stars could therefore be similar to our Earth, and they may experience similar stable environmental conditions since F and K-type stars have similar life times as the Sun, compared to other types of stars. This also holds for M dwarf stars. However planets around such stars have not been addressed, since they may be tidally locked to their central star, hence possess a permanent day and night sight. The effect of tidal locking has been studied in detail (see cha. 4). It introduces a large change in the planetary climate system, which leads to very different atmospheric dynamics. In this work, however, rather small disturbances are imposed to the climate system, since the focus lies on the amplification of such small differences by dynamical processes.

The planets considered are assumed to be Earth-like, hence rocky planets of Earth size and mass with Earth-like atmospheres, composed mainly of nitrogen and oxygen with traces of water, carbon dioxide and other compounds as well as with an ozone layer. The distribution of continents and oceans is kept to that of the present Earth. The model allows not only for studying the influence of the stellar spectral energy distribution upon climate as already done with 1D models, but also studying the impact of different orbital periods. A possible change in atmospheric dynamics and the impact of changing surface properties, such as albedo, can be taken into account. Furthermore, the response of the hydrological cycle, i.e. concentration and cycling of water compounds in the atmosphere and associated convective heat transport can be investigated in detail. A possible buffering or enhancement of climatic response due to the effect of clouds is also taken into account. Note however, that the influence of clouds is a critical issue in climate modeling. Their contribution to Earth's climate change is the one of the largest uncertainties in today's complex general circulation models (GCMs) (Houghton et al., 2001).

Studying the response of a planetary atmosphere to the change in stellar radiation and planetary orbital period, as well as the feedback of surface properties and the hydrological cycle in detail with a complex climate model allows to estimate how important dynamical atmospheric processes and their interplay are for the determination of surface temperatures, hence habitability. A comparison of the 3D model results to those of a 1D model is carried out to determine the applicability of such simplified 1D climate models for assessing planetary habitability.

Outline

In the next chapter a short introduction to extrasolar planets and to factors relevant for the habitability of terrestrial planets are presented. In Chapter 3 the theoretical background needed for the presented studies is given. Modeling studies dealing with the influence

of stellar irradiation and atmospheric dynamics for extrasolar planets are presented in Chapter 4. Chapter 5 describes the atmospheric models and the introduced adaptations. There follows the validation of the models in Chapter 6 and the description of the model scenarios (Chapter 7). The model results are then presented in four chapters which follow. First the influence of the different model setups are evaluated for the Earth around the Sun (Chapter 8). Chapter 9 discusses the climatic response of Earth-like planets around different types of stars. In Chapter 10 the influence of the change in orbital upon the global mean climate of the Earth-like planets is briefly described. The results part closes with the comparison of the global annual mean results of the 3D model with those of a 1D radiative convective model (Chapter 11). In Chapter 12 the major results of this thesis are summarized. An outlook on future model improvements and interesting model scenarios is given in Chapter 13.

CHAPTER 2

Extrasolar planets and habitability

2.1 Introduction to extrasolar planets

In 1992 the first exoplanets were announced by Wolszczan and Frail (1992). They found two planets around the pulsar PSR1257+12 with masses of 2.8 and 3.4 M_{Earth} by observing pulsar timing variations. Three years later the first planet around a main sequence star was published by Mayor and Queloz (1995). The planet of 0.5 $M_{Jupiter}$ with an orbital period of 4.2 days around a G-type star was found by the radial velocity method. Already six years earlier Latham et al. (1989) detected a stellar companion with a minimum mass of 13 $M_{Jupiter}$ around a main sequence star, but since the radial velocity only gives a lower limit of the mass, they were not sure whether it was a planet or a brown dwarf. Since then the number of exoplanets detected increased steadily revealing strange new worlds of so-called Hot Jupiters, Hot Neptunes, Super-Earths and even free floating planets.
In Fig. 2.1 all so far detected exoplanets listed in the The Extrasolar Planets Encyclopedia (`exoplanet.eu` on January, 20 2012) are shown. The left panel displays the number of detections over the years, whereas the right panel shows the planetary mass as a function of orbital distance illustrating that mainly large planets close to their host star have been found, and the number of detected smaller planets decreases with distance. This is most likely due to an observational bias, since the most successful detection methods, radial velocity and transit method, are most sensitive to large planets close to their central star.

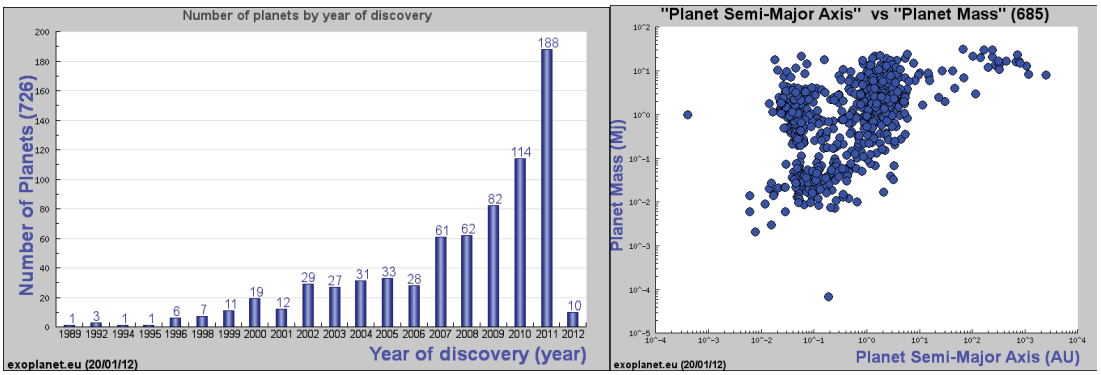

Figure 2.1: Left: Number of planets over year of discovery, right: planetary mass as a function of orbital distance. Data from exoplanet.eu, January, 20 2012

The radial velocity method uses the fact that star and planet orbit a common barycenter. This causes a Doppler shift in the spectral lines of the star to shorter wavelengths when the star approaches the observer, and to longer wavelengths when it moves away from the observer. Since only the velocity change along the line of sight of the observer contributes to the Doppler shift, this method only allows for the determination of a lower mass limit of the companion ($Msin(i)$) as long as the inclination (i) of the planetary orbit is unknown.

For some planetary systems the geometrical configuration is such, that the observer can detect the planet during its passage in front of the star, during its transit. From the dimming of the stellar light by the planet the ratio of the planetary to stellar radius can be derived, and, since the planet is transiting, the inclination (i) of the planetary orbit can be inferred.

Both methods are most sensitive to large planets orbiting close to their central star. For the radial velocity method this observational bias is due to the fact that the observed stellar velocity is higher for massive planets close to their central star.

For the transit method planets on close-in orbits are favored since the geometric probability of finding a planet in transit is higher. The preference of larger planets is due to the fact that planets with a larger radius block more stellar light, hence cause a larger dip in the light curve. Furthermore, if a planet is closer to its central star, it revolves the planet on shorter time scales. Thereby less observing time is needed to cover an orbital period, hence to detect more than one transit to ensure that the decrease in stellar luminosity is periodic and may be due to the existence of a planet.

For planets that have been observed in transit and with the radial velocity method planetary mass and radius are known. Hence, the mean density of the object can be estimated, which allows for a first characterization. According to their mean density planets can be classified as gas giants, icy or water planets and Earth-like planets made of rocky material and possibly an iron core, see Fig. 2.2 .

The transit geometry has further advantages. During the primary eclipse, when the planet crosses in front of the star, the transmission of the stellar light through the planetary atmosphere can in principle be observed and therefore the chemical composition of the atmosphere may be derived. This has been done for some giant planets (see e.g. Sing et al., 2011; Gibson et al., 2011; Redfield et al., 2008; Charbonneau et al., 2008), and has been tried also for some smaller planets (e.g. Bean et al., 2011; Croll et al., 2011; Guenther et al., 2011).
In some cases, especially for hot planets, also the secondary eclipse can be observed, the occultation of the planet by the star. This can be measured best at IR wavelengths, where the ratio of the planetary to stellar light is most favorable, since planets have their radiation maximum at IR wavelengths. From these observations the effective temperature of the planet, the atmospheric temperature structure and chemical composition of the atmospheres can in principle be derived. The thermal emission has already been measured for some Hot Jupiters and Neptunes (e.g. Crossfield et al., 2010, Knutson et al., 2008), but also for super-Earths (Demory et al., 2012).

Although the radial velocity and transit method are the most successful planet detection methods so far, other methods have been used to find more and more planets, such as

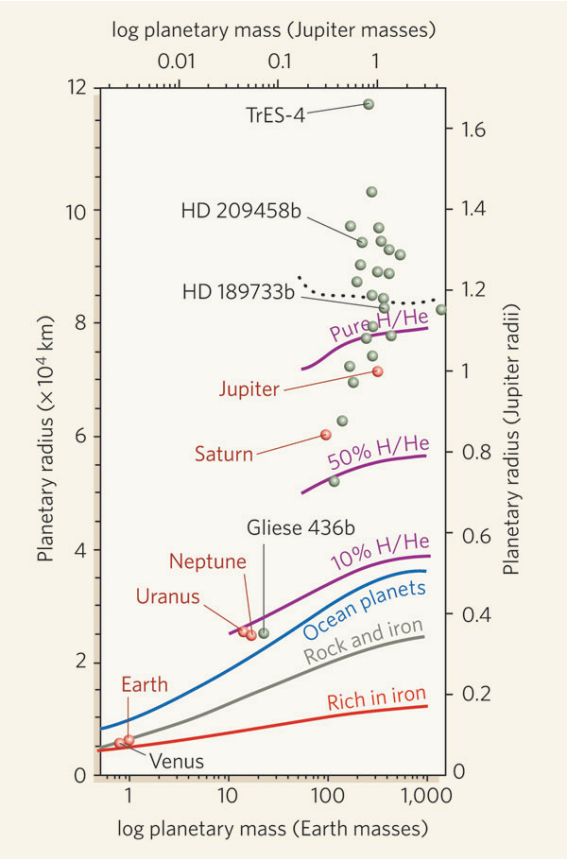

Figure 2.2: The figure shows the mass and the radius of some of the known exoplanets and the planets of our Solar System for comparison. Taken from Sasselov (2008).

astrometry, gravitational lensing, timing variations and direct imaging. Astrometry uses the fact, as the radial velocity method, that planet and star orbit a common center of mass causing a movement of the star on the sky. In contrast to the radial velocity method, astrometry measures the movement of the star orthogonal to the line of sight of the observer. This so-called *wobble* can be observed for nearby stars, since the shift of the stellar position has to be spatially resolved. This spatial movement is larger for heavy planets with a large semi major axis, because in this case the barycenter lies further away from the center of the star. Gravitational lensing utilizes the effect that masses act as a lens when passing through the line of sight to a background object, magnifying its light. Even low mass planets can cause a detectable magnification. However, the method suffers from the fact that lensing events are one time events and that planets found by this method are usually too far away for further characterization. Transit timing variations (TTVs) are used to detect additional planets in a system in which transiting planets have already been found. By the shift in the transit times, the size and orbital period of possible other companions can be derived. The most demonstrative detection method is direct imaging. To resolve a planet in the IR or in the visible the stellar light has to be eliminated by interferometry or coronagraphs. This has been accomplished for very bright, hence massive, mainly young planets far away from their central star.

The main goal and driver of exoplanet research is to find habitable, maybe even inhabited planets. Therefore much current effort focuses on the characterization of potential habitable planets and especially their atmospheres. To identify which planets could be habitable the complex interplay of various processes has to be understood.

2.2 Accessing the habitability of exoplanets

What does a planet need to be habitable, hence to hold the potential to sustain life? For the Earth, the only known habitable planet, but also for the other planets in the Solar System, the planetary conditions and their evolution are caused by the interplay of many factors such as processes in the planetary interior, in the atmosphere, on the surface, or by the interaction with space and for the Earth even with life itself. For such a complex system it is hard to define which conditions have to be met to call a planet habitable.
Life as we know it needs an energy source, nutrients, a solvent, and complex chemistry (e.g. McKay 2007). There are various energy sources used by life such as solar light by photosynthesizing life but also chemical energy by chemotrophic bacteria. Hence, energy sources are available in many forms throughout the Universe. Nutrients used by different lifeforms in their metabolism are very diverse and due to the high adaptability of life to its environment the seeking out of nutrients should not be a large problem. The building block molecules of life on Earth are complex carbon chains, forming large organic molecules. In the interstellar medium, a very different environment from Earth, organic molecules have been detected, which shows that even under such harsh environments complex molecules can form.

Furthermore, habitability is constrained by the need for an environment which allows for the existence of the liquid phase of chemical compounds, which can act as a good solvent. Focusing on the solvent used by Earth's life, liquid water, the temperature pressure range for planetary habitability can be constrained. However, these requirements could be met in the planetary interior or subsurface, only temporarily or locally, and the temperature

pressure range can be widened e.g. by impurification of water by salts.
However, in the search for habitable extrasolar planets the focus lies on surface habitability, determined by the potential presence of liquid water on the surface.
Even for this simplification, deciding whether or not a planet offers the right conditions for liquid water to exist on the planetary surface, is not an easy task, since planetary climate is controlled by complex processes and their interactions, as discussed above.
Already accessing the surface temperature for a given atmospheric composition, needs a detailed knowledge of the radiative properties of the atmospheric constituents, transport processes, boundary conditions at the surface, the energy distribution of the stellar light, etc. Whether such an atmospheric composition can exist at all, depends on the delivery during planetary formation, the outgassing and atmospheric escape history of the planet as well as interaction with the planetary interior and surface or even an biosphere, if existing, and on chemical processes in the atmosphere.
The interaction of the atmosphere with the surface depends on the surface type, its temperature but also on the possibility of recycling of surface material. For the Earth it is believed that plate tectonics lead to a replenishment of nutrients needed by the biosphere, but also to recycling of carbon-bearing species through the carbon-silicate cycle (e.g. Walker et al. 1981). This cycle is accredited to regulate Earth's climate on long time scales by enhanced (weakened) dissolution of the greenhouse gas CO_2 in warm (cool) periods, leading to a weaker (stronger) greenhouse effect, stabilizing the surface temperature.
Whether a terrestrial planet features plate tectonics depends on the interior structure, temperature, and composition of the crust and the mantle, as well as on planetary size, i.e. gravity (e.g. Valencia et al. 2007). Whereas Mars is too cold and too small to posses a mobile lid, for Venus the high surface temperatures might allow for surface mobilization (Noack et al., 2012), which rather occurs in some episodic events than in steady replenishment of the surface, as is the case for plate tectonics. Interior dynamics, such as convective processes, determine whether molten material in the form of partial melt can ascend up to heights, where, via volcanism, volatiles can be fed into the atmosphere by outgassing. Furthermore, effective convective cooling of the mantle is needed for the magnetic dynamo to work, generating a protecting magnetic field. Without a magnetic field atmospheric erosion by e.g. interaction with stellar wind might be intense, and cosmic rays may penetrate further down in the planetary atmosphere influencing e.g. the ozone layer (Grenfell et al., 2007).
The interior and atmospheric composition, planetary size, as well as other planetary and orbital parameter all depend on the initial conditions, hence on the formation of the stellar system. The inventory of chemical compounds, such as water and organics, is constrained by the molecular cloud from which the planetary system forms. Whether or not they are incorporated into a planet depends on the accretion history, planetary migration, and later delivery or blow-off of compounds due to impacts. These impacts can have a large influence on interior processes via heat generation, on the atmospheric composition, and of course the biosphere, causing extinction or could even sow life that originated on another planet.
For the planets and moons of our own Solar System the evolution in time is mostly derived from geological records. It can be estimated when liquid water has been present, by combining information from (hydrated) minerals with age determinations, either by measurements of radioactive elements, if they can be analyzed in the laboratory, or by counting of impact remnants on a planetary surface, since it is believed that the impact frequency and impactor sizes have changed during the evolution of the Solar System. The age of the planetary surface is then determined by comparison with crater characteristics

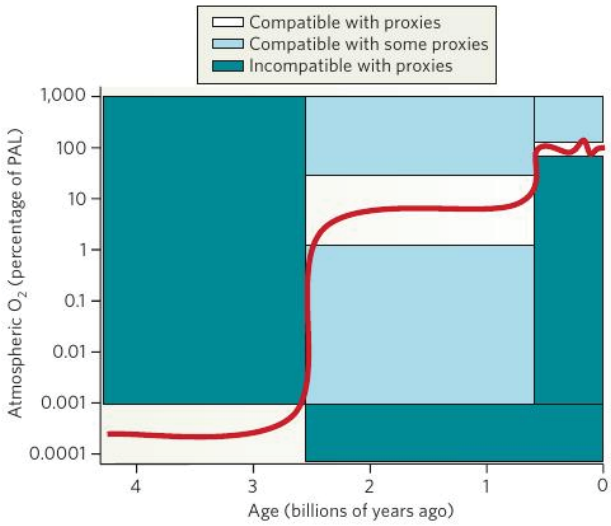

Figure 2.3: Illustration of the rise in oxygen over the evolution of the Earth's atmosphere leading to today tertiary atmosphere with 21% O_2. Taken from Kump (2008)

measured for the moon, where an age determination of the surface was possible due to sample return and detailed analysis in the laboratory.
It has been determined that the Earth must have had standing bodies of liquid water since, where it is discussed whether Mars has gone through a very cold and dry, or a wet and warm evolution.
Also traces of the first life forms are found in the geological record dating back to 3.8 Gyrs ago (e.g. Schopf and Packer, 1987). Life, by its utilization of any source of energy and substances in its metabolism, can alter surface minerals by metamorphism. On Earth the existence of a biosphere led to a change of the atmospheric composition from a reduced (probably CO_2 dominated) to an oxygen bearing atmosphere, after the onset of oxygen producing photosynthesis (see Fig. 2.3).
Hence, also life itself might alter its environment and adapt to the new conditions. During planetary evolution life on Earth has adapted to extreme environments such as hypothermal vents, permafrost, alkaline and acidic lakes, to high pressures in the deep oceans or the subsurface, as well as to very high radiative and desiccation stresses. Experiments in space show that life can even survive hostile conditions for a certain time, and laboratory experiments suggest that even under Martian conditions some microorganisms might actually be active (de Vera et al., 2010). Testing the adaptability of organisms to the wide range of stresses, might lead to a much broader understanding of habitable environments, as does the investigation of water properties under extreme conditions. Water can be liquid down to very low temperatures if it is present in the form of brines, and might also be available at interfaces.
Using theoretical and experimental approaches for studying the interaction of life with planetary environments and possible habitats for our Solar System, helps to identify circumstances under which life as we know it on other planets is in principle possible, and under which conditions it is rather unlikely to find Earth-like life forms.

CHAPTER 3

Theory

In this chapter the theoretical background for the studies presented in this work is given. First the processes relevant for atmospheres of terrestrial planets are presented (sec. 3.1), followed by a description of the Earth climatology, since Earth-like extrasolar planets are studied (sec. 3.2). Sections 3.3 and 3.4 give the basic equations used to describe terrestrial atmospheres.

3.1 Processes governing a terrestrial planetary atmosphere

Atmospheres of terrestrial planets are usually divided into atmospheric layers, which are governed by different physical processes. Starting at the planetary surface, the thin atmospheric layer which is governed by surface interactions is called the boundary layer, followed by the troposphere, a well mixed convective layer, where the temperature decreases with height, and where most of the weather phenomena take place. Above the troposphere lies the middle atmosphere, which is itself divided into the stratosphere, which is stably stratified, hence stable against convective processes, and the mesosphere. While the stratosphere has either a nearly constant temperature, as is the case for Mars and Venus, or temperatures which increase with height due to radiative heating, mesospheric temperatures decrease again with height. The mesosphere is followed by the thermosphere, where temperatures again increase with height due to heating by hard stellar radiation, which also leads to ionization of the atmospheric compounds. The atmosphere ends with the exobase, above which the exosphere starts, the loosely bound sphere, where atmospheric escape takes place.
Fig. 3.1 shows the annual global mean temperature profiles of the Earth, Venus and Mars from the surface up to the lower thermosphere for Earth and Mars and up to the upper stratosphere for Venus. The different structures of the middle atmospheres of Mars and Venus compared to Earth are clearly visible, showing the temperature inversion in the Earth's atmosphere in the stratosphere, with its maximum at the stratopause around 50 km. This temperature inversion is due to absorption of stellar light by ozone, which has its maximum abundance in the stratosphere. The Martian and Venusian atmosphere are different in composition and especially lack a high abundance of oxygen which is the precursor for the ozone layer. While the Earth's atmosphere is mainly composed of molecular nitrogen (N_2) and molecular oxygen (O_2), their atmospheres are CO_2–dominated, consisting of about 95% of carbon dioxide, and therefore do not absorb strongly in the ultraviolet/visible wavelength regime, hence no stratospheric temperature inversion is ob-

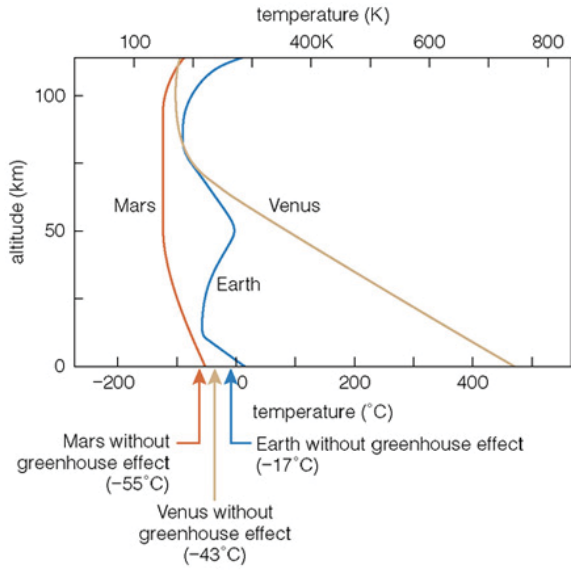

Figure 3.1: The atmospheric temperatures of the Earth, Mars and Venus all decrease with height in the troposphere. Above the tropopause the Earth sticks out with an increase in temperature due to ozone heating in the stratosphere, whereas Mars and Venus show only little temperature variation in the middle atmosphere. The equilibrium temperatures derived from the solar insolation and planetary albedo are indicated by arrows below the graph.

served for those atmospheres.

The temperature structures, and corresponding surface temperatures vary with atmospheric composition and mass. The atmospheric mass depends on the reservoir of volatiles given by the planetary formation process, as well as on the impact, outgassing, and escape history of the planet. The chemical composition in addition is influenced by chemical reactions within the atmosphere and the interaction with stellar light and the surface, which can lead to an increase/decrease of concentrations. Furthermore, surface emissions from the biosphere and interior as well as deposition on land or solution in the ocean alter the atmospheric concentrations.

Depending on the atmospheric composition and mass the stellar radiation is absorbed and scattered by atmospheric constituents. Furthermore, it is reflected and absorbed at the planetary surface. The absorption of stellar radiation leads to heating of the atmosphere and the surface, which then radiates predominately in the IR region due to their low temperatures. This reradiation of energy by the planet itself leads to a cooling of the atmosphere, but can also lead to an increase in surface and tropospheric temperatures by the greenhouse effect. The impact of greenhouse warming for the three terrestrial planets of the Solar System with substantial atmospheres is indicated in Fig. 3.1, where the arrows show the effective temperature calculated from the net incoming solar radiation, which are lower than the actual temperatures shown by the solid lines. The strength of the greenhouse effect depends on the amount and the corresponding opacity of so-called greenhouse gases in the atmosphere, which absorb the thermal radiation in the IR and homogeneously

reradiate it. In this way an additional heating of the underlying atmosphere and surface occurs. For the Earth the most important greenhouse gas is water vapor, which blocks a large part of the thermal radiation in the IR except for some *window regions*, followed by carbon dioxide and methane. A detailed description of the radiative energy transfer in a terrestrial atmosphere is given in section 3.3.5.1.

The concentrations of carbon dioxide and methane are dominated by emissions from the surface, boundary layer or the interior, whereas water concentrations are governed by a much more complex process, the hydrological cycle. Since water can exist in all three major phases on the Earth's surface but also in its atmosphere, the cycling of water due to evaporation from the surface into the atmosphere, formation of clouds and thereby corresponding precipitation determines the concentration of water vapor in the atmosphere. Additionally, also the temperature structure of the troposphere is influenced by the hydrological cycle, via latent heat release/storage during condensation/evaporation. During evaporation latent heat is stored as internal energy of the molecule and released during condensation. Clouds, as an important part of the hydrological cycle, can contribute to cooling of the atmosphere by scattering of incident radiation but also to the greenhouse effect by absorption of the IR radiation of the planet, depending on the optical properties, sizes and temperatures of the cloud particles.
The hydrological cycle further depends on convective processes and atmospheric dynamics. Convection strongly influences the vertical movement of air in the troposphere. It occurs when an air parcel is disturbed in such a way that it has a lower density than the surrounding air, which is often due to differential heating. Therefore, it can ascend until it reaches the density of its surrounding and thereby the same gravitational acceleration. Details about the treatment of convective processes can be found in section 3.4.

Both, the hydrological cycle, as well as the temperature structure of the atmosphere, hence the local variation of the temperature are coupled with atmospheric dynamics. In the troposphere atmospheric circulation is driven by the differential heating of the surface, which introduces temperature gradients. For the Earth the equatorial regions receive on average more stellar energy than the poles, which leads to the build up of meridional circulation cells. These transport air from the warm equator towards the poles. Due to the Coriolis force the poleward moving air is deflected to east, causing the tropospheric zonal winds. This deflection decreases the poleward directed velocity component and the air descends at latitudes of about 30°. Near the surface the air flows equatorwards and is deflected westwards. Adjacent to the Hadley cell, the mean meridional circulation is carried out by the Ferrel and the polar cell as will be described in section 3.2. In the middle atmosphere of the Earth, the meridional circulation transports air from the summer to the winter hemisphere. A comparison of an Earth-like atmosphere without dynamics in radiative equilibrium and one where atmospheric dynamics even out those contrasts is shown in Fig. 3.2. The circulation of the atmosphere also leads to a redistribution of chemical species by transport, so that e.g. ozone is most abundant during polar nights. Ozone is produced by the photodissociation of molecular oxygen where stellar light is available and then transported to the polar night regions where it cannot be destroyed by photolysis as is the case at the equator or in the summer hemisphere and can therefore accumulate.
Atmospheric dynamics are influenced by the differential heating of the atmosphere due to the diurnal cycle, the tilt in the Earth's rotational axis, the obliquity, and corresponding seasonal variations of incoming stellar radiation, as well as by the rotation rate of the

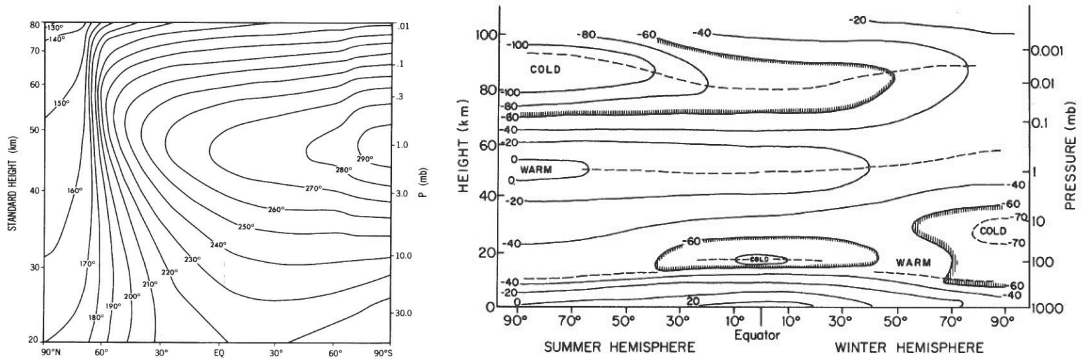

Figure 3.2: Left: atmospheric temperatures derived from radiative equilibrium, right: the atmospheric temperature structure taking into account atmospheric dynamics, where the solid lines represent temperature and the dashed lines indicate the tropopause, stratopause and mesopause. Taken from Andrews et al. (1987).

planet, and the resulting Coriolis force. Furthermore, planetary waves are generated by the shear forces within the atmosphere due to the decline in Coriolis force with latitude. Gravity waves develop at the surface, in the troposphere and the lower stratosphere either by differential heating or dynamical processes, such as the flow over an elevated, mountainous region. Those waves disturb the mean flow of the atmosphere, and therefore alter temperatures and wind systems. For the determination of the atmospheric flow, the hydrodynamic equations have to be solved which will be introduced in section 3.3.
As a lower boundary of the atmosphere the surface properties play an important role. The surface albedo determines the amount of stellar radiation absorbed or reflected, surface materials posses different heat capacities so that an ocean can store much more heat than a sandy surface in the desert. Also in terms of water reservoir the surface plays an important role, whereas the Earth's ocean has a nearly unlimited reservoir of water, deserts, by contrast, can store hardly any water at all. The ocean plays an important role for Earth's climate by transporting heat, evaporation of water, dissolution of carbon dioxide, release of sea salt to the atmosphere which can act as nuclei for cloud formation.
Since in this work neither the atmospheric escape nor the influence of volcanic outgassing will be addressed the detailed description of those processes will not be carried out. Also the interaction with the biosphere or the influence of chemical reactions is omitted.

Therefore only the relevant processes for this work will be described in the following, hence the equations governing the atmospheric flow (section 3.3), the radiative transfer in a terrestrial atmosphere (section 3.3.5.1) and convective and cloud processes (section 3.4). First, section 3.2 describes the general circulation and the resulting climatology of the Earth's atmosphere.

3.2 General Circulation and Earth climatology

In this thesis a complex state-of-the-art Earth climate model, described in section 5.3 will be applied to study extrasolar planetary scenarios. Since the change in climate for these planetary scenarios will be evaluated by comparing the results to those obtained for the

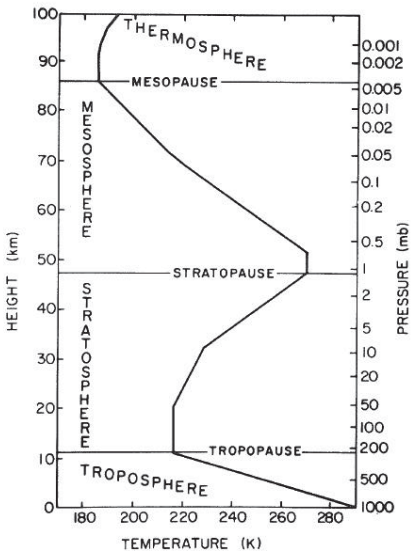

Figure 3.3: Mid-latitude vertical temperature structure of the Earth's atmosphere, indicating the different atmospheric layers and boundaries. Taken from Andrews et al. (1987) based on the US Standard Atmosphere 1976 (US1, 1976).

Earth around the Sun the climatology of the Earth is summarized in this section. For an Earth-like exoplanet localized phenomena are not the main focus but rather the mean properties in larger regions, such as the polar region, mid latitudes or equatorial regions. Therefore mostly zonal mean properties, i.e. averaged over longitudes, are shown in this thesis. This is mostly satisfactory for a quickly rotating planet like Earth. However, the circulation cannot be explained by zonally symmetric processes only.

The mean vertical temperature structure of the Earth's atmosphere (see Fig. 3.3) is mainly determined by radiative processes, hence the concentrations of radiative active gases and particles, and convection up to a height of 80 km. It is usually divided into layers, starting at the surface with the troposphere, where temperatures decrease with height. Above this lies the stratosphere with at first rather constant then increasing temperatures with height, followed by the mesosphere with decreasing temperatures. In the lower thermosphere temperatures are again increasing. These layers are divided by the tropopause, with a temperature minimum, the stratopause with a temperature maximum, and the mesopause with a temperature minimum. In the upper thermosphere and in the exosphere conditions for local thermodynamic equilibrium are no longer fulfilled and temperature cannot be defined in the thermodynamic picture.
The mean vertical temperature structure of the Earth results from heating of different layers, where the planetary surface is heated by absorption of solar and thermal radiation, the stratosphere is heated by the absorption of UV radiation by ozone, and the mesosphere and thermosphere are heated by the absorption of even higher energy radiation by molecular and atomic oxygen and nitrogen. In the upper atmospheric layers approximately above the ozone layer, which lies at heights of about 20–30 km, the vertical structure is the result of radiative equilibrium. In the lower atmosphere non-negligible heat fluxes of latent and sensible heat are present.

The zonal mean temperature averaged over longitudes or the meridional temperature structure are mainly the result of the differential heating of the atmosphere due to the higher mean solar insolation in the equatorial regions and lower insolation at the poles. These temperature gradients initiate the meridional atmospheric circulation, which evens out temperature differences and leads to a temperature profile different from that one would obtain in radiative equilibrium. Fig. 3.2 shows the different zonal mean temperature structures for excluding (left) or including atmospheric dynamics (right) for the Earth.

Due to the higher heating of the equatorial region, the equatorial air ascends and the air flows polewards. If the Earth would rotate more slowly the air would flow until the pole building a Hadley cell spanning over the entire hemisphere. However, due to the Coriolis force the poleward moving air is deflected eastwards and sinks at a latitude of about 30°. From there the air flows back towards the equator at low altitudes causing the westward directed trade winds and ends in the intertropical convergence zone (ITCZ), where large cloud clusters build up.
At mid latitudes the mean meridional circulation flows in the opposite direction of the temperature gradients, with ascending air in the subpolar regions and descending air at subtropical latitudes. This so-called Ferrel cell is driven dynamically. The adjacent Polar cell is, like the Hadley cell, thermally direct, transporting warmer air from the subpolar regions towards the pole. Hence, on average in each hemisphere three cells transport air from the warm equatorial regions towards the colder pole.

The above described meridional circulation is confined in the troposphere. The rising of the warm air in the equatorial region causes, due to adiabatic expansion, a cold equatorial tropopause at small pressures. Since the cold temperatures lead to the condensation of water vapor it is also often called cold trap.

The zonal mean temperature structure is shown in the left panels of Fig. 3.4 for January (upper panel) and July (lower panel). The stratospheric temperatures in the polar regions strongly depend on seasons. During the polar day the lower stratosphere is warm, and cold during polar night. Therefore, the lower stratospheric temperature increases towards the pole in summer and holds two cold regions in the winter hemisphere around the equator and the pole.

In the middle and the upper stratosphere the temperature is dominated by the absorption of UV-radiation by ozone. Many features in the temperature structure are associated with dynamics. The strongest temperature increase occurs in the summer polar stratosphere, and is smallest in the winter stratosphere, leading to a temperature gradient between the summer polar stratopause and the winter polar stratopause. In this region a meridional circulation, called the Brewer-Dobson circulation, spans over both hemispheres. The air rises through the polar summer stratopause into the mesosphere, where it cools adiabatically leading to a cold summer mesopause. From there it moves towards the winter pole where the air sinks and heats adiabatically, causing a warm mesopause and a heating of the winter stratopause.

The direction and strength of the zonal wind is a result of the horizontal temperature gradient. The zonal wind is depicted in the right panels of Fig. 3.4. In the troposphere the pole-to-equator temperature gradient causes strong westerlies, whereas in the stratosphere,

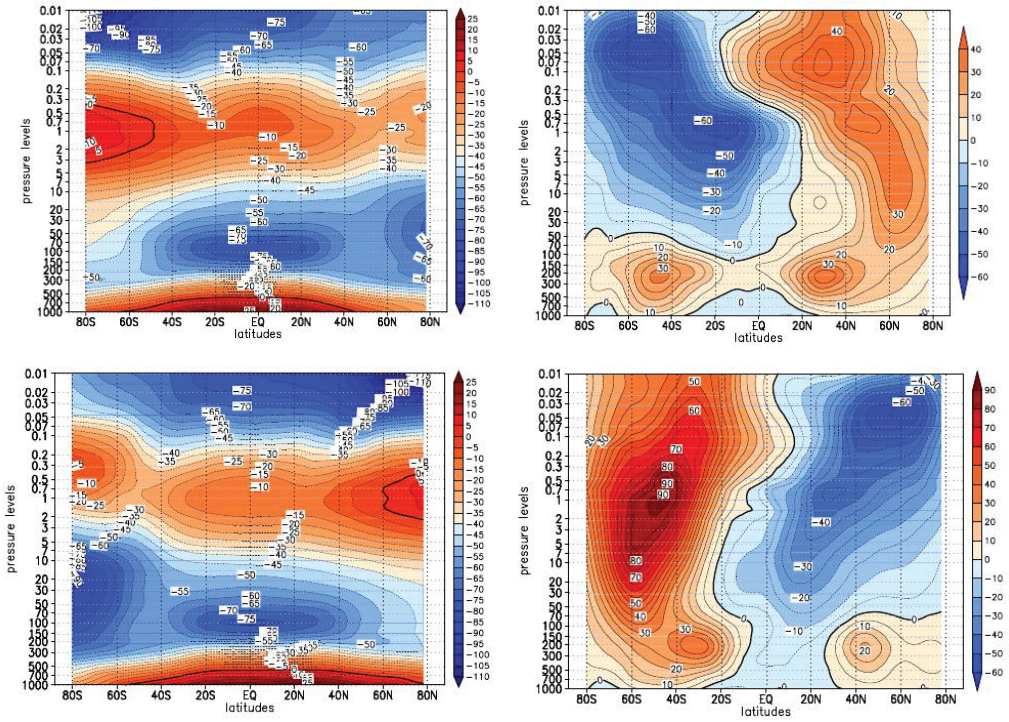

Figure 3.4: Zonal mean temperature structure and wind of the Earth's atmosphere. Upper panel: January temperature (left) and zonal wind (right), lower panel: July temperature (left) and zonal wind (right). Taken from the SPARC-Climatology (Stratospheric Processes And their Role in Climate), e.g. Randel et al. (2004).

due to the different temperature gradients in the hemispheres, the summer stratosphere shows easterlies and the winter stratosphere strong westerly winds. Regions of high zonal winds are often referred to as jet streams, such as the polar night jet stream near the winter stratopause.

The surface temperatures are highest in the equatorial regions, and northern and southern hemispheric temperatures vary with season. The northern hemispheric (NH) seasonal temperature variation is stronger due to the larger continental coverage in the NH, whereas the southern hemispheric (SH) temperature variations are buffered by the thermal inertia of the ocean.

3.3 Basic equations

In this section the basic equations governing the atmospheric circulation of an atmosphere are described. The formulations in this and the following sections mainly follow Satoh (2004) and Holton et al. (1995).
An attempt to describe the complex physical system of an atmosphere is by treating it as an ensemble of fluid particles. In fluid dynamics the fluid particle is treated as a mass point which interacts mechanically and does not change its properties. These fluid particles than make up an air parcel, which owns thermodynamic properties and can gain or lose

energy. It can change its humidity and its phase to become a set of real fluid particles as water droplets or even solid in the form of ice. Therefore the movement of the air parcels can be described by the equation of motion, whereas the energy of the air parcel is not only governed by external forces acting on the parcel but is furthermore determined by the inner energy affected by thermodynamics.

3.3.1 Conservation of mass

The conservation of mass can be written either in flux form from the continuity equation:

$$\frac{\partial \rho}{\partial t} + \nabla \cdot (\rho \vec{v}) = 0 \tag{3.1}$$

or in advective form:

$$\frac{d\rho}{dt} + \rho \nabla \cdot \vec{v} = 0 \tag{3.2}$$

using the material derivative $\frac{d}{dt} = \frac{\partial}{\partial t} + \vec{v} \cdot \nabla$, where $\rho = \sum_k \rho_k$ is the density of moist air,$\vec{v}$ the velocity.

For the components of moist air $\rho_k = \rho q_k$ (with $k = d, v, c$ for the components of moist air: dry air, water vapor and the condensed phases of water) the continuity equations are written as:

$$\begin{aligned} \frac{\partial \rho_d}{\partial t} + \nabla \cdot (\rho_d \vec{v}) &= 0 \\ \frac{\partial \rho_v}{\partial t} + \nabla \cdot (\rho_v \vec{v}) &= S(q_v) \\ \frac{\partial \rho_c}{\partial t} + \nabla \cdot (\rho_c \vec{v}) &= -S(q_v) \end{aligned} \tag{3.3}$$

where $S(q_v)$ is the source or sink of water vapor due to condensation, q_v the specific humidity and q_c the mass concentration of condensed water compounds (solid or liquid).

3.3.2 Conservation of momentum

The conservation of momentum is given by

$$\frac{d\vec{v}}{dt} = -\frac{1}{\rho} \nabla p - \nabla \Phi + \vec{f} \tag{3.4}$$

with p pressure, Φ the gravitational potential, and $\vec{f}$ the frictional force, which has the components:

$$f_i = \frac{1}{\rho} \frac{\partial}{\partial x_j} \sigma'_{ij}, \tag{3.5}$$

σ'_{ij} being the viscous stress tensor. This form of the equation of motion is also called the Navier-Stokes equation.

The motions in an atmosphere are usually in a rotating inertial frame. So for an arbitrary variable $\vec{A}$ this relates the time derivative in the inertial frame $\left(\frac{d\vec{A}}{dt}\right)_a$ to the time derivative

in the rotating frame $\left(\frac{d\vec{A}}{dt}\right)_r$ as

$$\left(\frac{d\vec{A}}{dt}\right)_a = \left(\frac{d\vec{A}}{dt}\right)_r + \vec{\Omega} \times \vec{A}, \tag{3.6}$$

hence for the position $\vec{x}$ it follows: $\vec{v_a} = \vec{v_r} + \vec{\Omega} \times \vec{x}$ and for the derivative of $\vec{v_a}$:

$$\begin{aligned} \left(\frac{d\vec{v_a}}{dt}\right)_a &= \left(\frac{d\vec{v_r}}{dt}\right)_r + 2\vec{\Omega} \times \vec{v_r} + \vec{\Omega} \times \left(\vec{\Omega} \times \vec{x}\right) \\ &= \left(\frac{d\vec{v_r}}{dt}\right)_r + 2\vec{\Omega} \times \vec{v_r} - \nabla \left(\frac{1}{2}\vec{\Omega}^2 \left(\vec{x} - \frac{(\vec{x} \cdot \vec{\Omega})\vec{\Omega}}{|\vec{\Omega}^2|}\right)\right) \end{aligned} \tag{3.7}$$

with $-2\vec{\Omega} \times \vec{v_r}$ the Coriolis force, $\vec{\Omega} \times \left(\vec{\Omega} \times \vec{x}\right)$ the centrifugal force and $\nabla \left(\frac{1}{2}\vec{\Omega}^2 \left(\vec{x} - \frac{(\vec{x} \cdot \vec{\Omega})\vec{\Omega}}{|\vec{\Omega}^2|}\right)\right)$ the gradient of the centrifugal potential energy. The centrifugal potential energy is usually combined with the gravitational potential Φ to the geopotential

$$\Phi_r = \Phi + \frac{1}{2}\vec{\Omega}^2 \left(\vec{x} - \frac{(x \cdot \vec{\Omega})\vec{\Omega}}{|\vec{\Omega}^2|}\right). \tag{3.8}$$

With this we obtain the equation of motion within the rotating frame

$$\frac{d\vec{v_r}}{dt} - 2\vec{\Omega} \times \vec{v_r} = -\frac{1}{\rho}\nabla p - \nabla \Phi_r + \vec{f}. \tag{3.9}$$

If we assume that the atmosphere is at rest ($\vec{v_r} = 0$) we obtain the hydrostatic balance:

$$\nabla \Phi_r = \frac{1}{\rho}\nabla p, \tag{3.10}$$

which is assumed to be satisfied for large-scale fields on planet like Earth, where the horizontal velocity is much larger than the vertical velocity component.

Further assumptions, such as a spherical geopotential Φ_r, which only varies with height z, and an atmosphere which has a thickness which is small compared to the radius of the planet, lead to a simplified form of the hydrostatic balance:

$$\frac{1}{\rho}\frac{\partial p}{\partial z} = \frac{\partial \Phi}{\partial z} = g = \frac{GM}{R^2} \tag{3.11}$$

with g the gravitational acceleration which is determined by the mass of the planet M, the gravitational constant G and the radius of the planet R.
For the assumption of hydrostatic equilibrium the equation of motion can be split into a vertical part, which is approximated by the hydrostatic balance and a horizontal part:

$$\frac{d\vec{v_H}}{dt} - f\vec{k} \times \vec{v_H} = -\frac{1}{\rho}\nabla_H p - \nabla_H \Phi_r + \vec{f_H} \tag{3.12}$$

with $f = 2\Omega$ the Coriolis parameter and $\vec{k}$ the unit vector in the vertical direction.

3.3.3 Conservation of energy

The conservation of energy is given by the continuity equation for the kinetic, potential and internal energy as:

$$\frac{\partial}{\partial t}\left(\rho\left(\frac{\vec{v}^2}{2}+\Phi+e\right)\right)+\nabla\cdot\left(\rho\vec{v}\left(\frac{\vec{v}^2}{2}+\Phi+e\right)+p\vec{v}-v_j\sigma'_{ij}+F_H\right)=0 \tag{3.13}$$

with F_H the heat flux, which has contributions from thermal and radiative heat fluxes, hence $F_H = F_{therm} + F_{rad}$.
The thermodynamic equation is obtained by the equation for internal energy

$$\frac{\partial(\rho e)}{\partial t}+\nabla\left(\rho e\vec{v}+F_H\right)=-p\nabla\cdot\vec{v}+\epsilon \tag{3.14}$$

which can be rewritten by using the continuity equation (3.2) and the thermodynamic relation from the first and second law of thermodynamics

$$de = Tds + pdv_s + \sum_k \mu_k dn_k \tag{3.15}$$

to

$$\frac{dh}{dt}=\frac{dp}{dt}+\epsilon-\nabla\cdot F_H, \tag{3.16}$$

the equation for the specific enthalpy ($h = u + pv_s$).

From $h = C_pT + Lq$ an equation for the change in temperature can be written as

$$\rho\frac{d}{dt}(C_pT)=\frac{dp}{dt}+\epsilon-\nabla\cdot(F_{rad}+F_{sh})-LS_q \tag{3.17}$$

where it has been used that $F_{therm} = L\vec{i_v} - \kappa_T\nabla T = F_{lh} + F_{sh}$ the latent and sensible heat flux with $\vec{i_v} = \rho_v(\vec{v}-\vec{v})$ the density of the diffusion flux of water vapor, which results from the velocity difference of the vapor phase $\vec{v_v}$ to the bulk velocity of moist air $\vec{v}$. κ_T is the thermal conductivity, and $\epsilon = \sigma'_{ij}\frac{\partial}{\partial x_j}v_i$ the dissipation rate of kinetic energy.
With this the balance of total energy can be written as:

$$\frac{\partial}{\partial t}\left(\rho\left(\frac{\vec{v}^2}{2}+\Phi+e\right)\right)+\nabla\cdot\left(\rho\vec{v}\left(\frac{\vec{v}^2}{2}+\sigma\right)-v_j\sigma'_{ij}+F_{rad}+F_{sh}+F_{lh}\right)=0 \tag{3.18}$$

with $\sigma = h + \Phi$ the moist static energy, which relates to the dry static energy (σ_d) as $\sigma = \sigma_d + L_0 q_v$.

3.3.4 Basic thermodynamic quantities of moist air

To describe the behavior of the atmosphere it is assumed that the gaseous phase is composed of dry air and water vapor and that the gaseous phase and the condensed phases of water are in equilibrium. Furthermore it is assumed that air, a mixture of uniformly mixed gases and water vapor, can be regarded as an ideal gas.

The thermodynamic state of the air parcel is determined by temperature T and pressure p. The volume of the fluid is then given by the equation of state. $p = p(\rho, T)$ with $\rho = \frac{1}{v_s}$

is the density, v_s the specific volume, hence the volume per unit mass. For an ideal gas the equation of state can be written as

$$p = \frac{\rho R^* T}{m}, \tag{3.19}$$

with R^* =8.31436 $\mathrm{Jmol^{-1}K^{-1}}$ the gas constant of an ideal gas, T temperature, m the molecular weight of the ideal gas, and p pressure. For a mixture of ideal gases the equation of state is then:

$$p = \sum_k n_k \rho R^* T. \tag{3.20}$$

n_k the moles of compound k per unit mass, also called molar concentration. For dry air

$$p = \rho R_d T \tag{3.21}$$

the equation of state is obtained with $R_d = R^*/m_d$ the gas constant of dry air, with $m_d = \frac{1}{\sum_k n_k}$ the molar mass of dry air, where k denotes the components of dry air.

For moist air the equation of state changes to

$$p = (n_d + n_v)\rho R^* T = (q_d R_d + q_v R_v)\rho T = p_d + p_v, \tag{3.22}$$

where $n_{d/v}$ are the moles of dry air and vapor per unit mass, $q_{d/v} = n_{d/v} m_{d/v}$ are the mass concentrations of dry air and water vapor (specific humidity), and $p_{d/v}$ are the partial pressures.

From this an expression for the density can be derived:

$$\rho = \frac{p}{R_d T_v} = \frac{p}{R_d T (q_d + q_v \frac{R_v}{R_d})} \tag{3.23}$$

with T_v being the virtual temperature.

Furthermore, following mass conservation

$$q_d + q_w = q_d + q_v + q_c = 1 \tag{3.24}$$

has to be fulfilled with q_w the mass concentration of the water compounds in the atmosphere and with q_c the mass concentration of the condensed water phase. The equation of state is not easily derived for the condensed phase, therefore it is usually assumed that the condensed phase and the gaseous phase of the substance, here water, are in equilibrium. Then the thermodynamic properties of the condensed phase are derived from the equilibrium.
Furthermore, with n_w the molar concentration of water compounds, the molar water mixing ratio r can be defined as

$$r = \frac{n_w}{n_d}. \tag{3.25}$$

The specific heat at constant pressure C_p is given by

$$C_p = q_d C_{pd} + q_v C_{pv} + q_c C_{pc}, \tag{3.26}$$

the specific enthalpy by

$$h = q_d h_d + q_v h_v + q_c h_c, \tag{3.27}$$

the internal energy

$$e = q_d e_d + q_v e_v + q_c e_c, \tag{3.28}$$

and the entropy by

$$s = q_d s_d + q_v s_v + q_c s_c, \tag{3.29}$$

where the subscript d denotes the values for dry air, v for water vapor, and c for the condensed phase of water.
For dry air the enthalpy, internal energy, and entropy are given by:

$$\begin{aligned} h_d &= C_{pd} T \\ e_d &= C_{vd} T \end{aligned} \tag{3.30}$$

and

$$s_d = C_{pd} ln \frac{T}{T_0} - R_d ln \frac{p_d}{p_0}. \tag{3.31}$$

For water vapor and the condensed phase release of latent heat has to be taken into account. Therefore, these thermodynamic quantities are then given by:

$$\begin{aligned} h_v &= C_{pc} T + L \\ e_v &= C_{vv} T - L - R_v T \\ s_v = C_{pv} ln \frac{T}{T_0} - R_v ln \frac{p_v}{p_{0,sat}} + \frac{L_0}{T_0} &\text{and} \end{aligned} \tag{3.32}$$

$$\begin{aligned} h_c &= C_{pc} T \\ e_c &= C_{pc} T \\ s_c &= C_{pc} ln \frac{T}{T_0} \end{aligned} \tag{3.33}$$

where L is the latent heat per unit mass, L_0 the latent heat at 0°C=T_0, for p_0 usually 1000 hPa is used and $p_{0,sat}$ is the water vapor saturation pressure at 0°C.
The enthalpy of moist air can be written as

$$h = C_{pd} T + L_0 q_v \tag{3.34}$$

when assuming that the amount of water vapor is relatively low in the atmosphere ($q_d \approx 1$), that latent heat does not change with temperature $L = L_0$ and that the specific heat of the water phase is much lower than for dry air $q_w C_{pc} \ll C_{pd}$.
From the entropy of moist air one obtains by assuming that water vapor is saturated and the pressure is dominated by the partial pressure of dry air the definition of the potential temperature:

$$\theta = T \left(\frac{p_0}{p} \right)^{\frac{R_d}{C_{pd}}} \tag{3.35}$$

and the equivalent potential temperature θ_e

$$\theta_e = \theta exp \left(\frac{L_0 q_v}{C_{pd} T} \right), \tag{3.36}$$

which are both conserved quantities in thermodynamic reversible processes and often used in meteorology.

It is furthermore useful to define the adiabatic lapse rate which gives the temperature change of an air parcel in an isentropic, entropy conserving, process. Under the assumption that the molar concentration of dry air and the total molar concentration of water do not change in this process the moist adiabatic lapse rate

$$\gamma_m = \left(\frac{\partial T}{\partial p}\right)_s = \gamma_d \frac{n_d + n_v}{n_d} \frac{1 + \frac{n_v}{n_d}\frac{l}{R^* T}}{1 + \frac{n_v c_{pv} + n_c c_{pc}}{n_d c_{pd}} + \frac{l^2}{c_{pd} R^* T^2}\frac{n_v(n_v+n_d)}{n_d^2}} \tag{3.37}$$

can be obtained with $\gamma_d = \frac{R^* T}{c_{pd}}$ the dry adiabatic lapse rate. The above equation describes the temperature change in the case of no rain fall, hence for reversible thermodynamic processes, since it is assumed that the total amount of water is preserved. As another extreme it can be assumed that all condensed water precipitates (n_c =0), which leads to the pseudo-adiabatic lapse rate:

$$\gamma'_m = \left(\frac{\partial T}{\partial p}\right)_s = \gamma_d \frac{n_d + n_v}{n_d} \frac{1 + \frac{n_v}{n_d}\frac{l}{R^* T}}{1 + \frac{n_v c_{pv}}{n_d c_{pd}} + \frac{l^2}{c_{pd} R^* T^2}\frac{n_v(n_v+n_d)}{n_d^2}}. \tag{3.38}$$

Both moist adiabatic lapse rates above simplify to the dry adiabat when humidity is zero.

3.3.5 Energy transport

For an average over time and horizontal space and by neglecting the kinetic energy and viscous stress, the energy balance for the moist atmosphere can be written as:

$$\frac{\partial}{\partial z}\left(F_{rad} + F_{sh} + F_{conv}\right) = 0, \tag{3.39}$$

with $F_{conv} = \rho\sigma w$, the convective energy flux. Assuming that the sensible heat flux F_{sh} only contributes to the energy at layers close to the surface the energy balance for the main energy transport processes, radiation and convection is given. While on average the upper atmosphere is in radiative equilibrium ($\frac{\partial F_{rad}}{\partial z}$=0), in the lower atmosphere energy transport by convection plays an important role (see 3.4).

3.3.5.1 Radiative transfer

To obtain the heating or cooling of the atmosphere by radiative processes the radiative transfer equation has to be solved:

$$\frac{dI_\nu(\vec{s})}{ds} = -k_\nu \rho_i I_\nu(\vec{s}) + j_\nu \rho_i \tag{3.40}$$

with $I_\nu(\vec{s})$ the spectral intensity per solid angle, which depends on direction $\vec{s}$, k_ν the extinction, j_ν the emission coefficient per unit mass and ρ_i the density of absorbing or scattering species. The extinction coefficient covers the reduction of spectral energy due to absorption or scattering of light, while emission of light and scattered light can contribute to the emission coefficient. Eq. 3.40 may also be written as

$$-\frac{1}{k_\nu \rho_i}\frac{dI_\nu(\vec{s})}{ds} = I_\nu(\vec{s}) - J_\nu(\vec{s}) \tag{3.41}$$

where $J_\nu(\vec{s}) = \frac{j_\nu}{k_\nu}$ is the source function.
If only absorption is present $J_\nu(\vec{s}) = 0$ integration from 0 to s leads to Beer-Lambert's Law:

$$I_\nu(s, \vec{s}) = I_\nu(0, \vec{s}) exp(-\tau_\nu(0, s)) = I_\nu(0, \vec{s}) T_\nu(0, s) \tag{3.42}$$

with $\tau_\nu(0, s) = \int_0^s k_\nu \rho_i ds$ the optical depth and T_ν the transmission.
In the case where emission and scattering occur the source function is given by

$$J_\nu(\vec{s}) = \frac{1}{k_\nu}(j_\nu^a + j_\nu^s) = \frac{1}{k_\nu}\left(k_\nu^a B_\nu(T) + k_\nu^s \int I_\nu(\vec{s'}) P(\vec{s}, \vec{s'}) \frac{do'}{4\pi}\right) \tag{3.43}$$

where j_ν^a is the emission coefficient, which results from reradiation of absorbed radiation. j_ν^s is the emission coefficient which results from the scattering of radiation. $P(\vec{s}, \vec{s'})$ is the phase function which represents the ratio of the scattering of incident radiation with direction $\vec{s'}$ into the new direction $\vec{s}$. The phase function depends on the scattering properties of the substance. If we assume scattering by molecules only, the phase function for Rayleigh-scattering, $P(\mu) = \frac{3}{4}(1 + \mu^2)$ with μ the cosine of the angle between direction $\vec{s}$ and $\vec{s'}$ can be assumed. The total energy flux by radiation is obtained by integration over all frequencies and angles.

For the emission of the atmosphere the energy flux emitted by a black body of a certain temperature is assumed. According to Planck's law the energy flux emitted per unit solid angle and frequency interval $d\nu$ is

$$B_\nu d\nu = \frac{2h\nu^3}{c^2} \frac{d\nu}{exp(\frac{h\nu}{k_B T}) - 1} \tag{3.44}$$

where c is the speed of light and k_B the Boltzmann constant. Integration over all frequency gives the total energy emitted per unit solid angle:

$$B(T) = \int_0^\infty B_\nu d\nu = \frac{2h}{c^2} \int_0^\infty \frac{v^3 d\nu}{exp(\frac{h\nu}{k_B T}) - 1} = \frac{\sigma_B}{\pi} T^4 \tag{3.45}$$

with σ_B the Stefan Boltzmann constant. The total energy per area is then given by $F = \sigma_B T^4$.

3.3.5.2 Global energy budget

For the Earth and the other terrestrial planets of the Solar System, and probably for most of the evolved extrasolar planets it can be assumed that the atmosphere is on average in radiative equilibrium. This can be expressed as

$$F_{net,\downarrow} = F_{net,\uparrow}. \tag{3.46}$$

The net incoming radiation $F_{net,sol\downarrow}$ is given by the net stellar energy flux $F_{net,sol\downarrow} = F_{sol,\downarrow} + F_{sol,\uparrow} = (1 - A)F_{sol,\downarrow}$ where A is the planetary albedo $F_{sol,\downarrow}$ the incoming stellar radiation and $F_{sol,\uparrow}$ the radiation reflected by the planet. $F_{sol,\downarrow}$ relates to the total stellar irradiance (F_{TSI}) as $F_{sol,\downarrow} = F_{TSI}\pi R^2$, where πR^2 is the area of the planet that absorbs stellar radiation.
The net outgoing radiation $F_{net,\uparrow}$ has an additional contribution by the thermal emission

of the planet.

Assuming that the planet radiates as a black body the net energy can be expressed in terms of temperature by the Stefan-Boltzmann Law (see Eq.3.45). $F_{net,therm\uparrow} = 4\pi R^2 \sigma_B T^4$ is the total net radiative energy flux emitted by the planet where $4\pi R^2$ is the surface area of the planet, since the planet emits to all directions. With this the global energy balance can be written as:

$$\sigma_B T^4 = \frac{(1-A)F_{TSI}}{4}. \tag{3.47}$$

This equation gives the effective temperature in dependence of the stellar irradiance and the planetary albedo. The effective temperature is usually different from the surface temperature of a planet due to the greenhouse effect.

3.4 Convection

In this section the processes leading to convection as well as different methods used to describe the influence are introduced. Convection influences atmospheric temperatures, motions and mass transport.

Atmospheric temperatures determined by radiative equilibrium usually lead to a statically unstable vertical temperature structure, since the temperature lapse rate is larger than that of a dry adiabat in the lower layers of the atmosphere. This leads to convection, which will establish a new equilibrium state of the atmosphere by movement of air parcels which transport heat and moisture. Energy is then transported by both, convection and radiation in the lower atmospheric layers. There are different approaches to handle the effect of convection on the atmosphere, either by accounting for the influence of convection only on temperature, this is done by convective adjustment, or by modeling the convective energy flux, which is for example done by mixing length theory or by mass-flux schemes, which account for the transport of heat and moisture. In a dry atmosphere convection will be similar to turbulent mixing, where warm air rises due to differential heating of the atmosphere leading to higher temperatures, hence lower densities. This gives positive buoyancy to the air parcel with higher temperature.

For a moist atmosphere, the influence of moisture has to be taken into account. Moist air can become buoyant by an increase of temperature or humidity, since water vapor is lighter than dry air. Therefore, moist air is much more easily convecting as dry air as can be seen by the large convective cells in the tropics of the Earth. When moist air rises the release of latent heat has to be taken into account, which is known to be asymmetric. Latent heat is mostly released during upward motion of air. This cannot be taken into account by a moist-adiabatic lapse rate nor by mixing length theory. An attempt to account for this effect is made in so-called cumulus convection models for moist convection, which include different processes for ascending and descending air in convective regions.

3.4.1 Convective adjustment

The simplest way to account for convection is by its influence on the temperature. This is done by first evaluating the stability of the vertical temperature profile with the Schwarzschild-

criterion, which is given by

$$\left|\frac{\partial T}{\partial z}\right|_{rad} < \left|\frac{\partial T}{\partial z}\right|_{ad}, \tag{3.48}$$

where $\left|\frac{\partial T}{\partial z}\right|_{rad}$ is the lapse rate determined by radiative transfer and $\left|\frac{\partial T}{\partial z}\right|_{ad}$ is the adiabatic lapse rate determined for moist or dry air (see eq. 3.37).

As long as $|\frac{\partial T}{\partial z}|_{rad}$ is smaller than the moist adiabatic lapse rate, the atmosphere is absolutely stable. For a radiative temperature lapse rate $|\frac{\partial T}{\partial z}|_{rad}$, which is larger than the moist adiabat, but smaller than the dry adiabatic lapse rate the atmosphere is conditionally unstable. In this case a saturated parcel will convect and its temperature will change with height following the moist adiabat. An unsaturated air parcel is not convecting in this case, however, in case of an perturbation it may saturate, which will increase its buoyancy and lead to convection. The atmosphere is absolutely unstable if the radiative temperature lapse rate is larger than the dry adiabatic lapse rate. For unstable conditions the vertical temperature profile may be approximated by the appropriate adiabatic lapse rate.

3.4.2 Convective available potential energy (CAPE)

Another approach to test whether or not an air parcel will convect is to evaluate the buoyancy a parcel will gain by a small displacement. The buoyancy of the air parcel depends on the density difference to the environment:

$$b = -\frac{\rho_{parcel} - \rho_{environemnt}}{\rho_{environemnt}} g \tag{3.49}$$

where ρ_{parcel} is the density of the air parcel and $\rho_{environemnt}$ the density of the environment. For this small displacement it is assumed that the air parcel has the same pressure as the environment and no heat or moisture exchange takes place between the parcel and the environment. In an conditionally unstable environment the buoyancy of the parcel is negative as long as it is unsaturated. If the parcel is however lifted above the level where the parcel starts to saturate, called the cloud base or lifting condensation level, it will gain positive buoyancy and convection sets in. Since the environmental lapse rate usually decreases with height close to the tropopause and the temperature in the stratosphere of the Earth increases, the buoyancy of the air parcel will decrease and vanish. The level where buoyancy vanishes is called the cloud top, since usually cumulus cloud can be associated with convective active regions. From this the convective available potential energy (CAPE) can be calculated by:

$$CAPE = \int_{z_B}^{z_T} b dz = -\int_{z_B}^{z_T} \frac{\rho_{parcel} - \rho_{environemnt}}{\rho_{environemnt}} g dz \tag{3.50}$$

where z_B is the level from where the parcel has been displaced and z_T the level where the buoyancy vanishes. CAPE gives the upper limit of energy available for convective motion. In reality not all of this energy will be converted into kinetic energy since dissipative processes will lead to exchange of moisture and heat with the environment.

3.4.3 Cumulus convection

Cumulus convection is convection of moist air usually associated with cloud formation due to condensation and an upward mass flux, which carries momentum, energy and moisture. In cumulus convection models usually three different types of convection are distinguished: deep and shallow convection, which both start at the surface, and mid-level convection which may start also at higher atmospheric layers.
Usually in cumulus convection models an ensemble of updrafts and downdrafts are considered. As a first approach one may assume that updrafts, regions with upwards moving air parcels are separated from downdraft. Then latent heat is released during upward motion when condensation due to saturation takes place. Mixing of air in this simplified picture only takes place at the base or the top of the convective cell, and no latent heat is released or deposited in the downdrafts. In reality, however, environmental air will mix into the updraft, called entrainment, and air in the downdraft will be transfered to the environment, which is called detrainment.

3.5 Clouds

Clouds may form when air becomes supersaturated. This is often the case in convective active regions, since upward moving parcels will cool adiabatically, and may therefore be saturated. A small water droplet which forms due to supersaturation is not stable and will evaporate if it has not reached a certain size, the critical radius. In the Earth's atmosphere growth until this critical radius is difficult for homogeneous nucleation, since supersaturation only rarely exceeds a few percent. Therefore, the formation of cloud particles mostly occurs by heterogeneous nucleation, where the so-called cloud condensation nuclei help to overcome the critical radius. The aggregate state of the cloud particle depends on the temperature, and saturation of the air with respect to liquid water or ice. If cloud particles have condensed and are stable they may grow, either by further condensation or by deposition of water vapor onto the particle. Since during condensation and deposition latent heat is released, the environmental temperature will increase which lowers the condensation (deposition) rate, hence growth of cloud particles by these processes is slow. Other processes which contribute to the growth of particles are freezing of water droplets to ice and coagulation, where smaller cloud particles merge to larger ones. If a cloud consists of water droplets and ice crystals, the ice crystals will tend to grow at expense of the water droplets since the saturation of the air with respect to ice will be larger than this with respect to supercooled water. Since gravity act on the cloud particles they will tend to fall out as precipitation, rain or snow fall. While falling the particles can grow further due to collisions with other particles. Within the cloud and during precipitation cloud droplets may evaporate, ice crystals may melt and form water droplets or sublimate depending on the environmental properties. The properties of the cloud particles, such as e.g. the size distribution depend on the microphysical processes described above and on the environmental properties.

3.6 Summary

In this chapter the major processes determining the climate of an terrestrial planet and the basic equations have been presented. These build the basis for the models described in the next chapter.

CHAPTER 4

Studies of rocky extrasolar planets

Planetary climate is governed by the interplay of many different processes, as discussed in the previous section. Some of these processes and influences have been studied already, others still need to be investigated in detail. This section will give an overview of literature dealing with exoplanet climate studies. Since this work deals with three dimensional (3D) modeling of planetary climate there will be a special focus on studies of planetary climate modeling with 3D models rather than in one dimension (1D), although of course the important 1D studies for this thesis will be discussed.
In this work it is investigated how planetary climate changes for a habitable planet around different stellar types. For such a planet the stellar radiation is different as well as the orbital period to obtain a similar energy supply by the star. Therefore in section 4.1 studies investigating the influence of different stellar types will be reviewed. In section 4.2 studies accounting for orbital parameters such as eccentricity and obliquity, but also planetary parameters such as rotation rate are discussed. Section 4.2 will deal with a sample of climate studies focusing on the influence of surface properties and their interaction with the atmosphere, which are hard to tangle with 1D models. Most of the studies include a change of more than one of these parameters, they are therefore divided according to their main focus.

4.1 Influence of stellar type

For extrasolar planets around different stellar types, the first major difference is the stellar luminosity, which depends on the stellar type, its size and effective temperature. This leads to the fact that habitable planets around smaller, cooler stars than the Sun have to be located closer to the star, and conversely for larger, hotter stars to obtain enough energy by stellar radiation. In addition, also the spectral energy distribution is different for other stellar types, leading to different planetary climates for the same atmospheric composition due to different heating and cooling of the planet, caused by the change in the absorption and scattering by the planetary atmosphere of the stellar light. Furthermore, stars evolve in time and with it their net luminosity, e.g. Gough (1981). The impact of these factors upon the planetary habitability has been studied by Hart (1978) for the Earth and by Hart (1979) for other stars, where the influence of the spectral energy distribution was not taken into account.

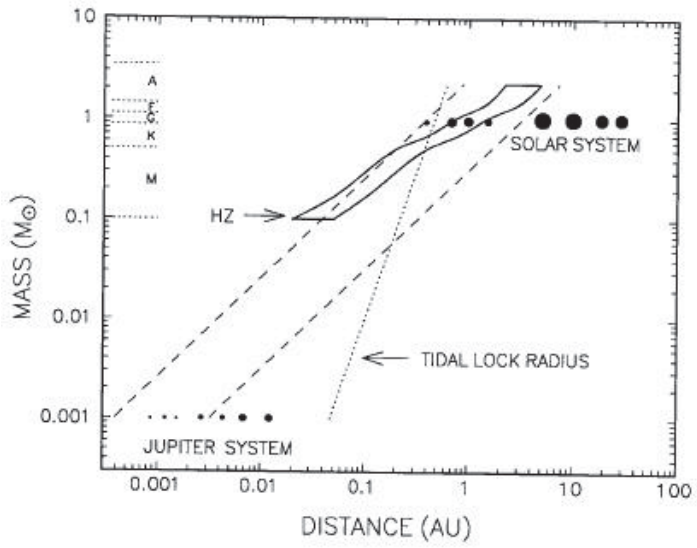

Figure 4.1: Continuous HZ (indicated by solid lines) after Kasting et al. (1993) for an extrasolar planet with an Earth-like atmosphere around main sequence stars. The long dashed lines indicate possible planet positions after planet formation models, the dotted line shows at which distance an Earth-like planet in a circular orbit would be bound in synchronous rotation within 4.5 billion years.

Hart (1979) concluded that the continuous habitable zone (CHZ), the region around a star where an Earth-like planet can maintain liquid water over a time span of about 4 billion years (4 Gyrs), would be either very small or absent for planets around cooler stars, such as K and M-dwarfs.

To reevaluate the result of Hart (1979) **Kasting et al. (1993)** made use of a 1D radiative-convective climate model with a non-gray radiative transfer. They defined four different boundaries of the habitable zone (HZ). The water loss limit and the runaway greenhouse limit at the inner edge of the habitable zone. For the water loss limit a water reservoir of one Earth ocean can be lost during the lifetime of the planet (assumed to be the current lifetime of the Earth) by diffusion through the atmosphere. The runaway greenhouse limit is determined by reaching a surface temperature of the critical point of water (647 K). For the outer edge the two boundaries are called 1st condensation limit and the maximum greenhouse effect. The first condensation limit is defined by the first occurrence of such low temperatures in the planetary atmosphere that carbon dioxide (CO_2) would start to condense. The maximum greenhouse boundary is found where for a stellar insolation even increasing the amount of CO_2 in the atmosphere would not lead to surface temperatures above the freezing point of water. For atmospheres with large amounts of CO_2 the Rayleigh scattering of the stellar radiation will dominate over the greenhouse effect. This leads to a blocking of stellar radiation rather than to a warming of the surface.

As a conclusion Kasting et al. (1993) found that the width of the habitable zone about low mass main sequence stars (late K and M dwarf stars) is not negligible for an Earth-like planet with an Earth-like atmosphere as opposed to the findings of Hart (1979). Fig. 4.1 shows the continuous habitable zone as suggested by Kasting et al. (1993).

Segura et al. (2003, 2005) evaluated how chemical processes and a difference in the oxygen abundance influence an Earth-like atmosphere and especially its spectral appearance in the most prominent bands of molecules produced by a biosphere, such as O_2, O_3, CH_4 and N_2O. From geological record it was deduced that Earth's O_2 abundance was much lower in early evolutionary stages and has evolved with time due to the occurrence of cyanobacteria around 2.2–2.5 Gyrs ago (Kump, 2008). Since O_3 is produced in the Earth's atmosphere predominantly by photochemistry via the Chapman mechanism, and the spectral band of ozone at 9.6 μm is believed to be one of the most important biosignatures, photochemistry was accounted for in their model. Photodissociation is strongly wavelength dependent, since a molecule has to be able to absorb the energy provided by the light which depends on the energetic states of the molecule itself, see e.g. Yung and DeMore (1998). This leads to the fact that for photochemical modeling it is important to account for the spectral energy distribution of the stellar light and the wavelength depended absorption and scattering by the atmospheric constituents. For this reason Segura et al. (2003, 2005) constructed stellar spectra of a sufficiently high resolution taking into account also the far UV part of the spectra, which is less important for climate modeling. Kasting et al. (1993), for example, used black body spectra for the determination of the habitable zone. However, since Segura et al. (2003, 2005) focused on the photochemical response of the atmosphere to stellar radiation, the stellar spectra were chosen such that the surface temperature of the scenarios was 288 K, present Earth's global mean, annual mean temperature.
Segura et al. (2003, 2005) found that ozone stays stable even for low oxygen abundances of one per mille and state that the detection of methane and oxygen, as for an mid-proterozoic Earth scenario would give the best hint for an inhabited planet. Also for M-dwarfs ozone layers build up shielding the planetary surface from harmful UV radiation, leading to the conclusion that M dwarfs should not be ruled out as possible host stars for habitable or even inhabited planets.

The special case of planets around M dwarf stars

The previous studies focused on the determination of mean states of terrestrial exoplanetary atmospheres. However, climate is a local phenomenon, strongly influenced by the locally varying stellar irradiation and heat transport by atmospheric and ocean dynamics. For M dwarf stars it is believed that, due to the needed close–in orbits for temperatures allowing for liquid water on the planetary surface, planets evolve quickly into a tidally locked state so that they posses a permanent day and night side. For such synchronous rotating planets atmospheric dynamics are very different from Earth's and were therefore the first exoplanet scenarios studied with general circulation models (GCMs).

Joshi et al. (1997)

The first study of atmospheric dynamics for an exoplanet has been carried out by Joshi et al. (1997). They investigated for which atmospheric properties the atmosphere of a planet in synchronous orbit is stable against atmospheric collapse. Kasting et al. (1993) claimed that planets in the HZ around M-stars should be tidally locked and should therefore have a permanent day and a permanent night side. This led to the speculation that an atmospheric collapse could occur on the night side making it difficult for those planets to hold a stable atmosphere, hence being habitable. Therefore, it was necessary to investigate

whether atmospheric dynamics even out these dramatic temperature differences to prevent this collapse. The results of Joshi et al. (1997), showing that atmospheric dynamics can indeed prevent from an atmospheric collapse for sufficiently thick atmospheres, led to the conclusion to include M-stars in the search for habitable planets.
In Joshi et al. (1997) a simple general circulation model (SGCM) (Joshi et al., 1995) was applied in coarse resolution (T10L10) with a grey radiative transfer, investigating the influence of the following planetary parameters:

- surface pressures of 100, 1000 and 1500 mbar and corresponding optical thicknesses τ (0.25, 1.0, 1.5) representing pure CO_2 atmospheres
- for a surface pressure of 1000 mbar different optical thicknesses (τ=0.25, 0.5, 2.0), to account for different chemical compositions
- rotation rates $\omega = 4.5\text{x}10^{-6}\,\text{s}^{-1}$(Titan), $10^{-6}\,\text{s}^{-1}$ (corresponding to an Earth-like planet around a star with $0.1\text{M}_\odot$) and $10^{-5}\,\text{s}^{-1}$ (corresponding to a stellar mass of $0.5\text{M}_\odot$)
- planetary radii: $\text{R}_{pl} = 3400$ km (R_{Mars}), 6400 km (R_{Earth}), 13000 km (2xR_{Earth})
- planetary masses yielding gravities: g= 9.8 ms^{-2} (g_{Earth}), 30 ms^{-2} (3g_{Earth}), 3.72 ms^{-2} (g_{Mars})
- dimming of the solar insolation to 60%, demonstrating the effect of an eight Titan days lasting stellar spot

The stellar energy input was mostly assumed to be the same as the present total solar irradiance (TSI), the surface albedo was assumed to be 0.2, as in previous 1D model studies. They found the following atmospheric responses:

Dynamical response Atmospheric dynamics even out temperature differences caused by the permanent radiation on the dayside (see left panel of Fig. 4.2). Superrotation, strong zonal wind (along latitudes), occurs at high altitudes transporting heat from dayside to nightside. Horizontal winds flow from the substellar point to both sides towards the nightside close to the surface. At high altitudes (at 150 mbar for the case with a surface pressure of 1 bar) eastward superrotation occurs. Furthermore, a longitudinal (meridional) circulation arises, stretching from the substellar point over the pole to the nightside at upper levels which returns at lower levels (see Fig.4.2). They found strong upward mass flow at the substellar point, which is not balanced by horizontal mass flow at low levels as was expected, but high vertical velocities near the terminator, which is the transition zone between day and night side.

Influence of different pressures and atmospheric compositions A pure CO_2 atmosphere keeps surface temperatures above the freezing point of CO_2 for surface pressures above 30 mbar. For a pressure of 1500 mbar and τ=1.5 (corresponding to a pure CO_2 atmosphere) even the night side could hold liquid water. Temperatures on the nightside rise with τ as well as with pressure and the heat transport becomes more efficient (see Fig. 4.3). For a surface pressure of 100 mbar the melting point of water at the nighttime is reached for three times the present solar irradiance (3TSI). They claim this could support water flow from night side to dayside to end up in evaporation of the total water content, since temperatures at the substellar point are

≈500 K.
For N_2 dominated atmospheres, atmospheric collapse does not occur until the temperatures fall below 80 K, therefore synchronously rotating planets should be able to hold N_2 atmospheres down to very low temperatures even with small optical depths.

Influence of planetary parameters Varying the planetary size shows a smaller effect on atmospheric temperatures than different masses, hence gravities. Slightly higher surface temperatures are obtained for a larger planetary radius with a maximum temperature difference of ±10K. For higher gravities the temperature at the model top is already 10K cooler. For Martian values of radius and gravity (R=3400 km and g=3.72 ms^{-2}), a 1 bar atmosphere with an optical thickness of τ=1, temperature differences between day and night side decreases by 40 K. Atmospheric collapse occurred for this setup at an insolation of 0.3 times the present TSI.

Influence of planetary rotation A change in rotation rate does not show a strong impact on the results. Little higher zonal wind speeds occur for faster rotation. In general the influence of the synchronous heating dominates.

Influence of irradiation decrease due to a star spot The largest response to the star spot occurs at the substellar point with a maximum temperature difference of 27 K at 20 days after the star spot. Without atmospheric dynamics this difference would be about 40K. The atmosphere needs about about 120 days after the star spot for relaxation. It is stated that since the decrease in stellar radiation due to a star spot lasts only for about a few month but the relaxation time of the atmosphere is in the order of years, only a part of a thick atmosphere would freeze out due to the temperature decrease. Only for pressures of about 100 mbar and lower a total atmospheric collapse due to stellar spots would arise.

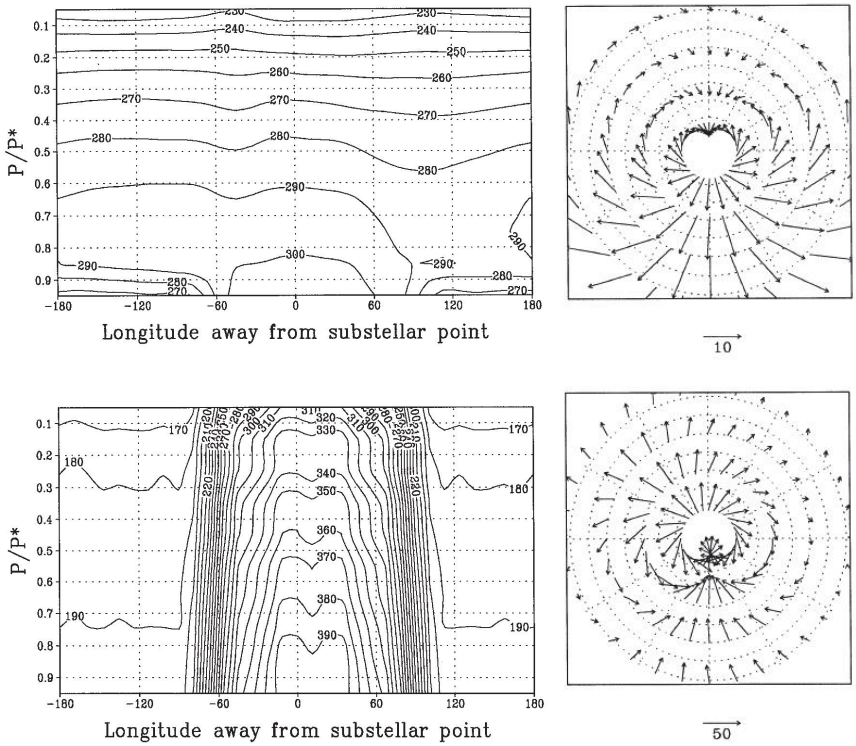

Figure 4.2: Left: Atmospheric temperatures taking into account atmospheric dynamics (upper panel) and in radiative equilibrium (lower panel). Right: Zonal wind velocities over the pole of the planet after subtracting the zonal mean temperatures reveal the meridional circulation which transports air from the day side (bottom of the panels) in the upper atmospheric layers (at 150 mbar, lower panel) to the night side (top of the panels). Near the surface (at 950 mbar, upper panel) the cold air streams back to the daylit side. Taken from Joshi et al. (1997)

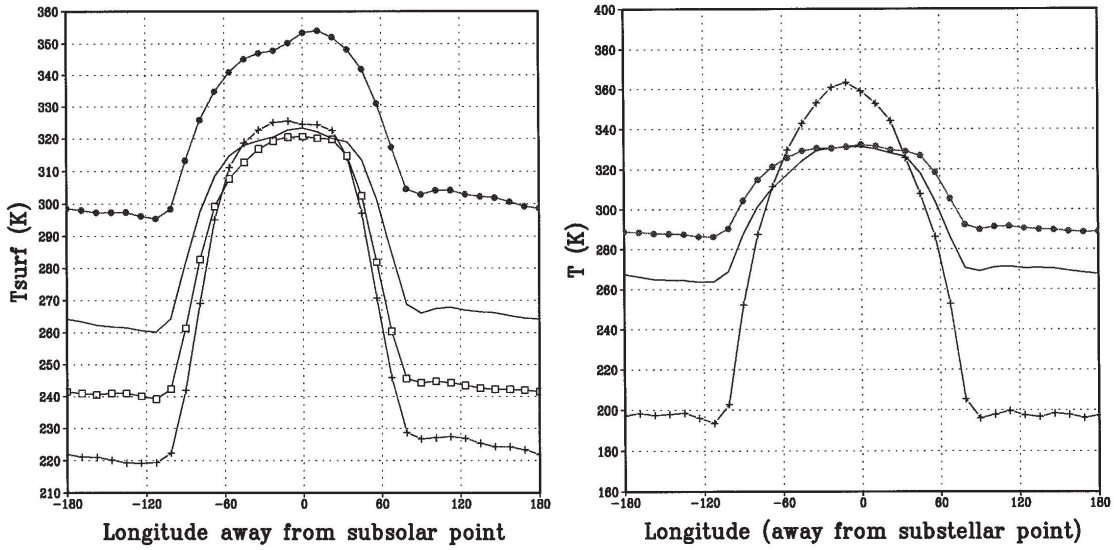

Figure 4.3: Influence of optical depth (left) and surface pressure (right) upon meridional mean surface temperatures. Left: temperatures for optical depths of $\tau = 0.25$ (crosses), 0.5 (squares), 1.0 (unmarked), and 2.0 (circles), for a surface pressure of 1000 mbar, showing the increase of temperatures with increasing optical depth at the night side, and the leveling of temperatures at the substellar point up to τ =1.0. Right: temperatures for 100 (crosses), 1000 (unmarked), and 1500 mbar (filled circles) pure CO_2 atmospheres, showing the temperature increase with surface pressure and corresponding τ. Taken from Joshi et al. (1997)

Wordsworth et al. (2011)

studied the special case of Gliese 581d with a GCM in order to understand the influence of synchronous orbits on habitability. Gliese 581d (Gl581d) is claimed to be the first potential habitable exoplanet, since various modeling studies (e.g. von Paris et al., 2010, Wordsworth et al. 2010) with 1D radiative-convective models implied that surface temperatures above the freezing point of water are possible for thick, CO_2-dominated atmospheres. Gl 581d was detected by Udry et al. (2007) with the radial velocity method, being one of the four planets in the Gl 581 system, which is build of M dwarf star (T_{eff}=3498±56 K, R=0.3±0.01 R_{Sun}, M=0.31±0.02 M_{Sun}, age=8^{+3}_{-1} Gyrs, distance=6.21±0.1 pc), a Neptune-mass planet, Gl 581b, and three so-called super-Earth planets, Gl 581c, Gl 581d, and Gl 581e. Gl 581c and e are believed to lie to close to their host star to allow for liquid water, see the left viewgraph of Fig. 4.4. Since the orbit of Gl 581d is estimated to be non circular but eccentric (e=0.25±0.09), it is questionable whether or not the planet is tidally locked to its host star. There are dynamical studies (e.g. Correia et al. (2008)), which claim that for a non-circularized orbit, the probability of a 1:1 synchronous orbit is rather small, and that such planets are unlikely trapped in 1:1 resonance with their central star. Other, more probable resonances would allow for a slow diurnal cycle. Wordsworth et al. (2011) used a stellar spectrum of AD Leo, an active M dwarf, resolved the stellar radiation in 36 bands, and used 38 bands for the radiative transfer of the thermal radiation stemming from the planet. Gliese 581d was assumed to have a mass of 5.6M_{Earth}, and an atmosphere composed of CO_2 and water only, except for the ice planet scenarios. The model is based on the LMD Mars GCM (Forget et al., 1999), and was adapted to exoplanet scenarios. The model was applied in a resolution of 32x32x20 (lat x lon x height points).
Gl 581d's habitability was investigated taking into account the orbital and rotational motion for the following scenarios:

- different surface pressures (p=5, 10, 20, 30 bar)
- different resonances of the orbital and rotational period of the planet (1:1, 1:2, 1:10)
- different surface properties, i.e. land planet, water planet (w/o ocean dynamics) , ice planet

Response to rotational period The atmospheric stability is strongly affected in the 1:1 resonance scenario, due to the permanent day and night side showing the largest temperature contrast. For the fast rotation (1:10 resonance) the meridional heat transport becomes less efficient, due to the Coriolis force than for the 1:2 resonance, right of Fig. 4.4.

Response to atmospheric pressures and surface properties For a rocky planet with surface pressures above 10 bar the atmosphere is prevented from collapse. Nevertheless, atmospheric temperatures are sometimes below the freezing point of CO_2, therefore CO_2-ice clouds form, leading to an additional greenhouse effect. The horizontal heat transport and greenhouse effect of the atmosphere are so efficient, that even the melting point of water is reached.
For the ocean scenarios they found that up to pressures of 10 bar cooling due to H_2O-cloud formation in the lower atmosphere dominates and runaway glaciation occurs. For high densities the atmospheres reached equilibrium states with only little variations in surface temperatures even for the 1:1-resonance.

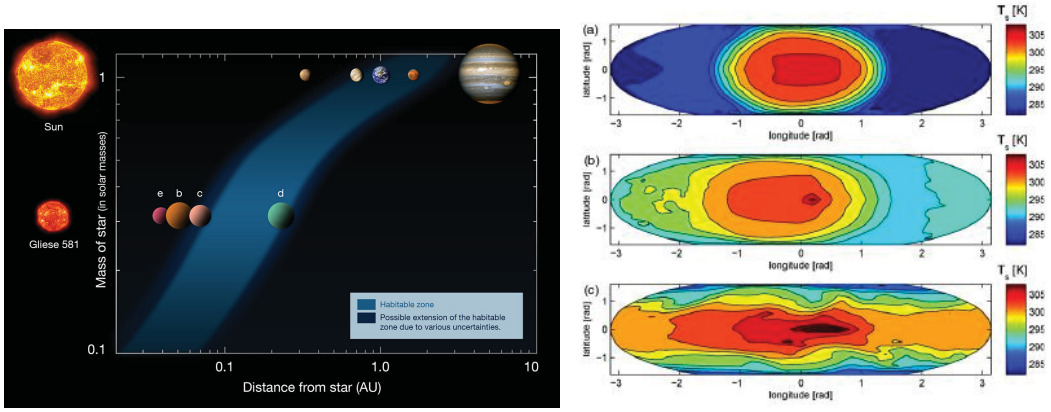

Figure 4.4: Left: Illustration of the habitable zone in the Gliese 581 system, compared to our solar system, from ESO, based on Selsis et al. (2007), Right: Influence of resonances, i.e. rotation rate, on the surface temperatures of Gliese 581d for a rocky planet, upper panel: 1:1 resonance, mid panel 1:2 resonance, lower panel: 1:10 resonance, taken from Wordsworth et al. (2011)

For the ice planet scenarios, starting with an ice covered ocean, surface pressures of at least 20 bar are needed for melting of ice.

4.2 Influence of orbital parameters and rotation rate on climate & atmospheric properties

Orbital parameters, such as eccentricity and obliquity, but also orbital period mainly have an influence on the local and seasonal stellar irradiation. For a high eccentricity the total stellar insolation changes strongly over the year, whereas the obliquity determines, whether seasons exist. The orbital period mainly changes the length of the year. The influence of the rotation rate as a planetary parameter, is rather twofold. It not only determines the length of the day and night, but also influences the atmospheric circulation via the Coriolis force and the centripetal force occurring in a rotating system. In the following, studies dealing with the influence of the eccentricity, obliquity and rotational rate of the planet on planetary climate will be summarized.

del Genio and Suozzo (1987)

A detailed study of the influence of the rotational rate upon atmospheric properties has been carried out by del Genio and Suozzo (1987). Their motivation was rather to understand the atmospheric dynamics, especially the mechanisms driving superrotation, than determination of the habitability of slow rotating planets. They used an Earth climate model of the NASA Goddard Institute for Space Studies (GISS1, Hansen et al. 1983), without the hydrological cycle, nor land or sea ice. Furthermore, the atmosphere was coupled to a swamp ocean, i.e. an ocean model which does not take the heat capacity or the dynamics of the ocean into account. Investigated was the dynamical behavior for:

- rotational periods of 2/3, 1, 2, 4, 8, 16, 64, and 256 days

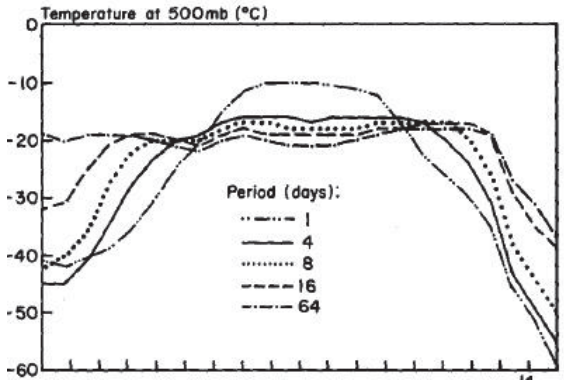

Figure 4.5: Influence of the rotation period upon annual zonal mean temperatures, taken from del Genio and Suozzo (1987). The temperature distribution at 500 mbar over latitudes (displayed on the x-axis, ranging from the north pole, left, to the south pole, right) flattens with increasing rotational period.

They found that :

- superrotation occurs at high altitudes for rotational periods of 4, 8, and 16 days
- the present 3 cell meridional circulation changes to a circulation with only one Hadley cell for rotational periods larger than 4 days because of the weaker Coriolis force
- the temperature difference flattens for higher periods (see Fig. 4.5)

Williams and Pollard (2002)

Since many of the newly discovered exoplanets where found to orbit their host stars on very eccentric orbits, Williams and Pollard (2002) investigated how a large eccentricity might effect the habitability of an Earth-like planet. Even though no such Earth-like planet has been found so far, one can of course speculate that they would exist. Even if Earth-like planets might more likely orbit their host star in circular orbits due to tidal interactions, it is still possible, that Hot Jupiters found on very eccentric orbits might posses moons which are comparable to an Earth-like planet. They utilized an Earth climate model, Genesis 2 (Thompson and Pollard, 1997) including a mixed layer ocean, and compared their results to those of an energy balance model (EBM) (Williams et al., 1997), which takes into account the Carbonate-Silicate cycle. They assumed an Earth-like geography, an orbital distance of a=1 AU, an orbital period of P_{orb}=365 days, present Earth's obliquity and a constant CO_2-concentration of 345 ppmv for all scenarios. They investigated the following cases:

- eccentricities of e= 0.1, 0.3, 0.4 with the present solar luminosity
- eccentricity 0.7 with 71% of solar luminosity

They found that:

- for all runs the Earth-like planet stays habitable in the sense of maintaining liquid water on the surface
- the global mean surface temperature rises from 14.6°C for the present Earth scenario to 30.1°C at an eccentricity of e=0.4

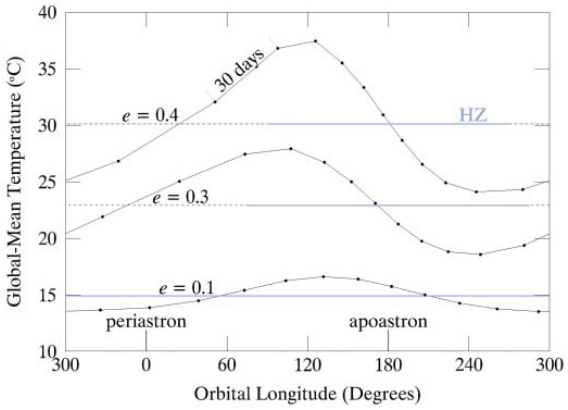

Figure 4.6: Influence of the eccentricity on global mean temperatures over orbital period, taken from Williams and Pollard (2002). Global mean temperatures increase with eccentricity, the time spent in the HZ (indicated by the solid light blue line) decreases.

- the time spent in the habitable zone decreases with eccentricity
- for highest eccentricity surface temperatures can regionally exceed 80°C

Furthermore they give a formula for the annual global mean flux received by the planet during a whole revolution which increases with eccentricity: $\langle F \rangle = \frac{L}{4\pi a^2 \sqrt{1-e^2}}$, with L being the luminosity of the star, F the stellar flux received at top of the atmosphere, a the orbital distance. The comparison with the EBM revealed that surface temperatures seem to be colder for the EBM calculations, but still comparable.
Fig. 4.6 shows the variation of the global mean temperature over one orbit. It can be seen that the temperatures and their variation increase with eccentricity and the time spent in the HZ decreases.

Williams and Pollard (2003)

Motivated by the possibility that Earth's obliquity might have been different from the present day obliquity of 23.5° during its evolution (Williams, 1993), and the chance of very different obliquities for extrasolar planets, Williams and Pollard (2003) performed a parameter study, investigating mainly the influence of obliquities higher than present and different continental setups. As in Williams and Pollard (2002) they utilized the Earth GCM Genesis 2. They studied the influence of the following parameters:

- obliquities of 0°, 23°, 54°, 70° and 85° for a present Earth setup (solar luminosity, CO_2 concentration, land mask)
- 10x present atmosphere level (PAL) of CO_2 (3450 ppmv) for obliquities of 23°, 54°, and 85°
- continental setups, for which they chose geographies, which are believed to reproduce Earth's continental distribution at the time of major glaciations. Therefore, they adapted an equator centered continent corresponding to the time of the Sturtian glaciation at 750Myr ago, with obliquities of 0° and 85° and south pole centered continent as it might have been 540 Myr ago, around the time of the Varanger glaciation (610-575Myr), with an obliquity of 85°

- a lower solar luminosity (0.94L$\odot$) and 420 ppmv CO_2 for an obliquity of 85°

All model scenarios result in habitable conditions, where habitability is defined as the possibility of holding liquid water. Furthermore, they state the following results for the parameters varied:

Influence of obliquity The high obliquity did not initiate low latitude glaciations for the modeled CO_2 content at sea level for all continental setups, so low latitude glaciation records cannot be explained in the framework of this study. The assumption of high obliquities is anyway questionable. The lowest mean surface temperature was reached for the present day obliquity, the highest temperatures for an obliquity of 54° for present day CO_2 levels, see Fig. 4.7. For higher CO_2 concentrations the present day obliquity scenario reached the highest mean temperature. For an obliquity of 85 ° extreme summertime droughts occur at latitudes above 40°N due to extreme summertime heating, where the temperatures over the continents reach 80-90°C. For lower obliquities this summertime droughts are present but less pronounced with temperatures over land still exceeding 50°C. For an obliquity of 0° snowfall suggests icy regions down to latitudes of 50°, so for present Earth's geography the snow-ice line extends down to regions were glaciations are expected for a time around 21kyrs ago, usually assigned to higher obliquity. The area covered with snow for this scenario is even five times larger than what is known from glacial records.

Influence of continental setup The most hostile conditions occur for the south pole centered geography with an obliquity of 85°, where temperature differences higher than 120°C arise between poles and equator. Also for a present Earth geography very high temperatures near the boiling point of water occur at the pole in January, while blizzards and heavy snowfall occur at the equator for present day CO_2 concentrations. The smallest variations in annual mean temperature occurred for the equator centered geography with an obliquity of 85°, which are close to the variations of our Earth today. For an obliquity of 85°, seasonal variation is smallest for Sturian geography (equator centered), because the amplitude of the seasonal insolation cycle is smallest with highest temperatures being around 70°C, which is 20-30°C less than for present day geography. For the south pole centered continent the seasonal cycle is nearly three times as high in amplitude as for equator centered continent, with a phase shift of 180°. For an obliquity of 0° lower temperatures are obtained for the equator centered continent due to a smaller continental coverage than for present day geography. This leads to more ice at the high latitudes than for the present day continental setup.

Influence on atmospheric dynamics Wind speeds do not change more than 10 ms^{-1} for high obliquities in comparison to low obliquities. The tropical convergence zone disappears due to changed meridional circulation described above.

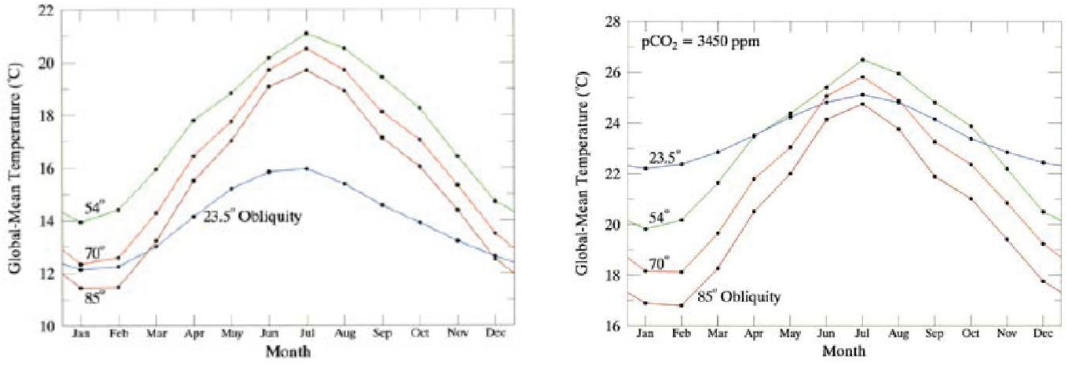

Figure 4.7: Influence of the obliquity upon global mean temperatures over the year for present Earth's geography. Left panel: present CO_2 concentrations, right: 10xPAL CO_2, taken from Williams and Pollard (2003). Global mean temperatures decrease with obliquity for obliquities higher that 54°. For present CO_2 concentrations, present Earth obliquity leads to lowest temperatures, whereas for 10PAL CO_2 an obliquity of 85° the temperatures are minimal.

Influence of surface conditions and feedbacks

As has been discussed for other studies already (e.g. Wordsworth et al. (2011)), surface properties are crucial for the determination of planetary climate. Not only do they change the radiation budget due to the radiative properties of the surface, but they also have an impact on hydrology by different water reservoirs in dry and wet soil, or oceans. Furthermore, a change in surface properties, e.g. due to build up of ice, is difficult to handle with 1D models. The different impacts of surface properties have been addressed by the following studies.

Joshi (2003)

Whereas Joshi et al. (1997) studied the possibility of atmospheric dynamics preventing an atmospheric collapse, in Joshi (2003), the focus was on determining the surface temperatures of a tidally-locked Earth-like exoplanet in synchronous orbit. Joshi (2003) applied a GCM of intermediate complexity (IGCM, de F. Forster et al. (2000)) with a coupled swamp ocean, calculating atmospheric properties of an atmosphere from 1 down to 0.001 bar. The rotation rate of the Earth was used, which corresponds to a semi-major axis of 0.042AU for a M Star with $0.1 M_{\odot}$, and a prescribed ozone profile. A black body spectrum of the Sun as the stellar input spectrum was assumed, and the shortwave radiation was calculated in two bands. The following scenarios were investigated:

- an aquaplanet with 2m thick sea-ice on dark side and a surface albedo of 0.2
- a continent on the northern hemisphere without any elevation and also an surface albedo of 0.2
- a dry land planet without any water reservoir in the ground, but with present Earth's humidity stored in the atmosphere

In general, for all cases the temperatures stayed above freezing. Furthermore, they found that:

The hydrological cycle plays a major role in terms of heat transport, which is much more efficient for planets with a large water reservoir (aquaplanet) than with a small one (dry land).

Atmospheric dynamics led to wind speeds at the surface as strong as 4 Beaufort ($\approx 8 \frac{m}{s}$), which depend of course on the rotation rate of the planet.

For the aquaplanet temperatures are 30°C at maximum, and half of the planet has temperatures above the freezing point of water. Most of the nightside and the polar regions is covered with ice. The radiative feedback of this albedo change was not included in the calculations. Furthermore, heavy rainfall can be found at the substellar point and very low precipitation at the dark side, comparable to present Earth's poles. The maximum amount of clouds, mainly low clouds, is found at the nightside, whereas at the day side convective cumulus clouds dominate. The terminator region receives about the same amount of precipitation as western Europe.

For a northern hemisphere continent the hemisphere with the continent is much warmer with temperatures as high as 80°C, but no water is transported over the tropopause despite the high substellar point temperatures. On the nightside snow builds up and

could become as high as 1 km in 10000 yrs, but the model run was interrupted before. The total cloud cover is smaller than for the aquaplanet due to a lack of moisture stored in the ground. Furthermore, less clouds can be found over the continent.

For the dry land planet the largest differences between nightside and dayside occur, ranging from -70°C to 80°C. The initial water vapor in the atmosphere is removed very quickly, which lowers IR optical depth as well as the heat transport.

Polar caps should massively build up for the aquaplanet, though this is not realized in the model since sea-ice depth was limited to 2 m. For the northern hemispheric (NH) continent scenario an ice cap should form over land at the pole due to the precipitation. For aquaplanet the ocean does not totally condense on poles and nightside, since sea-ice depth is automatically assumed to be 2m thick. However, it is claimed that a huge floating polar ice cap would form.

The equatorial terminator is proposed to be most hospitable, since there less flares occur and a moderate amount of precipitation was found as well as moderate to low wind speeds

Fraedrich et al. (2005b), Kleidon et al. (2000) and Fraedrich et al. (1999)

As seen in Joshi (2003), the hydrological cycle has a major impact on the heat transport. In the studies of Fraedrich et al. (2005b), Kleidon et al. (2000) and Fraedrich et al. (1999) the hydrological cycle was influenced via the choice of the continental surface properties. In these studies it was investigated how different kinds of vegetation, hence surface albedos, water reservoirs in soil, and the roughness length of the surface affect land surface climate. Therefore, two different models were applied, one complex Earth climate model, ECHAM4 (Roeckner et al., 1996), in Kleidon et al. (2000) and Fraedrich et al. (1999), and a GCM of intermediate complexity, the planet simulator (Fraedrich et al., 2005a), in Fraedrich et al. (2005b). A land-sea mask as for present Earth was assumed in these studies, but it was completely covered with either forest, *green planet*, or dry land, *desert world*, excluding the presently ice covered regions. Furthermore, the sea surface temperatures (SSTs) were prescribed in ECHAM4 (Kleidon et al., 2000, Fraedrich et al., 1999), whereas they where calculated interactively in the planet simulator for one scenario by coupling a mixed layer ocean (Fraedrich et al., 2005b). The surface properties of the green planet and desert world were chosen to be:

- green planet: all non-icy surfaces are covered with forest of an albedo of 0.12, a roughness length of 2 m, furthermore the ability of the soil to store water was adapted accordingly
- desert world: all non-icy surfaces have no vegetation at all and an albedo of 0.28, a very small roughness length and water storage capability is assumed.

All three studies found, that

The hydrological cycle dominates the climatic response. One might expect that surface temperatures are higher on the green planet, but they are reduced due to enhanced evapotranspiration which removes latent heat. Furthermore, due to a higher cloud coverage resulting from the higher humidity for the green planet, the effect of the reduced surface albedo is compensated.

Surface temperatures over the continents differ by only 2.1 K for the green planet from the desert world for prescribed SSTs, and about 4 K when taking the ocean into account. The highest surface temperatures occur in the arid regions in summer.

Atmospheric circulation changes due to enhanced latent heat release in the Intertropical Convergence Zone (ITCZ) for the green world, leading to an intensification of the Hadley cell, and a substantially warmer upper troposphere (Fraedrich et al., 1999)

Marotzke and Botzet (2007)

It is speculated that Earth has gone through several so called snowball Earth events during its evolution, meaning that the entire surface was ice covered. Marotzke and Botzet (2007) studied, what amount of greenhouse gases is needed to return from a snowball Earth state back to a surface with only partly ice covered surfaces as found on Earth today. Furthermore, they were interested if a snow covered Earth would be in equilibrium with present amounts of greenhouse gases and solar irradiation. Therefore, they utilized an Earth atmospheric-ocean general circulation model, ECHAM5/MPI-OM (Roeckner et al., 2006, Marsland, 2003). They gain an ice covered Earth by reducing the solar radiation to $\frac{1}{10000}$ of the present TSI (total solar irradiance). Then they performed the following experiments:

- After the ice cover is complete (15 model years), they increase the solar radiation stepwise reaching the present TSI in year 19
- Before the ice cover is complete in model year 12 they set the solar radiation back to 100% TSI.
- After the ice cover is complete they set the solar radiation to the present TSI and increase CO_2 concentrations to 10PAL (present atmosphere level)
- After the ice cover is complete they set the solar radiation to the present TSI and increase CO_2 concentrations to 100PAL

They find that:

For a completely frozen Earth setting the solar radiation back to the present value, does not change the global sea ice area and the Earth stays in a snowball state. Also increasing the CO_2 concentrations to 10 PAL (3480 ppmv) does not change the area covered by ice. However, increasing the CO_2 concentrations to 100PAL results in defreezing of the Earth to an even lower ice fraction than today, see Fig. 4.8.

For a nearly frozen Earth at model year 12, resetting the solar insolation to the present value leads to defreezing, and the present climate state is restored.

Surface temperature decreases to below -100 °C for the completely frozen Earth due to very low water vapor concentrations in the atmosphere.

4.3 Summary

In the above sections studies relevant for this thesis and their result were summarized. The influence of different stellar radiations was mainly investigated by 1D radiative-convective

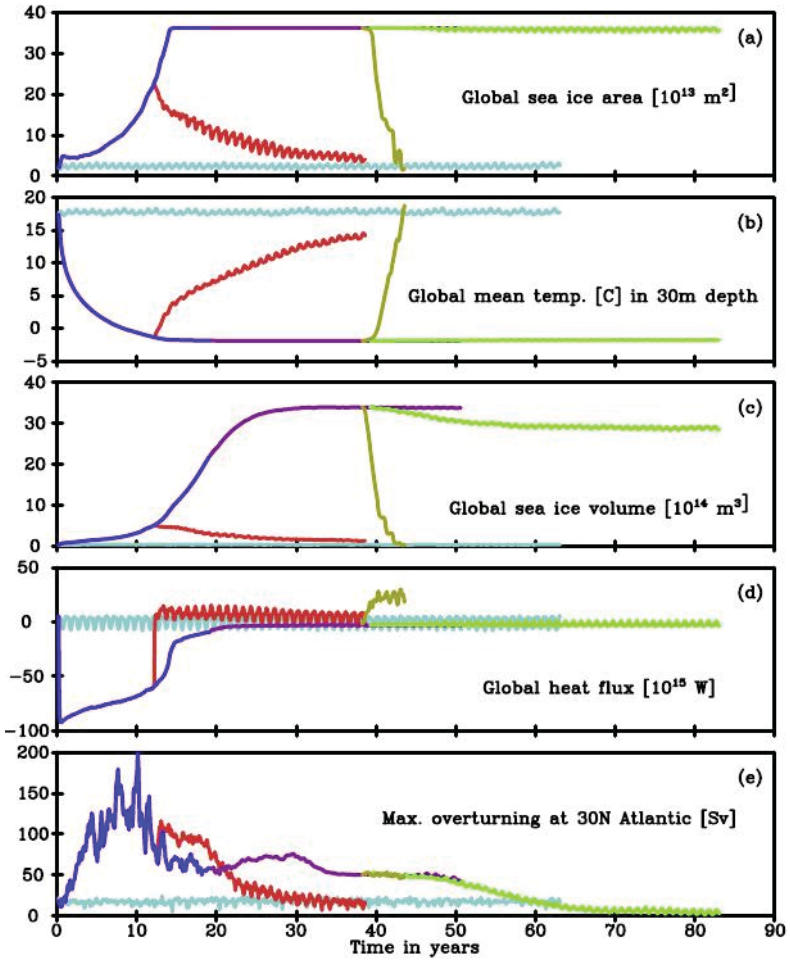

Figure 4.8: Global mean sea ice are, global mean temperature at a depth of 3m, global sea ice volume, global heat flux, and maximum Atlantic over turning of the ocean for the scenarios from Marotzke and Botzet (2007) over model years. In light blue the present Earth's climate state, dark blue the climate state with reduced solar irradiance, in purple the scenario with restored solar irradiance after complete freezing, in red resetting to present solar irradiance in model year 12, olive with a 100PAL CO_2 and green with 10PAL CO_2.

models (Kasting et al., 1993, Segura et al., 2003, 2005), except for the special case of Gl 581d (Wordsworth et al., 2011). This study as well as the studies of Joshi et al. (1997), Joshi (2003) considered planetary scenarios around M dwarfs, which are of special interest, because these planets tend to be tidally locked and could therefore have a permanent day and night side, which changes the atmospheric dynamics dramatically, though atmospheric collapse only occurs for thin atmospheres.
Furthermore, some 3D modeling studies of exoplanets were discussed, which focused on the influence of orbital parameters such as eccentricity (Williams and Pollard, 2002) and obliquity (Williams and Pollard, 2003). These planetary parameters were also investigated with 2D models, e.g. Spiegel et al. (2009), Dressing et al. (2010). A result of many of these studies, especially also of these focusing on the atmosphere-surface interactions, e.g. Kleidon et al. (2000), Fraedrich et al. (2005b, 1999) and Joshi (2003), was that the hydrological cycle plays a major role for the heat redistribution.

Part II

Model descriptions

CHAPTER 5

Model descriptions

The aim of this thesis is to study the influence of different stellar spectra, their impact on dynamical processes and the consequences of this interaction for planetary habitability are evaluated.

5.1 Choice of model

To evaluate the influence of the different stellar spectra upon atmospheric dynamics and other dynamical processes an atmospheric model is needed, which accounts for dynamical processes in the atmosphere and at the surface. Furthermore, it needs to resolve the differences in the incident stellar spectra to capture their influence on the atmospheric temperatures.

The 3D model used in this work, EMAC-FUB, a state of the art three-dimensional climate model of the Earth, described in 5.3, accounts for dynamical processes such as the atmospheric circulation, the hydrological cycle and surface interactions. It furthermore uses a radiative transfer scheme (FUBRAD, described in 5.3.2.1) which is capable of resolving differences in the spectral energy distribution. Hence, it is suited to evaluate the interaction of the different stellar irradiations and dynamical processes and their impact on planetary habitability.

To evaluate the importance of dynamical atmospheric processes on the habitability of exoplanets a second model is applied in this work, a one-dimensional radiative-convective model, which calculates the global annual mean temperature and water profile in steady state. In this model no atmospheric dynamics or surface interactions are taken into account. Hence, comparing the 1D and 3D models can be used to infer, whether the change in atmospheric properties, such as temperature and water vapor concentrations, due to different stellar irradiations can be inferred without accounting for the dynamical processes. The 1D model is described in 5.2.

5.2 1D model

In this section a short description of the 1D cloud-free radiative-convective atmospheric model used in this thesis is given. A more detailed description can be found in Stracke

(2012), von Paris (2010) and von Paris et al. (2008).
The model is based on the 1D cloud-free radiative-convective photochemistry model originally from Kasting et al. (1984), which has been modified e.g. by Segura et al. (2003, 2005), Grenfell et al. (2007) and Rauer et al. (2011). The model can be run coupled to a photochemistry model which is however omitted for this study.

The 1D model calculates mean atmospheric temperature and water vapor profiles in steady state from the surface up to pressures of 0.066 hPa (6.6×10^{-5} bar). The temperature profile is calculated from radiative equilibrium in the stratosphere and convective adjustment is applied in the troposphere whenever the temperature lapse rate calculated via radiative equilibrium exceeds the adiabatic lapse rate. The water profile calculations are based on a relative humidity profile.

5.2.1 Model equations

The basic model equations are based on the conservation of momentum, the conservation of energy and the equation of state. It is assumed that the atmosphere is in hydrostatic equilibrium and that horizontal motions can be neglected. Thereby, the equation of momentum simplifies to

$$\frac{\partial p(z)}{\partial z} = \rho(z)g, \tag{5.1}$$

where $p(z)$ is the pressure at an atmospheric height z, $\rho(z)$ the density and g the gravitational acceleration.
It is assumed that the atmosphere behaves as an ideal gas, hence the equation of state is given by:

$$p = \frac{\rho R^* T}{m}, \tag{5.2}$$

with R^* the universal gas constant, and m the mean molecular weight of the atmosphere. The mean molecular weight is calculated for the assumed composition, where Nitrogen (N_2) is treated as a filling gas.
Based on the conservation of energy, the temperature is calculated from:

$$\frac{\partial T(p)}{\partial t} = -\frac{g}{c_p(T,p)}\frac{\partial F_{rad}}{\partial p}, \tag{5.3}$$

where c_p is the heat capacity and F_{rad} the net radiative energy flux.

In the case that the temperature at a height z calculated via the above equation is smaller than the adiabatic temperature given by the moist pseudo-adiabatic lapse rate (see eq. 3.38), convective adjustment is carried out. Depending on the atmospheric temperature, different parameterizations of the pseudo moist-adiabatic lapse rate are used as described in Kasting (1988). For atmospheric temperatures between 273.15 and 647 K the moist adiabatic lapse rate is given by the approach of Ingersoll (1969).

5.2.2 Calculation of the water vapor profile

The water vapor profile is calculated from the temperature profile and an assumed relative humidity profile. The volume mixing ratio of water is calculated by:

$$c_{H_2O}(p) = \frac{p_{sat}(T(p))}{p} RH(p), \tag{5.4}$$

where $RH(p)$ is the relative humidity profile.

In the standard model setup for Earth-like atmospheres the relative humidity profile of Manabe and Wetherald (1967) is used, which is given by:

$$RH(p) = RH_{surf} \frac{\frac{p}{p_{surf}} - 0.02}{0.98}, \tag{5.5}$$

where RH_{surf} is the relative humidity at the surface, which is usually set to 0.77.

Furthermore, it is also possible to assume a relative humidity of 100% throughout the entire atmosphere. Such a high relative humidity may be assumed for high atmospheric temperatures, as it has been done to determine the inner boundary of the habitable zone (Kasting et al., 1993, Stracke, 2012).

The water vapor concentrations are set constant to the value of the cold trap in the upper atmosphere above the cold trap. The cold trap is defined by the model layer where $f_{sat} = \frac{p_{sat}(T(p))}{p}$ starts to increase with height. The water vapor concentration is then set to the value at the cold trap.

5.2.3 Radiative transfer

The net radiative energy flux F_{rad} (Eq. 5.3) is determined by solving the radiative transfer in the longwave and the shortwave regime. F_{rad} is given by

$$F_{rad} = F_{sw\uparrow} + F_{sw\downarrow} + F_{lw\uparrow} + F_{lw\downarrow}, \tag{5.6}$$

where $F_{sw\uparrow}$ and $F_{sw\downarrow}$ are the up and downwelling radiative energy fluxes in the short wavelength regime and $F_{lw\uparrow}$ and $F_{lw\downarrow}$ the upwelling and downwelling radiative fluxes in the long wavelengths regime.

Radiative transfer in the short wavelength regime

The radiative transfer in the short wavelength regime accounts for the absorption and scattering of incoming stellar radiation by molecules and the surface. It covers a wavelength regime from 237.6 nm to 4.545 μm, which is split into 38 spectral bands.
Water vapor, carbon dioxide, ozone, methane, and molecular oxygen are treated as absorbing species, and Rayleigh scattering by molecular nitrogen, molecular oxygen and carbon dioxide are taken into account.
In a modified version of the 1D model, which is applicable for carbon dioxide and water dominated atmospheres (von Paris, 2010, Stracke, 2012), Rayleigh scattering of water vapor is considered as well.

The radiative flux in the 38 spectral bands is calculated based on correlated-k exponential sums, which accounts for the frequency integration of the radiative fluxes. For the angular integration a quadrature δ-2-stream approximation is used following Toon et al. (1989). To account for the diurnal variation a factor of 0.5 is multiplied to the incoming stellar flux, as well as a factor of $cos\alpha$. α is the solar zenith angle and usually set to 60 °, which is the mean solar zenith over a sphere.

Radiative transfer in the long wavelength regime

The radiative transfer in the long wavelengths regime accounts for the thermal emission of the planetary surface and the atmosphere and for the absorption of the thermal energy flux. The 1D model includes two longwave radiative transfer schemes, the Rapid Radiative Transfer Model (RRTM), described in detail by Mlawer et al. (1997), and the Modified RRTM for Application in CO_2-dominated Atmospheres (MRAC), described by von Paris et al. (2008) and von Paris et al. (2010). Since in this work Earth-like atmospheres are investigated, RRTM is used for most of the comparison studies unless otherwise stated.

RRTM covers a wavelength regime from 3 to 1000 μm in 16 wavelengths intervals. It accounts for the absorption by water vapor, carbon dioxide, methane, ozone and nitrous oxide, which are the main absorbers. Absorption by minor constituents, such as carbon monoxide or chlorofluorocarbons (CFCs) may also be considered.
A more detailed description of RRTM is given in the 3D model description (sec. 5.3.2.2). Integration over frequencies is carried out using the correlated-k approach (Mlawer et al., 1997). Since the 1D model assumes cloud-free conditions and scattering by any other particles is not considered in the long wavelengths regime, the angular integration of the radiative transfer equations is carried out using the diffusivity approximation.

5.3 EMAC Model

The ECHAM/MESSy Atmospheric Chemistry (EMAC) model is a numerical chemistry and climate simulation system that includes sub-models describing tropospheric and middle atmosphere processes and their interaction with oceans, land and human influences (Jöckel et al., 2006). It uses the first version of the Modular Earth Submodel System (MESSy1) to link multi-institutional computer codes. The core atmospheric model is the 5th generation European Centre Hamburg general circulation model ECHAM5. The model description is based on the documentation of ECHAM5 (Roeckner et al., 2003), ECHAM4 (Roeckner et al., 1996) and ECHAM3 (Deutsches Klimarechenzentrum (DKRZ), 1992). Only basic model equations and assumptions can be given in this description due to the complexity of the model. For further details refer to the model documentations above and references therein.

In this work the middle atmosphere version of EMAC is applied, ranging from the surface up pressures of 0.01 hPa. In order to resolve the differences in the stellar spectra, the shortwave radiative transfer module FUBRAD has been used. This version of the model is often referred to as EMAC-FUB. Furthermore, the model has been applied to climate calculations only, although it is in principle capable of including the interaction with chemistry.

5.3.1 Basic model equations

The basic model equations are derived from the primitive equations (see section 3.3) by assuming that density does not change due to evaporation and condensation, latent heat does not vary with temperature, and that no heat is transferred from falling snow and rain. This leads to the following governing model equations, which build the dynamical core of EMAC.
Conservation of momentum:

$$\frac{\vec{v}_h}{dt} = -\frac{1}{\rho}\nabla_h p - 2(\Omega \times \vec{v}_h)_h - \frac{1}{\rho}\frac{\partial J_{\vec{v}_h}}{\partial z} + K_{\vec{v}_h} \tag{5.7}$$

Conservation of energy:

$$\frac{dT}{dt} = \frac{R_d T_v}{pC_p}\frac{dp}{dt} + \frac{1}{C_p}\left(Q_R + Q_L + Q_D - \frac{1}{\rho}\left(\frac{\partial J_s}{\partial z} - C_{pd}T(\delta - 1)\frac{\partial J_{q_v}}{\partial z}\right)\right) + K_T \tag{5.8}$$

Conservation of mass:

$$\frac{dq_i}{dt} = S_{q_i} - \frac{1}{\rho}\frac{\partial J_{q_i}}{\partial z} \tag{5.9}$$

Equation of state:

$$p = \rho R_d T_v \tag{5.10}$$

Hydrostatic equilibrium:

$$\frac{\partial p}{\partial z} = -g\rho \tag{5.11}$$

$\vec{v}_h$ is the horizontal velocity, $J_{\vec{v}_h}$ is the parametrized vertical momentum flux. K_x takes into account the contribution to a variable x by due to unresolved schemes. These are not based on any physical model, but rather depend on the resolution of the model. T_v is the virtual temperature, $C_p = C_{pd}(1 - q_v) + C_{pv}q = C_{pd}(1 + (\delta - 1)q_v$, the heat capacity of the gas. Q_R, Q_L and Q_D represent the heat due to radiation, phase changes and internal dissipation of kinetic energy. $\frac{\partial J_s}{\partial z}$ gives the vertical flux of static energy. q_i represents the mass concentration of water compounds, q_v specific humidity, q_l liquid water, and q_i the mass concentration of the solid water phase. $\frac{\partial J_{q_v}}{\partial z}$ is the vertical flux of specific humidity (q_v), S_{q_i} the changes of q_i due to phase changes and precipitation.

These equations are transformed into spherical coordinates (see sec. 5.65) and the momentum equation is reformulated as a function of vorticity $\xi = \nabla \times \vec{v}_h$ and divergence $D = \nabla \cdot \vec{v}_h$. The basic prognostic variables of the model are ξ (vorticity), D (divergence), T (temperature), q_i and $\ln p_s$, where q_i the mass mixing ratios of water vapor, cloud water or cloud ice and p_s is the surface pressure. The vertical velocity has been removed from the equations by assuming hydrostatic equilibrium. It is therefore calculated from the change of pressure and not a prognostic variable by assuming $\frac{\partial(\frac{p}{p_s})}{\partial t} = 0$ at the surface and the top of the atmosphere.

It follows a description of some important additional physical processes, which contribute to the upper basic model equations.

5.3.2 Radiation

The radiative transfer in EMAC to obtain radiative heating and cooling rates is calculated separately for the short wavelength and the long wavelength regime. For both regimes it is assumed that the atmosphere is plane parallel, that gas constituents are homogeneously mixed and that the gas constituents are in local thermal equilibrium (LTE). In the shortwave radiative transfer scheme, however, an effective solar zenith angle is introduced to account for the non-sphericity of the atmosphere. The resulting radiative fluxes depend on the composition of the atmosphere, including gaseous and condensed compounds, the stellar insolation, the solar zenith angle and the position of the Earth in its orbit, as well as on the temperature structure of the atmosphere. Since radiative transfer calculations form one of the most time consuming parts of the calculation, the radiative fluxes are usually not evaluated every time step, so that the change of stellar insolation and the zenith angle over the time step has to be taken into account.

The radiative heating rate is then calculated from the difference of the total net radiation flux between the lower and the upper boundary of the cell in the vertical by:

$$Q_{rad} = -\frac{F_{rad}^{low} - F_{rad}^{up}}{mc_p} \tag{5.12}$$

with F_{rad} being the net total radiation, including the net shortwave and longwave radiative fluxes ($F_{rad} = F_{net,sw} + F_{net,lw}$). m is the mass of the air which is derived from the pressure difference between the lower and the upper vertical boundary of the cell by assuming hydrostatic equilibrium

$$m = \frac{p^{low} - p^{up}}{g} \tag{5.13}$$

and c_p the heat capacity of moist air which is calculated from

$$c_p = (1 - q_v)c_{pd} + q_v c_{pv} \tag{5.14}$$

with q_v the specific humidity, c_{pd} the heat capacity of dry air and c_{pv} the heat capacity of water.

5.3.2.1 Short wavelength regime

The source of shortwave radiation is the stellar radiation at top of the atmosphere (TOA) which depends, e.g. on orbital parameters and hence varies with location and in time. The incoming stellar radiation is absorbed or scattered in the atmosphere or at the surface, depending on the local composition of the atmosphere and the surface type. Shortwave radiation from the ultraviolet to the near infrared is taken into account for studies of planetary climate, since radiation at shorter wavelengths is usually effectively absorbed in the upper atmosphere. At lower wavelengths the stellar energy flux is usually much smaller than in the visible and is therefore omitted. First the calculation of the stellar insolation at the top of the atmosphere is described followed by the parametrization of absorption and scattering by atmosphere.

Calculation of incoming stellar radiation

The diurnal and annual variations of incoming stellar radiation depend on the orbital parameters of the planet such as the semi-major axis, which can change depending on the

eccentricity of the orbit, the tilt of the rotation axis of the planet, and on the rotational period of the planet.

Calculation of the orbital parameters

EMAC offers two ways of calculating the position of the Sun above the planet. One parametrization uses tabulated values belonging to a Poisson series expansion as a result of an analytical solution of the equations of motion of the planets called VSOP87 (Variations Séculaires des Orbites Planétaires), based on Bretagnon and Francou (1988).

The other parametrization calculates the solar position by solving the two-body problem for the Sun and the Earth. For the second method the orbital eccentricity and obliquity as well as the longitude of periastron have to be specified as input parameters. From these the orbital distance as well as the right ascension and the declination of the Sun are calculated in every time step by solving the Kepler equation for the eccentric anomaly (E):

$$E = M + esinE \tag{5.15}$$

with M the mean anomaly, and e the eccentricity of the orbit.
In this work the second method is used for the calculation of the stellar insolation for Earth-like planets orbiting different types of central stars (see Chapter 9).

The Kepler equation 5.15 is solved iteratively using the Newton method. For the first iteration a mean anomaly has to be given for a certain time. In the model mean anomaly for the 1^{st} of January 1900 is used, which is calculated from the longitude of perihelion. With this the eccentric anomaly for the current time step is calculated.

The orbital period enters the calculations as the lengths of the year. From the eccentric anomaly E the true anomaly ν is calculated using

$$\nu = 2arctan\frac{tan\left(\frac{E}{2}\right)}{\sqrt{(1+e)\,(1-e)}}. \tag{5.16}$$

which enters the calculation of the solar (stellar) position. From E and e furthermore the current orbital distance r is calculated using

$$r = a\,(1 - ecosE)\,, \tag{5.17}$$

where a is the mean orbital distance. With the current distance from the Sun r the current solar insolation at the top of the atmosphere is calculated:

$$F(\lambda, \phi, t) = I_0 \left(\frac{a}{r}\right)^2 \mu_0(\lambda, \phi, t) \tag{5.18}$$

with I_0 the total solar irradiance, or solar constant, and $\mu_0 = cos\theta(\lambda, \phi, t)$ with θ the local solar zenith angle.

Change of orbital period

The length of the year has been changed for the model scenarios presented in Chapter 9 to account for the different orbital distances at which a planet around a K or an F-type star receives the same amount of energy as the Earth receives from the Sun (see sec. 7.2.1 for the calculation of the length of the year).

Effective zenith angle

The curvature of the atmosphere is taken into account by defining an effective solar zenith angle ($\mu_{0,eff}$)with

$$\mu_{0,eff} = \frac{r_{ae}}{\sqrt{\mu_0^2 + r_{ae}(2 + r_{ae}) - \mu_0}} \tag{5.19}$$

where $r_{ae} = \frac{H}{R_{Earth}}$ =0.001277 is the ratio of the atmospheric scale height to the radius of the Earth.

The standard ECHAM shortwave radiation scheme

The standard ECHAM5 radiation scheme used in EMAC originates from Fouquart and Bonnel (1980) and was further modified by Morcrette (1990). It takes into account absorption and scattering of shortwave radiation in the atmosphere. The shortwave radiative transfer is calculated in four bands from 250 nm to 4.0 μm. The first band includes the transmission and scattering in the UV and visible (from 250 nm to 690 nm), in the other three bands the radiative flux in the near IR (690 nm to 1.19 μm, 1.19 μm to 2.38 μm, and 2.38 μm to 4.0 μm) is calculated. The computation of the transmission and the scattering is split into calculations for the cloud-free and cloudy section of the grid-cell column. For the angular integration a two-stream Eddington approximation is used, see e.g. Meador and Weaver (1980).
In the cloudy part of the cell additional absorption and reflection by clouds have to be considered. The absorption and scattering are derived from Mie scattering calculations such that in the different spectral bands, the single scattering properties, the extinction and the asymmetry parameter are defined as functions of effective radii, which are given by the cloud microphysical scheme, described later in this chapter.

The radiative transfer equation (see also Eq. 3.3.5.1) is solved by the model in the following form.

$$\mu \frac{dL(\tau, \mu, \alpha)}{d\tau} = L(\tau, \mu, \alpha) - J_{diff}(\tau, \mu, \alpha) - J_{dir}(\tau, \mu, \alpha) \tag{5.20}$$

with L the radiance at an optical depth τ with $\frac{d\tau}{\mu(p)} = -\frac{dp}{g}$, J_{diff} the source function for scattering of diffuse radiation from all angles due to already scattered photons, J_{dir} source function for scattering of the direct solar beam, and α the azimuth angle. The source functions are given by:

$$J_{diff}(\tau, \mu, \alpha) = \tilde{\omega} \frac{1}{2\pi} \int_0^{2\pi} d\alpha' \frac{1}{2} \int_{-1}^{1} d\mu' L(\tau, \mu', \alpha') P(\mu, \alpha; \mu', \alpha') \tag{5.21}$$

and

$$J_{dir}(\tau, \mu, \alpha) = \frac{\tilde{\omega}}{4\pi} F_0 exp(-\frac{\tau}{\mu}) P(\mu, \alpha; -\mu_0, \alpha_0) \tag{5.22}$$

where $P(\mu, \alpha; \mu', \alpha')$ is the scattering phase function, which describes the probability that a photon from direction μ' and α' is scattered into the direction of μ and α, F_0 is the radiative flux at top of the atmosphere.

The radiative energy flux is calculated from the radiance $L(\tau, \mu, \alpha)$ by taking into account the absorption by weak and strong absorbers in different bands by distinguishing which molecules show strong or weak absorption in a particular band. The radiative flux in band b is given by:

$$F_b(p) = F_{b,cons}(p) T_b(\langle u \rangle) \tag{5.23}$$

for weak absorbers and

$$F_b(p) = F_{b,cons}(p) T_b(\langle \sqrt{u} \rangle) \tag{5.24}$$

for strong absorbers, where $F_{b,cons}(p)$ is the incident flux at pressure p, T_b the transmissivity for an absorber amount u and $\langle u(p) \rangle = \int_0^\infty \Pi(x) u(p) dp$ with $\Pi(x)$ a probability density function, which gives the amount of photons which pass through a purely scattering atmosphere.
The spectral integration is carried out using transmission functions in each band which are given by a Pade approximation:

$$T_b(u) = \frac{\sum_{i=0}^{7} A_B u^i}{\sum_{i=0}^{6} B_B u^i}, \tag{5.25}$$

with A_B and B_B being the Pade approximants (see e.g. Saad et al.,1988), which depend on the atmospheric composition and are included in the model as fixed parameters.

In this standard scheme The absorption by water, carbon dioxide, ozone, nitrous oxide, carbon monoxide and molecular oxygen are taken into account. While water and ozone may vary with time, the other gases are assumed to have constant mixing ratios in time and space. For water and carbon dioxide the line spreading with temperature and pressure is taken into account by defining an effective absorber amount which depends on the pressure and temperature of the layer in comparison to reference values. Rayleigh scattering is accounted for with a mean Rayleigh optical thickness of 0.06.

The FUBRAD radiation scheme in EMAC

For a better representation of the solar cycle in General Circulation Models (GCMs) a radiation scheme for the solar wavelength regime called FUBRAD was implemented into EMAC (Nissen et al., 2007). It has been developed at the Freie Universität Berlin (FUB) and operates at pressures smaller than 70 hPa, hence in the middle atmosphere. It takes into account absorption of solar radiation by molecular oxygen (O_2) and ozone (O_3) in 49 bands in the UV and visible (from 121.4 to 682.5 nm). It allows for more accurate heating rates due to e.g absorption by ozone in the stratosphere for varying solar or stellar insolations. In the near infrared (690 nm–4.0 μm) it uses the three bands of the standard radiation scheme, described above (see Tab. 5.1 for the division of the bands). For pressures larger than 70hPa, i.e. closer to the surface, the standard radiation scheme (see above) is applied.

The heating rates in the 49 bands of FUBRAD are parameterized based on different references. Heating in the Lyman α line (121.4–121.6 nm) is parameterized using effective cross sections as suggested by Chabrillat and Kockarts (1997), where the absorption cross section depends on the O_2 number density and on a reduction factor of the solar radiation at each height. Heating by O_2 in the Schumann-Runge bands and continuum (125–205 nm) is parameterized according to Strobel (1978). Heating in the Schumann-Runge bands is important above 60 km for the Earth. The parameterization uses a mean solar flux in the Schumann Runge continuum and mean cross sections. Net heating rates are obtained in two continuum intervals, where scaling factors (see Tab. 5.1) have to be multiplied with the mean solar flux to gain realistic heating rates. In the Schumann-Runge bands the parameterization gives net heating rates within an accuracy of 25%. This parametrization depends on O_2 concentration only. For heating due to O_3 absorption different wavelengths bands (Hertzberg, Hartley, Huggins and Chappuis bands) are treated differently. Temperature independent cross sections from Molina and Molina (1986) are used for wavelengths between 206 and 347 nm and from the World Meteorological Organization (WMO) report (1986) between 347 and 362 nm are used in the Hertzberg, Hartley and Huggins bands. In the Chappuis bands (407 to 682.5 nm) the heating rates are fitted to WMO heating rates as done by Shine and Rickaby (1989). In order to achieve this the integrated flux in the Chappuis band is fitted to 322 W/m^2. Backscattering by O_3 in the Chappuis and Huggins bands are included following Strobel (1978), which depends on the reflectivity of the ground and the lower atmosphere. The absorption of backscattered radiation by O_3 is taken into account for wavelengths lower than 300 nm.

Flux adjustment in the Chappuis band

The standard treatment of the shortwave radiative flux in the wavelength regime of the Chappuis band of ozone assumes an integrated solar flux of 322 $\frac{W}{m^2}$ following the parametrization of Shine and Rickaby (1989). However, the integration of a standard solar spectrum, e.g. by Gueymard (2004) in the corresponding wavelength regime results in 497 $\frac{W}{m^2}$. For Earth climate studies with FUBRAD, the solar energy flux in the Chappuis band is adjusted to 322 $\frac{W}{m^2}$ to obtain realistic heating rates. Since in this work the influence of strongly changing distributions of stellar radiation upon atmospheric properties is investigated this adjustment cannot be applied. The impact of using an unadjusted flux of 497 $\frac{W}{m^2}$ is investigated in Section 6.2.2 for the Earth around the Sun.

Table 5.1: Division of spectral bands in the shortwave radiative transfer scheme FUBRAD.

Band No	bands	lower wavelength (Å)	upper wavelength(Å)	flux unit and possible scaling
1	Lyman α	1214	1219	$W/m^2/nm$
2	Schumann-Runge continuum	1250	1520.0	$erg/s/cm^2$
3	Schumann-Runge continuum	1520	1660.0	$erg/s/cm^2$ x0.5
4	Schumann-Runge continuum	1660	1750.0	$erg/s/cm^2$ x 0.6
5	Schumann-Runge bands	1750	2050.0	ratio to the solar flux in this band
6	Hertzberg continuum	2061.9	2083.3	W/m^2
7	Hertzberg continuum	2083.3	2105.3	W/m^2
8	Hertzberg continuum	2105.3	2127.7	W/m^2
9	Hertzberg continuum	2127.7	2150.5	W/m^2
10	Hertzberg continuum	2150.5	2173.9	W/m^2
11	Hertzberg continuum	2173.9	2197.8	W/m^2
12	Hertzberg continuum	2197.8	2222.2	W/m^2
13	Hertzberg continuum	2222.2	2247.2	W/m^2
14	Hertzberg continuum	2247.2	2272.7	W/m^2
15	Hertzberg continuum	2272.7	2298.9	W/m^2
16	Hertzberg continuum	2298.9	2325.6	W/m^2
17	Hertzberg continuum	2325.6	2352.9	W/m^2
18	Hertzberg continuum	2352.9	2380.9	W/m^2
19	Hertzberg continuum	2380.9	2409.6	W/m^2
20	Hertzberg continuum	2409.6	2439.0	W/m^2
21	Hartley bands	2439.0	2469.1	W/m^2
22	Hartley bands	2469.1	2500.0	W/m^2
23	Hartley bands	2500.0	2531.6	W/m^2
24	Hartley bands	2531.6	2564.1	W/m^2
25	Hartley bands	2564.1	2597.4	W/m^2
26	Hartley bands	2597.4	2631.6	W/m^2
27	Hartley bands	2631.6	2666.7	W/m^2
28	Hartley bands	2666.7	2702.7	W/m^2
29	Hartley bands	2702.7	2739.7	W/m^2
30	Hartley bands	2739.7	2777.8	W/m^2
31	Huggins bands	2777.8	2816.9	W/m^2
32	Huggins bands	2816.9	2857.1	W/m^2
33	Huggins bands	2857.1	2898.6	W/m^2
34	Huggins bands	2898.6	2941.2	W/m^2
35	Huggins bands	2941.2	2985.1	W/m^2
36	Huggins bands	2985.1	3030.3	W/m^2
37	Huggins bands	3030.3	3076.9	W/m^2
38	Huggins bands	3076.9	3125	W/m^2
39	Huggins bands	3125	3175	W/m^2
40	Huggins bands	3175	3225	W/m^2
41	Huggins bands	3225	3275	W/m^2
42	Huggins bands	3275	3325	W/m^2
43	Huggins bands	3325	3375	W/m^2
44	Huggins bands	3375	3425	W/m^2
45	Huggins bands	3425	3475	W/m^2
46	Huggins bands	3475	3525	W/m^2
47	Huggins bands	3525	3575	W/m^2
48	Huggins bands	3575	3625	W/m^2
49	Chappuis band	4070	6825	W/m^2
50	Band without explicit input flux	6825	6900	
51	NIR band 1	6900	11900	ratio of the solar constant
52	NIR band 2	11900	23800	ratio of the solar constant
53	NIR band 3	23800	40000	ratio of the solar constant

5.3.2.2 Radiation in the thermal infrared

The radiative transfer in the thermal infrared takes into account the emission by the atmosphere and the surface as well as the absorption of this emission. Scattering is neglected. The radiative flux is calculated using the rapid radiative transfer model (RRTM) based on Mlawer et al. (1997), which has been developed for Earth climate applications. It calculates the radiative transfer of the thermal radiation by the planetary surface and atmosphere and covers a wavelength range from 10–3000 cm^{-1} (i.e. 3.3–1000 μm) in 16 spectral bands. It takes into account thermal emission by the atmosphere as well as absorption by key atmospheric constituents (water vapor, carbon dioxide, nitrous oxide, chlorofluorocarbons (CFCs), ozone and methane as gases as well as aerosols, water and ice clouds). The frequency integration in RRTM is performed using the correlated–k method (e.g. Goody et al., 1989).

RRTM was originally designed to be used in Earth climate calculations. The reference Earth profile enters RRTM via the reference temperature-pressure profile and the binary species parameter, as well as by pre-deciding, which species are the major absorbers in the upper and lower atmosphere (see Fig. 5.1). The reference temperature-pressure profile is a mid-latitude summer profile (T_{ref}(p)) and the absorption coefficients (k–distributions) have been constructed for interpolation between $\mathrm{T}_{ref}\pm30\,\mathrm{K}$. Absorption coefficients (k-distributions) depend on temperature, pressure and relative concentrations of the radiative species. This concentration dependence is parameterized by the so–called binary species parameter, and k–distributions have been calculated for a range of values of relative concentrations. From this interpolation to actual atmospheric T-p conditions is performed. The optical thickness of cloud particles is calculated from an effective radius as for shortwave radiation, where absorption by water particles can be expressed as a function E^{-cR_l} with c a constant and R_l the effective radius of the cloud droplets. For ice clouds a dependency of the absorption on the particle radius R_i as $1/R_i$ has been found by measurements. The cloud overlap is calculated using the maximum-random overlap assumption. For aerosols the emissivity has been derived from the Tanre climatology (Tanré et al., 1984), which gives an optical depth at 0.55 μm. The angular integration is solved in two-stream approximation since the influence of cloud and aerosol particles has to be taken into account.

Change of the extrapolation of absorption coefficients in thermal radiative transfer RRTM

Since the rapid radiative transfer model (RRTM) was developed for Earth climate calculations, the absorption coefficients are tabulated only for a narrow temperature and pressure range, e.g. $\mathrm{T}_{ref}\pm30\,\mathrm{K}$, where T_{ref} is a mid-latitude summer temperature profile of the Earth. Outside this temperature range, the absorption coefficients can no longer be interpolated but are extrapolated. This is clearly less reliable than interpolation, and does sometimes result in negative optical depths. In order to overcome this potential shortcoming in the extrapolation, the values of optical depths were set to zero, whenever extrapolation led to negative values. This change was introduced into the model following a suggestion Ponater (private communication), and is included in all EMAC versions from messy 1.10.

The 1D model applied in this thesis, described in sec. 5.2 also uses RRTM for the IR-

Band Number	Wavenumber Range, cm^{-1}	Species Implemented in RRTM: Lower* Atmosphere — Key Species	Lower* Atmosphere — Minor Species	Middle/Upper† Atmosphere — Key Species	Middle/Upper† Atmosphere — Minor Species
1	10–250	H_2O		H_2O	
2	250–500	H_2O		H_2O	
3	500–630	H_2O, CO_2		H_2O, CO_2	
4	630–700	H_2O, CO_2		CO_2, O_3	
5	700–820	H_2O, CO_2	CCl_4	CO_2, O_3	CCl_4
6	820–980	H_2O	CO_2, CFC-11,‡ CFC-12	···	CFC-11,‡ CFC-12
7	980–1080	H_2O, O_3	CO_2	O_3	
8	1080–1180	H_2O	CO_2, CFC-12, CFC-22‡	O_3	
9	1180–1390	H_2O, CH_4		CH_4	
10	1390–1480	H_2O		H_2O	
11	1480–1800	H_2O		H_2O	
12	1800–2080	H_2O, CO_2		···	
13	2080–2250	H_2O, N_2O		···	
14	2250–2380	CO_2		CO_2	
15	2380–2600	N_2O, CO_2		···	
16	2600–3000	H_2O, CH_4		···	

*1050–96 mbar except for band 8 (1050–317 mbar).
†96–0.01 mbar except for band 8 (317–0.01 mbar).
‡Optical depths of these halocarbons are increased to account for other absorption bands of these species that are not implemented.

Figure 5.1: Species included in the thermal infrared radiative transfer scheme RRTM. Taken from Mlawer et al. 1997

radiative transfer. Also in this model, the optical depths are set to zero whenever extrapolation leads to negative values.

5.3.3 Convection

EMAC offers the possibility to choose between various convection schemes. All available schemes are mass-flux cumulus convection schemes described in Tost et al. (2006). Generally sub-grid mass-flux schemes account for the contribution of convection to the transport of mass, momentum, moisture and heat on the large scale, see Section 3.4.3. Thereby, convection leads to the formation of clouds, so-called cumulus clouds.

These processes are realized in mass-flux parametrization by defining updrafts and downdrafts of air. The updraft of mass is described by

$$\frac{\partial M_u}{\partial z} = E_u - D_u \tag{5.26}$$

where M_u is the mass flux in the updraft and M is defined as

$$M = \sum_i M_i = \sum_i \bar{\rho}\sigma_i w_i, \tag{5.27}$$

with $\bar{\rho}$ the large-scale air density, σ_i the fractional area, w_i the vertical velocity, z the vertical coordinate, E_u entrainment and D_u detrainment. The index i denotes individual updrafts. The updraft s_u of the dry static energy ($s = c_p T + gz$) is given by

$$\frac{\partial}{\partial z}\left(M_u s_u\right) = E_u \bar{s} - D_u s_u + L\bar{\rho}c_u \tag{5.28}$$

with $\bar{s}$ the large-scale dry static energy, L the latent heat, ρ the density of air and c_u the release of latent heat due to condensation. The updraft of specific humidity q is defined as

$$\frac{\partial}{\partial z}\left(M_u q_u\right) = E_u \bar{q} - D_u q_u - \bar{\rho}c_u \tag{5.29}$$

and the updraft of cloud water by

$$\frac{\partial}{\partial z}\left(M_u l_u\right) = -D_u l_u + \bar{\rho} c_u - \bar{\rho} P_u, \tag{5.30}$$

with l the mixing ratio of cloud water and P_u the conversion of cloud water into precipitation. The transport of momentum by cumulus convection is given by the following two equations:

$$\frac{\partial}{\partial z}\left(M_u u_u\right) = E_u \bar{u} - D_u u_u \tag{5.31}$$

and

$$\frac{\partial}{\partial z}\left(M_u v_u\right) = E_u \bar{v} - D_u v_u \tag{5.32}$$

where $\bar{u}$ and $\bar{v}$ are the mean components of the horizontal wind. The downdrafts are defined by a corresponding set of equations, which assume mixing of the updrafted air with the environment. It is included that detraining air may contribute to the formation of stratiform clouds (see next section).
The entrainment and detrainment are given by

$$E = M\epsilon = \sum_i M_i \epsilon_i \tag{5.33}$$

and

$$D = M\delta = \sum_i M_i \delta_i \tag{5.34}$$

with ϵ the entrainment, δ the detrainment rate.
The organized detrainment (i.e. non-turbulent) describes the mass loss due to clouds which lose their buoyancy:

$$D = E - \frac{\partial M}{\partial z} = -\sum_i \bar{\rho} w_i \frac{\partial \sigma_i}{\partial z} \tag{5.35}$$

where σ_i is a function giving the distribution of detraining clouds over height. It is chosen to fulfill the conditions that at cloud base and cloud top it is equal to the fractional area of entrainment.
Assuming steady state the vertical momentum equation for an individual updraft is defined as

$$w_i \frac{\partial w_i}{\partial z} = b_i - \epsilon_i w_i^2 \tag{5.36}$$

with the buoyancy b_i. The buoyancy of the ensemble of individual updrafts is given by

$$b = \frac{g}{\bar{T}_v}\left(T_v - \bar{T}_v\right) - gl \tag{5.37}$$

where T_v is the virtual temperature of the ensemble and $\bar{T}_v$ the virtual temperature of the environment. The entrainment rate ϵ for organized entrainment is calculated from

$$\epsilon = \frac{b}{2(w_0^2 + \int_0^z b dz)} + \frac{1}{\bar{\rho}} \frac{\partial \bar{\rho}}{\partial z} \tag{5.38}$$

with w_0 the vertical velocity at the cloud base ($z = 0$) and the integral ranging from the cloud base to the layer z.
Due to convective processes the environment is heated and dried. Due to this the available

energy for convection will decrease which is expressed in terms of the so-called convective available potential energy (CAPE):

$$CAPE = \int_{base}^{top} b dz. \tag{5.39}$$

It is assumed that convection reduces $CAPE$ over a certain time scale τ, which has to be specified in the model, such that

$$\frac{\partial}{\partial t} CAPE \approx -\frac{CAPE}{\tau}. \tag{5.40}$$

From a first guess of the mass-flux at the cloud base CAPE is determined from which the mass-flux at the cloud base is calculated.

In this work the mass-flux scheme also applied in the forecast model of the European Centre for Medium-Range Weather Forecasts (Bechtold et al., 2004) is used. This scheme makes a distinction between shallow and deep convection, which depends on the pressure difference of the lowest and highest level where convection occurs. If convection occurs for a pressure regime that spans over 200 hPa deep convection parametrization is applied, otherwise it is assumed to be shallow convection. When neither shallow nor deep convection are found but the relative humidity at layers with heights lower than 500 m is higher than 80% and the vertical velocity is positive mid-level convection can be activated. Convection is triggered when the virtual potential energy (Θ_v) in the cloud at the cloud base is 0.5 K higher than the virtual potential energy of the environment. If convection sets in, organized and turbulent entrainment are calculated. Turbulent entrainment rates follow profiles of fixed values, which are higher for shallow convection than for deep convection.
Whether or not convection occurs is decided by testing for positive buoyancy of an air parcel that has a slightly different moisture and temperature content (e.g. 0.2 K and 0.1 g/kg) at the levels close to the surface. At the cloud base no buoyancy test is applied. Here, convection sets in whenever the vertical velocity at the cloud base is positive. Convection occurs as long as CAPE is non zero. The cloud top is set at the level where the vertical velocity vanishes or where the buoyancy is zero.

5.3.4 Stratiform cloud processes

Stratiform clouds are characterized by their large horizontal dimension, opposed to cumulus clouds, which are rather extended in the vertical dimension.
These clouds are calculated based on a microphysical scheme (Lohmann and Roeckner, 1996) and a cloud cover scheme. Two different cloud cover schemes can be chosen, either a stochastic cloud cover scheme by Tompkins (2002) or a scheme based on the approach by Sundqvist (1978) (see sec. 5.3.4.1).

The mean mass mixing ratios are calculated taking into account various processes, which are only described quantitatively. Details can be found in the model descriptions (Roeckner et al., 2003, Roeckner et al., 1996, Deutsches Klimarechenzentrum (DKRZ), 1992) and references therein.
The mixing ratio of water vapor is determined from contributions by advective, diffusive and convective transport of vapor, evaporation of rain fall, evaporation of liquid water, sublimation of snow and cloud ice, condensation of water vapor to cloud water, or deposition

to cloud ice as well as dissipation of cloud condensates due to turbulent fluctuations. For cloud water additional to transport, the mixing ratio is affected by condensation of water vapor, melting of cloud ice, turbulent fluctuations, evaporation, homogeneous, stochastic, heterogeneous and contact freezing, autoconversion of cloud liquid water into rain (coagulation), and accretion of cloud water by falling rain and snow. For the solid cloud phase, hence snow and ice, transport, freezing of cloud water, deposition of water vapor, generation of cloud ice by turbulent effects, as well as melting, sublimation, sedimentation, aggregation and accretion of cloud ice by snow are taken into account. When phase changes occur, the temperature changes due to the release of latent heat.

5.3.4.1 Cloud cover calculations

The model includes two cloud cover schemes.

The statistical-dynamical approach of Tompkins (2002) assumes that cloud formation is caused by fluctuations of the total water content (r_w) only. The fractional cloud cover f_{cloud} is expressed as:

$$f_{cloud} = \int_{r_s}^{\infty} G(r_w) dr_w \tag{5.41}$$

where r_s is the saturation water vapor pressure and $G(r_w)$ is the probability density function, which is based on simulation with a cloud resolving model. The scheme applies a bell-shaped beta distribution, which is a continuous probability distribution. It is described by four parameters, two which determine the skewness and the variance of the distribution, and two which give the upper and lower boundaries of the distribution. It has been found this gives a good fit to the water distribution in clouds. One of the shape parameters is set to be constant, the other is calculated based on prescribed relations to the constant shape parameter and prognostic variables. The boundary parameters are evaluated by iteration and based the mean content of r_w in the grid-cell.

For cloud cover calculations after Sundqvist (1978) the fractional cloud cover f_{cloud} is parametrized as a function of the mean relative humidity in the grid cell (rh) by

$$f_{cloud} = 1 - \sqrt{1 - f_{cloud,0}} \tag{5.42}$$

for a $rh > rh_0$ and $f_{cloud} = 0$ if $rh \leq rh_0$. rh_0 is the condensation threshold defined as

$$rh_0(p) = rh_{0,top} + (rh_{0,surf} - rh_{0,top}) exp\left(1 - \left(\frac{p_s}{p}\right)^n\right) \tag{5.43}$$

with $rh_{0,surf}$ =0.99 and $rh_{0,top}$ =0.6 being fixed parameters, p_s the surface pressure, and n =4 a fitting parameter. $f_{cloud,0}$ is determined from:

$$f_{cloud,0} = \frac{rh - rh_0}{rh_{sat} - rh_0} \tag{5.44}$$

with rh_{sat} =1.
In this work the cloud cover scheme after Sundqvist (1978) is used, since it has been found, that when coupling a mixed layer ocean to the model (see Sec. 5.3.8.6), the scheme by Tompkins (2002) may produce large deviations from the observed cloud covers depending on model resolution (Ponater, private communication).

5.3.4.2 Phase changes

Since the cloud cover is given by the beta distribution, no cloud water or ice should be present in the cloud free parts of the grid cell. Therefore, instantaneous evaporation or sublimation has to take place as soon as cloud water or ice are transported into the clear sky part of the grid cell. Important cloud generation processes are condensation and deposition of water vapor. Whether one or the other takes place depends on the temperature of the environment. For temperatures below -35°C only deposition of ice takes place while above 0°C only condensation to water droplets occurs. For temperatures between -35 and 0°C condensation of water vapor is favored as long as a threshold value of water ice is not reached. For higher cloud ice concentrations only deposition of water vapor is assumed.
The total amount of cloud water freezes homogeneously and instantaneously in one time step for temperatures lower than -35 °C, and cloud ice melts completely for temperatures larger than 0°C. In between these two extremes stochastic and heterogeneous freezing of cloud water is assumed. This process depends on the cloud droplet number concentration, the number of active contact nuclei and the cloud drop size. The cloud droplet number concentration follows a prescribed profile depending on the surface type (land or sea). The cloud droplet size is calculated depending on the cloud water. The total water concentration and the concentration of the active contact nuclei is assumed to be a linear function of temperature.

5.3.4.3 Precipitation

For temperatures above -35 °C the liquid cloud water content may be reduced by formation or growth of rain drops as well as accretion of cloud water by snow. Snow forms through the aggregation of cloud ice and can furthermore grow by the accretion of cloud ice, except where no cloud ice is present for temperatures higher than 0°C, as described above. The evaporation of falling rain depends on the rain flux and the saturation of the surrounding air, which is calculated with respect to liquid water. The sublimation of snow and falling ice then depends on the saturation of the surrounding air with respect to ice. The melting of snow and ice depends on the heat budget and temperature of the surrounding air.
These processes determine the rain and snow flux from which the mixing ratio of rain and snow/ice are calculated taking into account the fraction of the grid cell where precipitation takes place.
The cloud microphysics scheme includes a large set of parameters which are partly set to constant values in the parameterizations. Others are used as tunable parameters, which, however, have not been changed in the course of this work.

5.3.5 Saturation water vapor pressure

The saturation water vapor pressure formulation implemented in EMAC stems from Sonntag (1994). Here two expressions are used, one for the calculation of the saturation water vapor pressure over ice ($p_{sat,ice}$), and one for the calculation of the water vapor pressure over liquid water ($p_{sat,liq}$).

Saturation water vapor pressure over ice

The formulation from Sonntag (1994) for $p_{sat,ice}$ is valid for a temperature range from 173.15–237.16 K. For $p_{sat,ice}$ in Pa, as used in EMAC, it is:

$$ln\left(p_{sat,ice}(T)\right) = -6024.5282T^{-1} + 29.32707 + 1.0613868 \cdot 10^{-2}T - 1.3198825 \cdot 10^{-5}T^2 - 0.49382577lnT. \quad (5.45)$$

The above is applied whenever the temperature falls below the melting temperature of water (T_{melt} =273.15 K).

Saturation water vapor pressure over liquid water

In Sonntag (1994) the formulation for $p_{sat,liq}$ is valid for temperatures from 173.15 to 373.15 K, so also for supercooled water. For $p_{sat,liq}$ in Pa it is:

$$ln\left(p_{sat,liq}\right) = -6096.9385T^{-1} + 21.2409642 - 2.71193 \cdot 10^{-2}T + 1.673952 \cdot 10^{-5}T^2 + 2.433502lnT. \quad (5.46)$$

Adaptation of EMAC to higher temperatures – new $p_{sat,liq}$ expression

For the application of EMAC to exoplanet scenarios, it was necessary to update the model's treatment of water vapor pressure at high temperatures. In the original EMAC model version ECHAM5/MESSy1.8 applied in this work the saturation water vapor pressure was calculated for a temperature range from 50–400 K. Whenever the calculated temperature exceeded these values model calculations stopped. Therefore, for this work, the temperature range was extended to higher temperatures up to the critical point of water T_{crit}=647 K.

Saturation water vapor pressure over liquid water from Wagner and Pruß 2002

To extend the temperature range for which the saturation water vapor pressure is calculated in EMAC the following expression was implemented to replace the formulation by Sonntag (1994) (Eq. 5.46).
In Wagner and Pruß (2002) a formulation for $p_{sat,liq}$ can be found which is valid up to the critical point of water (T_{crit} =647 K, p_{crit} =22 MPa).

$$ln\left(\frac{p_{sat,liq}(T)}{p_{crit}}\right) = \frac{T_{crit}}{T}\left[-7.85951783 \cdot \left(1-\frac{T}{T_{crit}}\right) + 1.84408259 \cdot \left(1-\frac{T}{T_{crit}}\right)^{1.5} - 11.7866497 \cdot \left(1-\frac{T}{T_{crit}}\right)^{3} + 22.06807411 \cdot \left(1-\frac{T}{T_{crit}}\right)^{3.5} - 15.9618719 \cdot \left(1-\frac{T}{T_{crit}}\right)^{4} + 1.80122502 \cdot \left(1-\frac{T}{T_{crit}}\right)^{7.5}\right] \quad (5.47)$$

The above was implemented into EMAC replacing the original expression by Sonntag (1994), which is strictly only valid up to 374.15 K, but was used up to temperatures of 400 K.
Fig. 5.2 shows a set of formulations and data for the saturation water vapor pressure with reference to liquid water. Formulations shown are the one from Sonntag (1994), eq. 5.46,

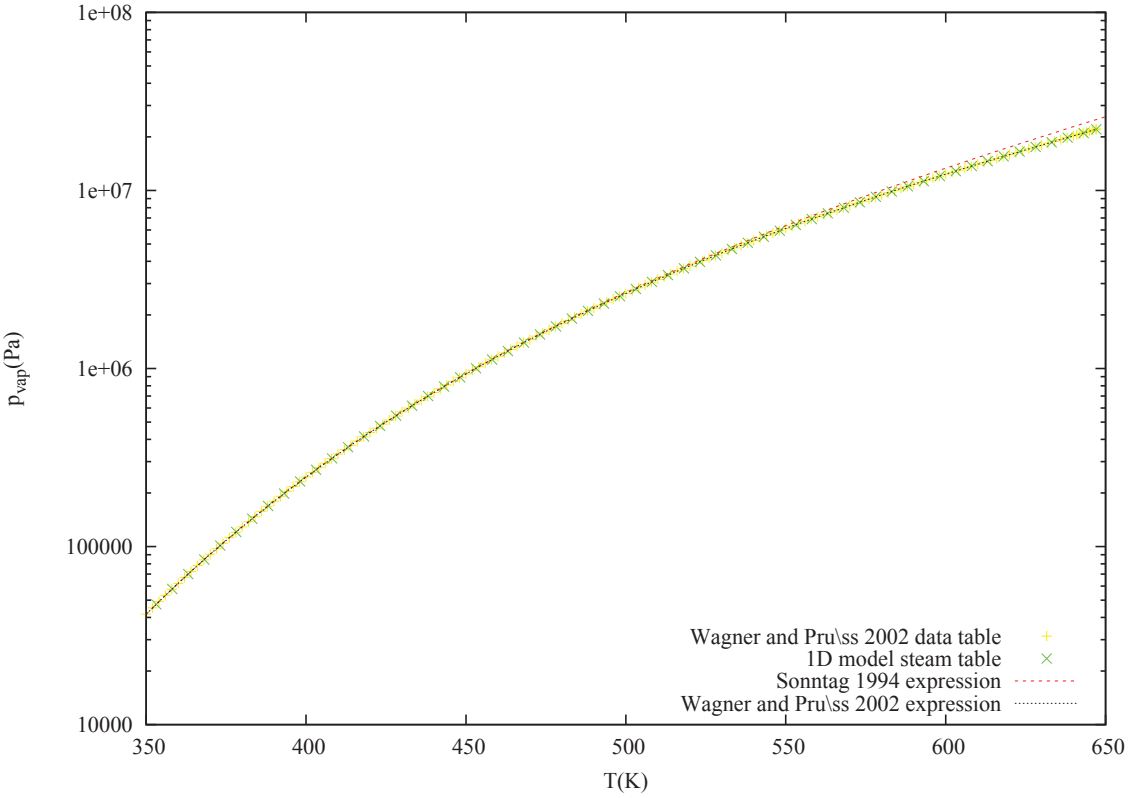

Figure 5.2: Saturation water vapor pressures formulations and data

and the one from Wagner and Pruß (2002), eq. 5.47. Furthermore, data is shown from Wagner and Pruß (2002) and data used in the 1D radiative-convective model described in Sec. 5.2. One can see that all expressions and data compare reasonably well, except for a small deviation at very high temperatures for the formulation of Sonntag (1994). The influence of this change is evaluated in Chapter 6 for the Earth around the Sun.

The replacement of this expression allowed for more stable model calculations, especially for the model scenarios Earth-like planets around the K-type star, which result in much higher surface temperatures. Nevertheless, it should be noted that for these scenarios, occasionally temperatures higher than 647 K occurred during the model spin-up due to numerical instabilities (even for small time steps of 120 s) occurred. In these cases the saturation water vapor pressure over liquid water for 647 K was used. As soon as the model atmosphere reached a new equilibrium state, such high temperatures were no longer obtained.

5.3.6 Orography parametrization

A sub-grid scale orography parametrization is implemented in EMAC to account for orographic variations on scales smaller than the horizontal resolution of the model. The two main effects of orography on the atmospheric flow are the transfer of momentum from the ground to the atmosphere by gravity waves and the drag to the atmospheric flow which is caused by mountains which block the air flow at low atmospheric levels. The sub-grid orography is described by seven parameters linked to the orography, the standard deviation,

the anisotropy, the slope, the orientation and minimum, mean and maximum elevation of the orographic features. These are derived from a high resolution topographic dataset and are an input to the model. Whenever a mountain is high enough a part of the low level air flow is blocked and the rest of the flow follows the terrain which causes vertical motion of the air and gravity waves are generated. The amount of blocked air and gravity wave stress depend on the orographic parameters as well as on the characteristics on the air flow such as wind speed, air density and the buoyancy frequency ($N = \sqrt{\frac{\alpha g T}{C_p} \frac{\partial d}{\partial z}}$).
Above the source region of gravity waves the gravity wave stress is set constant until they break or reach a critical level, typically in the mesosphere.
When gravity waves break or reach a critical level they produce a drag on the atmospheric flow, which leads to heating. A change in wind direction with height can lead to such a critical level, when the flow does not lie in the plane of the low level stress, hence the gravity stress turns zero. The drag produced is the vertical derivative of the gravity wave stress. The breaking of gravity waves is parametrized based on the Richardson Number and on the assumption that gravity waves reach saturation. When the height dependent Richardson number of the flow reaches the critical value of 0.25, gravity waves are assumed to be saturated. The gravity wave stress is then set constant to the saturation value for layers above until the saturation condition is met again.

5.3.7 Gravity wave spectrum

In addition to the gravity waves generated by orography described above, gravity waves can also be excited by e.g. convective activity or front systems. Since the sources of gravity waves mostly reside in the troposphere they mostly only propagate through the middle atmosphere. While dissipation of vertically moving gravity waves is taken into account by the model, horizontal movement of gravity waves on scales larger than the horizontal resolution is neglected. The deposition of momentum flux by vertically propagating gravity waves is parametrized following the Hines Doppler Spread theory. The deposited momentum flux depends on the large scale flow, the buoyancy frequency, the input gravity wave spectrum and the horizontal wind variance. Furthermore, parameters related to the gravity waves have to be calculated by the parametrization such as the cutoff vertical wavenumber, which specifies which wavenumbers of the input spectrum can continue to propagate upwards.

5.3.8 Surface processes

5.3.8.1 Surface albedo

The mean surface albedo of a grid cell depends on the fraction of land and sea surfaces (f_{sea}) in the grid cell and is based on a background albedo (A_{bg}) which has been derived from satellite observations of the Earth. The mean surface albedo A_{surf} is given by

$$A_{surf} = f_{sea} A_{sea} + (1 - f_{sea}) A_{land} \tag{5.48}$$

For sea surfaces the sea ice fraction (f_{seaice}) is taken into account and the albedo of the sea (A_{sea}) is calculated from:

$$A_{sea} = f_{seaice} A_{snow} + (1 - f_{seaice}) A_{opensea}, \tag{5.49}$$

where $A_{opensea}$ is the albedo of sea water (set to 0.07) and f_{seaice} is either an input parameter or calculated by the ocean module (see section 5.3.8.6). A_{snow} is the albedo of snow

or ice. It depends on the surface below the snow/ice cover. The albedo of the snow/ice covered ground is assumed to depend linearly on temperature, where lowest temperatures lead to lowest snow albedo and vice versa.
For land surfaces it is taken into account how much of the grid cell is covered with forest and/or snow.

$$A_{land} = f_{forest} A_{forest} + (1 - f_{forest}) A_{ground} \tag{5.50}$$

with

$$A_{ground} = f_{sn} A_{snow} + (1 - f_{sn}) A_{bg} \tag{5.51}$$

and

$$A_{forest} = f_{sv} A_{ground} + (1 - f_{SV}) A_{canopy} \tag{5.52}$$

where f_{forest} is the fraction of forest, A_{forest} the albedo of the forest, A_{ground} the albedo of the forest free land surface, f_{sn} the snow cover of the ground. f_{sv} is the so-called sky-view factor, which is a measure of the visibility of the ground through a forest. The sky-view factor depends on the type of forest present, which is expressed in the leaf area index, which is and input parameter. The albedo of the canopy A_{canopy} is defined as

$$A_{canopy} = f_{csn} A_{csn} + (1 - f_{csn}) A_{csnf} \tag{5.53}$$

where f_{csn} is the snow load of the canopy which depends on temperature, wind and the type of forest (see also the paragraph about surface water reservoirs below). A_{csn} is set to 0.2. A_{csnf} is the albedo of the canopy without snow which is an input parameter.

5.3.8.2 Surface fluxes

In the lowest model layer the surface fluxes of momentum (J_u, J_v), static energy (J_s), moisture (J_{q_v}) and other water phases (J_{q_w}) are calculated, which depend on the drag coefficient C_m, the heat transfer coefficient C_h and the absolute value of the horizontal velocity $|v_h|$ as follows:

$$J_u = \rho C_m |v_h| u \tag{5.54}$$

$$J_v = \rho C_m |v_h| v \tag{5.55}$$

$$J_s = \rho C_h |v_h| (s - s_{surf}) \tag{5.56}$$

$$J_{q_w} = \rho C_h |v_h| (q_w - q_{w,surf}) \tag{5.57}$$

$$J_{q_v} = \rho C_h |v_h| (q_v - q_{sat}(T_{surf}, p_{surf})) \tag{5.58}$$

for the moisture flux (evaporation) above sea and

$$\begin{aligned} J_{q_v} = \rho C_h |v_h| ((f_{sn} + (1 - f_{sn}) f_{land})(q_v - q_{sat}) + \\ (1 - f_{sn})(1 - f_{land})(1 - f_{veg})(q_v - rh q_{sat}) + \\ (1 - f_{sn})(1 - f_{land}) f_{veg} E (q_v - q_{sat})) \end{aligned} \tag{5.59}$$

above land. Here, u and v are the horizontal velocity components, s the static energy, s_{surf} static energy at the surface q_w cloud water, $q_{w,surf}$ cloud water mass mixing ratio at the surface, which is set to zero, q_v is the specific humidity and $q_{sat}(T_{surf}, p_{surf})$ the saturation water vapor specific humidity at the surface. For the moisture flux over land the fractions of land covered by snow (f_{sn}), land with a water reservoir (f_{land}), land covered with vegetation (f_{veg}) and land with bare soil are taken into account, since it is assumed

that they provide different amounts of moisture to the atmosphere. Over snow covered and land covered regions the moisture flux depends on the difference of the specific humidity to the saturation specific humidity, while for land covered with vegetation an efficiency factor (E) for evaporation is used, whereas for land covered with bare soil it is assumed that the relative humidity (rh) is related to the water content of the soil.

5.3.8.3 Surface temperature calculation

Land surface temperature is calculated according to the following equation is solved:

$$C_L \frac{\partial T_{surf}}{\partial t} = F_{RAD,net} + F_{LH} + F_{SH} + F_{GH}, \tag{5.60}$$

where C_L is the heat capacity of land in $\mathrm{Jm^{-2}K^{-1}}$, F_{LH} the latent heat flux, F_{SH} the sensible heat flux, F_{GH} the ground heat flux and $F_{RAD,net}$ the net radiative flux which is:

$$F_{RAD,net} = (1 - A_{surf})F_{s,\downarrow} + \epsilon F_{l,\downarrow} - \epsilon\sigma T_{surf}^4 \tag{5.61}$$

with A_{surf} the surface albedo, $F_{s,\downarrow}$ the downwelling shortwave stellar radiation, ϵ the surface emissivity $F_{l,\downarrow}$ the downwelling longwave radiation and σT_{surf}^4 the total energy flux due to the surface temperature via the Stefan Boltzmann's law.

5.3.8.4 Water reservoirs

The water reservoir of the surface is determined e.g. by the snow and rain at the surface and amount intercepted by the canopy. It is assumed that a quarter of the snow or rainfall is intercepted by the canopy. The amount of water stored then depends on the sublimation and deposition of snow or the evaporation or condensation (dew deposition) of liquid water, the unloading of the canopy by either slipping of snow due to wind speed or melting/evaporation of snow and rain depending on temperature. Melting of snow or evaporation of liquid water at the canopy cools the lowest surface layer depending on its pressure thickness. The amount of water which can be stored in the canopy depends on the leaf area index (LAI). Melting snow is converted into liquid water and then adds to liquid water reservoir of the canopy or to the surface reservoir. The remaining three quarters of precipitation reach the surface. Snow is either deposited, sublimated or melts, depending on the surface temperature (Eq. 5.60). Furthermore, the snow which slipped from the canopy adds to the snow reservoir. For the liquid water reservoir, the soil wetness, additional processes are taken into account such as the surface runoff and drainage.

5.3.8.5 Lakes

Lakes in the model are assumed to be either frozen or ice free. Furthermore, a constant lake depth of 10 m (h_m) is assumed. The temperature of a lake is the determined by

$$C_w \frac{\partial T_w}{\partial t} = H \tag{5.62}$$

where H is the net surface heat flux, including radiative and turbulent heat fluxes, $C_w = c_q \rho_w h_m$ is the heat capacity of the lake, which depends on the heat capacity and density of water and the thickness of the lake.

5.3.8.6 Oceanic processes

For the part of the surface covered by ocean EMAC offers two possibilities, either to use fixed climatological sea surface temperatures (SSTs) and sea ice concentrations, or to calculate these quantities with a mixed layer ocean (MLO) model.

SSTs and sea ice prescription

When sea surface temperatures and sea ice concentrations and sea ice thickness are prescribed, e.g. the dataset of the Atmospheric Model Intercomparison Project (AMIP) II (Taylor et al., 2000) can be used, which has been derived from Earth's observations.

Mixed layer ocean and slab ice model

The MLO model, which can be used to interactively calculate the SSTs and sea ice concentrations and sea ice thickness is based on the ocean model by Roeckner et al. (1995). The SSTs are then calculated similar to the lake temperatures:

$$C_{sw}\frac{\partial T_{sea}}{\partial t} = H + Q \tag{5.63}$$

where T_{sea} is the calculated SST, H the net surface heat flux, C_{sw} the heat capacity of sea water heat capacity and Q is an additional heat flux which accounts for the transport of heat by the ocean. This q-flux Q is generally not well known and has to be derived from a reference simulation with fixed sea surface temperatures:

$$Q = H_{clim} - C_{sw}\frac{\partial T_{clim}}{\partial t} \tag{5.64}$$

where T_{clim} are the fixed sea surface temperatures and H_{clim} the net heat flux which is calculated in the reference simulation by the atmosphere model. This q-flux introduces an additional heat flux to or from the atmosphere. For scenarios too far from the reference scenario this may introduce a large uncertainty. Furthermore, a depth of 50 m is assumed for the calculation of the sea water heat capacity C_{sw}.
In the mixed layer ocean model a thermodynamic sea ice model is integrated which calculates the temperature and the sea ice thickness following a similar procedure as above. To avoid massive sea-ice build up in the southern hemisphere, a constant heat flux of 20 Wm^{-2} is applied in the southern-ocean regions in the sea-ice calculations.

Including the mixed layer ocean model in EMAC

The MLO model described above was not implemented in EMAC, and has been included in the model in the course of this work. It has been provided by S. Dietmüller and M. Ponater. The effect of using a mixed layer ocean instead of fixed SSTs and sea ice is evaluated in Chapter 8 for the Earth around the Sun.

5.3.9 Discretization of the basic equations

The model equations presented above are solved using different approaches for the horizontal and vertical discretization. In the horizontal the variables are either represented by a truncated series of spherical harmonics or on a Gaussian grid of latitudes and longitudes, while the vertical discretization uses a hybrid coordinate.

5.3.9.1 Horizontal representation

The variables ξ, D, T, Φ_s and $\ln p_s$ (vorticity, divergence, temperature, surface geopotential and surface pressure) are represented as a truncated series of spherical harmonics. This is done by expressing a variable $X = X(\lambda, \mu, \eta, t)$ as:

$$X(\lambda, \mu, \eta, t) = \sum_{m=-M}^{M} \sum_{n=m}^{N(M)} X_n^m(\eta, t) P_n^m(\mu) e^{im\lambda}. \tag{5.65}$$

Where λ is longitude, $\mu = sin\phi$ and ϕ latitude, η is the vertical coordinate, t time, m the zonal wave number and n the meridional index. P_n^m are the associated Legendre Polynomials of first kind:

$$P_n^m(\mu) = \sqrt{(2n+1)\frac{n-m!}{n+m!}} \frac{1}{2^n n!} (1-\mu^2)^{\frac{m}{2}} \frac{d^{(n+m)}}{d\mu^{(n+m)}} (\mu^2 - 1), (m \geq 0) \tag{5.66}$$

for which $P_n^m(\mu) = P_n^{-m}(\mu)$ is valid. This definition leads to

$$\frac{1}{2} \int_{-1}^{1} P_n^m(\mu) P_s^m(\mu) d\mu = \delta_{ns} \tag{5.67}$$

with δ being the Kronecker delta. The spectral coefficients $X_n^m(\eta, t)$ of the variable X are given by

$$X_n^m(\eta, t) = \frac{1}{4\pi} \int_{-1}^{1} \int_{0}^{2\pi} X(\lambda, \mu, \eta, t) P_n^m(\mu) e^{-im\lambda} d\lambda d\mu. \tag{5.68}$$

The horizontal derivatives of the variable X are then given by:

$$\left(\frac{\partial X}{\partial \lambda}_m \right) = imX_m \tag{5.69}$$

and

$$\left(\frac{\partial X}{\partial \mu}_m \right) = \sum_{n=m}^{N(m)} X_n^m \frac{dP_n^m}{d\mu} \tag{5.70}$$

with

$$(1-\mu^2)\frac{dP_n^m}{d\mu} = n\epsilon_{n+1}^m P_{n+1}^m + (n+1)\epsilon_n^m P_{n-1}^m \tag{5.71}$$

and $\epsilon_n^m = \sqrt{\frac{n^2-m^2}{4n^2-1}}$.

In EMAC, which is based on ECHAM5 only triangular truncations of the spherical harmonics can be used due to the parallelization of the spectral part. This means that M=N and eq. 5.65 becomes:

$$X(\lambda, \mu, \eta, t) = \sum_{m=-M}^{M} \sum_{n=|m|}^{M} X_n^m(\eta, t) P_n^m(\mu) e^{im\lambda}. \tag{5.72}$$

For a chosen triangular truncation, a grid of points on the sphere is then defined on which the prognostic variables and their tendencies are calculated. The tendencies include contributions from the change of spectral variables and from other parameterizations included.

These parameterizations are calculated on a Gaussian grid of latitudes and longitudes, which can be found for each triangular truncation.

For example in this work a triangular truncation of the spherical harmonics at a wavenumber M of 42 is applied (T42). This corresponds to a Gaussian grid with 128 points in longitude and 64 points in latitude and thereby gives an resolution of ≈2.8°×2.8°, which is about 300 km×300 km. At this resolution the EMAC model behaves well in comparison to lower resolutions, hence the basic quantities do not show too large deviations from the observed climate state of the Earth. A higher resolution would allow for a more accurate determination of these properties including also effects which are due to processes on smaller scales. However, since the interest of this work is influence of dynamical processes on the mean climate state of an Earth-like planet, is sufficient and less expensive in terms of computing time.

5.3.9.2 Vertical coordinate

In the vertical a coordinate is used, which is terrain following in the lower atmosphere and flattens to surfaces of constant pressure in the stratosphere. It is defined as

$$p_{k+\frac{1}{2}} = A_{k+\frac{1}{2}} + B_{k+\frac{1}{2}} p_s \tag{5.73}$$

with p_s being the surface pressure and k runs from 1 to N_{lev}. The values for $A_{k+\frac{1}{2}}$ and $B_{k+\frac{1}{2}}$ are given in Table 5.2 as well as the estimated pressure $p_{k+\frac{1}{2}}$ for p_s =1000 hPa, which is approximately the mean surface pressure of the Earth.
The prognostic variables are calculated on full pressure levels (p_k) which are defined by

$$p_k = \frac{1}{2}(p_{k+\frac{1}{2}} + p_{k-\frac{1}{2}}). \tag{5.74}$$

These are also listed in Table 5.2.

5.4 Model assumptions and approximations

Several assumptions and approximations have been made for the representation of the physics governing a planetary atmosphere in the models described above. The most important ones for this work are given below, starting with a comparison of the most important differences in the assumptions in the 1D and the 3D model.

For the 1D model the momentum equation is approximated by hydrostatic balance. It is assumed that in the vertical the structure of the atmosphere is given by the balance of the gravitational and the pressure force. The difference in the atmospheric structure in the horizontal direction due to winds is assumed to be small. The contribution of evaporation or condensation upon the surface pressure at the surface is accounted for by addition of the water vapor pressure to the atmospheric background pressure.
The 3D model also approximates the vertical structure of the atmosphere by hydrostatic equilibrium, however the contribution of horizontal winds on the structure is taken into account by solving the equation of momentum. A contribution of evaporation or condensation of water vapor at the surface is neglected in the 3D model. The difference in the

Table 5.2: Parameters used to calculate the vertical levels with Eq. 5.73.

k	$A_{k+\frac{1}{2}}$	$B_{k+\frac{1}{2}}$	$p_{k+\frac{1}{2}}(1000hPa)$	$p_k(1000hPa)$
1	0	0	0	0.00994591
2	1.989182	0	0.02	0.03543221
3	5.09726	0	0.05	0.07804715
4	10.51217	0	0.11	0.1463488
5	18.75759	0	0.19	0.2457438
6	30.39117	0	0.3	0.38758885
7	47.1266	0	0.47	0.59346765
8	71.56693	0	0.72	0.89054165
9	106.5414	0	1.07	1.310861
10	155.6308	0	1.56	1.8945175
11	223.2727	0	2.23	2.695855
12	315.8983	0	3.16	3.791768
13	442.4553	0	4.42	5.280589
14	613.6625	0	6.14	7.283551
15	843.0477	0	8.43	9.9528035
16	1147.513	0	11.48	13.47742
17	1547.971	0	15.48	18.09012
18	2070.053	0	20.7	24.07468
19	2744.883	0	27.45	31.773995
20	3609.916	0	36.1	41.59872
21	4709.828	0	47.1	54.036425
22	6097.457	0	60.97	69.661115
23	7834.766	0	78.35	89.1407566
24	9959.486	0.0003389933	99.93	113.2338701
25	12317.67	0.003357187	126.53	142.7903635
26	14597.68	0.01307004	159.05	178.770345
27	16441.67	0.03407715	198.49	222.26619
28	17538.87	0.07064983	246.04	274.522015
29	17708.88	0.1259167	303.01	336.95075
30	16970.06	0.2011954	370.9	411.1473
31	15587.9	0.2955196	451.4	496.5112
32	13621.46	0.4054092	541.62	588.7858
33	11101.56	0.5249322	635.95	681.663675
34	8127.155	0.646108	727.38	769.164685
35	5125.142	0.7596984	810.95	846.443555
36	2549.969	0.8564376	881.94	909.25807
37	783.195	0.9287469	936.58	954.782025
38	0	0.9729852	972.99	982.63335
39	0	0.9922815	992.28	996.14075
40	0	1	1000	

atmospheric structure due to these assumption is evaluated by comparison of the temperature structures resulting from the two models.

The 1D model calculates the atmospheric temperatures by solving the radiative transfer equation and convective adjustment. A global mean stellar irradiance is assumed, which does not vary in time and space, and temperatures are then evaluated in steady state.
In the 3D model the contribution of various processes is included in the calculation of the atmospheric temperature, such as radiation, phase changes, dissipation of kinetic energy and the vertical transport of static energy and moisture, e.g. by convection. The contribution of phases changes is neglected for rain and snow fall. In the lower most layers sensible heat is also taken into account.

In the 1D model mass transport is neglected and the water vapor profile is calculated on the basis of the temperature profile and on a parametrization of the atmospheric relative humidity. Water in the form of liquid droplets or solid particles is omitted. The 3D model calculates the atmospheric content of all three water phases by solving the conservation of mass, taking into account phase changes depending on the atmospheric conditions. In addition, various microphysical processes are parametrized in the cloud scheme. The impact of all three water phases upon radiative energy fluxes is included in the 3D model.

The 1D model assumes fixed surface albedos, which are usually chosen to reproduce the mean surface temperature of the Earth around the Sun (288.1 K). Since the model is cloud-free this albedo is larger than the mean surface albedo of the Earth (0.21 in comparison to $\approx$0.15). This is needed to account for the reflectivity of clouds. In the 3D model the surface albedo is calculated, when coupling the model to a mixed layer ocean model, by the calculation of sea ice concentrations and sea ice thickness (see sec. 5.3.8.6). These sea surface conditions do however depend on the not well known q-fluxes which have to be introduced into the model, to account for the heat flux from the ocean to the atmosphere.

The density of the atmosphere is calculated from the pressure, composition and temperature of the atmosphere via the equation of state for an ideal gas. While in the 1D model the molecular weight of the atmosphere is calculated via the composition of the atmosphere, in the 3D model the background atmosphere is fixed to that of the modern Earths, and only changes of density due to higher concentrations of water are taken into account. For the model calculations carried out in this work this assumption is fine since Earth-like atmospheres are assumed. However, this should be kept in mind for future model scenarios.

There are various other assumptions which are included in the model equations. It is assumed that the radiative transfer can be solved in two separate wavelength regimes. This assumption is acceptable when investigating planets, which have very different temperatures from their host stars, as it is the case in this study. Furthermore, the absorption coefficients in the thermal infrared radiative transfer (RRTM, sec. 5.3.2.2) are calculated for mean Earth conditions in both models. Hence, for temperatures, pressures and compositions too far away from those of modern Earth, these are not applicable. The impact upon the model results shown here however is small (see sec. 6.2.1 and sec. 11.3).

5.5 General Model Setup

In this section the general model setup of the 1D and 3D model are given. The adaptation of the models to the various scenarios studied in this work is given in Chapter 7 and in the results chapters (Chapter 8, 9, 10, 11).

The atmospheric composition has been kept to that of the modern Earth (except as stated otherwise) in both models with constant mixing ratios of molecular oxygen (21 % O_2), carbon dioxide (355 ppm CO_2), methane (1.64 ppm CH_4) and nitrous oxide (1.8 ppb N_2O). Ozone concentrations according to the climatology of Fortuin and Kelder (1998)) are used in the 3D model and a global mean profile as calculated by Grenfell et al. (2007) in the 1D model.

1D model

The 1D model model is used in the standard setup for the present Earth. Atmospheric temperature and water vapor profiles are calculated from the planetary surface up to pressures of 0.066 hPa, which corresponds to a height of about 64 km for the Earth. The water vapor profile is calculated using the relative humidity profile of Manabe and Wetherald (1967), except for section 11.3, where it has been calculated with a relative humidity of 100% (provided by B. Stracke). For the latter also the thermal radiative transfer scheme MRAC has been used, while for all other model calculations RRTM has been utilized.
At the lower boundary the surface albedo is fixed to 0.21 (except as in sec. 11.3 where it is 0.22). The upper boundary is given by the incident stellar radiation (see sec. 7.1) and by assuming that the downwards thermal infrared radiation is zero. Furthermore, model results give radiative equilibrium at top of the atmosphere.
The initial temperature and water profile are those of the modern Earth.

3D model

The 3D chemistry climate model EMAC, described in section 5.3, is applied in the ECHAM5 version 5.3.01, MESSy version 1.8 with a T42L39-resolution, i.e. with a spherical truncation of T42 (corresponding to a quadratic Gaussian grid of approx. 2.8 by 2.8 degrees in latitude and longitude) with 39 hybrid pressure levels from the planetary surface up to 0.01 hPa, which corresponds to about 80 km for the Earth. Basic atmospheric processes are taken into account, i.e. radiative transfer, convection, cloud processes, water transport, and its feedback on specific humidity. Chemistry calculations have not been carried out. In general the heating rates have been calculated using the FUBRAD scheme (see sec. 5.3.2.1), except for one model scenario for comparison 11.1. The stratiform cloud cover calculations use the parametrization of Sundqvist (1978), and the cumulus convection scheme of Bechtold et al. (2004) has been applied. Note that, results may be different for other cloud and cumulus parametrizations.
At the lower boundary e.g. an albedo map (see sec. 7.2.3.2) is needed as input as well as the leaf area index (LAI), the sky view factor (see sec. 5.3.8) and an orography map are used. For the sea surface either prescribed SSTs or the mixed layer ocean can be applied, see section 5.3.8 and section 7.2.3.1. At the upper boundary as for the 1D model the incident stellar spectra are considered (see sec. 7.1) and the local and temporal insolation are calculated depending on orbital parameters (sec. 5.3.2 and sec. 7.2.1). Downward thermal

infrared radiation is neglected at TOA. The vertical velocity is calculated by assuming that it decreases to zero at the lower and upper boundary of the atmosphere.

The initial state of the atmosphere for the 3D model is given by the mean state of the modern Earth, as for the 1D model. Model calculations are performed until a new equilibrium state of the atmosphere is reached (determined by the 2m temperature for the scenarios with the mixed layer ocean model). Results presented are longterm means of the atmosphere in the new equilibrium state.

5.6 Summary

In this chapter section the two atmosphere models applied in this work have been described. Both models are capable of evaluating the influence of different stellar spectra on the climate of Earth-like planets. While the 1D model calculates only vertical temperature and water vapor profiles in steady state by accounting for heating by radiation and convection, the 3D model includes various processes which determine the state of the atmosphere in time and spatially resolved. These two different approaches to determine the mean climate of the atmosphere are utilized to determine the influence of dynamical processes on planetary habitability. More detailed model descriptions can be found in von Paris (2010) and Stracke (2012) for the 1D model and in Roeckner et al. (2003), Roeckner et al. (1996) and Deutsches Klimarechenzentrum (DKRZ) (1992) for the 3D model.

Some adaptations have been introduced in the 3D model to allow for the modeling of Earth-like extrasolar planets around different types of stars as the adjustment of the orbital period (see sec. 5.3.2), the use of the actual integrated fluxes in the Chappuis band in the shortwave radiative transfer and the suppression of extrapolation of optical depth to negative values in the thermal radiative transfer (see sec. 5.3.2.2). The calculation of the sea surface temperatures may now be carried out by a mixed layer ocean model (sec. 5.3.8.6). Furthermore, the expression for the calculation of the saturation water vapor pressure with respect to liquid water has been replaced (see sec. 5.3.5) to allow for its calculation at temperatures larger than 400 K.

In the next Chapter the two model are validated for the Earth around the Sun.

CHAPTER 6

Model validation

For model validation a comparison of the global annual mean temperature of the 3D model and 1D model profiles for the Earth around the Sun with the temperature profile of the US Standard Atmosphere 1976 (US1, 1976) are carried out. Furthermore, a comparison of the 3D model results with the SPARC climatology are shown (sec. 6.1).

In sec. 6.2 the impact of the changes made to the 3D model are evaluated including the changes introduced to the thermal radiative transfer (RRTM, see sec. 5.3.2.2), the replacement of the saturation water vapor pressure ($p_{sat,liq}$) expression (see sec. 6.2.3) as well as the use of an unadjusted stellar flux in the Chappuis band (see sec. 5.3.2.1)

All 3D model scenarios described in this chapter use prescribed sea surface temperatures and sea ice (Taylor et al., 2000). The different setups for the model scenarios shown in this chapter are summarized in table 6.1.

The difference due to the use of the mixed layer ocean model in the 3D model, and for the different model setups can be found in Chapter 8.

6.1 Validation of the models

In this section the results of the 1D and 3D model for the Earth around the Sun are compared to the US Standard Atmosphere and the 3D model results for the sunsst scenario are compared to the SPARC climatology (Randel et al., 2004), provided by M. Kunze.

Table 6.1: Model scenarios for the validation of the 1D and 3D model.

Scenario	Solar spectrum	RRTM	Chappuis band	$p_{sat,liq}$
Sun1D	Gueymard (2004)			
sunsst	Gueymard (2004)	new	unadjusted	Wagner and Pruß (2002)
sunRRTMfix	Gueymard (2004)	new	unadjusted	Sonntag (1994)
sunRRTMold	Gueymard (2004)	old	unadjusted	Sonntag (1994)
sunchap	Lean and Frohlich (1998)	new	adjusted	Sonntag (1994)

6.1.1 Global mean temperature profiles

Figure 6.1 shows the comparison of the global annual mean temperature profile for the Earth (sunsst), as modeled with the 3D model EMAC-FUB and the 1D radiative convective climate model, with the US Standard Atmosphere 1976.

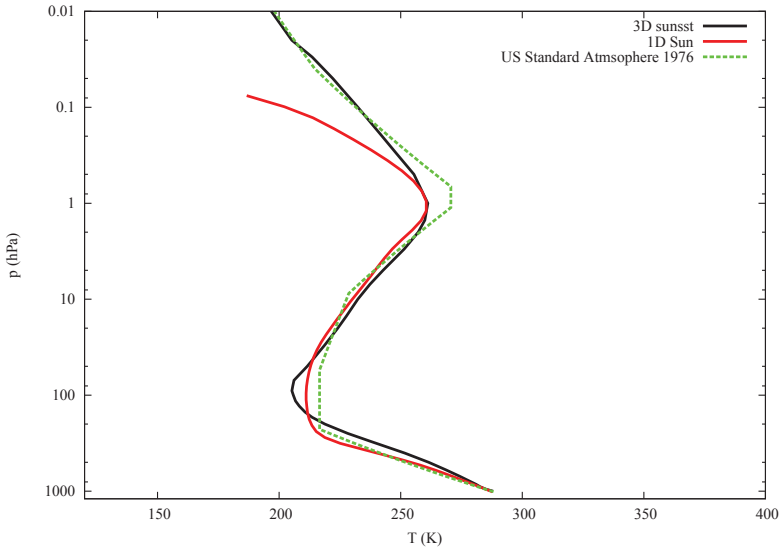

Figure 6.1: Comparison of the 1D and 3D model results with the US Standardatmosphere 1976. Sunsst in black, Sun1D in red, US Standardatmosphere in green.

The largest deviation from the US Standard Atmosphere is found for the 1D model in the upper atmosphere for pressures smaller than 1 hPa. This results from the choice of the upper model lid at a pressure of 0.066 hPa and the unconsidered absorption of radiation by molecular oxygen, which is important for these atmospheric heights.

Both models show some deviation from the Standard Atmosphere at the tropopause, the temperature inversion between the lower and the upper atmosphere, and at the stratopause, the temperature inversion in the upper atmosphere. At the tropopause both models show lower temperatures, with a larger deviation for the 3D model. While in the Standard Atmosphere and in the 1D model temperatures are constant from about 220 to 90 hPa, for the 3D model the tropopause does not show such a constant temperature over pressure.

At the stratopause the temperatures from the Standard atmosphere are higher than those of both models which agree very well in this region.

It can be however concluded, that both models agree well with the overall temperature structure of the Standard Atmosphere, especially when taking into account the variations in the temperature profile given in US1 (1976). For the 1D model however, results obtained for pressures smaller than 1 hPa should be treated with caution.

6.1.2 Comparison of 3D model results with SPARC climatology

In this section the sunsst scenario is compared to the SPARC climatology, which has been derived from observations. Figure 6.2 shows the comparison of the zonal mean temperature and zonal wind for January and July. The comparison shows an overall consistent climate. However, some differences between the sunsst scenario and the climatology occur. The largest temperature difference occurs for the southern upper stratopause in July (second and forth left panels), where the sunsst scenario results in higher temperatures as the climatology (280 K compared to -5 °C=268.15 K). In addition to this warm southern winter stratopause, the northern summer stratopause in July (same panels) is colder than the winter stratopause for the sunsst scenario. This results from the use of a non adjusted solar flux in the Chappuis band as will be shown in sec. 6.2.2.
Furthermore, the maximum zonal wind speeds in the southern hemisphere are about 10 m/s higher for the sunsst scenario than in the climatology.

Since the discrepancies from the climatology are not too large, it is concluded that the 3D model can be used also with the introduced changes to the model to derive the climate state of an Earth-like extrasolar planet. For Earth-climate calculations however, the differences in the stratopause temperatures may be of concern.

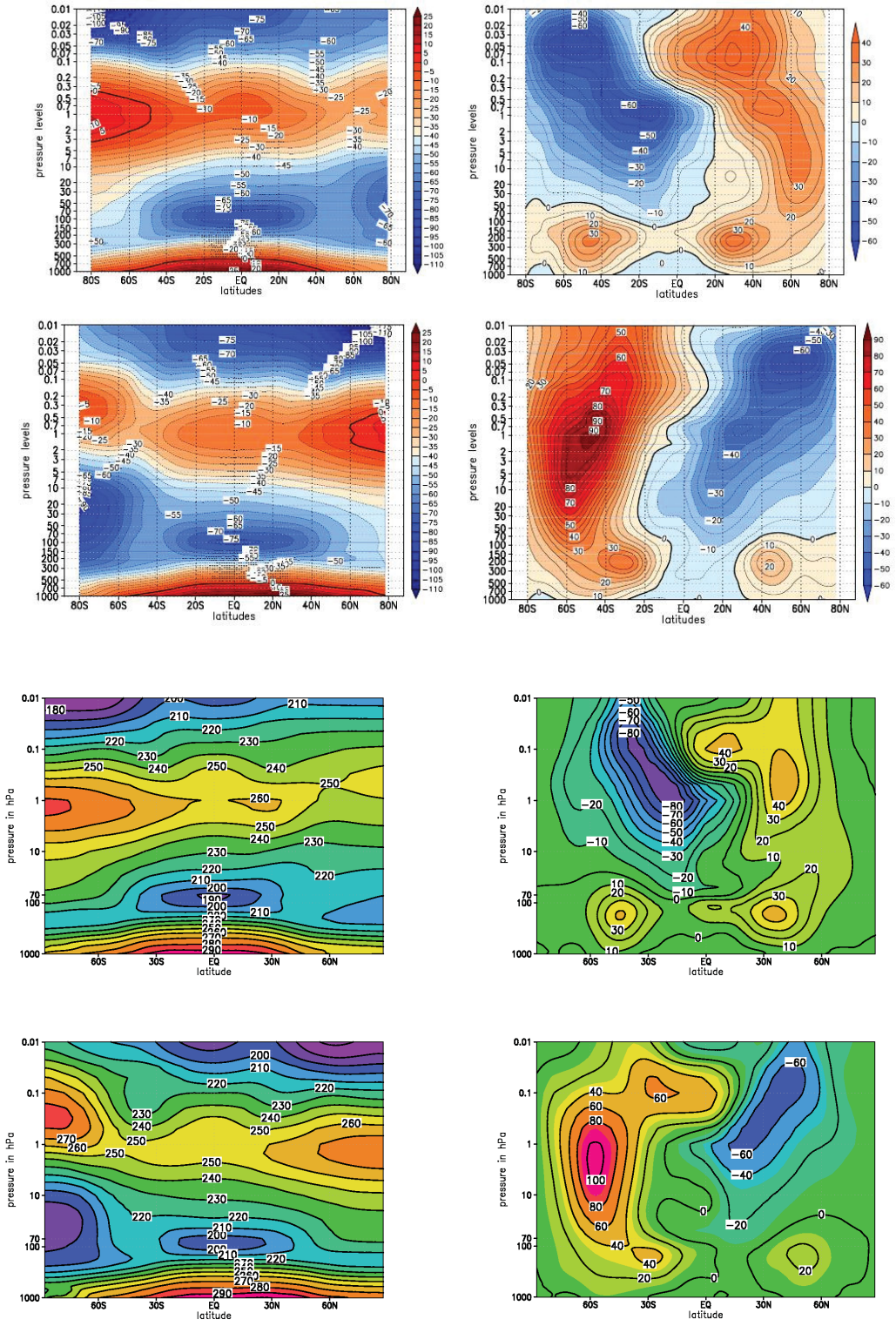

Figure 6.2: Comparison of 3D model results for sunsst to the SPARC climatology. Upper four panels: Zonal mean temperature in °C (left) and wind in m/s (right) from the SPARC climatology. January in the upper panels, July below. Lower four panels: zonal mean temperature in K (left) and wind in m/s (right) for sunsst. Lower panels show July, January above.

6.2 Influence of the model changes

In this section the impact of the changes made to the 3D climate model (see section 5.3) are discussed. The changes were introduced to allow for the calculation of the the exoplanet scenarios, which are presented in Chapter 9.

6.2.1 Modification of the thermal radiative transfer scheme (RRTM)

The rapid radiative transfer model (RRTM), described in sec. 5.3.2.2 and in Mlawer et al. (1997), has been developed for Earth climate studies. It used tabulated absorption coefficients which have been derived for a narrow temperature, pressure and concentration grid. Whenever calculated atmospheric conditions lie outside the boundaries of this grid, extrapolation of the absorption coefficients is carried out. This is clearly less reliable then interpolation between the tabulated grid points. Because of this RRTM occasionally calculated the radiative transfer with negative optical depth, which are clearly unphysical. This has been suppressed in the applied version of EMAC. A short analysis of this change in the model is given below. Scenarios sunRRTMfix and sunRRTMold summarized in Table 6.1 are therefore compared. Results presented are 14 year means after 7 years spin-up.

Influence on zonal mean temperatures and wind

The zonal mean temperature profiles and differences are shown in Fig. 6.3 and zonal wind speeds in Fig. 6.4 for mean January (left) and July (right) conditions, comparing scenario sunRRTMfix (upper panels) with and sunRRTMold (middle panels) without the modification described above. The lower panels show the temperature and wind speed differences and their statistical significance calculated via the student's t-test, to test whether the differences in a quantity are statistically significant by comparing them to the standard deviation, here given by the internal model variability of the climate. The grey shading (from light to dark grey) indicates the 1, and 3σ confidence levels derived by this test.

In July (right panels) significant differences appear for the northern stratopause and the equatorial tropopause, which are however small.

For the zonal wind speed (Fig. 6.4) the largest differences with high confidence levels occur around the northern hemispheric (NH) stratopause, indicating a more extended and stronger stratospheric jet for the sunRRTMfix scenario with a difference in wind speed of about 10 $\frac{m}{s}$ in January (left panel) and of about 2.5 $\frac{m}{s}$ in July (right panel).

The differences resulting from the modification in the thermal radiative transfer are relatively small for the reference scenario, for which the model was built. For exoplanet scenarios it is important to keep in mind, that for atmospheric temperatures outside the validity range of RRTM a significant change in the greenhouse effect or cooling of the atmosphere may be possible. However, adapting the thermal radiative transfer model is beyond the scope of this thesis, and is work in progress (von Paris, 2010). Nevertheless, preventing an extrapolation to negative values of optical depth is essential, since these generate a non-physical state of the atmosphere.

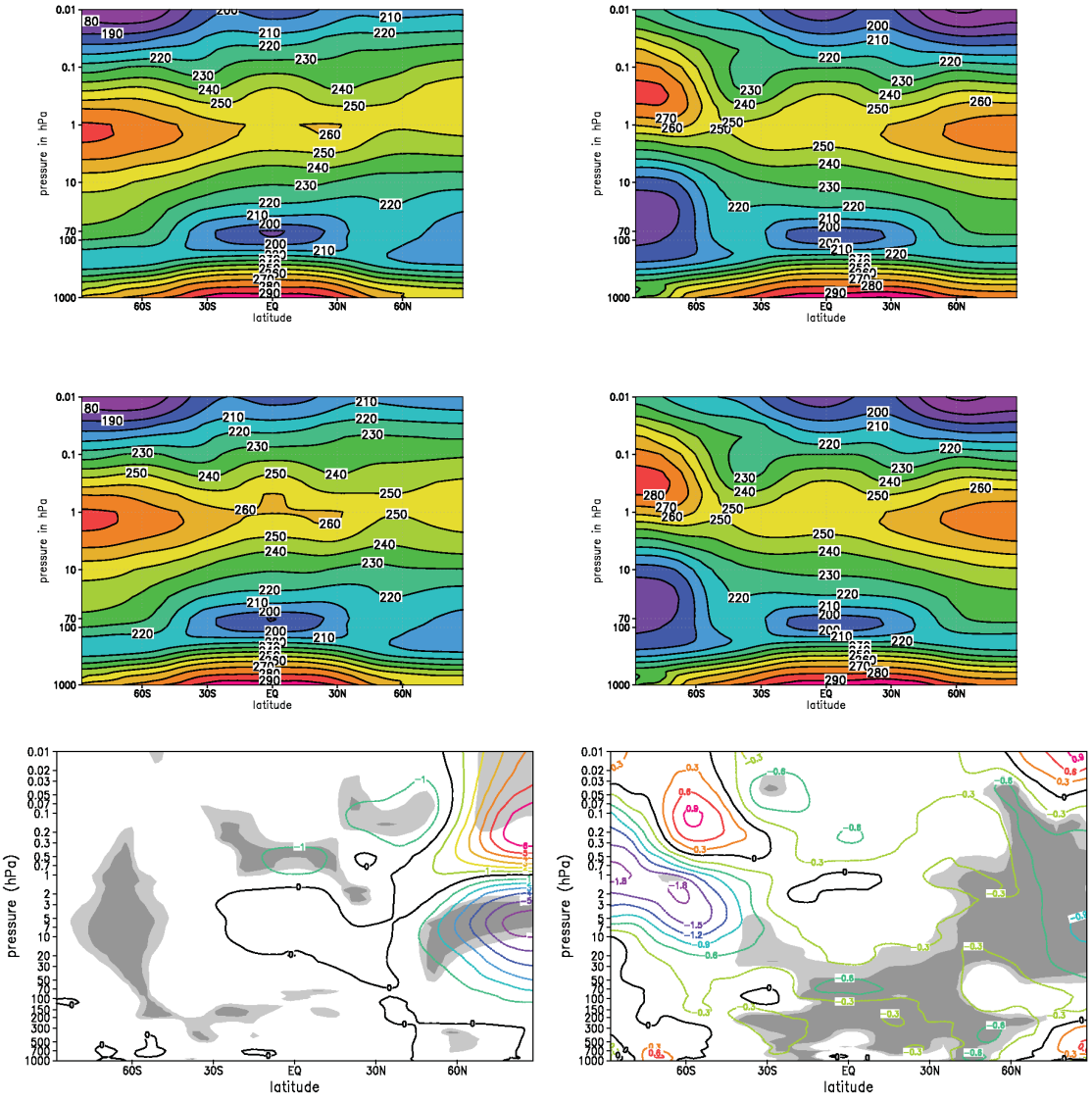

Figure 6.3: Effect of the modification in the thermal radiative transfer RRTM on zonal mean temperatures (K) for January (left) and July (right). Upper panels show the zonal mean temperatures for the sunRRTMfix, middle panels these for sunRRTMold. Lower panels show the temperature difference (sunRRTMfix-sunRRTMold) and the grey shading indicates the student's test confidence level of 1 σ (light grey) and 3σ (dark grey).

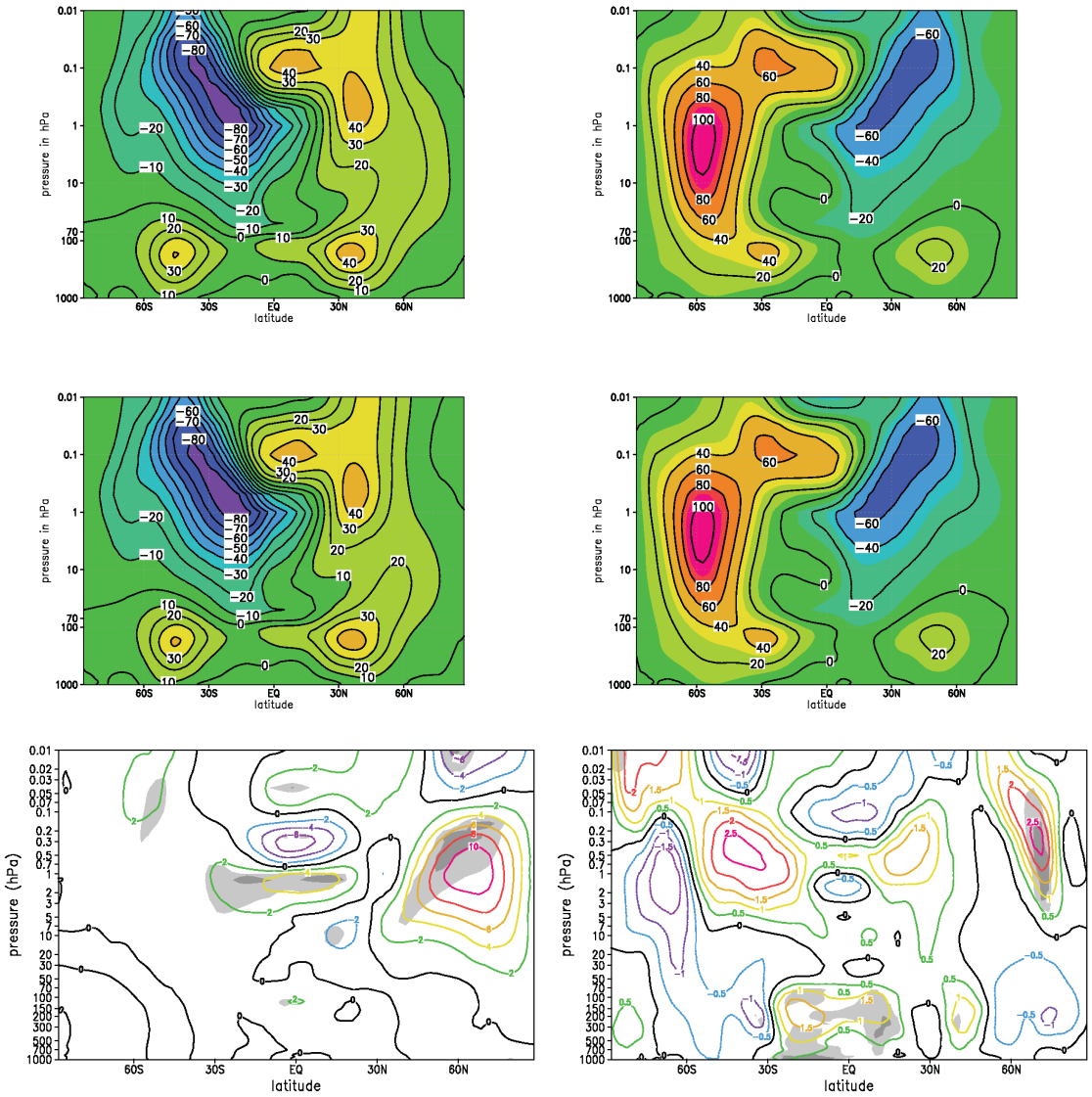

Figure 6.4: Effect of the modification in RRTM on zonal wind speed ($\frac{m}{s}$) for January (left) and July (right) as in Fig. 6.3.

6.2.2 Influence of the solar flux adjustment

The standard treatment of the shortwave radiative flux in the wavelength regime of the Chappuis band of ozone (from 407 to 682.5 nm) in the FUBRAD radiative transfer scheme (see 5.3.2.1) assumes an integrated solar flux of 322 $\frac{W}{m^2}$ following the parametrization of Shine and Rickaby (1989). However, the integration of a standard solar spectrum, e.g. by Gueymard (2004) in the corresponding wavelength regime results in 497 $\frac{W}{m^2}$, as described in sec. 5.3.2.1. Usually, for Earth climate studies with FUBRAD, the solar energy flux in the Chappuis band is therefore adjusted to maintain today's heating rates. Clearly in this work, investigating planets around different types of stars this adjustment cannot be applied. Therefore, this section investigates the influence of a non–adjusted stellar flux in the Chappuis band on present Earth's climate.

Two scenarios (sunRRTMfix and sunchap in Tab. 6.1) with adjusted and with non–adjusted solar flux are compared. The described modification of RRTM (see Sec. 6.2.1) is includedand the results presented in Fig. 6.7 and Fig. 6.8 are long–term means over 14 years from 21 year model runs after 7 years of spin–up.

Results

Due to higher energy input in the Chappuis band in the non–adjusted flux scenario a stronger heating of the stratosphere occurs, as can be seen in Fig. 6.5. The upper panels show the global mean annual mean heating rates for the sunRRTMfix scenario (left) without and the sunchap scenario (right) with flux adjustment. The lower panel shows the difference between the two scenarios. Omitting the flux adjustment leads to higher heating rates of about 0.5 K/day at maximum mainly due to differences in the ozone heating.

In Figure 6.6 the resulting annual mean global mean temperatures (left) of the sunRRTMfix scenario (black solid line) without flux adjustment and the sunchap scenario (red dashed line) with flux adjustment are shown. The higher heating rates lead to higher global mean annual mean temperatures in the upper atmosphere up to about 6 K, as can be inferred from the right panel of Fig. 6.6.

In Fig. 6.7 the zonal mean temperatures for January (left) and July (right) for the scenarios without (upper panels) and with flux adjustment (middle panels) are shown.
According to the student's t-test the differences in the lower atmosphere are not statistically significant, as indicated by the non shading of this region in the lower panels of Fig. 6.7. However, the differences in the middle atmosphere are nearly all statistically significant, except for the regions with high variability, such as the lower winter stratosphere. These however may become significant when averaging over a longer time period. For the sunRRTMfix scenario the temperatures are higher in the entire middle atmosphere.
Noteworthy is the fact, that the temperature maximum in the winter stratosphere, which is caused by adiabatically heated descending air brought in by the meridional circulation transporting air from the summer to the winter hemisphere, shows a larger temperature increase than the summer stratopause for the sunRRTMfix scenario. This does not reproduce the Earth climatology.

The temperature differences described above influence the temperature gradient between

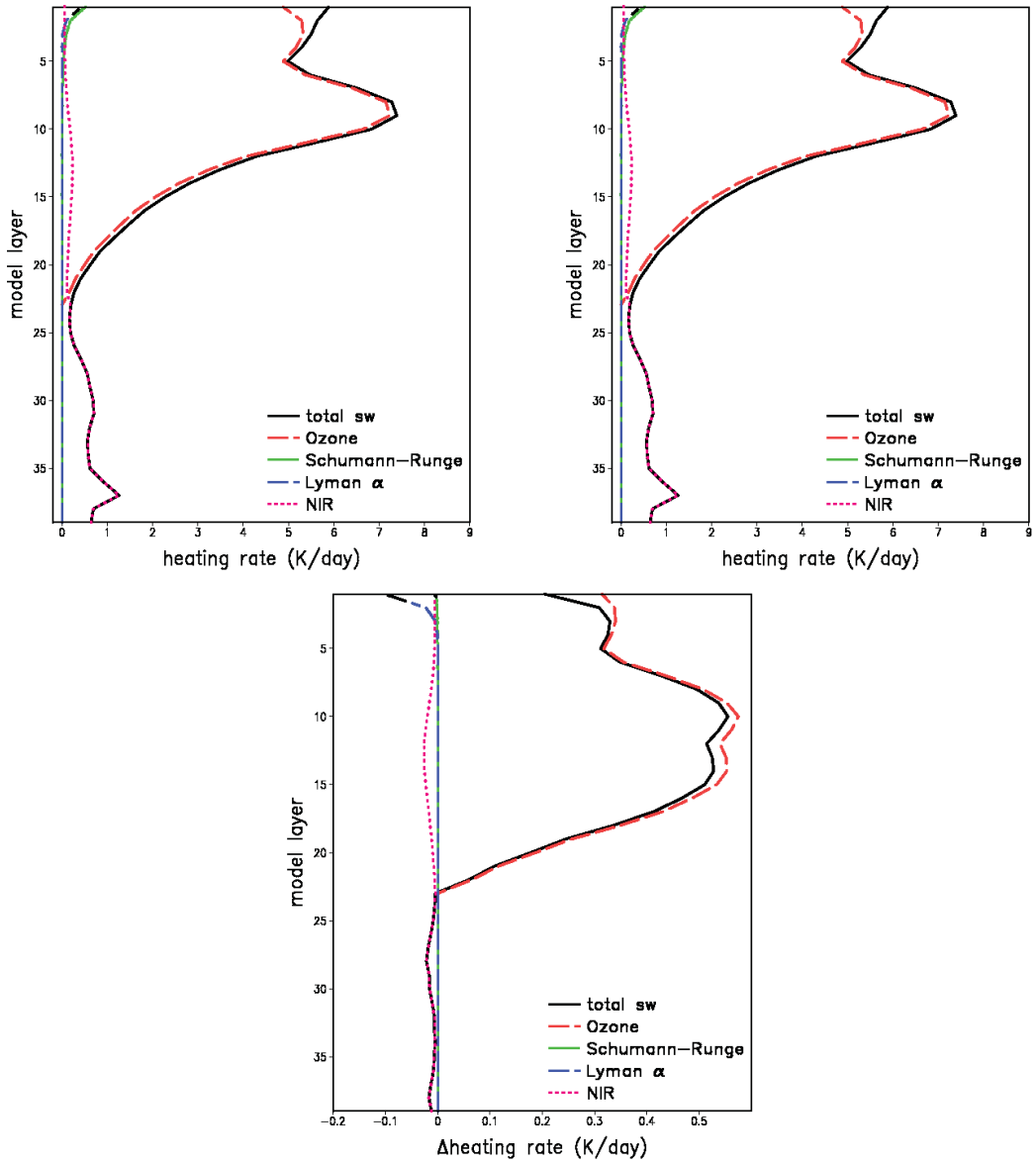

Figure 6.5: Effect of flux adjustment in the Chappuis band on shortwave heating rates. Upper panels: Global mean annual mean shortwave heating rates for the sunRRTMfix scenario (left) without flux adjustment in the Chappuis band and sunchap (right) with flux adjustment. Lower panel: Difference of the global mean annual mean shortwave heating rates between the model scenarios (sunRRTMfix-sunchap).

polar regions and equator leading to a change in zonal wind speeds as can be seen in Fig. 6.8. In January (left panels) the summer hemispheric jet is about 9 $\frac{m}{s}$ stronger for the sunRRTMfix (upper panel) than for the sunchap scenario (middle panel), whereas the winter hemispheric jet appears to be spread over a larger region. The difference plot (lower panel) indicates a statistically significant wind speed difference of up to 15 $\frac{m}{s}$.
In July (right panels) the winter hemispheric jet in the southern hemisphere is stronger by about 18 $\frac{m}{s}$ for the sunRRTMfix scenario.

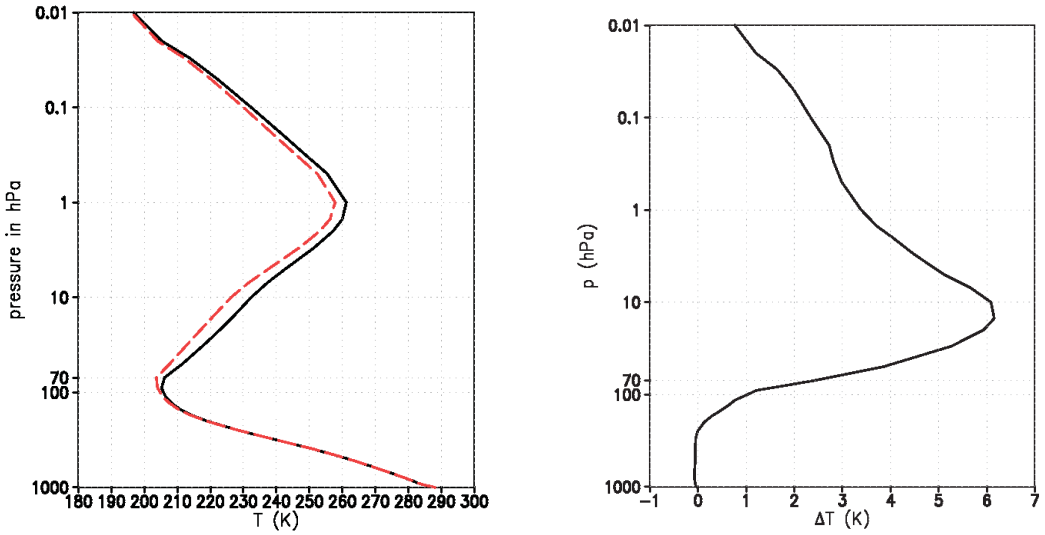

Figure 6.6: Effect of flux adjustment in the Chappuis band on global annual mean temperatures. Left: Global annual mean temperature profile for the sunRRTMfix (black solid line) and the sunchap model scenario (red dashed line). Right: Global annual mean temperature difference between the model scenarios (sunRRTMfix-sunchap).

In the summer hemisphere the the wind speeds increase only little, which agrees with the smaller temperature increase in the northern compared to the southern hemisphere.

The use of an unadjusted flux in the Chappuis band shows a strong influence on the temperature structure and thereby on zonal wind especially in the middle atmosphere, due to an increase in the shortwave heating rates. The lower atmosphere is less influenced Therefore it is assumed that the use of an unadjusted flux in the Chappuis band for the investigation of the habitability of planets around different types of stars, which is clearly more appropriate, does not change the conclusions. However, a test of this assumption should be carried out in the future (see Chapter 13).

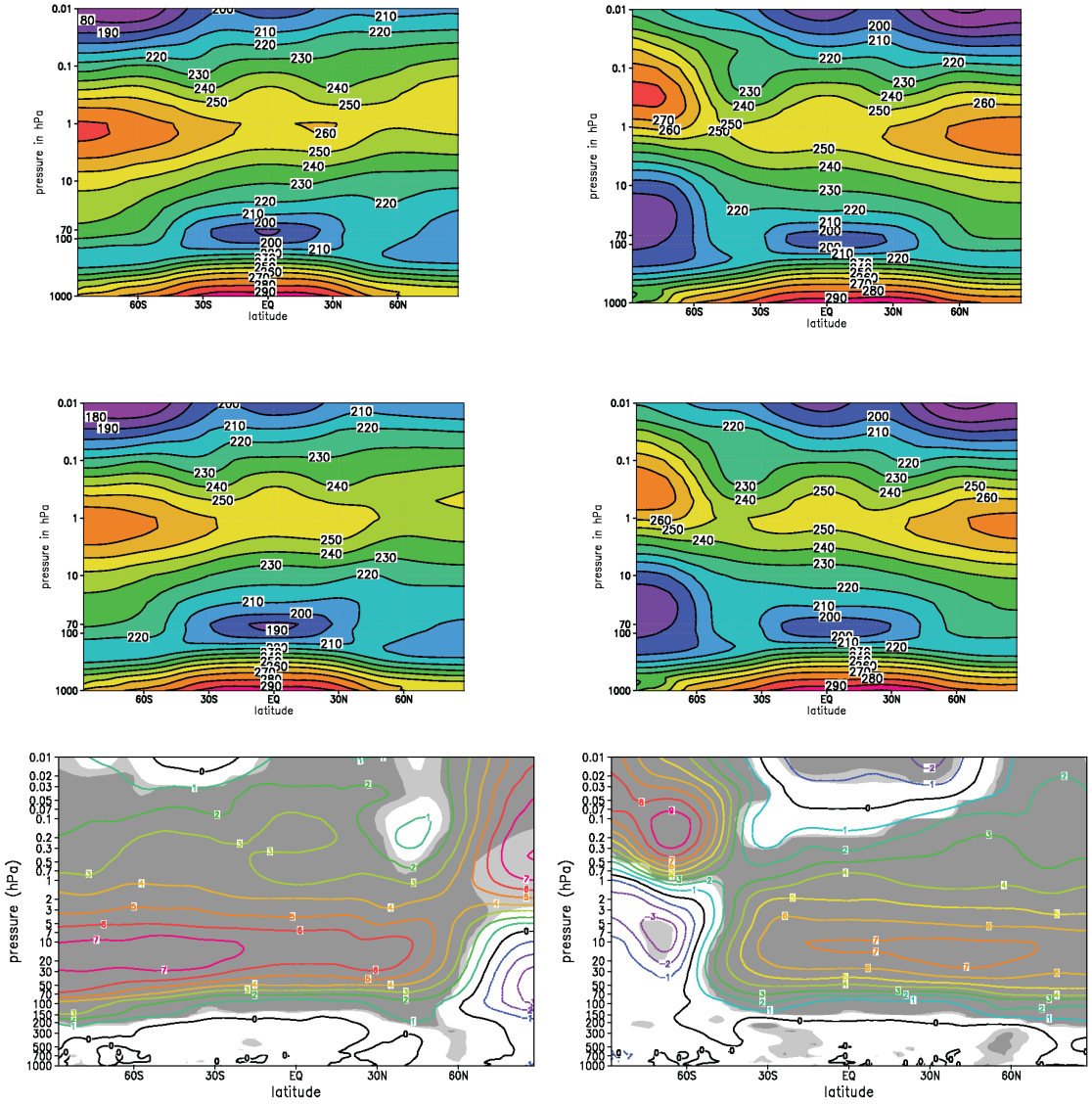

Figure 6.7: Effect of flux adjustment in the Chappuis band on zonal mean temperatures (K). Zonal mean temperatures for the sunRRTMfix scenario (upper panels) and the sunchap scenario (middle panels) in January (left) and July (right). Lower panels: Zonal mean temperature difference (sunRRTMfix-sunchap). Grey shading indicates the student's t-test confidence levels of 1 (light grey) and 3σ (dark grey).

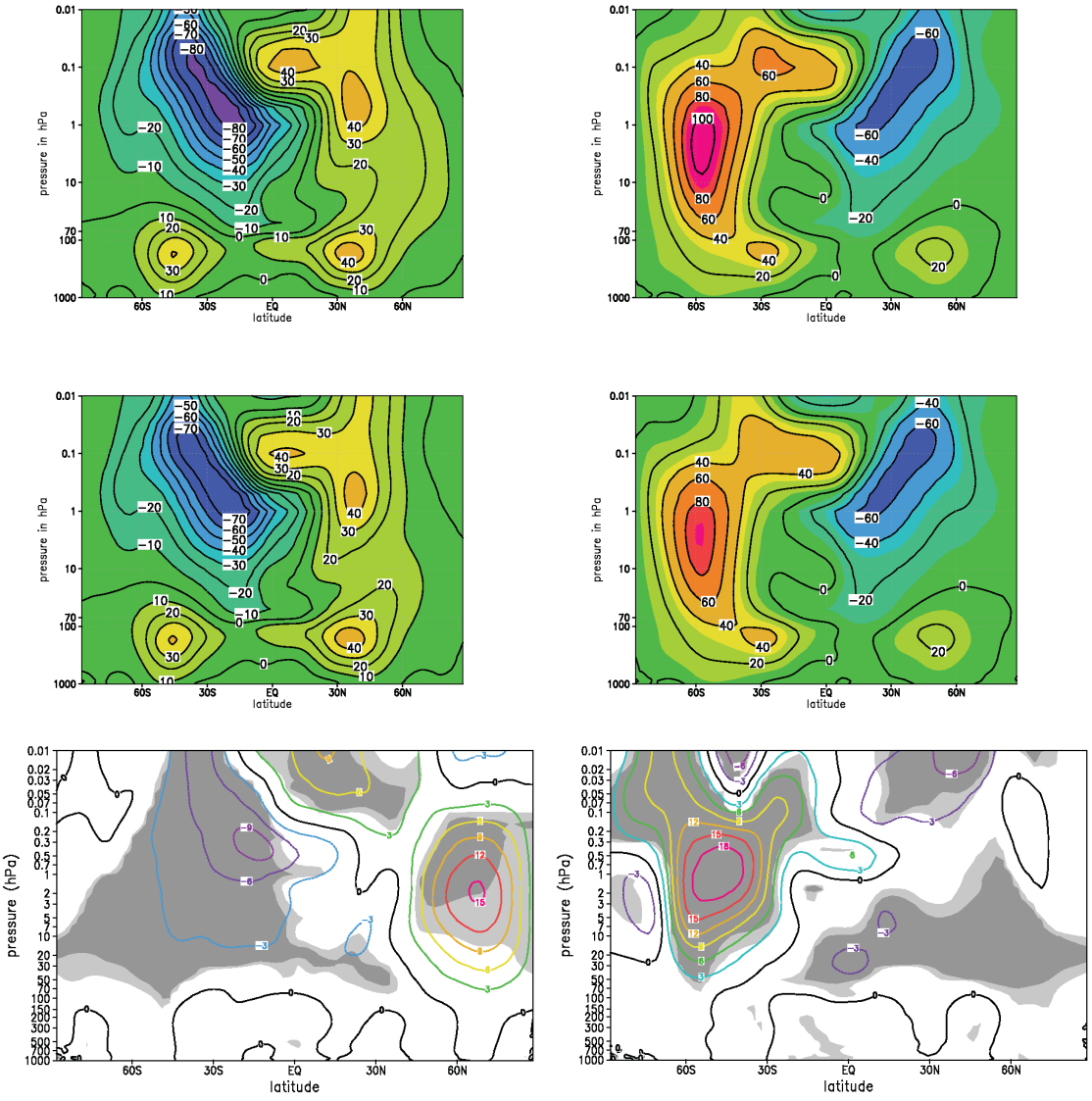

Figure 6.8: Effect of flux adjustment in the Chappuis band on zonal mean wind speed u $\frac{m}{s}$. Zonal wind for the sunRRTMfix scenario (upper panels) and the sunchap scenario (middle panels) in January (left) and July (right). Lower panels: Zonal wind difference (sunRRTMfix-sunchap). Positive (negative) values denote eastward (westward) wind velocities.

6.2.3 Influence of the saturation water vapor pressure from Wagner and Pruß 2002

For application of EMAC to exoplanet scenarios, it was necessary to replace the expression for the calculation of the saturation water vapor pressure by Sonntag (1994) by an expression which is valid for a larger temperature range, i.e. by the one of Wagner and Pruß (2002), see sec. 5.3.5.

In this section the influence of the new expression is analyzed, by comparing the model results for the scenarios sunRRTMfix (with expression from Sonntag 1994) with sunsst (with expression from Wagner and Pruß 2002) of Table 6.1.

Effect of the new saturation water vapor pressure expression

Figure 6.9 shows the resulting zonal mean temperatures for January and July and Fig. 6.10 the corresponding zonal wind. As can be seen significant differences in these properties are rather small.
For the zonal wind the t-test (lower panels of Fig. 6.10) indicates lower westward wind velocities (indicated by negative values) of the summer stratospheric jet in the southern hemisphere (SH) at mid-latitudes and higher wind speeds in the lower northern hemispheric (NH) stratosphere in mid-latitudes in January (left). For July (right) only small changes up to 2 $\frac{m}{s}$ in the lower equatorial stratosphere and the NH polar troposphere and stratopause are obtained.

Also the changes of the specific humidity are negligible, as shown in Fig. 6.11. Only small significant differences of up to 100 ppmv are obvious in the lower panel for July (right), which occur at mid-latitudes in the SH and NH.

6.3 Summary

In this chapter it has been shown that the 1D and the 3D model compare in general well with the US Standard atmosphere, despite some small discrepancies. Also, by comparing the 3D model results to the observed climatology it has been shown that the adjustments made in the 3D model introduce some differences, which are mainly due to the use of a non-adjusted stellar flux in the Chappuis band, which is not appropriate for the used parametrization. For inferring the habitability of an Earth-like extrasolar planet however this differences are not a major concern, since they occur in the middle atmosphere.

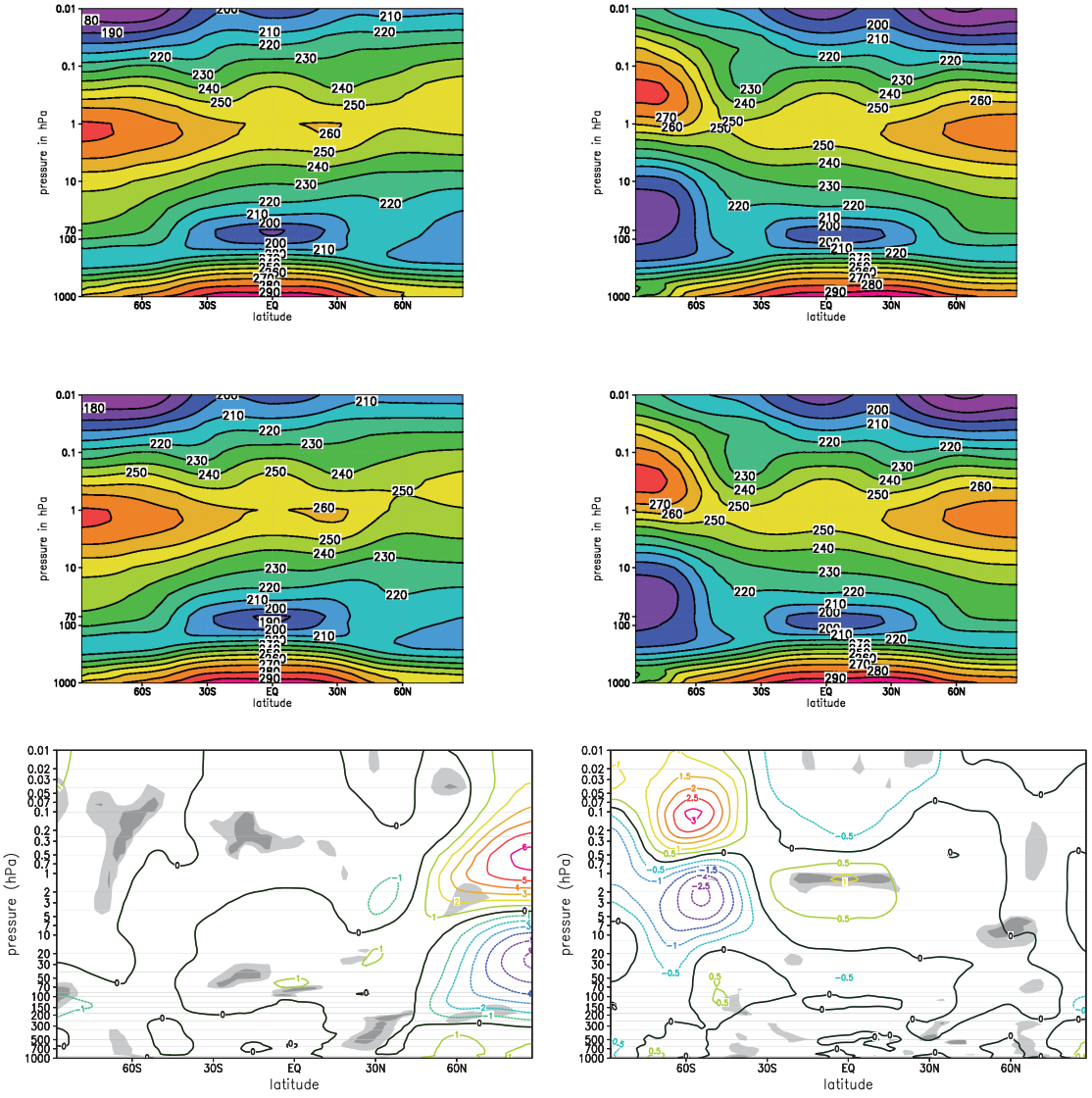

Figure 6.9: Effect of new saturation water vapor expression over liquid water upon zonal mean temperature (K) in January (left) and July (right). Zonal mean temperatures for the sunRRTMfix scenario are displayed in the upper panels, the middle panels show the temperatures for the sunsst scenario and the lower panels the differences (sunRRTMfix-sunsst), where grey shaded areas indicate the statistical significance of the results in 1 and 3σ-levels, as calculated with the student's t-test.

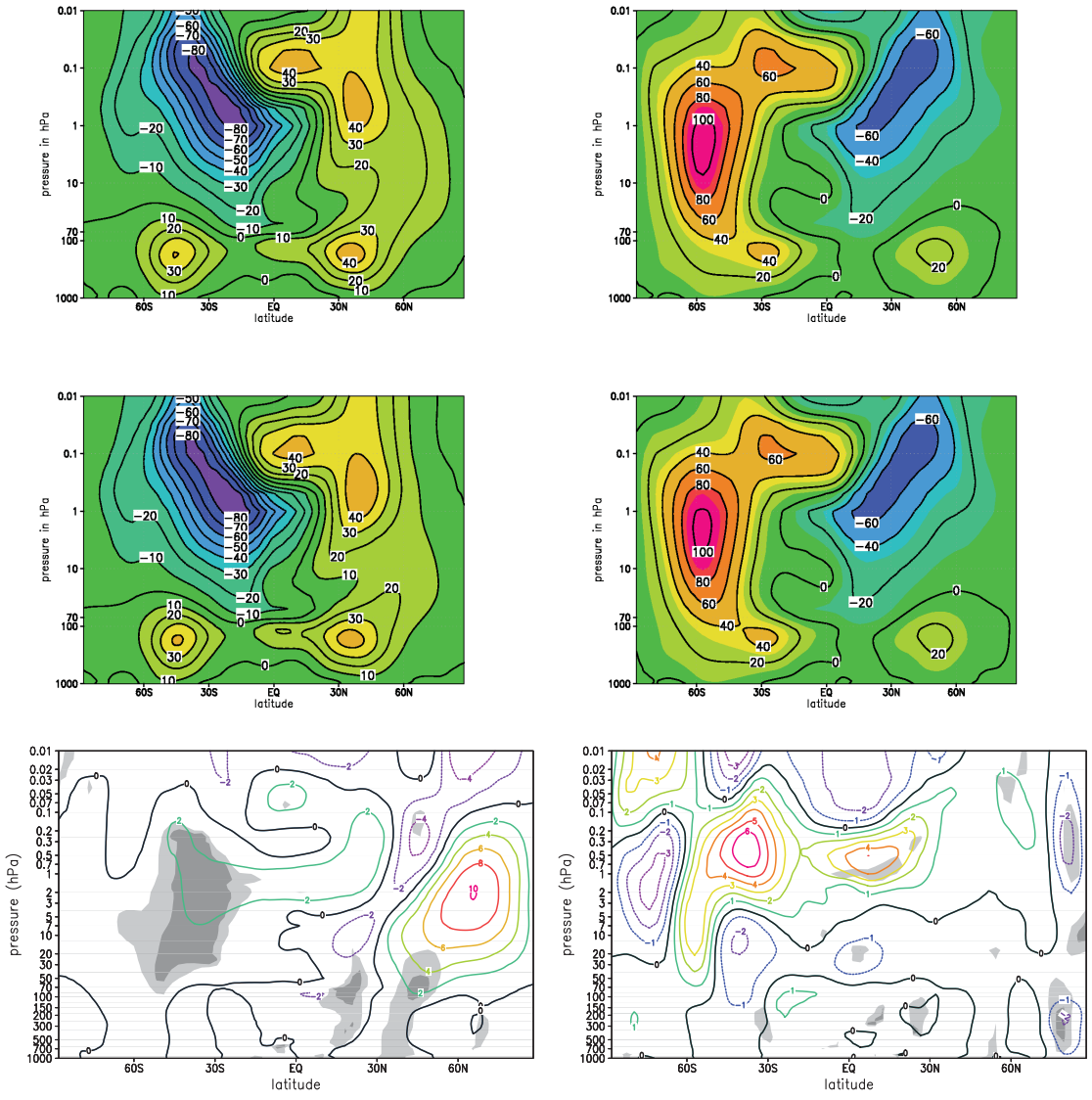

Figure 6.10: Effect of new saturation water vapor expression over liquid water upon zonal wind (m/s) in January (left) and July (right). The zonal wind for the sunRRTMfix scenario is displayed in the upper panels, the middle panels show the zonal wind for the sunsst scenario and the lower panels the differences (sunRRTMfix-sunsst), where grey shaded areas indicate the statistical significance of the results in 1 and 3σ-levels, as calculated with the student's t-test.

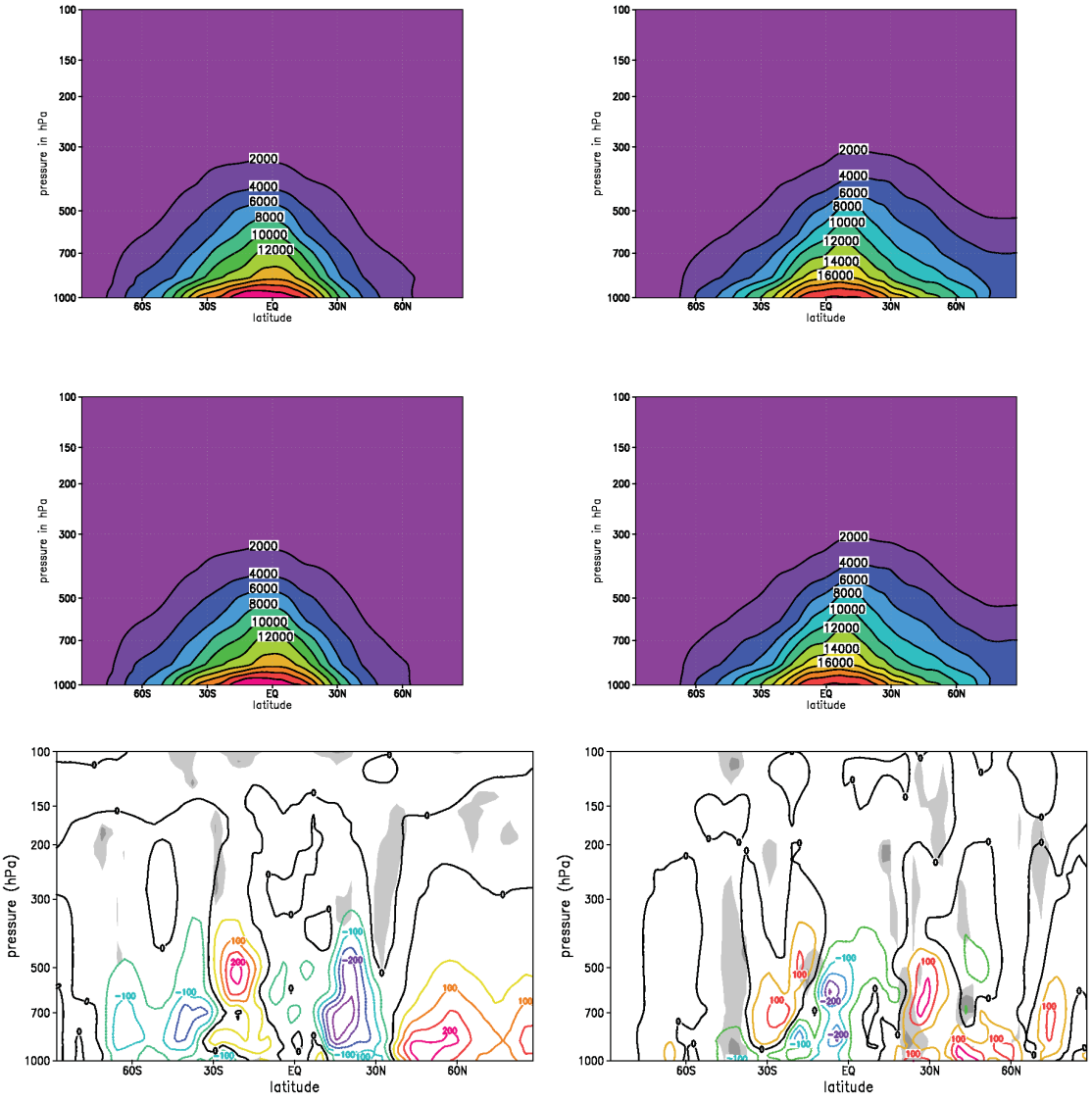

Figure 6.11: Effect of new saturation water vapor expression over liquid water upon specific humidity (kg/kg) in January (left) and July (right). The specific humidity for the sunRRTMfix scenario is displayed in the upper panels, the middle panels show the specific humidity for the sunsst scenario and the lower panels the differences (sunRRTMfix-sunsst), where grey shaded areas indicate the statistical significance of the results in 1 and 3σ-levels, as calculated with the student's t-test.

CHAPTER 7

Model scenarios

In this work the impact of dynamical processes upon the climate of Earth-like extrasolar planets around different types of stars is studied. This chapter gives an overview of the parameters used in the various model scenarios.

Despite the still missing detailed knowledge about single planetary objects, it can be expected that potentially habitable planets will orbit different types of central stars. This makes it necessary to study the influence of different types of stars on planetary climate.
A first step to approach the diversity of possibly habitable terrestrial exoplanets is by studying the influence of different central stars upon a planet like Earth, which has already been done with 1D climate models (e.g. Kasting et al. (1993), Segura et al. (2003)). For the Earth we have a detailed, albeit possibly incomplete, picture of the processes leading to its habitability. In this thesis the direct influence of different stellar types upon an Earth-like planet is studied. This neglects the impact different central stars may have on the planetary evolution.
Two important impacts of the central star upon a habitable planet are:

Influence of Radiation

Stars of different type differ in mass and therefore in luminosity. Less massive stars have smaller luminosities and smaller effective temperatures. Clearly, for less luminous stars, smaller orbital distances are required for the net incoming stellar energy at the top of the atmosphere of a planet to equal that of the Earth around the Sun. Nevertheless, the spectral energy distribution varies with the type of star. Brighter, hotter stars, such as F-type stars have their maximum of radiation at shorter wavelengths, whereas less massive stars at longer wavelengths, following Wien's displacement law.
This has an impact on the planetary atmosphere since it consist of molecules, which undergo wavelength dependent absorption and scattering properties. Therefore, a change in the spectral energy distribution of the stellar light directly changes the amount of energy which can be scattered and absorbed by the atmosphere and may also lead to a change in the atmospheric composition. This leads to different temperature profiles as has been shown by Segura et al. (2003, 2005) (see Sec. 4).

Influence of orbital period

As mentioned, with changing the stellar type, a planet has to be situated at a different orbital distance than the Earth around the Sun, to be habitable, as has been studied by Hart

Table 7.1: Stellar parameters

Star	stellar type	T_{eff} (K)	log g	$[Fe/H]$
ϵ Eridani	K-dwarf	5072	4.43	-0.13
Sun	G-dwarf	5777	4.5	0.0
σ Bootis	F-dwarf	6733	4.38	0.0

(1979), Kasting et al. (1993). Therefore the orbital period, whereby the planet counteracts the gravity field of the star via its orbital velocity, will also change. Following Kepler's third law, this leads to shorter orbital periods for planets around less massive stars and longer orbital periods for more massive stars and results in a change in the length of the year.

While the influence of radiation can be accounted for in the 1D and the 3D model, the difference in orbital period can only be taken into account by the 3D model applied here.

In the next section the stellar spectra used in this work are described. Section 7.2 describes the different input parameters used for the 3D modeling studies.

7.1 Stellar spectra

For the investigation of the influence of different stellar radiations upon atmospheric dynamics and habitability three main sequence stars of different stellar types (F, G, K) are chosen. Main sequence stars exhibit very stable energy production over long periods, hence a relatively constant luminosity,in comparison to other star types. It is believed that life needs such stable conditions for a long time to originate and evolve, therefore the search for habitable exoplanets focuses on main sequence stars. For the calculation of the influence of stellar radiation upon an Earth-like atmosphere stellar spectra for sample main sequence stars are needed. Stellar atmosphere and spectra models (e.g. the PHOENIX, Hauschildt et al. (1999), or Kurucz model, Kurucz (1979)) are found to reproduce stellar spectra of different type in the visible and IR wavelength regime. For the stellar UV radiation, however. the performance is more problematic, therefore stellar spectra over the required wavelength range have to be composed from observed spectra at UV wavelength with model spectra for the visible and IR.

Segura et al. (2003) constructed spectra of main sequence stars and studied their influence on global mean atmospheric temperatures of Earth-like planets and chemistry as shown in 4.1. In this thesis the same sample stars are used. For the K-type sample star a new spectrum was composed in collaboration with Philip von Paris. The sample stars used in this study and the construction of the spectra is described below.

High resolution stellar spectra

The stellar spectra used in this work have been prepared in close collaboration with Ph. von Paris and have been published in von Paris (2010) and Kitzmann et al. (2010).

The stellar parameters of the sample stars are summarized in Table 7.1. The sample stars used for the calculations are σ Bootis (HD128167) for the F-type star, which is an F-dwarf star at a distance of about 15.5 pc (Habing et al., 2001) from the Earth with an effective temperature of 6722 K, a log g of 4.38 and a [Fe/H]-ratio of -0.39 (Cenarro et al., 2007).

ϵ Eridani (HD22049) is taken as an example of a K-type star, which is a young active star about 3.2 pc (Habing et al., 2001) away from the Earth with an effective temperature of 5072($\pm$42) K and a $[Fe/H]$-ratio of $-0.13(\pm0.04)$ (Santos et al., 2004).

The Sun is taken as an example of a G-type star and defines the reference scenario. The high resolution spectrum of the Sun was taken from Gueymard (2004).

According to Segura et al. (2003) the F-type stellar spectrum is a composition of observations by the International Ultraviolet Explorer (IUE) of σ Bootis between 115 and 335 nm and a synthetic Kurucz spectrum with an effective temperature of 6733 K, log g of 4.33 and solar metallicity.

The K-type star spectrum has been composed in the course of this work in collaboration with Ph. von Paris (von Paris, 2010) of IUE satellite data of ϵ Eridani between 115 and 355 nm (http://archive.stsci.edu/iue/) and a synthetic NextGen spectrum taken from (http://perso.ens-lyon.fr/france.allard/) with an effective T of 5000 K , a log g of 4.5 and a $[Fe/H]$-ratio of 0.0.

All high resolution spectra were scaled to a total energy flux corresponding to the total solar irradiance at TOA of the Earth (1366 Wm^{-2}) derived by integration of the high resolution solar spectrum of Gueymard (2004) from 0.5 nm to 1000 μm.

For the F-type star the wavelength range for the scaling of the total flux lies between 115 nm and 160 μm, for the K-type star between 115 nm and 82 μm, since only for these wavelength ranges data is available. The scaling to the solar constant corresponds to orbital distances a of 1.89 AU for the F-type star, and 0.6 AU for the K-type star derived via eq. 7.1.

$$a = 1\mathrm{AU}\left(\frac{L/L\odot}{F/F\odot}\right)^{\frac{1}{2}} \tag{7.1}$$

The resulting scaled spectra are shown in Fig. 7.1. The spectrum of the Sun is shown in red, the scaled spectrum of the K dwarf star in green, and the F-type star spectrum in blue. The spectrum of the Sun spans over a wider wavelength range, since for the Sun more data is available. The F-type spectrum radiates more flux in the UV and visible compared to the Sun, since the star has a higher effective temperature. The opposite is the case for the K-type star, which radiates less flux in the UV and visible but more flux in the near infrared due to the lower effective temperature of the star. It has been shown by 1D modeling studies (see sec. 4.1) that these different spectral flux distributions could have an impact on an Earth-like atmosphere, since processes such as stratospheric heating due absorption of UV radiation by ozone molecules, or Rayleigh scattering depend on the stellar energy flux available at distinctive wavelengths.

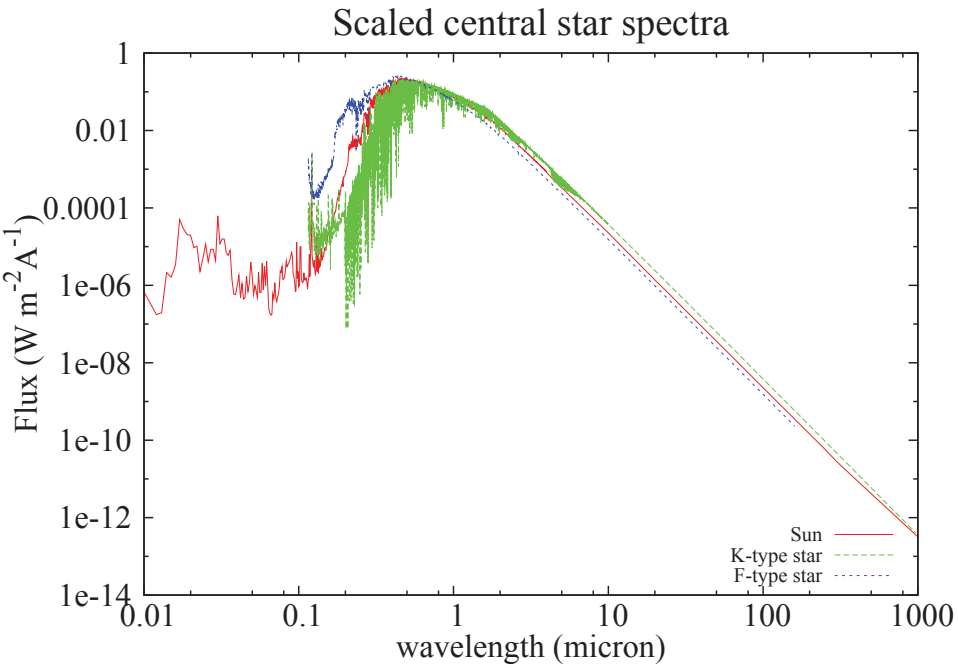

Figure 7.1: High resolution spectra of the three central stars considered. Red shows the spectrum of the Sun, taken from Gueymard (2004). Green shows the spectrum of the K-type star ϵ Eridani and blue shows the spectrum of the F-type star σ Bootis, both scaled to a total energy flux of 1366 $\frac{W}{m^2}$.

Binning of the stellar spectra

For modeling the influence of the stellar radiation upon an atmosphere, the stellar spectra are binned to the resolution and wavelength range covered by the radiative transfer scheme covering the stellar wavelength regime used in the model. As described in section 5.3.2.1, the 3D model offers the possibility of calculating the radiative transfer in two different resolutions. In the standard RAD4ALL scheme, the stellar radiation is binned in four bands, one spanning the UV and visible wavelengths and three bands covering the near infrared. The stellar spectra binned to four bands are shown in the upper panel of Fig. 7.2.

For the high resolution radiative transfer scheme FUBRAD (sec. 5.3.2.1), the UV and visible wavelength regime is split into 49 bands and the wavelength coverage is expanded to lower wavelengths, i.e. down to Lyman α instead of 250 nm for the standard scheme. Therefore differences in the stellar energy flux distribution are more pronounced in the binned spectra as can be seen in the middle panel of Fig. 7.2.
For comparison with the 1D model, the same stellar spectra are binned according to the wavelength bands in the short-wave radiative transfer in the 1D radiative-convective climate module. As described in section 5.2, the covered wavelengths range from 237 nm to 4.454 μm, and are split into 38 bands. The corresponding spectra are shown in the lower panel of Fig. 7.2.
This work mainly applies FUBRAD in the 3D model, which calculates the stellar radiation in 52 bands for pressures smaller than 70 hPa (see section 5.3.2.1). For all scenarios no

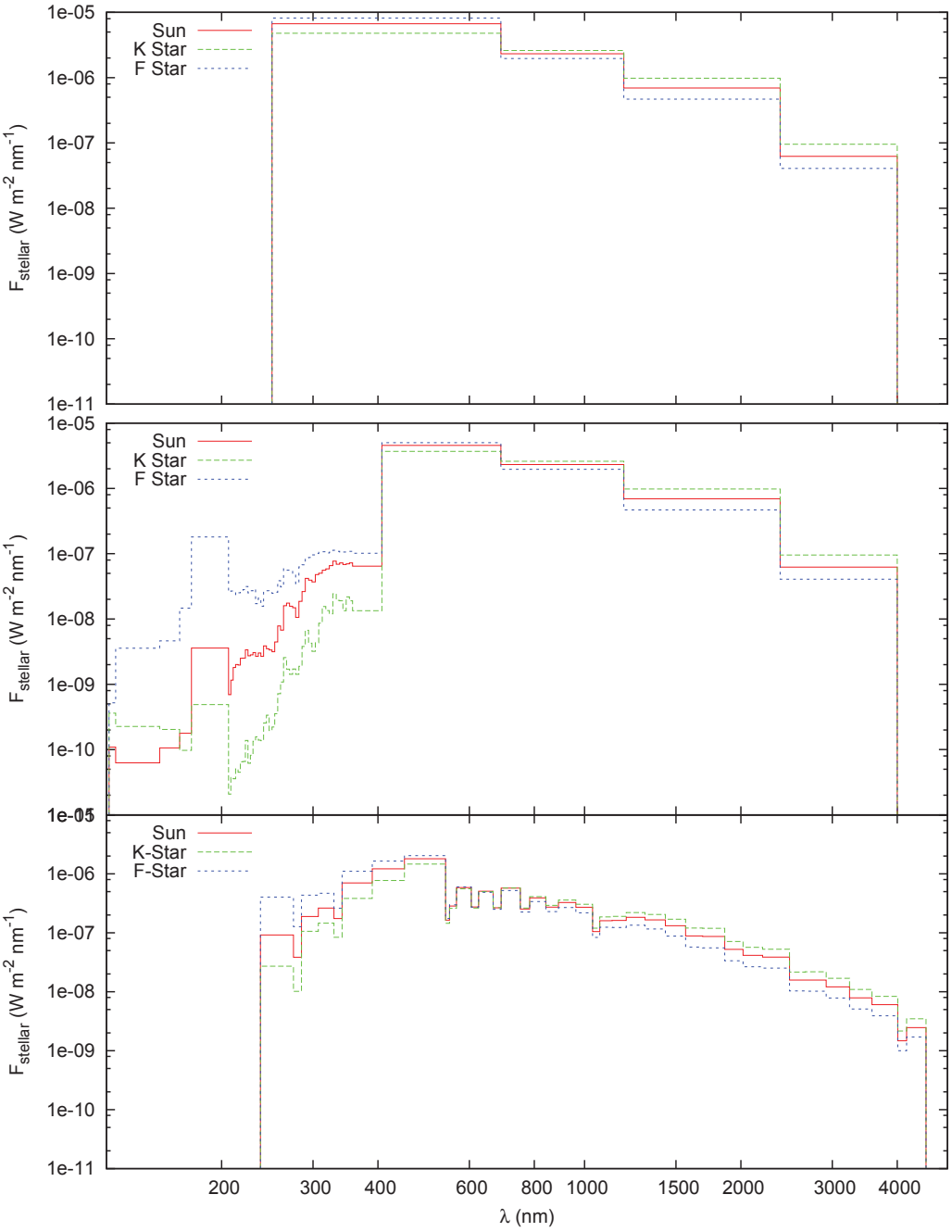

Figure 7.2: Spectral energy flux distribution of the three central stars (Sun in red, K-type star in green, F-type star in blue) as considered by the short wavelength radiation schemes in the models. Upper panel: Binning of the central star spectra into four bands as used in standard RAD4ALL radiative transfer scheme of the 3D model. Middle panel: Binning of the central star spectra into 52 bands as needed for the high resolution radiative transfer scheme FUBRAD of the 3D model. Lower panel: Binned stellar spectra (38 bands) as used by the short wavelength radiative transfer scheme of the 1D climate model.

scaling of the flux in the Chappuis band is applied, as discussed in Chapter 6.

Table 7.2: Orbital parameters

Star	stellar type	M_{Star} (M_{Sun})	a (AU)	P (days)
ϵ Eridani	K-dwarf	0.856	0.6	184.00
Sun	G-dwarf	1.000	1.00	365.25
σ Bootis	F-dwarf	1.244	1.89	450.00

7.2 3D model scenarios

The scenarios and the corresponding model inputs for the 3D model are summarized in Table 7.3.

7.2.1 Adjustment of orbit

Clearly, for consistent planetary scenarios in the 3D model the orbital period also has to be adjusted. The orbital periods, hence orbital distances are chosen to obtain a total energy input at the top of the atmosphere (TOA) from the star of one solar constant (1366 $\frac{W}{m^2}$). These have been calculated via Kepler's third law ($\frac{P^2}{a^3} = const = \frac{4\pi^2}{M_{Star}G}$) from the orbital distances a calculated in sec. 7.1.

$$P = \sqrt{\frac{4\pi^2}{M_{Star}G}a^3} \tag{7.2}$$

The resulting orbital distances and periods resulting in an energy input by the star at TOA of one solar constant (1366 $\frac{W}{m^2}$) are summarized in Table 7.2.
The stellar masses of ϵ Eridani and σ Bootis have been taken from Takeda et al. (2007).

Fig. 7.3 shows the variation of the incident stellar flux over a time period of five Earth years and latitude for a planet around the Sun, a K-type and an F-type star. While the planet revolves the K-type star about ten times in five Earth years, the planet around the F-type star completes only four orbits. The eccentricity and the axial tilt of all scenarios are those of the present Earth.

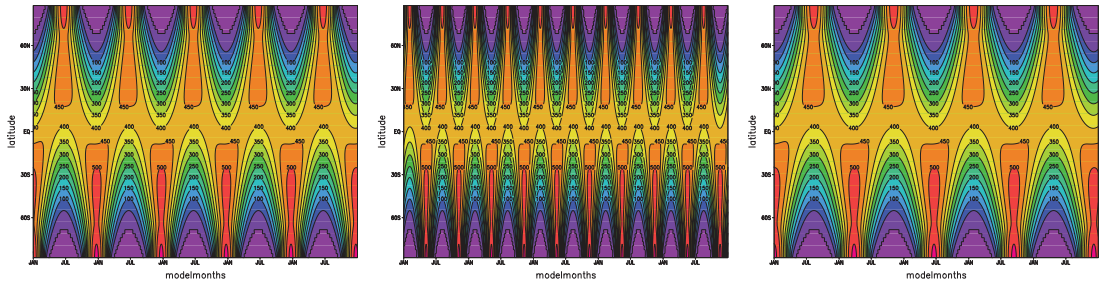

Figure 7.3: Zonal mean incident radiation (W/m^2) at TOA over five Earth years for planets orbiting different types of stars. Left: Sun, Middle: K-type star, Right: F-type star.

7.2.2 Ozone concentrations

The concentrations of radiative active species are the same in all scenarios, except for water which is calculated interactively, and ozone. Radiative gases, other than water and ozone, are set to constant values (see sec. 5.5). For 3D model scenarios with an orbital period of one Earth year the ozone climatology of Fortuin and Kelder (1998) is used, which prescribes monthly zonal mean ozone concentrations, see Fig. 7.4 for zonal mean concentrations in January and July. For other orbital periods the annual mean of this climatology is used, see Fig. 7.5.

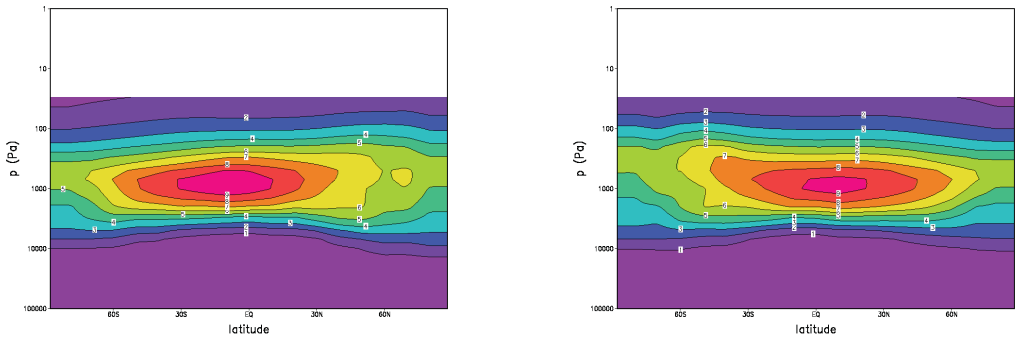

Figure 7.4: Earth's ozone climatology by Fortuin and Kelder (1998). Left: Zonal mean ozone concentrations in ppmv for January. Right: Zonal mean ozone concentrations in ppmv for January.

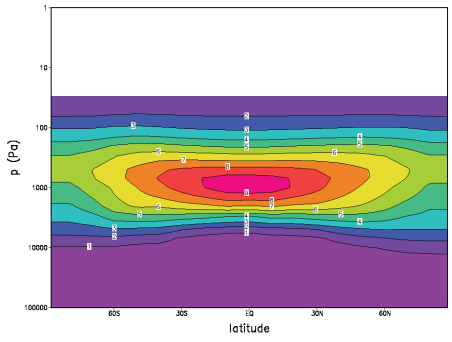

Figure 7.5: Annual mean of the Earth's ozone climatology by Fortuin and Kelder (1998) in ppmv.

7.2.3 Lower boundary

7.2.3.1 Sea surface temperatures

Two different setups are chosen concerning the sea surface temperatures (SSTs) and sea ice concentrations. For the investigation of the stellar radiation upon the stratosphere (see sec. 11.1) fixed sea surface temperatures and sea ice concentrations are prescribed using

the AMIP II climatology (Taylor et al., 2000), which is derived to obtain observed monthly mean sea surface temperatures for present day conditions.
To study the influence of the stellar radiation upon the climate, the mixed layer ocean (MLO) model, described in section 5.3.8.6, is coupled to the atmosphere. It calculates the SSTs and the sea ice concentration and depth interactively. The correction fluxes (q-fluxes) needed to reproduce present day climate are calculated from the reference scenario with solar radiation and fixed SSTs, here called sunsst. This is done by the following equation (see also sec. 5.3.8.6).

$$Q = H_{clim} - C_{sw}\frac{\partial T_{clim}}{\partial t} \tag{7.3}$$

where Q is the q-flux, T_{clim} are the fixed sea surface temperatures for which the net heat flux H_{clim} is calculated by the atmosphere model. C_{sw} is the heat capacity of sea water.

These fluxes can induce a forcing of the calculated SSTs towards a one Earth year seasonality. This boundary condition is not known for Earth-like planets around different types of stars, especially when including a change in the orbital period. Therefore, in this work three sets of q-fluxes were used for the calculation of the sea surface temperatures.

q-flux1 These fluxes, shown in Fig. 7.6, are calculated as they are used for Earth climate studies by calculating a monthly mean H_{clim} from a reference scenario with fixed sea surface conditions (sunsst). The model then calculates the q-flux for every time step (see Eq. 7.3) by interpolation of the input values (monthly mean H_{clim} and sea surface temperatures). These are used in the scenarios sunmlo, klomloalb and fmlo.

q-flux2 These are calculated as the q-flux1, but with a annual mean H_{clim}, see Fig. 7.7. These are introduced to the model for the scenarios sunorb, korb, forb.

q-flux3 These are monthly mean q-fluxes calculated offline from the q-flux1. For these no interpolation is carried out, hence they are constant over a period of one Earth month. They are used in the scenarios sunorbmq, korbmq and forbmq.

The annual global mean energy input to the atmosphere by these q-fluxes is about 15 Wm^{-2}, which is rather small compared to energy input by the star. Hence, especially the variability will be influenced by the different q-fluxes.
The influence of these q-fluxes for the Earth around the Sun are shown in Chapter 8 and discussed for the Earth-like planets around different types of stars in Chapter 10.

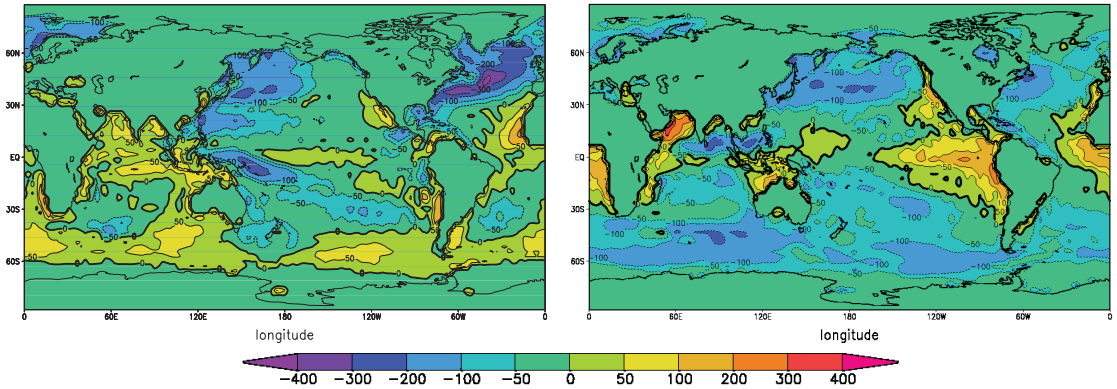

Figure 7.6: Monthly mean of q-flux1 ($\frac{W}{m^2}$) in January (left) and July (right).

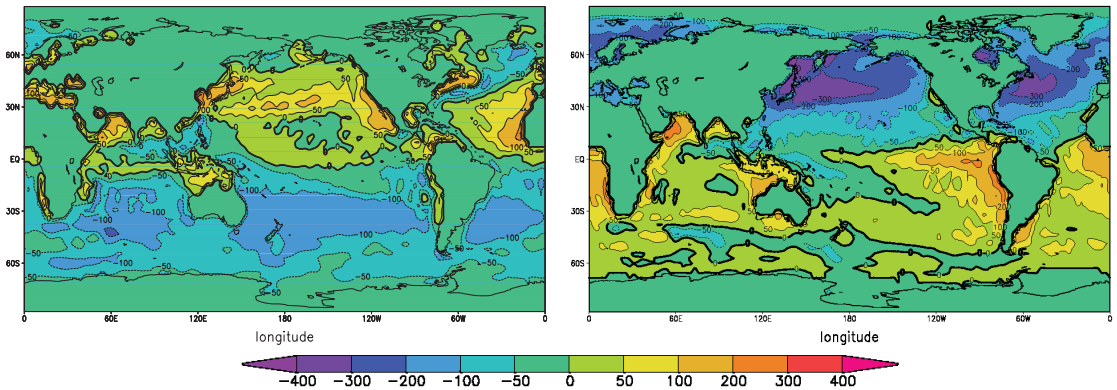

Figure 7.7: Monthly mean of q-flux2 ($\frac{W}{m^2}$) in January (left) and July (right).

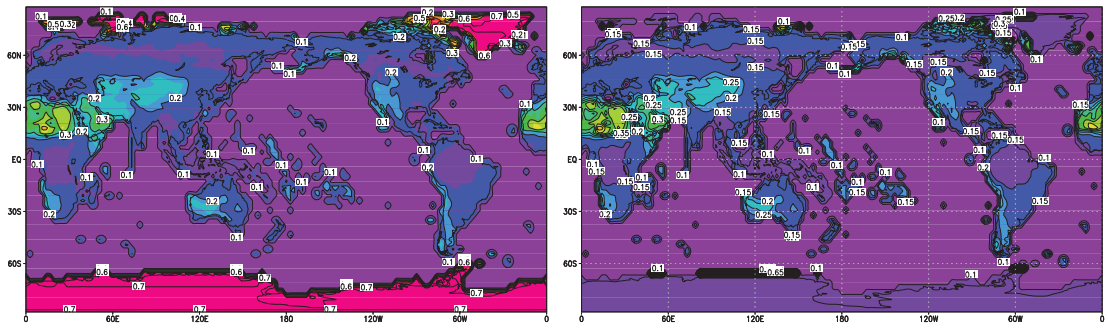

Figure 7.8: Background surface albedo maps. Left: Surface background albedo map as usually applied for Earth climate calculations. Very high surface albedo corresponding to ice cover are visible in the regions of Antarctica and Greenland. Right: Adjusted surface background albedo map. The surface albedo of Antarctica and Greenland are set to 0.15.

7.2.3.2 Surface background albedo

Another lower boundary condition which appeared to be important in the simulations is the surface background albedo. For K-type stellar radiation surface temperatures increase (see Chapter 9) leading to complete melting of ice. For this scenario it is therefore necessary to change the background surface albedo in the region of Antarctica and Greenland, since the standard background albedo map for the EMAC model assumes an ice albedo for this regions. This is reasonable for Earth climate calculations, since nowadays these regions are covered mainly by glaciers. For the evaluation of the climate of an Earth-like planet around different types of stars, however, the background albedo in these regions is set to the one of granite (0.15), which is assumed to lie below the thick ice cover in these regions. The two surface background albedo maps are shown in Fig. 7.8. Table 7 summarizes which surface albedo maps have been used in the scenarios. The influence of different surface background albedos for the Earth around the Sun is briefly discussed in Chapter 8 and 10.

7.3 Summary of model setups and scenarios

The model setups used to calculate the response of the atmosphere shown in the following sections are summarized in Table 7.3

Table 7.3: Summary of scenarios

scenario	stellar spectrum	sw radiation scheme	SSTs and sea ice	q-flux	surface albedo	ozone	orbital period (days)
sunsst	Sun	FUBRAD	fixed		high	monthly zonal mean	365.25
k52sst	K-type star	FUBRAD	fixed		high	monthly zonal mean	365.25
k4sst	K-type star	standard	fixed		high	monthly zonal mean	365.25
sunmlo	Sun	FUBRAD	mixed layer ocean	q-flux1	high	monthly zonal mean	365.25
kmlo	K-type star	FUBRAD	mixed layer ocean	q-flux1	high	monthly zonal mean	365.25
kmloalb	K-type star	FUBRAD	mixed layer ocean	q-flux1	low	monthly zonal mean	365.25
fmlo	F-type star	FUBRAD	mixed layer ocean	q-flux1	low	monthly zonal mean	365.25
sunorb	Sun	FUBRAD	mixed layer ocean	q-flux2	low	annual zonal mean	365.25
korb	K-type star	FUBRAD	mixed layer ocean	q-flux2	low	annual zonal mean	184
forb	F-type star	FUBRAD	mixed layer ocean	q-flux2	low	annual zonal mean	450
sunorbmq	Sun	FUBRAD	mixed layer ocean	q-flux3	low	annual zonal mean	365.25
korbmq	K-type star	FUBRAD	mixed layer ocean	q-flux3	low	annual zonal mean	184
forbmq	F-type star	FUBRAD	mixed layer ocean	q-flux3	low	annual zonal mean	450

Part III

Results

CHAPTER 8

Comparison of model setups for the Earth around the Sun

This Chapter evaluates the influence of the different 3D model setups (sea surface conditions, albedo) for an Earth-like planet around the Sun. This is done in order to estimate whether the change in climate due to different model setups may lead to different conclusions on the habitability of a planet, since clearly the change in some of the boundary conditions would not be appropriate for Earth climate simulations.

For comparison four scenarios are chosen which are summarized in Table 8.1. A major change in the model setups is using a mixed layer ocean model for the interactive calculation of the sea surface conditions (sunmlo) instead of keeping them fixed (sunsst).
For the sunorb scenario the low background surface albedo map was chosen, without ice albedo for Antarctica and Greenland. Furthermore, different q-fluxes are applied for the sunmlo, sunorb and sunorbmq scenario, see section 7.2.3.1. Furthermore, an annual mean ozone profile is applied (see section 7.2.2). The sunorb scenario is the reference scenario used in Chapter 9, where the 3D model results for the Earth-like planets around different types of stars are presented.

Table 8.1: Scenarios of Earth-like planets around the Sun

Scenario	ocean	q-fluxes	albedo map	ozone
sunsst	fixed SSTs and sea ice	none	high	monthly mean
sunmlo	mixed layer ocean	q-flux1	high	monthly mean
sunorb	mixed layer ocean	q-flux2	low	annual mean
sunorbmq	mixed layer ocean	q-flux3	low	annual mean

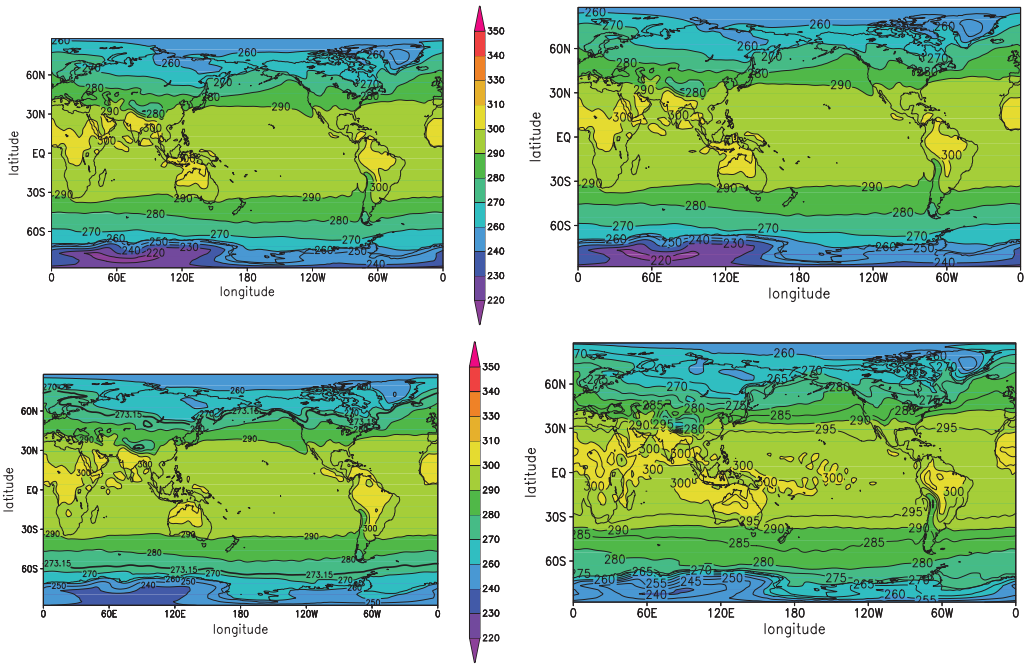

Figure 8.1: Global annual mean 2m temperature. Upper left: sunsst, upper right: sunmlo, lower left: sunorb, lower right: sunorbmq

8.1 Temperature response

8.1.1 Surface temperatures

First, the influence of the different model setups on the near surface temperature is evaluated, since it defines the surface habitability.
Figure 8.1 shows the annual mean 2m temperature (i.e. the temperature 2m above the surface), which is the temperature of the atmosphere in the lowermost model layer (see section 5.3.9.2, for the hybrid vertical coordinate).
For all scenarios the 2m temperature stays approximately the same, with largest temperatures at the equator of about 290-300 K, and lowest temperatures down to 220-240 K in the polar regions. Hence, the model setups do not show any influence on the habitability of the planet. This can also be inferred from table 8.2, which shows the global annual mean 2m temperature for the scenarios.

Although there exist changes between the different scenarios differences are not great.
Changing the model setup from prescribed SSTs (sunsst, upper left panel of Fig. 8.1) to interactively calculated SSTs with the MLO model (sunmlo, upper right panel), hardly any difference can be identified in the annual mean 2m temperature. This confirms that the MLO model works as required for Earth climate simulations.

For a change in the surface albedo (sunorb, lower left panel), some small differences occur above the Antarctic continent. The lower surface albedo leads to higher 2m temperatures in this region.

The change in the q-fluxes from q-flux2 (sunorb) to q-flux3 (sunorbmq) leads to some in-

Table 8.2: Global annual mean 2m temperature for the planet around the Sun

Scenario	2m temperature (K)
sunsst	287.6
sunmlo	287.7
sunorb	288.6
sunorbmq	289.7

creases in the 2m temperature especially above the ocean. This demonstrates the influence of the ocean circulation on the climate state of our planet.

Table 8.2 summarizes the global annual mean 2m temperatures for the different scenarios. It shows that the overall increase in global mean temperature is about 2 K for changing from the sunsst scenario to the sunorbmq scenario. This is rather significant for Earth climate simulations, however only a minor change for habitability investigations of extrasolar planets. The largest changes in temperature of about 1 K occur due to the background surface albedo map change (sunorb) and the assumption of monthly mean q-fluxes (sunorbmq).

8.1.2 Global annual mean temperature and water vapor profiles

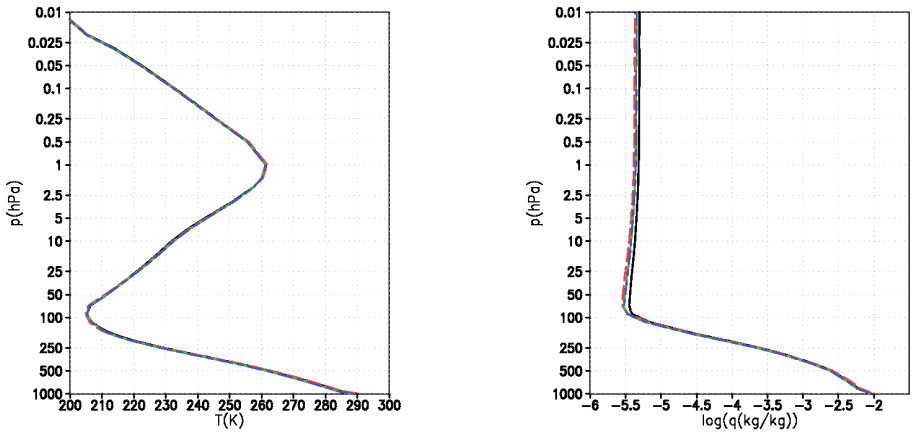

Figure 8.2: Global annual mean temperature and specific humidity profile. Sunsst in black, sunmlo in red, sunorb in green and sunorbmq in blue.

Fig. 8.2 shows the global mean temperature and the specific humidity profile for the differ-

ent scenarios. Hardly any changes can be identified in the global annual mean temperature profile (left). For all scenarios the mean temperature profile of the Earth is reproduced well.

Small changes in the specific humidity profile (right panel of Fig. 8.2) are obtained for the different scenarios. The sunorb scenario shows the highest specific humidity in the upper atmosphere, and similar specific humidities are obtained for the other scenarios. However, changes are very small and negligible for exoplanet scenarios.

8.2 Summary

The influence of the different model setups has been shown to be small for the Earth around the Sun. The largest difference in temperature occur due to a change in the surface background albedo map and due to the use of monthly mean q-fluxes for the calculation of the sea surface temperatures in the MLO model. The resulting temperature difference is as large up to 2 K for the various setups. For Earth climate simulations such model setups would not be appropriate, however for the determination of the habitability of an extrasolar planet, temperature uncertainties in this order of magnitude are acceptable.

CHAPTER 9

Climate of Earth-like extrasolar planets around different central stars

The two major questions motivating this work are addressed in this Chapter.

- What is the influence of dynamical atmospheric processes on the habitability of a planet?
- What is the influence of different stellar types on climate feedback cycles and how do they affect the habitability of the planet?

This chapter presents the results of the 3D modeling study for planets around different types of stars, including the change in stellar spectra and orbital period. The The sea surface conditions have been calculated with the MLO model (using q-flux2). The low background albedo map is chosen for all scenarios as well a mean ozone profile (see also Chapter 7). The most important parameters in the scenarios discussed here are summarized in Table 9.1.
First the temperature response (sec. 9.1) due to the different stellar radiations and the change in the greenhouse effect (sec. 9.2) is evaluated. There follows a discussion of the change in atmospheric dynamics in section 9.3. The response of the hydrological cycle is shown in section 9.4 and the surface properties in section 9.5. A discussion of the implications follows in section 9.6 and the results are summarized in 9.7. The influence of the orbital period upon the climate is briefly discussed in Chapter 10. The 3D model results are compared to those of the 1D model in Chapter 11, and differences due to dynamical processes are evaluated.

Table 9.1: Scenarios of Earth-like planets around different types of stars

Scenario	Star	Orbital period (days)
sunorb	Sun (G-type star)	365.25
korb	ϵ Eridani (K-type star)	184
forb	σ Bootis (F-type star)	450

9.1 Surface and atmospheric temperatures for planets around different types of central stars

In this section the temperature response of the Earth-like planets around different stars as calculated with the 3D model are shown. The important processes leading to these temperatures are discussed. A detailed analysis of the various processes causing the temperature response is given in the course of this chapter.

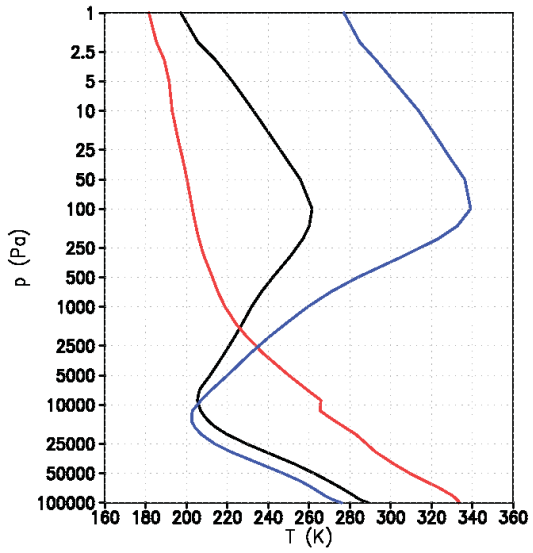

Figure 9.1: Global annual mean temperature profile (K) for Earth-like planets around different stars, where annual mean corresponds to the mean over the orbital period. The temperature profile for the Earth-like planet around the Sun is shown in black, around the K-type star in red, and in blue the temperature profile for the Earth-like planet around the F-type star.

Global annual mean temperatures

Figure 9.1 shows the global annual mean atmospheric temperature profile for an Earth-like planet around the Sun (black), a K-type (red) and an F-type star (blue).
For the planet around the F-type star a strong increase in stratospheric temperatures occurs, which even exceed the surface temperatures (e.g. at the stratopause). This is due to the high amount of stellar radiation at lower wavelengths where ozone absorbs. For the planet around the K-type star the stratospheric temperature inversion disappears. This is caused by a lack of radiation in the wavelength region where ozone absorbs. Ozone concentrations are the same in all scenarios.
The tropospheric temperatures are influenced by various processes, such as absorption of stellar radiation, the greenhouse effect and energy transport by convection.
While for the planet around the K-type star a strong increase in tropospheric temperatures can be observed, a decrease in tropospheric temperatures occurs for the planet around the F-type star with respect to the Earth-like planet around the Sun.

The increase in temperature in the lower atmosphere for the planet around the K-type star results from the coupling of the stellar energy flux to the water vapor feedback cycle. Due to the spectral energy flux distribution of the K-type star a stronger radiative heating occurs in the lower atmosphere (see sec. 9.2) caused by the absorption of NIR radiation by water vapor and carbon dioxide. This results in higher tropospheric and surface temperatures, leading to a higher amount of water vapor in the atmosphere by evaporation (see sec. 9.4). The increase in water vapor enhances the greenhouse effect and the absorption of stellar NIR radiation, hence the surface temperatures. This eventually leads to melting of the ice and snow covers lowering the surface albedo (see sec. 9.5), which results in less reflection of stellar light at the planetary surface, hence more absorption, causing even higher surface and tropospheric temperatures.

For the planet around the F-type star a cooler troposphere is found accompanied by lower surface temperatures in comparison to the Earth-like planet around the Sun. This is caused by the shift in the stellar flux distribution towards shorter wavelengths in comparison to the Sun.This leads to less absorption of stellar flux by water vapor and carbon dioxide in the troposphere (see sec. 9.2), hence lower surface temperatures. The lower surface temperatures lead to lower water vapor concentrations in the atmosphere (see sec. 9.4), decreasing the greenhouse effect. Furthermore, the surface albedo increases due to formation of sea ice, shown in sec. 9.5, which leads to less absorption of stellar radiation by the surface.

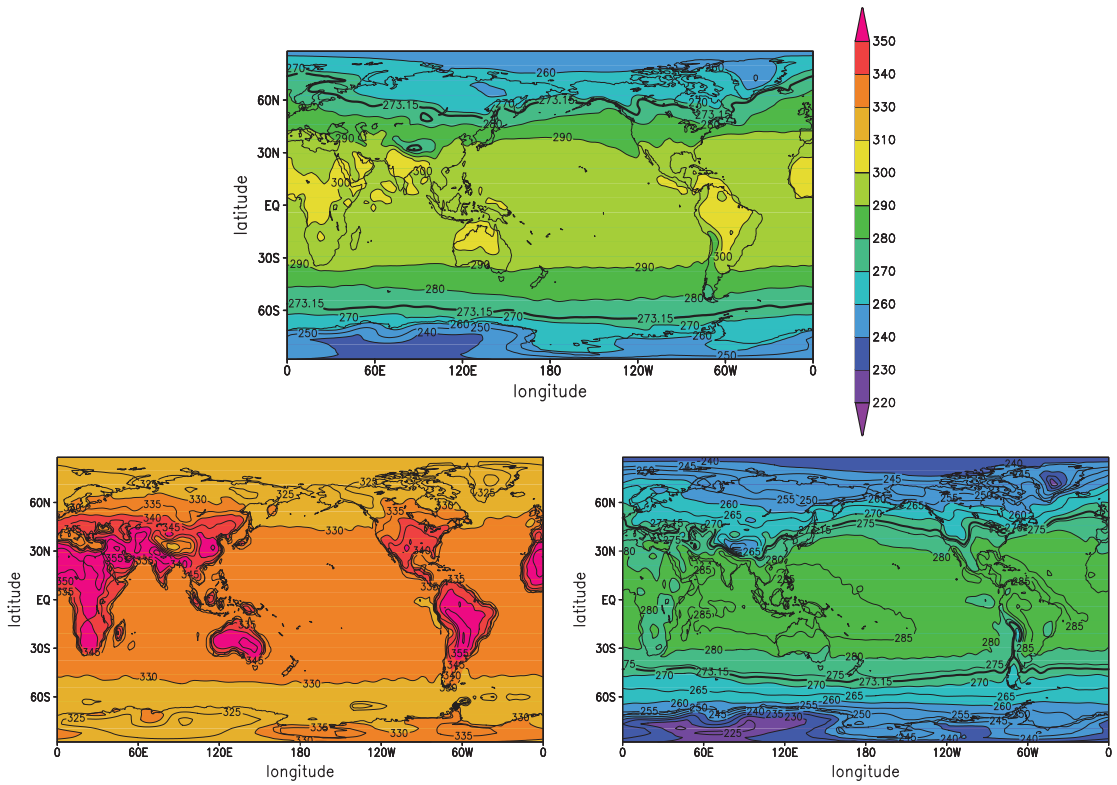

Figure 9.2: Annual mean temperatures for an Earth-like planet around the Sun (upper panel), a K-type star (lower left) and an F-type star (lower right).

2m temperatures

For surface habitability the temperatures near the surface are relevant, therefore the response of the 2m temperature is discussed.
Figure 9.2 depicts the annual mean 2m temperature of the Earth-like planet around different types of stars over latitudes and longitudes. The upper panel shows the 2m temperature for a planet around the Sun, the lower left the temperatures for a planet around the K-type star and the lower right the temperatures for a planet around the F-type star.

As already discussed, temperatures are higher for the planet around the K-type star and lower for the planet around the F-type star in comparison to the Earth around the Sun. For the planet around the K-type star (korb) the 2m temperatures are everywhere higher than the maximal temperature obtained for the planet around the Sun (sunorb). Hence, temperatures at high latitudes in the korb scenario are larger than low latitude temperatures for the sunorb scenario. For both scenarios highest temperatures occur at low and mid latitudes above land surfaces, since at low latitudes the mean stellar irradiation is largest and land has a smaller heat capacity than water, and heats up more strongly.
For the planet around the F-type star (forb) temperatures below the freezing point of water (273.15 K) are found down to latitudes of about 40°. Above the antarctic continent annual mean temperatures are as low as 225 K.
In comparison to the sunorb and korb scenario it is noteworthy that temperatures in low and mid latitudes above land surfaces are not higher than those above the sea.
The global annual mean 2m temperatures for the scenarios are summarized in Table 9.2.

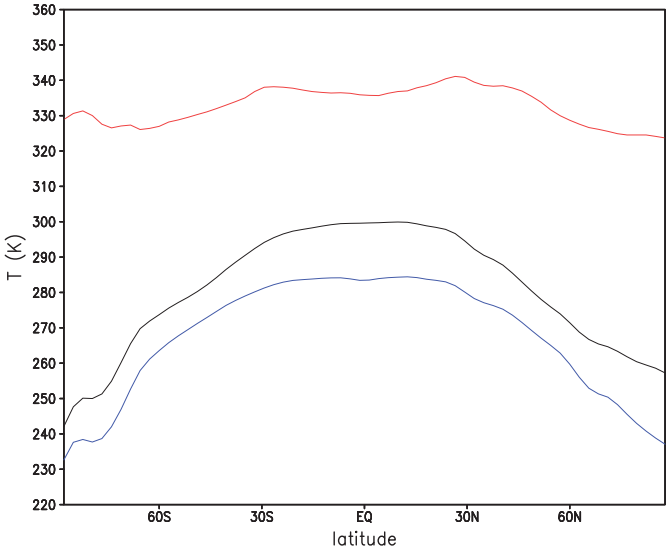

Figure 9.3: Zonal annual mean 2m temperature (K) over latitude for all scenarios. Colors: sunorb in black, korb in red, forb in blue.

Figure 9.3 shows the zonal annual mean 2m temperature for the three scenarios. For all scenarios higher temperatures at low latitudes are obtained than for polar latitudes, as expected for an obliquity of 23°. While the temperature difference between polar and equatorial region is very pronounced for the sunorb and the forb scenario ($\approx$ 60 and 50 K), for the korb scenarios the difference in zonal mean temperature between equator and pole is

Table 9.2: Global annual mean 2m temperature for planets around different stars

Scenario	Star/stellar type	2m temperature (K)
sunorb	Sun	288.6
korb	K-type star	334.9
forb	F-type star	275.2

much smaller ($\approx 15\,\mathrm{K}$). For the planet around the Sun and the F-type star the greenhouse effect is strongest in the equatorial region, since there atmospheric water vapor concentrations, as well as the thermal emission by the atmosphere and the surface are highest (see sec. 9.2 and sec. 9.4). For the planet around the K-type star, however large amounts of water vapor are present at all latitudes causing a greenhouse effect which is equally strong at all latitudes (see sec. 9.2). At high latitudes temperatures during polar night are smaller, and higher during polar day than the zonal annual mean 2m temperature depicted here.

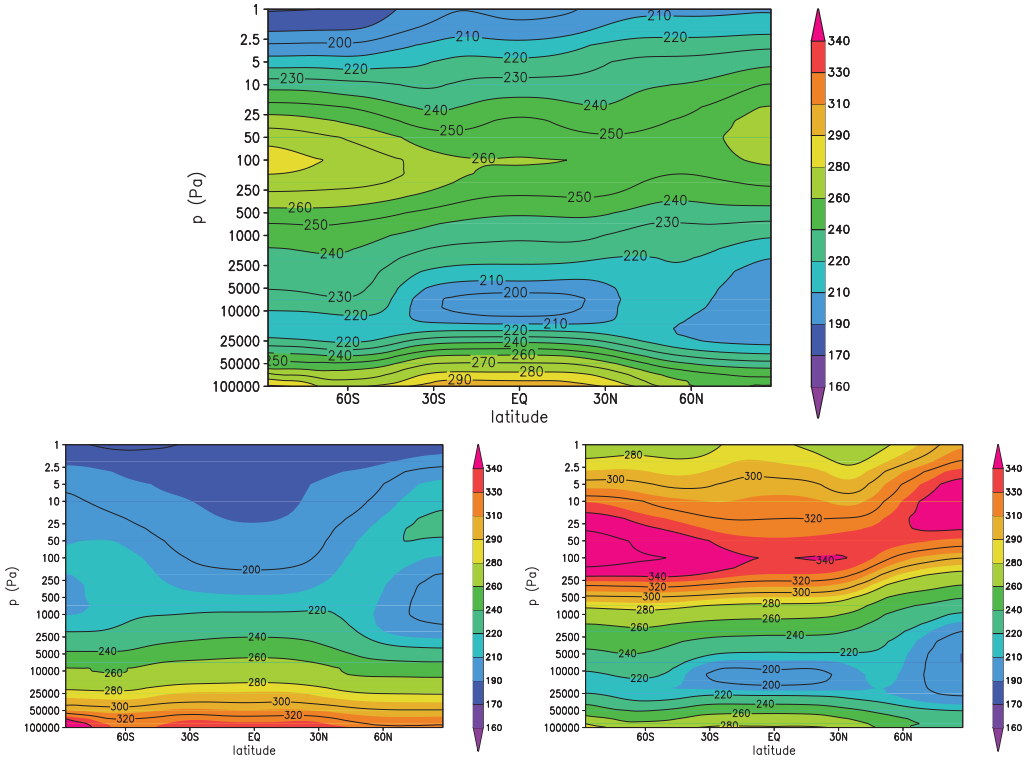

Figure 9.4: Zonal mean atmospheric temperature structure for planets around different stars. Planet around the Sun upper panel, planet around K-type star lower left panel, and planet around the F-type star radiation in the lower right panel for northern hemispheric winter (NHW).

Temperature structure

The atmospheric temperature structure results from the interaction of various processes (e.g. radiative transfer, atmospheric dynamics, convection). To understand their potential

change for Earth-like planets around different types of stars is a main motivation of this work.

Figure 9.4 shows the zonal mean temperature structures for the northern hemispheric winter (NHW) are shown. The zonal mean temperature structure for the southern hemispheric winter is not shown, since the differences in the overall response are small.

The northern hemispheric winter has different lengths depending on the orbital period and has been determined by the amount of stellar insolation over latitudes. Hence, for each scenario the atmospheric temperature has been averaged over a time period where the stellar insolation over latitudes corresponds to December, January and February for the Earth around the Sun. For the planet around the K-type star this corresponds to 44 days and to 110 days for the planet around the F-type star.

For the sunorb scenario the typical temperature structure of the Earth is visible with highest tropospheric temperatures in the equatorial region. The deviation of temperatures above the summer south pole result from the low albedo map as explained in Chapter 8. Temperatures are higher in the summer hemisphere than in the winter hemisphere and lowest temperatures occur for polar night. The cold tropopause in the equatorial region is visible as well as the temperature inversion in the summer and winter stratosphere. Cold temperatures occur in the lower winter stratosphere due to the lack of Sun light during polar night.

For the planet around the K-type star the overall temperature structure differs considerably from that of the Earth around the Sun. The pronounced temperature inversion in the summer stratosphere disappears and the pronounced cold tropopause in the equatorial region is missing. However, at smaller pressures atmospheric temperatures become very low (below 190 K) consistent with adiabatic cooling of air during ascent. Since the temperature inversion in the stratosphere is missing, the air parcels may ascend to high altitudes. Due to the high surface temperatures the troposphere expands and shows nearly constant temperatures over all latitudes up to a pressure of 5000 Pa (50 hPa). At pressures of about 500 Pa (5 hPa) features similar to the cold lower stratosphere of the Earth appear in both polar regions. Despite the fact that no pronounced stratospheric temperature inversion exists in the summer hemisphere, a temperature maximum in the winter stratosphere can be noticed. This results from the meridional circulation in the upper atmosphere from the summer to the winter hemisphere (see sec. 9.3), which leads to a warming of the upper winter hemisphere due to adiabatic warming of descending air parcels.

For the planet around the F-type star the overall temperature structure is similar to that of the Earth. However, tropospheric temperatures are lower than for solar radiation, and stratospheric temperatures much higher, reaching maximum temperatures of more than 350 K, as already noted in the global annual mean temperature profile (Fig. 9.1). The stratopause temperatures in the winter and summer hemisphere are similar, indicating a strong stratospheric meridional circulation. The tropopause is slightly colder than for the Earth around the Sun which results from less ascending air in the tropical region due to less convective activity.
Note, that the resulting temperatures for the planet around the K-type star, are partly outside the validity range of the thermal infrared radiative transfer scheme RRTM (see

sec. 5.3.2.2). A scheme with a larger validity range in temperature, pressure and concentration is highly desirable for further model scenarios, which is work in progress by Ph. von Paris (see Chapter 13).

9.2 Radiative fluxes for planets around different types of central stars

Since the temperature response just discussed is initiated by the different radiative heating and cooling rates, they are discussed in more detail in this section.

9.2.1 Heating and cooling rates

Fig. 9.5 shows the resulting global annual mean shortwave heating and long-wave cooling rates for the model atmospheres in model layers. The model layers correspond to full pressure levels of the hybrid vertical coordinate described in section 5.3.9.2 except for the net thermal infrared flux profile, where model layers are half pressure layers. Corresponding pressures for an approximate surface pressure of 1000 hPa are given in Table 5.2.

The direct influence of the different stellar radiations can be inferred from the shortwave heating rates, shown in Fig. 9.5.

From the total shortwave heating rates the direct impact of the different stellar radiations can be inferred. For solar radiation (black line) heating rates are largest in atmospheric layers, which correspond to the height of the stratopause, caused by absorption of radiation by ozone (left lower panel). For F-type stellar radiation (blue line) the highest heating rates occur in the uppermost part of the atmosphere due to absorption of radiation by molecular oxygen in the Schumann-Runge bands (right middle panel) and absorption by ozone. These are much higher than for the Earth-like planet around the Sun. For K-type stellar radiation (red line) highest radiative heating appears due to absorption of NIR radiation (lower right panel) in the uppermost atmosphere by mesospheric clouds and in lower atmosphere by absorption of radiation by water vapor and clouds. The NIR heating rates in the lower atmosphere are higher for the korb scenario than for the sunorb scenario.

The highest radiative heating rates arise for the F-type stellar radiation due to large amounts of radiation at low wavelengths. For this scenario stratospheric heating rates due to absorption of radiation by ozone are as high as 35 K/day compared to 6 K/day for solar radiation. It should be noted that the heating by ozone absorption may be overestimated due to the use of an unadjusted stellar energy flux in this wavelength regime as discussed for solar radiation in section 6.2.2.
With respect to the sunorb scenario the korb scenario shows a large increase in heating due to the absorption of near infrared radiation by water vapor and clouds (lower right panel of Fig. 9.5). Heating rates of up to 3 K/day are obtained in the lower atmosphere, which is more than three times as much as for solar radiation. Much lower heating rates due to absorption of radiation by ozone occur due to less radiation at these wavelengths.

The thermal infrared cooling rates can in most instances be explained by the reemission of absorbed stellar radiation. In the lower atmosphere higher cooling rates are obtained from increased temperatures due to the greenhouse effect. For the sunorb and the forb scenario

thermal infrared cooling rates in the lower atmosphere are lower than 5 K/day and cooling of the lower atmosphere takes place up to layer 22, which corresponds to an approximate pressure of 70 hPa. For the korb scenario, however, cooling rates are higher than 5 K/day reaching maxima of about 10 K/day at levels where clouds are present. This suggests that heating by the greenhouse effect is efficient for this scenario, and cooling takes place at much higher atmospheric layers than for the other two scenarios. This behavior is consistent with the net thermal infrared flux profiles shown in Fig. 9.6.

9.2.2 Net thermal infrared radiation

The net thermal flux profile (Fig. 9.6) is the sum of the upward and downward directed thermal infrared radiation which is emitted by the atmosphere, where the negative values represent outgoing radiation. In the upper atmospheric layers the net thermal flux is dominated by the upward directed flux, hence the global mean cooling of the atmosphere. The stratosphere contributes only little to the overall thermal infrared emission of the planet as air densities and thereby the optical depth is very low. The lower atmospheric thermal flux profile gives information about the strength of the greenhouse effect. In general, less net outgoing thermal infrared radiation may either be caused by very low temperatures, hence low emission by the atmosphere, or by equally high upward and downward thermal fluxes.

For the planet around the K-type star (red) the net thermal flux shows rather small negative values (lower than 20 Wm^{-2}) near the surface compared to the planet around the Sun (black) and the F-type star (blue) (around 60 Wm^{-2}), indicating that a large amount of emitted radiation (by the surface or the lower atmosphere) is absorbed in these lower layers and then reradiated contributing to the greenhouse effect. For the korb scenarios the higher values of the net outgoing thermal energy flux in the upper atmospheric layers are caused by the higher tropospheric temperatures for the korb scenario.

For the planet around the F-type star a small increase (in comparison to the sunorb scenario) in the net outgoing thermal flux is visible in the lowermost atmospheric layers, because of the decrease in the greenhouse effect. The stratospheric values of the net thermal flux are smaller for the planet around the F-type star than for the planet around the Sun due to the lower tropospheric temperatures. The increase in stratospheric temperatures for the forb scenario shows only a small impact on the outgoing thermal radiation, leading to a non-constant thermal flux profile up to layer five (≈ 0.25 hPa).

From the consideration of the global energy budget at top of the atmosphere (TOA) and assuming the atmosphere is on average in radiative equilibrium it may be implied that for the planet around the F-type star more stellar light is reflected back to space than for the Sun since the net outgoing infrared flux is lower which balances the net incoming radiation (see sec. 3.3.5.2). For the planet around the K-type star more stellar radiation is absorbed than for the planet around the Sun. This agrees with findings of 1D modeling studies and is shown in more detail by analyzing the shortwave fluxes at the surface (see Fig. 9.7). Shortwave flux profiles are not shown, because the standard model output provides only radiative fluxes for the standard radiative transfer scheme in the short wavelength bands used only for pressures larger than 70 hPa. Future versions of the model will allow for

a detailed analysis of the shortwave radiative fluxes (work in progress by M. Kunze, FU Berlin).

9.2.3 Shortwave radiation fluxes at the surface

The shortwave radiative fluxes at the surface influence the surface temperature (see sec. 5.3.8 of the model description), and are thereby important to understand the response of the 2m temperatures shown in sec. 9.1.
Figure 9.7 shows the shortwave fluxes at the surface for the planets around different types of stars. The solid lines show the net shortwave radiation at the surface, dashed lines show the upward shortwave flux. The dotted lines show the net shortwave flux, which would be obtained for cloud free conditions.
From the net shortwave fluxes for clear-sky conditions in the equatorial regions it can be inferred that approximately the same amount of shortwave flux would reach the surface for the planet around the F-type star and the Sun, and less for the planet around the K-type star if there were no clouds.
The fact that the same amount of energy would be incident for the forb scenario as for the sunorb scenario for clear-sky conditions, can be explained by decreased absorption of NIR radiation by water vapor. This decrease in absorption has been shown in the lower NIR heating rates for this scenario (see Fig. 9.5), which can only be caused by less water vapor or clouds, since all other constituents absorbing at this wavelengths (carbon dioxide, methane) are kept constant. So, despite that less net radiation for the planet around the F-type star is incident at TOA due to enhanced Rayleigh scattering, a similar amount of stellar radiation reaches the surface. The lower shortwave fluxes for the korb scenario can be explained by the same effect. The high water vapor concentrations in the atmosphere lead to increased absorption of NIR radiation, which may therefore not reach the surface. This is also consistent with the NIR heating rates.

Towards the poles the net radiation for clear sky conditions decreases strongly for the planet around the F-type star, which is due to the increased albedo (see sec. 9.5), hence increased amount of reflected light at the surface (dashed lines). Since the planet around the K-type star has the lowest surface albedo, upwards shortwave radiation is lower in this scenario.

The net shortwave surface fluxes with clouds suggests that clouds lead to less shortwave radiation at the surface for all scenarios. This is caused by absorption and scattering of stellar light by cloud particles. Note that with clouds the net surface radiation for the forb scenario is lower than for the sunorb scenario. Combining this with the information about the heating rates for the lower atmosphere, especially in the NIR, which are less, suggests that clouds increase the planetary albedo of the planet around the F-type star, hence lead to further cooling of the atmosphere and the surface.
For the korb scenario since strong heating occurs in the NIR at heights where clouds are present (the strong peaks of NIR heating in Fig. 9.5), it can be concluded that for this scenario clouds partly scatter the incoming radiation but also heat the atmosphere by absorption.

9.2.4 Thermal infrared radiative fluxes at top of the atmosphere and at the surface

The thermal infrared fluxes at the surface and the top of the atmosphere (TOA) give an insight in the strengths of the greenhouse effect.
Figure 9.8 shows the thermal infrared radiative fluxes at TOA and at the surface for the planets around different types of stars.

From the net thermal infrared radiative fluxes at TOA (left panel) it can be inferred how much energy is radiated to space. Shown are the thermal infrared fluxes for clear-sky and overcast (cloudy) conditions.
For clear-sky conditions (dotted lines) the thermal radiation is largest for the korb scenario and lowest for the forb scenario. This has been shown also in the thermal infrared flux profile (Fig. 9.6). Furthermore, for the sunorb and for the forb scenario the net thermal flux is highest at low latitudes and lower at high latitudes, which is in agreement with the higher tropospheric temperatures in the equatorial region. For the korb scenario, the thermal fluxes are similar over all latitudes caused by the nearly constant temperatures, which have been discussed in sec. 9.1.
For cloudy conditions (solid lines) less thermal infrared radiation leaves the planet, as expected. From this the greenhouse effect of clouds can be deduced. In the equatorial region the blocking of thermal infrared radiation by clouds is large for all three scenarios. At mid and high latitudes, however, the amount of radiation blocked by clouds is smaller for the planet around the Sun and the F-type star, which leads to the conclusion that for the korb scenario more thermal infrared radiation is blocked by clouds, hence they have a stronger greenhouse effect for this scenario.

In the right panel of Fig. 9.8 the thermal infrared fluxes at the surface are shown. The downward thermal infrared flux (dashed lines) is much larger for the korb scenario and lower for the forb scenario than for the planet around the Sun due to the increased and decreased greenhouse effect. The solid lines show the net thermal infrared radiation at the surface, dotted lines the net thermal infrared radiative flux without clouds. Negative values indicate upwards directed radiative flux. The comparison of the net fluxes implies that for the forb and the sunorb scenarios the downwards thermal infrared flux is larger if clouds are present, since the net upwards radiative flux is smaller (less negative). For the korb scenario, despite the larger greenhouse effect of clouds discussed above, clouds do not introduce a significant difference in the net thermal infrared fluxes at the surface. This can be explained by the large optical thickness of the lower atmosphere due to water vapor. Hence, the greenhouse effect in the lower atmosphere for the korb scenario is dominated by water vapor. At higher altitudes, however, absorption of thermal infrared radiation by clouds contributes to the greenhouse effect as inferred from the thermal radiative fluxes at TOA.
From the absolute values of the net thermal infrared fluxes the strength of the greenhouse effect can be inferred. As already discussed for the net thermal infrared flux profile, net upward fluxes for the korb scenario are very small, since upwards radiation is effectively absorbed and reradiated. A weaker greenhouse effect occurs for the forb scenario, indicated by the slightly more negative values of the net thermal infrared flux than for the sunorb scenario.

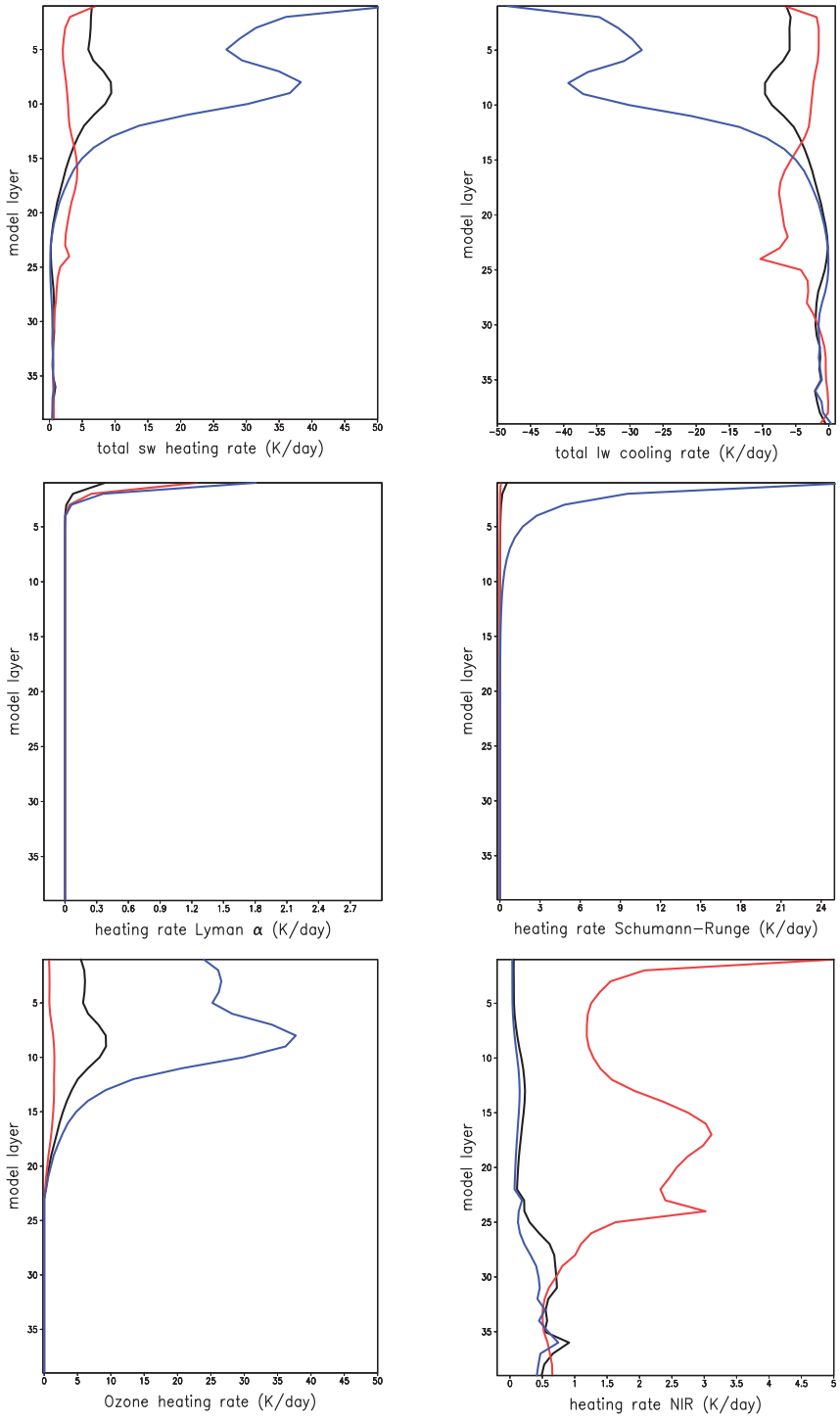

Figure 9.5: Global annual mean heating and cooling rates for planets around different types of stars, sunorb in black, korb in red, forb in blue. Model layers as in Tab. 5.2, layer 39 being the surface, layer 1 the TOA. Upper left: total shortwave heating rates, upper right: total cooling rates due to thermal infrared radiation. Mid left panel heating due to absorption of Lyman α radiation, mid right panel heating due to absorption of radiation by molecular oxygen in the Schumann-Runge bands and Schumann-Runge continuum, lower left heating due to absorption by ozone and lower right heating due to absorption of near infrared radiation by water vapor, clouds, carbon dioxide and methane.

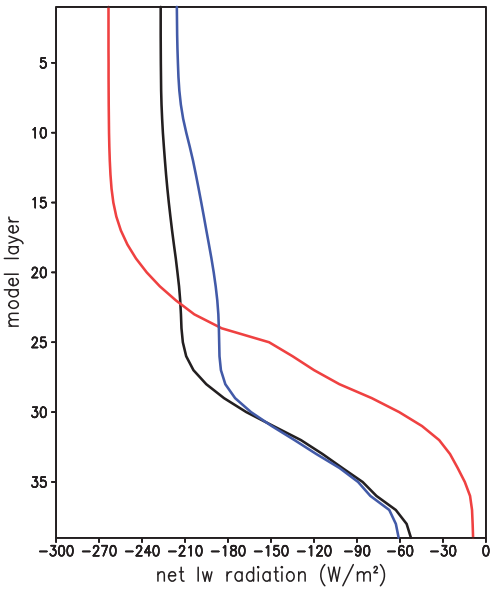

Figure 9.6: Global annual mean net radiative flux profiles in the thermal infrared for planets around different types of stars. Colors: sunorb in black, korb in red, forb in blue.

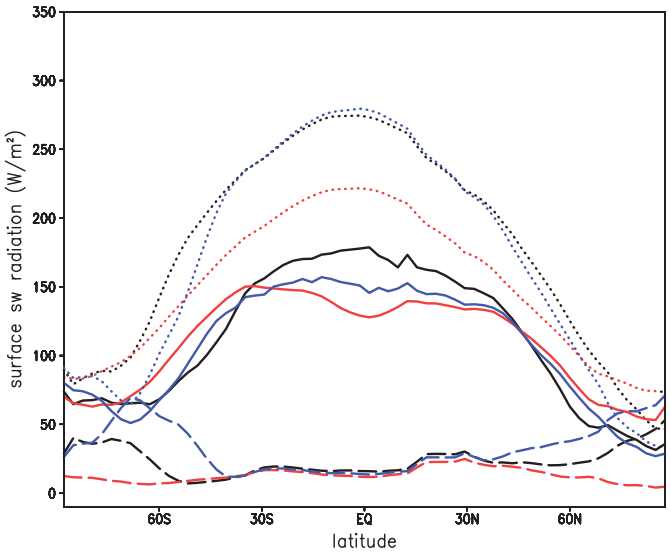

Figure 9.7: Shortwave fluxes at surface in Wm^{-2} for the planets around different types of stars, sunorb in black, korb in red and forb in blue. The solid lines show the net shortwave radiation at the surface, dashed lines the upward shortwave flux, and dotted lines the net shortwave fluxes calculated without cloud cover.

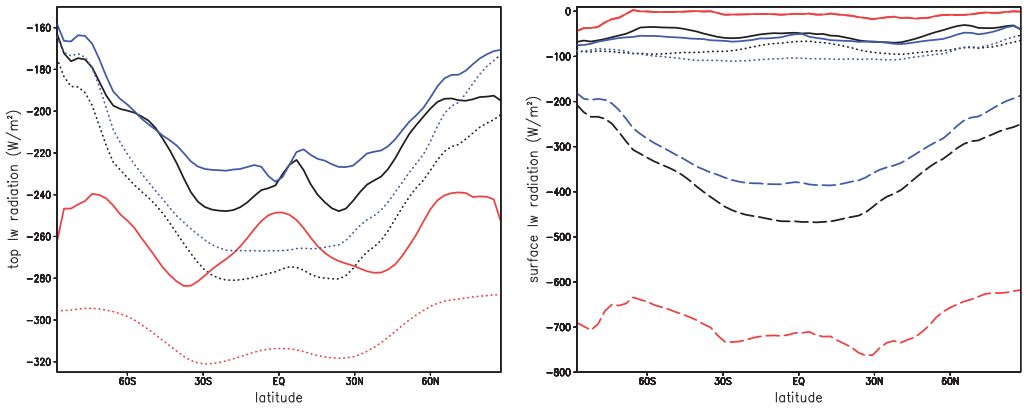

Figure 9.8: Annual zonal mean thermal infrared radiative fluxes at TOA (left) and at the surface (right) in Wm^{-2} for the planets around different types of stars, sunorb in black, korb in red and forb in blue. In both panels the solid lines show net thermal infrared radiation including clouds, dotted lines the net flux without clouds. In the right panel in addition to the net fluxes the dashed lines show the downwards thermal infrared radiation. Negative values indicate upwards directed radiative flux.

9.3 Atmospheric dynamics for planets around different types of central stars

This section discusses the dynamical response of the atmosphere. First the changes in zonal wind are analyzed, followed by a comparison of the meridional circulation in the troposphere and the stratosphere.

9.3.1 Zonal winds

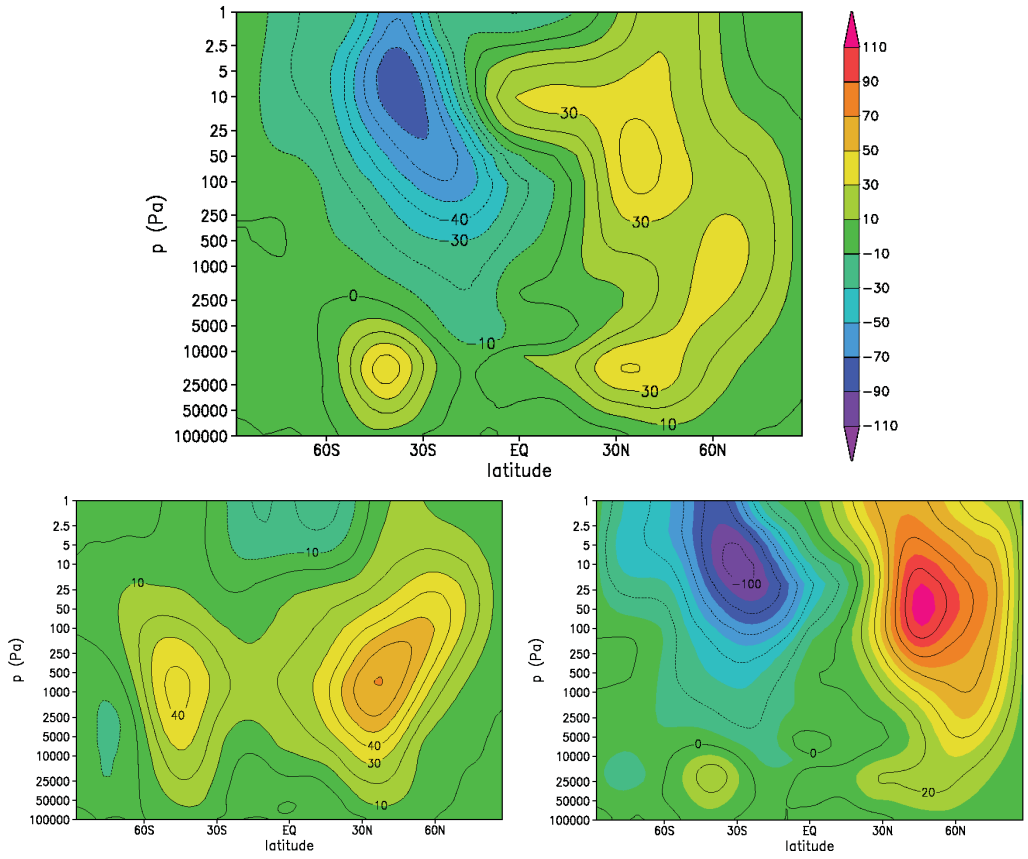

Figure 9.9: Mean zonal wind (m/s) for planets around different stars in northern hemispheric winter (NHW). The result for the planet around the Sun is shown in the upper panel, the planet around a K-type star in the lower left panel, and around an F-type star in the lower right panel. Positive values indicate westerly (from the west) winds, negative easterly winds.

The response of the zonal wind for the different stellar radiations is shown in Fig. 9.9. The upper panel shows the zonal wind in northern hemispheric winter (NHW) for the sunorb scenario. The lower panels display the zonal wind for the korb scenario (left) and the forb scenario (right).

For the sunorb scenario the troposphere and the winter hemisphere shows two westerly jet streams (denoted by positive values), as described in sec. 3.2. The summer hemisphere hemisphere features strong easterly winds (negative values).

For the korb scenario the most dominant feature are two westerly jet streams (denoted by positive values), which appear with maximum wind speeds at around 1000 Pa (10 hPa). The northern winter hemisphere jet stream is stronger than the southern summer jet stream and extends over a larger vertical domain. Maximum wind speeds in the winter are about 70 m/s, summer wind speeds are as high as 40 m/s. This zonal wind structure is different from that of the Earth around the Sun, since no stratospheric wind streams appear for the korb scenario. This is caused by the large change in the zonal temperature structure (see Fig. 9.4). Since no stratospheric temperature inversion is present in the summer hemisphere no easterly jet stream builds up in the upper atmosphere. Weak easterly wind bands (denoted by negative values) with velocities of about 10 m/s appear in the upper atmosphere and in the lower summer atmosphere. These are caused by the temperature gradients in the upper atmosphere (see Fig. 9.4) between the low and high latitudes and by the temperature gradient between the high surface temperatures above the antarctic continent and the lower temperatures at mid latitudes.

For the forb scenario the general structure of wind patterns of the Earth around the Sun are preserved. However, much larger wind speeds occur in the stratosphere reaching velocities above 100 m/s, which can be explained by the higher temperatures, hence a larger temperature gradient in the stratosphere for the planet around the F-type star. The tropospheric wind is weaker with wind speeds of about 20 m/s for the forb scenario than for the sunorb scenario, since the temperature gradient is lower than for the planet around the Sun.

9.3.2 Tropospheric meridional circulation

Fig. 9.10 shows the tropospheric meridional mass stream function in for the planets around different stars in northern hemispheric winter. The sunorb scenario is depicted in the upper panel, korb in the lower left and forb in the lower right panel.
For the planet around the Sun the three-cell structure of the Earth is readily identifiable. A strong Hadley cell transports air from the summer hemisphere over the equator to the winter hemisphere. In the winter hemisphere a Ferrel cell which circulates in the opposite direction follows in the mid latitudes and a weak Polar cell at high latitudes. In the summer hemisphere a weaker Hadley cell is obtained than in the winter hemisphere, followed by Ferrel cell and then a Polar cell. The cells in the summer hemisphere are shifted towards the equator and some minor circulation occurs above the Antarctic continent which is due to the low albedo used in this scenario.

For the korb scenario (lower left) a dominant Hadley cell builds up in the equatorial region with high mass transport up to smaller pressures than for the sunorb scenario. While the northern winter hemisphere shows an Earth-like three cell structure, with however weaker Ferrel and Polar cells, this structure is very weak in the summer hemisphere.
For the forb scenario a similar tropospheric meridional circulation as for the sunorb scenario is obtained. Mass transport is weaker in the Hadley cell than for the sunorb scenario and in the northern winter hemisphere the polar cell is absent.

At the boundaries between the meridional circulation cells vertical winds arise. Upward winds in between the Hadley cells and the polar and the Ferrel cell and downward wind are obtained at the boundary between the Hadley and the Ferrel cells and above the poles.

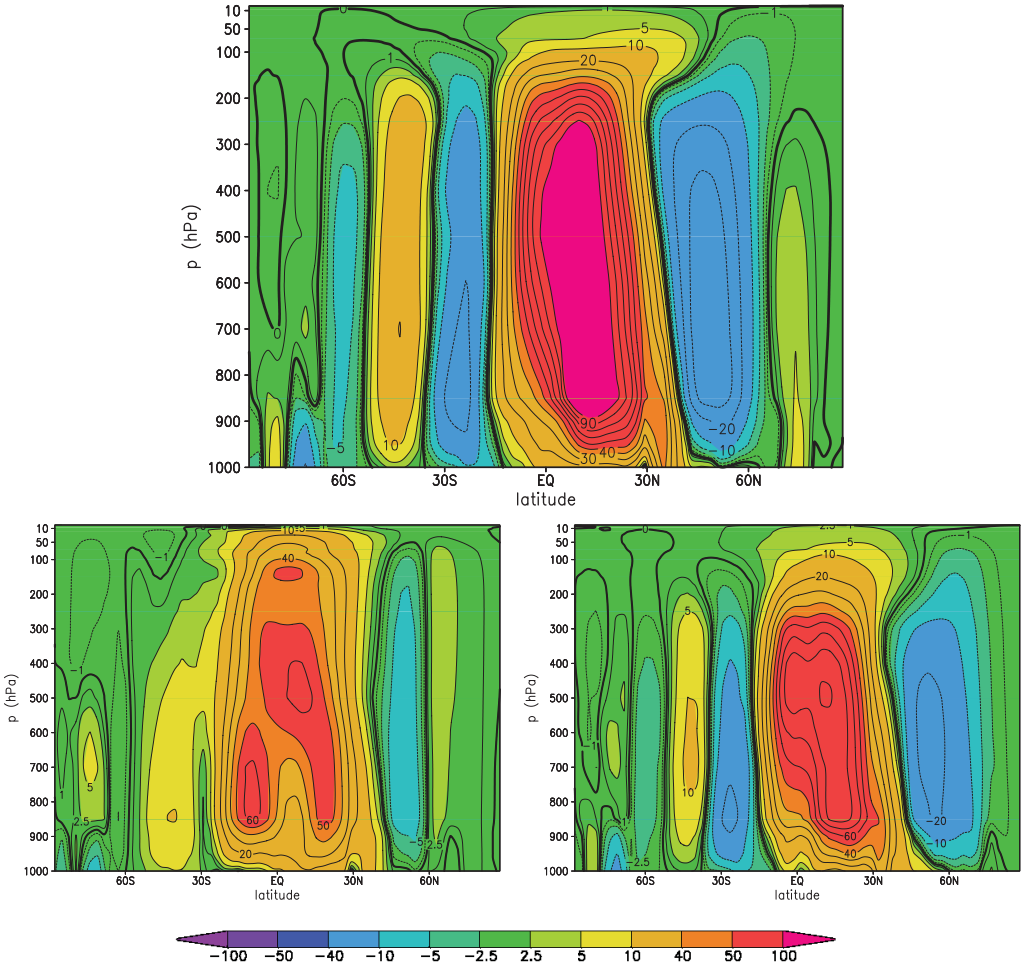

Figure 9.10: Tropospheric mass stream function for planets around different stars in $10^9 \frac{kg}{s}$ for northern hemispheric winter (NHW) from 1000-10 hPa (100000-1000 Pa). Order of scenarios as in Fig. 9.9. Positive (negative) values denote clockwise (anti-clockwise) circulation.

Upward winds are often accompanied by cloud formation as discussed in section 9.4.

9.3.3 Stratospheric meridional circulation

In the Earth's stratosphere the meridional circulation spans from the summer to the winter hemisphere rather than from the equator to the poles as in the troposphere. This circulation, called the Brewer-Dobson circulation, has an impact on, for example, the stratospheric temperature structure and is the cause for the warm stratopause at high latitudes in the winter hemisphere (see also section 3.2). This results from the descent of air in this region which heats adiabatically.

Fig. 9.11 shows the stratospheric circulation in terms of the residual mass stream function for the planets around the three different stars in northern hemispheric winter.

For the planet around the K-type star (lower left) the mass stream function in the lower

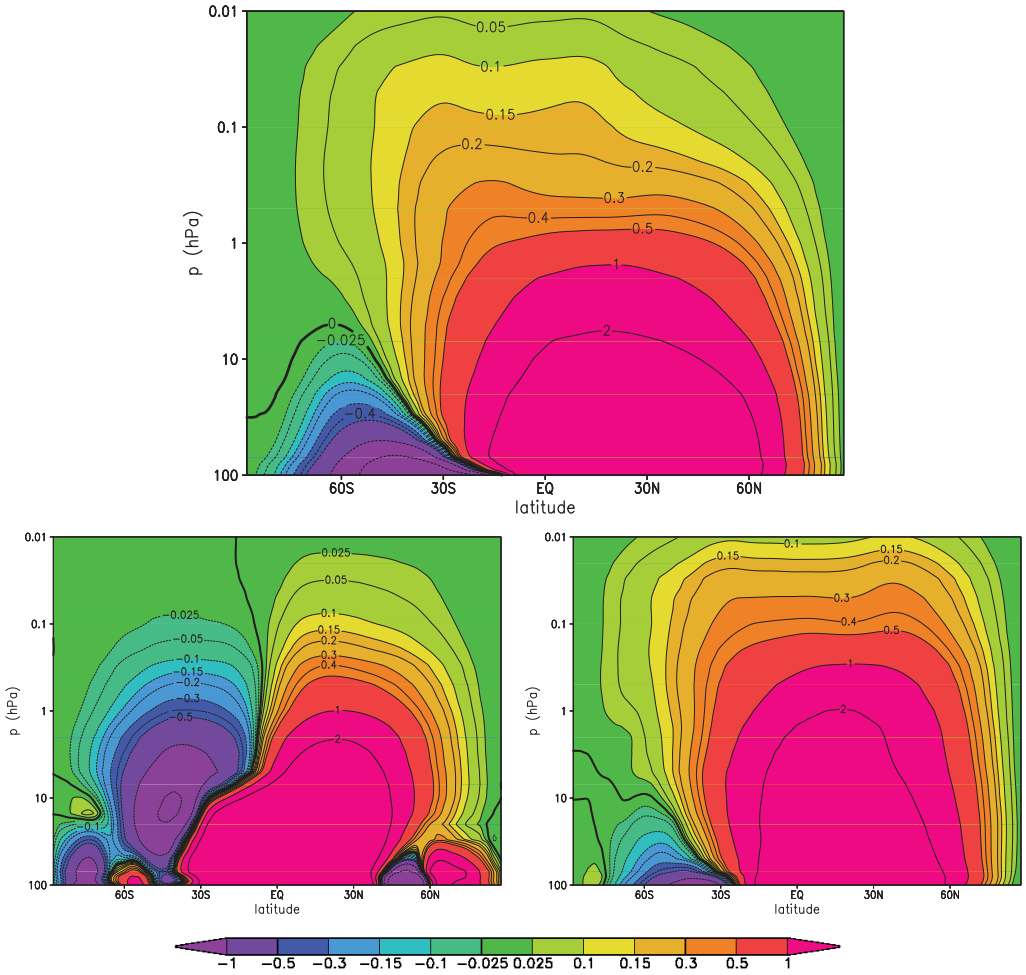

Figure 9.11: Stratospheric residual mass stream function for planets around different stars in $10^9 \frac{kg}{s}$ for northern hemispheric winter from 100-0.01 hPa (10000-1 Pa). Order of scenarios as in Fig. 9.9. Positive (negative) values denote clockwise (anti-clockwise) circulation.

stratosphere intensifies and reaches similar values as for solar radiation in the upper stratosphere. However, the patterns of the circulation are modified. At high pressures, whereas for solar irradiation only two cells, one spanning over the summer one over the winter hemisphere are found, for the korb scenario three cells appear in each hemisphere. These are simply the three tropospheric meridional circulation, which expand into the middle atmosphere. Another difference in the upper atmospheric circulation can be found, which is transport barrier of the summer and the winter hemisphere, indicated by the thick line for a mass transport of zero. For the planet around the Sun, a dominant circulation pattern is evident at high pressures in the equatorial region and rises through the summer hemisphere spanning over the entire meridional domain in the upper atmosphere and ascends at high winter latitudes. In the korb scenario, however, air rises in the equatorial region but does reach into the summer hemisphere. Thereby, the meridional circulation does not span over the entire meridional region but is rather separated in two hemispheres. Due to this changed pattern no transport from the summer to the winter hemisphere but rather from the equator to the polar regions occurs, analogous to two large Hadley cells. This may alter the transport of chemical species.

For the planet around the F-type star the structure of the stratospheric meridional circulation does not change as dramatically as for the planet around the K-type star. The typical characteristic pattern of the Brewer-Dobson circulation can be identified spanning over the entire upper atmosphere. The mass transport is however stronger for the forb scenario than for the sunorb scenario, consistent with the strong temperature inversion in the winter stratopause shown in Fig. 9.4.

9.4 Hydrological cycle for planets around different types of central stars

This section evaluates the response of the water content of the atmosphere for planets around different types of stars. Water not only influences the cooling and heating of the atmosphere by the interaction of radiation with water vapor and clouds, but also leads to release or consumption of energy during condensation or evaporation. In the following the response of the hydrological cycle will be analyzed by discussing water vapor concentrations, the total amount of water vapor stored in the atmosphere, cloud cover, cloud water, and cloud ice concentrations as well as changes in precipitation.

9.4.1 Water vapor

Water vapor plays an important role for the climate of a planet since it is an effective greenhouse gas. It absorbs radiation predominantly in the infrared, thereby blocking a part of the outgoing radiation at long wavelengths. This effect leads to an increase in surface and lower atmospheric temperatures. Higher surface temperatures cause a higher evaporation of water from the surface, hence lead to an additional increase in atmospheric water vapor. This is the water vapor feedback.

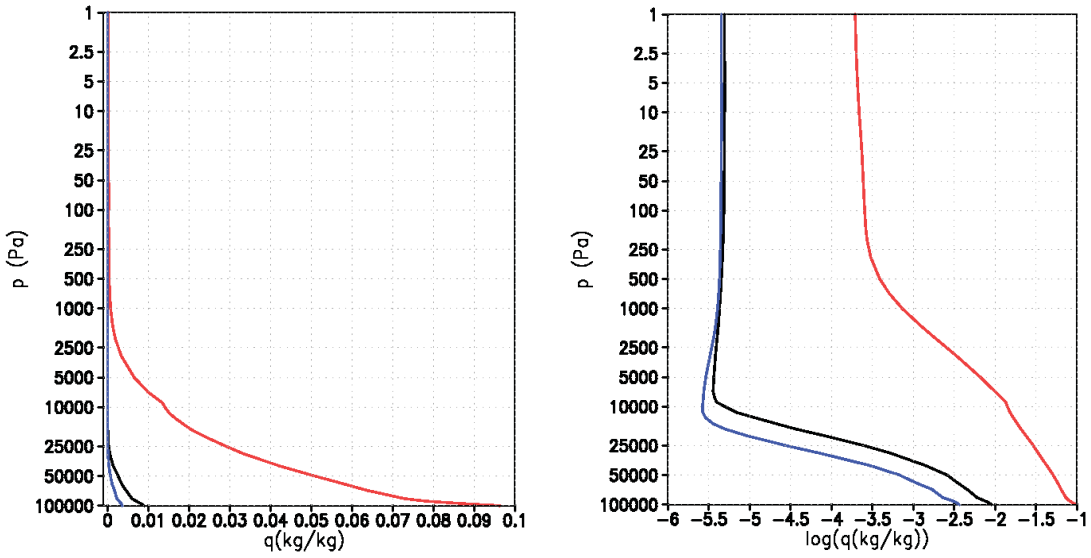

Figure 9.12: Global annual mean specific humidity (kg/kg) profiles for planets around different stars. Sunorb scenario in black, korb in red and forb in blue. Left panel shows specific humidity on a linear scale, right panel on a logarithmic scale.

To investigate the general behavior of water vapor the global annual mean profile of specific humidity is shown in Fig. 9.12. Specific humidity is the atmospheric mass concentration of water vapor, hence the ratio of mass of water vapor to the mass of dry air in the atmosphere, see section 3.3.4.

For the korb scenario (red) water vapor mass concentrations are higher than for the sunorb

scenario (black) reaching values of over 0.09 kg/kg (9 %). Values corresponding to the near surface specific humidity of the planet around the Sun (0.009 kg/kg) are reached at much higher altitudes at pressures of about 5000 Pa (50 hPa). Generally the upper atmospheric specific humidity is much larger for the korb scenario than for the planet around the Sun, about two orders of magnitude, see right panel of Fig. 9.12.

For the planet around the F-type star the specific humidity decreases to a global mean value near the surface of 0.003 kg/kg (0.3 %). The specific humidity is lower throughout the troposphere than for the planet around the Sun. In the upper atmosphere however, water vapor mass concentrations are comparable.

Water vapor distribution

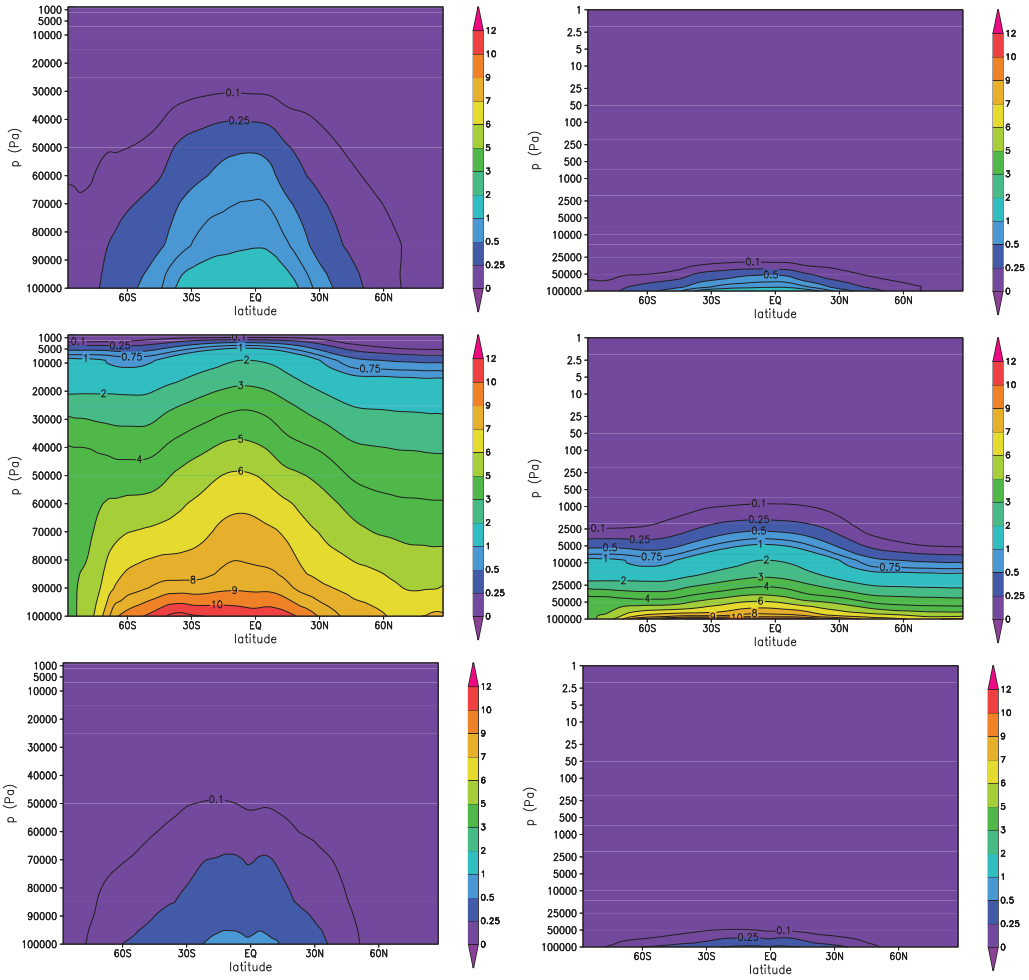

Figure 9.13: Zonal mean distribution of specific humidity (% kg/kg) for planets around different stars in NHW. Results for the sunorb scenario in the upper panels, for the korb scenario in the middle panels and for the forb scenario in the lower panels. In the left panels the pressure scale is linear in the right panels logarithmic.

Figure 9.13 shows the zonal mean specific humidity for northern hemispheric winter, for

the planet around the Sun in the upper panels, for the planet around the K-type star in the middle panels, and for the planet around the F-type star in the lower panels.

For the sunorb scenario the highest specific humidity of about 1.1% occurs for near surface equatorial regions, with little higher specific humidity in the southern summer hemispheres. Towards higher latitudes specific humidity decreases steeply .

For the korb scenario much higher specific humidities are obtained than for the sunorb scenario, reaching mass concentrations higher than 10% in the equatorial region near the surface. Specific humidities of 1% typical for the surface for the Earth occur much higher in the atmosphere, which can be inferred from the right panel of Fig. 9.13, where the water distribution is depicted over a logarithmic pressure scale. At these larger altitudes the concentrations are nearly constant over all latitudes. These high water vapor concentrations are caused by the coupling of the the water vapor feedback cycle and the NIR radiation of the star. Increased surface temperatures lead to an increased evaporation of water from the surface, increasing the amount of water in the atmosphere. This leads to a higher optical depth due to absorption by water. Since strong water absorption takes place in the infrared, near infrared stellar radiation and thermal infrared radiation originating at the surface and within the atmosphere are absorbed efficiently. This has been shown on the basis of the shortwave and thermal infrared fluxes in section 9.2. For the planet around the K-type star the water vapor feedback is enhanced due to the shift of the stellar spectrum towards longer wavelengths. Therefore, a small increase in water vapor leads to a larger climate effect for a planet around a K-type star than for a planet around the Sun, or hotter stars. The cycling of water vapor at high altitudes also contributes to these high concentrations (see sec. 9.4.3).

For the forb scenario specific humidity is lower than for the planet around the Sun. Maximum values of specific humidity are found in the summer equatorial regions, which have a maximum of about 0.5 %. As for the sunorb scenario water concentrations steeply decrease towards the poles. Due to the lower water vapor amount in the atmosphere the greenhouse effect becomes less efficient as has been shown in section 9.2.

9.4.2 Clouds

Clouds influence the climate of a planet by scattering and absorbing incident stellar radiation and absorbing outgoing thermal infrared radiation, as well as by releasing latent heat during their formation. The impact of clouds thereby depends on the cloud cover and the cloud properties, such as the composition (water droplets or ice crystals), on the particle sizes and crystal shapes, the thickness and on the temperature of the cloud. These properties are a strong function of various microphysical processes which act on very small temporal and spatial scales. It is usually impossible to resolve these small scales in a global climate model. Thus, they have to be included by using highly parametrized schemes, making the impact of clouds one of the major uncertainties in climate modeling (Houghton et al., 2001). Therefore, the results presented in this section strongly depend on the parametrization of the cloud microphysical processes, described in section 5.3.4 of the model description.
Table 9.3 summarizes the global annual mean cloud properties. For the korb scenario cloud cover is lower than for the planet around the Sun (sunorb) and it is higher for the

Table 9.3: Global mean annual mean cloud properties for planets around different stars

scenario	cloud cover (%)	cloud water column ($\frac{kg}{m^2}$)	cloud ice column ($\frac{kg}{m^2}$)
sunorb	70	0.106	0.029
korb	67	0.203	0.028
forb	74	0.107	0.036

planet around the F-type star (forb). Both the korb and the forb scenario show a larger cloud water column than the planet around the Sun. The planet around the F-type star holds more cloud ice than the planet around the Sun and the planet around the K-type star has less vertically integrated cloud ice. To infer the impact of these changed cloud particle amounts it is necessary to evaluate their distribution in height and latitude. The effect of clouds has been studied for extrasolar planets around different types of stars (Kitzmann et al., 2010) showing that low level water droplet clouds lead to a net albedo effect and that high level ice clouds lead to a net greenhouse effect.

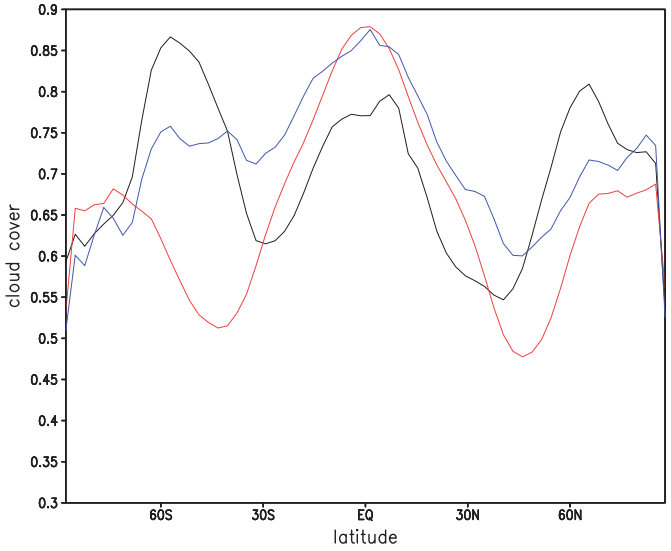

Figure 9.14: Zonal annual mean total cloud cover in fraction of the sky for the planets around different stars. Sunorb scenario in black, korb in red and forb in blue.

Total cloud cover

For the korb scenario the cloud cover increases at low latitudes but decreases at higher latitudes compared to the sunorb scenario (see Fig. 9.14), leading to a lower global mean cloud cover (see table 9.3). The cloud coverage maximum is at low latitudes, and weaker secondary maxima at high latitudes occur closer to the pole than for the sunorb scenario. This can be explained by the difference in tropospheric meridional circulation (Fig. 9.10). Clouds often form due to updrafts, i.e. from ascending air. In between the Hadley cells occurs a strong updraft of air which causes the Intertropical Convergence Zone (ITCZ) on the Earth. At higher latitudes updrafts can be found at the boundaries between the Polar and the Ferrel cell. The latter boundary is shifted towards higher latitudes for the planet around the K-type star and the cells are rather weak in comparison to the sunorb

scenario (see sec. 9.3). This agrees with the cloud cover distribution over latitudes shown in Fig. 9.15 and 9.16.

For the forb scenario the cloud cover is larger than for the planet around the Sun at low latitudes and lower at high latitudes. The highest cloud coverages are obtained at low latitudes for the forb scenario, secondary maxima in cloud coverage can be found at high latitudes. Whereas in the northern hemisphere the secondary maximum is found at higher latitudes than for the sunorb scenario, and at similar latitudes in the southern hemisphere.

Cloud water distribution

Figure 9.15 shows the zonal distribution of cloud water (in kg/kg of cloud water to dry air) for the planets around different types of stars. The planet around the Sun is depicted in the upper panels, the planet around the K-type star in the middle panels, and the planet around the F-type star in the lower panels. The left panels have a linear vertical pressure scale whereas the right ones show the distribution over a logarithmic pressure scale.

For the planet around the Sun cloud water is found throughout the entire lower atmosphere with a thick cloud layer at pressures between 90000–100000 Pa (900–1000 hPa) at low and mid latitudes. Another region of high cloud water concentrations is present in the upper equatorial troposphere at pressures of about 50000 Pa. The lower cloud layer has a clear impact on the NIR heating rates in Fig. 9.5 at layer 36-37, which correspond to these pressures (see Tab. 5.2). The upper cloud water layer on the other hand, does not exhibit such an impact on the heating rates.

For the planet around the K-type star, cloud water fills the entire lower atmosphere, up to larger height as for the Sun (see middle panels of Fig. 9.15). A thick cloud layer is present at much smaller pressures, higher up in the atmosphere, than for the sunorb scenario and which spans over nearly all latitudes, but is especially strong over the equator. This layer is associated with a strong peak in the NIR heating rates (see Fig. 9.5 at layer 24 and 25) at pressures of about 10000-20000 Pa (100-200 hPa), which are the approximate pressures of the cloud top. Note that despite the higher mass concentrations for the korb scenarios at high altitudes, the vertically integrated cloud water column is less for the korb scenario than for the sunorb scenarios (see Tab. 9.3). This is because air densities are much smaller at the corresponding pressures.

For the forb scenario, a cloud layer with cloud water exists at approximately the same pressures as for the planet around the Sun. However, it is vertically more and zonally slightly less extended. It causes a peak in the global mean NIR heating rates at the same model layers as for the sunorb scenarios, the heating is weaker though.

Cloud ice distribution

Figure 9.16 shows the zonal distribution of cloud ice particles for the three scenarios. In general, the ice clouds appear at smaller pressures than water clouds. This results from the fact that temperatures have to be near the freezing point of water for the formation of ice crystals.

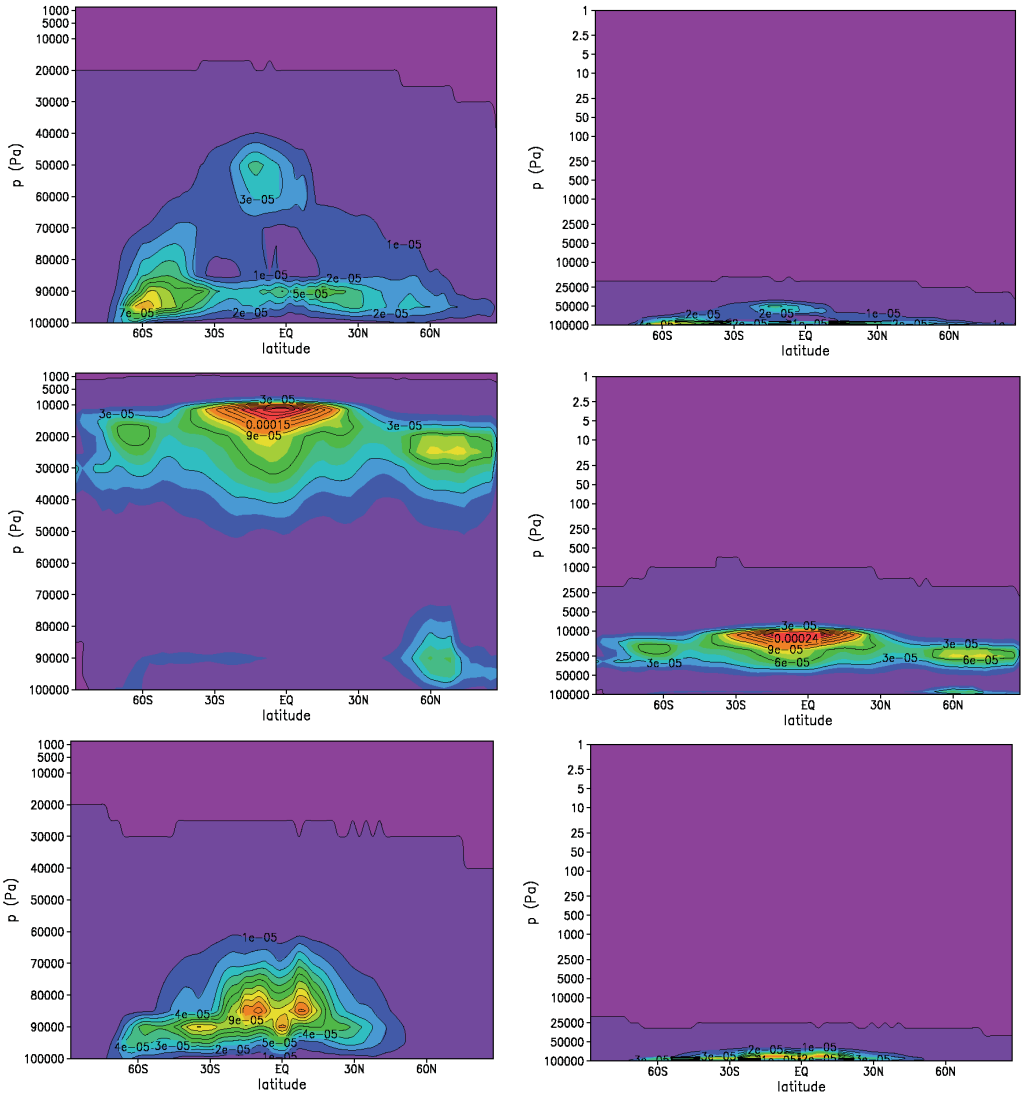

Figure 9.15: Zonal mean cloud water distribution for planets around different stars in NHW. Results for the sunorb scenario in the upper panels, for the korb scenario in the middle panels and for the forb scenario in the lower panels. In the left panels the pressure scale is linear in the right panels logarithmic.

For the sunorb scenario (upper panels) vertically spanning regions with cloud ice are present at latitudes of about 60°, which corresponds to the region of updrafts between the Ferrel and Polar cells. A cloud layer at pressures between 30000 and 40000 Pa in the upper troposphere is found, which spanning over all latitudes.

For the korb scenario cloud ice is only found at pressures smaller than about 10000 Pa, because of the high temperatures in the lower atmosphere which inhibit the formation of ice. The middle atmosphere, however, is entirely filled with ice particles. This is possible, since for the planet around the K-type star the temperature inversion in the stratosphere is absent. Such an inversion usually weakens the convective transport of water vapor and the high temperatures prevent the formation of ice crystals. This large amount of ice clouds leads to heating by absorption of NIR and thermal infrared radiation as can be inferred from Fig. 9.5.

The planet around the F-type star has a similar distribution of cloud ice as the planet around the Sun. Large cloud ice concentrations appear at higher pressures, due to lower temperatures in the lower troposphere, allowing for ice formation. The formation of a cloud ice layer at altitudes lower than for the planet around the Sun is also caused by the smaller water vapor concentrations and weaker convection.

9.4.3 Precipitation

Figure 9.17 shows the zonal annual mean rainfall (left), including large scale and convective precipitation, and snowfall (right panel) for the three scenarios.

For the sunorb scenario rainfall is strongest at low latitudes and secondary maxima occur at latitudes of about 60°. These are associated with upward vertical winds, as can be inferred from the tropospheric circulation (Fig. 9.10). The highest amount of snowfall occurs at high latitudes associated with the vertically extended region of cloud ice (see Fig. 9.16).

For the korb scenario rainfall intensifies. Maximum precipitation occurs at high latitudes, poleward of 60°. Despite the high cloud ice amount no snowfall occurs at the surface. This is caused by the high temperatures in the lower atmosphere which leads to melting and sublimation of falling cloud ice particles.

For the forb scenario rain and snowfall is smaller than for the planet around the Sun, because of the low water vapor amount in the atmosphere (see Table 9.4). An increase in rainfall for higher latitudes relative to the equatorial region is absent for the forb scenarios. Snowfall, however, is present for lower latitudes than for the Sun due to the lower temperatures.

Formation and destruction of precipitation

Due to the high water vapor, cloud water and cloud ice concentrations precipitation is expected to be strongly enhanced for the korb scenario. As the upper panels of Fig. 9.18 indicates, rain and snow fall increase for this scenario and originate at smaller pressures,

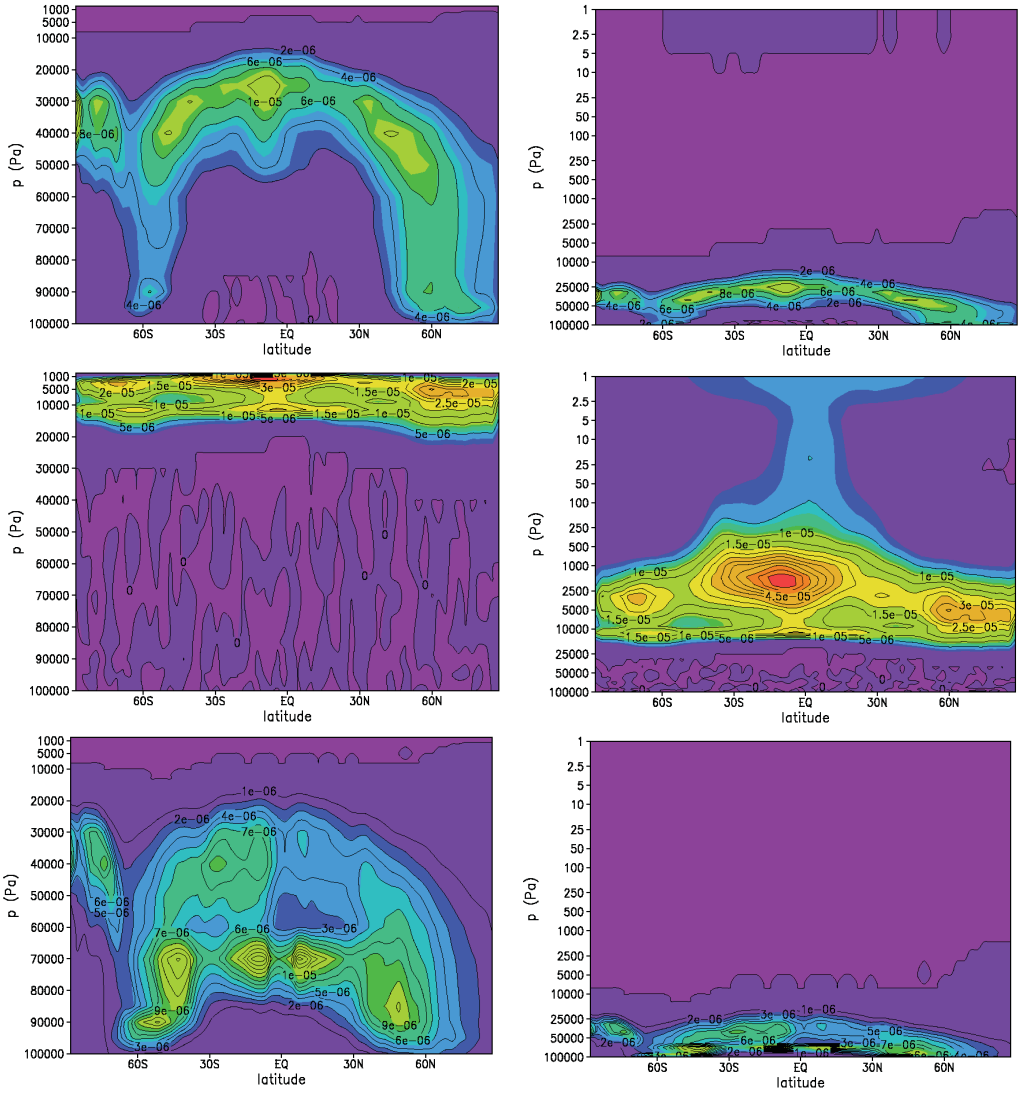

Figure 9.16: Zonal mean cloud ice distribution for planets around different stars in NHW. Results for the sunorb scenario in the upper panels, for the korb scenario in the middle panels and for the forb scenario in the lower panels. In the left panels the pressure scale is linear in the right panels logarithmic.

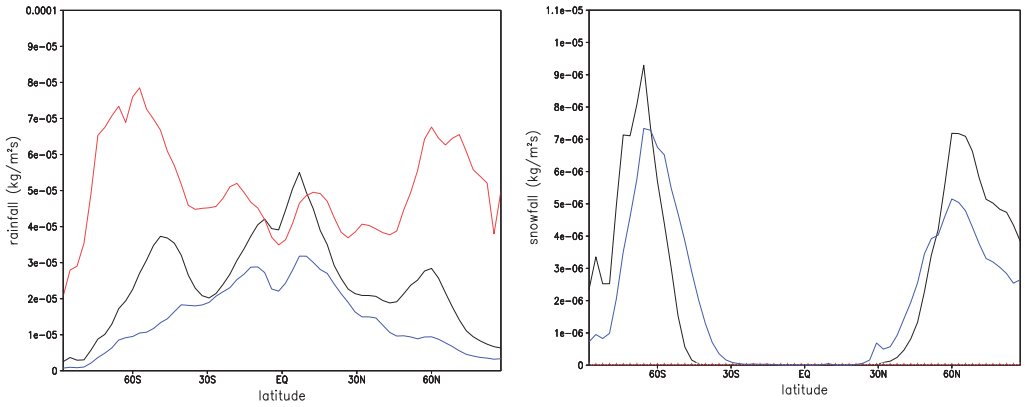

Figure 9.17: Zonal annual mean precipitation ($\frac{kg}{m^2 s}$) for planets around different stars. Left panel shows rainfall (large scale and convective), right panel snow fall. Sunorb scenario in black, korb in red and forb in blue.

Table 9.4: Global annual mean water amounts and precipitation for planets around different stars

scenario	specific humidity (kg/kg %)	water column $\frac{kg}{m^2}$	rainfall $\frac{kg}{m^2 s}$	snowfall $\frac{kg}{m^2 s}$
sunorb	0.90	30.1	2.9e-05	1.35e-06
korb	9.64	482.6	4.9e-05	0
forb	0.36	10.7	1.8e-05	1.5e-06

since cloud layers form at larger heights for the planet around the K-type star (see also Fig. 9.15 and 9.16). However, a large fraction of the precipitation is evaporated, melted or sublimated already at large heights. This can be inferred from the decrease in rainfall towards lower heights which is reduced to about half of its maximum value at larger heights. The effect on the snowfall is even larger leading to an absence of snowfall at the surface. This is caused by melting and sublimation of icy particles due to the high atmospheric temperatures. In the lower panels of Fig. 9.18 the formation and destruction of precipitation is shown. Precipitation forms within the cloud layers as expected, with large amounts of snow for the korb scenario. However, within the cloud layer a part of the snow sublimates and the rest melts (not shown) and is converted into rainfall. Rain formation takes places at lower heights than snowfall as may be noticed in the left lower panel of Fig. 9.18. It is partly evaporated when reaching the cloud free lower part of the atmosphere which leads to the reduction in rainfall. These processes lead to cycling of water compounds in the upper atmosphere preventing a reduction of water vapor at larger altitudes.

For the sunorb and forb scenario these processes are also important. However, in contrast to the korb scenario rain and snowfall originate at lower heights, due to lower cloud layers. Because of the shorter paths and lower atmospheric temperatures the precipitation is not reduced as strongly as for the korb scenario. This allows snowfall to reach the surface in these two scenarios. For the planet around the F-type star snow and rain formation are weaker than for the sunorb scenario, because of the lower water vapor content and the subsequent decrease in snow and rain formation.

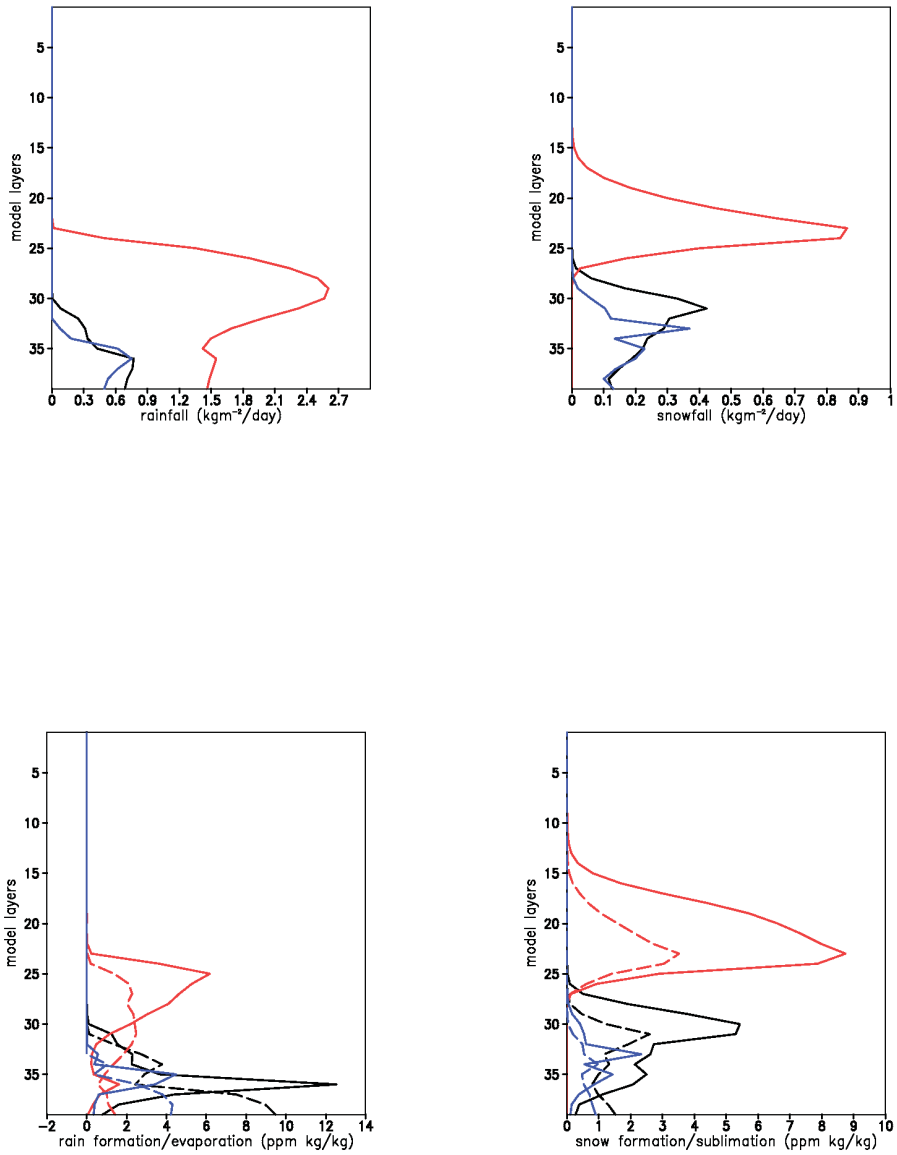

Figure 9.18: Global annual mean rain/snowfall, formation, evaporation and sublimation for planets around different stars. Upper panels show the vertical rainfall (left) and vertical snowfall profile (right) in $\frac{kg}{m^2 day}$. The lower left panel shows rain formation (solid lines) and rain evaporation (dashed lines), the lower right panel snow formation (solid lines) and sublimation (dashed lines) in ppm kg/kg. Sunorb scenario in black, korb in red and forb in blue.

Table 9.5: Global annual mean surface properties for planets around different stars.

scenario	albedo	sea ice concentration (%)	sea ice thickness (m)	snow depth (m)
sunorb	0.15	3.9	0.04	0.0039
korb	0.10	0.0	0	0
forb	0.19	10.0	0.19	0.0037

9.5 Surface response and albedo feedback for planets around different types of central stars

The response of the surface for the planets around different types of stars is discussed in this section, since for lower temperatures sea ice may build up causing an albedo feedback with decreasing surface temperatures due to an increase in surface albedo. A higher surface albedo leads to an increase in reflection of starlight at the surface, hence less absorption and thereby to even lower surface temperatures.

Table 9.5 summarizes the global annual mean response of the surface for the planets around the different types of stars. As may be expected the surface albedo is lower for the planet around the K-type star and higher for the planet around the F-type star. This albedo change is mainly caused by the change in sea ice concentration and sea ice thickness, as will be discussed.

Fig. 9.19 shows the zonal annual mean surface properties for the planet around the different types of stars, the surface albedo (upper left), the snow depth (upper right), the sea ice concentration (lower left) and the sea ice thickness (lower right).

At low and mid latitudes the albedo is the same for all scenarios, corresponding to the background surface albedo map (see section 7.2.3.2). At higher latitudes the albedo differs depending on snow and ice coverage. The highest albedos occur for the forb scenario at the north pole, which is a result of strong build up of sea ice with sea ice thicknesses up to 14 m, see lower right panel of Fig. 9.19. In the southern hemisphere highest albedos occur also for the forb scenario at latitudes, where sea ice is present. Over the south pole, however, the sunorb scenario shows a higher albedo than the planet around the F-type star. This is caused by a thick layer of snow (see upper right panel of Fig. 9.19), which does not build up for the forb scenario, due to the low humidity. The build up of sea ice in the southern hemisphere is damped due to a constant heat flux of 20 Wm^{-2} in the sea ice model (see section 5.3.8).

For the planet around the K-type star no sea ice or snow is present, leading to a low surface albedo, which is equal to the background surface albedo map. For the planet around the K-type star the complete melting of sea ice and snow leads to the lowest surface albedo, hence no further warming by the albedo feedback is possible. An effect that may be interesting to study is the wavelength dependence of the surface albedo. Here, a mean surface albedo over all wavelengths is used.
For the planet around the F-type star the albedo feedback causes an increase in surface albedo due to buildup of sea ice. Despite the fact that also water vapor concentrations are low, hence the greenhouse effect of water is less than for the planet around the Sun, the

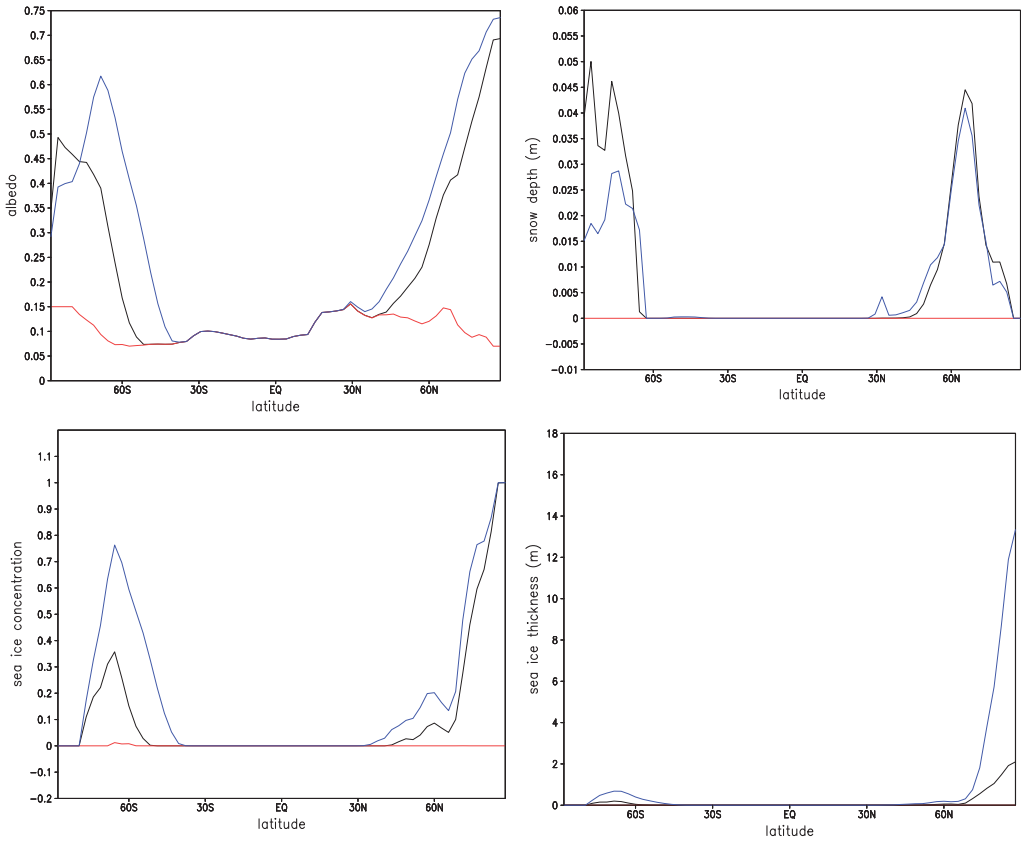

Figure 9.19: Zonal annual mean surface properties for planets around different stars. The upper left panel depicts the surface albedo, the upper right the snow depth in m. The lower panels show the sea ice concentrations as a fraction of sea cover and the lower right the sea ice thickness in m. Sunorb scenario in black, korb in red and forb in blue.

increase in surface albedo stops before runaway glaciation sets in. This results from the greenhouse effect of other greenhouse gases such as carbon dioxide and methane, which have been set to constant values for all scenarios. This leads to a colder but stable climate with habitable conditions occurring at low and most of the mid latitudes.

Note that the sea ice concentrations and sea ice depth depend on the heat flux (q-flux) included in the ocean model. A more sophisticated ocean model or a parameter study with the MLO model are needed for more robust results. The impact of the higher surface background albedo on the global mean temperature has been tested for the F-type star (not shown), which did however not exhibit any significant change.

9.6 Discussion of 3D modeling results

In the above sections the results of the 3D model have been presented for planets around different types of stars. In this section the main findings are summarized and implications for the habitability and the influence of feedback cycles are discussed.

Earth-like planet around an F-type star

For an Earth-like planet around an F-type star it has been found that surface temperatures decrease to an average global mean temperature of 275 K, only slightly above the melting point of water. The local surface temperatures averaged over the orbital period (Fig. 9.2 in section 9.1) show that the low and part of the mid latitudes are however ice free with temperatures above the freezing point of water, hence habitable conditions can be found at those latitudes (see sec. 9.1).

The lower temperatures are a result of various processes. An initial decrease in tropospheric and surface temperatures is caused by the enhanced Rayleigh scattering of stellar light and less absorption in the NIR, since an F-type star emits at shorter wavelengths than the Sun. This decrease in temperature triggers important positive feedback processes, such as the water vapor and the albedo feedback. By the decrease in temperature less water is evaporated from the surface, hence less water vapor is present in the atmosphere, as has been discussed in section 9.4. This leads to less heating of the lower atmosphere by the greenhouse effect (see section 9.2), hence even lower surface temperature are obtained.

At the surface the low temperatures trigger the build up of sea ice, which extends to lower latitudes than for the planet around the Sun (see section 9.5). The decrease in temperature is however limited due to the greenhouse effect of other gases such as carbon dioxide and methane which are set to constant values and by the amount of the incident stellar irradiation.

In addition to the water vapor feedback and the albedo feedback, a positive cloud feedback seems to be obtained as well. Water clouds form at lower heights for the forb scenario than for the planet around the Sun. Ice clouds are present but appear at lower heights than for the planet around the Sun, not causing any heating by absorption of stellar NIR radiation. The occurrence of ice clouds at low heights can be explained by less water vapor in the atmosphere due to weaker convection and the strong stratospheric temperature inversion, which is obtained due to increased absorption by ozone. It may be argued that the thicker low level water clouds scatter more radiation causing a net albedo effect, since the greenhouse effect of the ice clouds is rather low (see sec. 9.2). However, this should be analyzed in more detail in future, by using different cloud and convection parametrization, since different parametrization might lead to different cloud properties and radiative cloud forcing.

Earth-like planet around a K-type star

For an Earth-like planet around a K-type star, which receives the same amount of energy as the Earth from the Sun, surface temperatures are found to be much higher, with global mean temperatures of about 335 K. Locally mean land surface temperatures as high as 360 K are obtained, which are however still below the boiling point of water and well below the critical point of water 647 K, which is a hard limit for habitability. Therefore, despite the large increase of temperatures also this scenario leads to habitable surface conditions.

This large increase in surface temperatures is triggered by the stellar spectral energy distribution. A K-type star is cooler than the Sun, and has a red shift of the stellar spectrum.

Thereby for the same amount of total energy at top of the atmosphere, stronger heating of the lower atmosphere and the surface is obtained by less Rayleigh-scattering of the incident radiation and more absorption in the NIR by the lower atmosphere.

This increase causes stronger evaporation of water from the planetary surface, which enhances the optical depth at infrared wavelengths. This leads to an amplification of the temperature response due to a stronger greenhouse effect, known as the water vapor feedback cycle. In addition to this, due to the redshift of the stellar spectrum, the water vapor feedback is intensified since more near infrared radiation is present, which is absorbed by the water vapor in the atmosphere as has been shown in section 9.2. The amount of water vapor in the atmosphere thereby increases to a total water vapor column, which is about ten times larger than for the planet around the Sun. Despite the fact that cloud water and ice builds up, which precipitate, the cycling of water between the atmosphere and the surface is not efficient. A large part of the precipitation does not reach the surface since it is trapped in the upper atmosphere by the high temperatures. This "heat trap" leads to nearly constant water vapor concentrations over all latitudes at large heights (see section 9.4). The temperature structure for the planet around the K-type star changes (see sec. 9.1), the stratospheric temperature inversion disappears, due to less radiation at wavelengths where ozone absorbs, and the equatorial cold trap vanishes. Thereby upward transport of water due to convection is more effective.

The high amounts of water vapor in the upper atmosphere may lead to a loss of water to space by photodissociation of water molecules and subsequent atmospheric escape of hydrogen. Kasting et al. (1993) discussed that a stratospheric water vapor mixing ratio of 10^{-3} may lead to the loss of an entire Earth ocean (270 bar of water) during the current life time of the Earth (4.5 Gyrs). This value was calculated by including the solar radiation leading to photodissociation of water molecules and a diffusion limited vertical transport of hydrogen molecules. Water photodissociation occurs mostly via far UV radiation. Despite the fact that the K-type emits less radiation at visible wavelengths in comparison to the Sun, the sample K-type star used for this study emits more energy at far UV wavelengths than the Sun (see spectra in section 7.1), hence photodissociation of water could be possible for this stellar energy flux and might be even more efficient.
Fig. 9.20 shows the volume mixing ratio of water for the planets around the different stars. As can be seen the mixing ratio of water is much higher for the korb scenario in the upper atmosphere, as has been discussed in sec. 9.4. The upper atmospheric mixing ratio is not higher than the critical value suggested by Kasting et al. (1993), which is indicated by the dashed vertical line in Fig. 9.20. It is however not possible to directly compare the upper atmospheric water mixing ratios with the stratospheric mixing ratios Kasting et al. (1993) obtain, since they set the water mixing ratio to a constant value above the cold trap, while with the 3D model the water mixing ratios are calculated by transport in this regime. Since water mixing ratios are nevertheless high and the stellar flux at far UV wavelengths is higher than for the Sun, water loss may still occur. In order to estimate the actual loss of water from the atmosphere, photodissociation of water and its impact on the atmospheric chemistry as well as the atmospheric escape need to be taken into account, but this is beyond the scope of this thesis.

For this scenario also the atmospheric dynamics change drastically, see sec. 9.3. Typical zonal wind patterns as for the Earth around the Sun in the middle atmosphere are absent

due to the change in the temperature structure. Also the meridional circulation is altered. The change in the middle atmospheric meridional circulation, leading to a transport barrier between the summer and the winter hemisphere may be of importance especially for the transport and photochemistry of ozone.

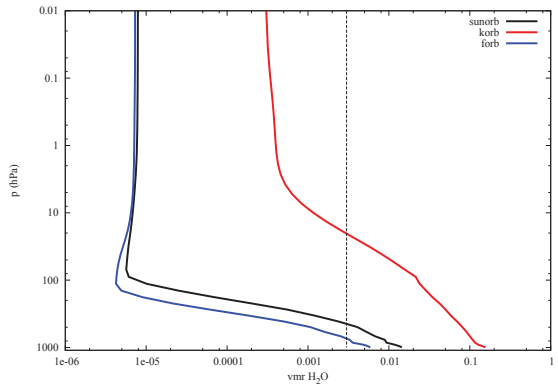

Figure 9.20: Global annual mean water vapor mixing ratio for the Earth-like planets around other types of stars, sunorb scenario in black, korb in red and forb in blue. The vertical black line indicates the stratospheric water vapor mixing ratio, which may lead to water loss for solar irradiation as calculated by Kasting et al. (1993).

The higher surface temperatures for the korb scenario trigger the positive albedo feedback process which leads to complete melting of sea ice and snow. Once all surface ice is melted, the albedo feedback stops and no further amplification of the warming is possible via this mechanism.

The cloud response for the planet around the K-type star suggests, that also for this scenario clouds rather act as a positive than as a negative feedback amplifying the temperatures response. Due to the changed temperature structure thick ice clouds build up at large heights, which efficiently absorb thermal infrared radiation from the lower atmosphere, increasing the greenhouse effect as has been shown in section 9.2. However as for the planet around the F-type star, since cloud feedbacks vary strongly depending on the parametrization in use in the 3D model, a more detailed study evaluating the cloud response for different cloud schemes would be needed.

9.7 Summary

In this chapter the results of 3D climate modeling of Earth-like planets around different types of stars has been discussed. It has been argued that different stellar spectral distributions may cause very different climate states of an Earth-like planet despite the fact that the total amount of stellar energy is the same at the top of the atmosphere for the studied scenarios. This results from the wavelength-dependent absorption and scattering properties of the atmosphere.

The initial temperature difference due to the different stellar radiations is further amplified by the albedo and the water vapor feedback process. It has been found that for the planet

around the K-type star the water vapor feedback is intensified by the absorption of NIR stellar radiation by water vapor.

Furthermore, the change in cloud properties suggests that clouds also lead to a positive feedback, intensifying the temperature response.

For both scenarios however the Earth-like planet shows habitable surface conditions.

The planet around the K-type star may experience water loss due to the high water vapor concentrations in the upper atmosphere, and enough stellar radiation for water dissociation. Hence, an Earth-like planet around a K-type star which receives the same total amount of energy as the Sun may not stay habitable over a long time period.

CHAPTER 10

Influence of orbital period upon the climate for planets around different types of central stars

This chapter shortly discusses the influence of the orbital period and the different model setups for the planets around different types of stars upon the climatic response is briefly discussed. For the Earth-like planets around different types of stars the orbital period has been changed, since to receive the same total amount of energy from the star, a planet around a K-type star has to be situated closer to its star, and a planet around an F-type star has to be further away.

As has been shown in Chapter 8 the different model setups (e.g. changing the albedo map or the oceanic q-fluxes) resulted in small changes in the climatic response for the Earth-like planet around the Sun, which are rather insignificant for the investigation of the habitability of extrasolar planets. The difference in orbital period may however have a larger impact due to longer or shorter seasons. The model scenarios compared in this chapter are summarized in Table 10.1.

Table 10.1: Scenarios of Earth-like planets around different stars

Scenario	Star	ocean	q-fluxes	albedo map	orbital period
sunmlo	Sun	mixed layer ocean	q-flux1	high	1 Earth year
kmloalb	K-Star	mixed layer ocean	q-flux1	low	1 Earth year
fmlo	F-Star	mixed layer ocean	q-flux1	low	1 Earth year
sunorb	Sun	mixed layer ocean	q-flux2	low	1 Earth year
korb	K-Star	mixed layer ocean	q-flux2	low	184 days
forb	F-Star	mixed layer ocean	q-flux2	low	450 days
sunorbmq	Sun	mixed layer ocean	q-flux3	low	1 Earth year
korbmq	K-Star	mixed layer ocean	q-flux3	low	184 days
forbmq	F-Star	mixed layer ocean	q-flux3	low	450 days

10.1 2m temperature

The 2m temperature is important quantity when evaluating the habitability of a planet. Fig. 10.1 shows the variation of the 2m temperature over 3 model years (in Earth years) for the planets around the different types of stars. The temperatures for all scenarios show maximum differences of about 5 K with season or model setup, which are comparably small in comparison to the general temperature response. Note that results shown are monthly means for the sunmlo, kmloalb and fmlo scenario and daily means for the other six.

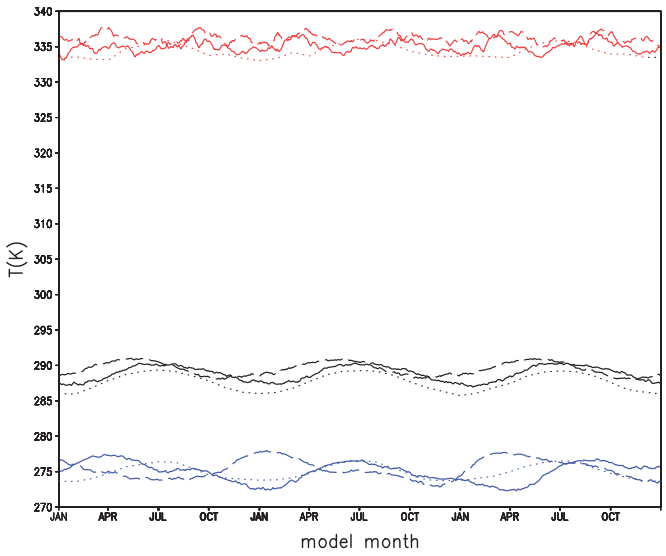

Figure 10.1: Orbital variation of the global mean 2m temperature for planets around different stars. Sun: black, K-type star: red, F-type star: blue. Scenarios with a change in orbital period are shown in solid lines: sunorb, korb, forb scenarios and dashed lines: sunorbmq, korbmq, forbmq. Dotted lines show scenarios with Earth orbit: sunmlo, kmloalb, fmlo.

The sunorb (solid black line) and the sunmlo (dotted black line) show a similar change in the 2m temperature with season. Highest temperatures occur in northern hemispheric summer (July) and lowest temperatures in northern hemispheric winter (January). This is caused by the larger amount of land mass at mid latitudes in the northern hemisphere, which heat and cool faster than the sea. The largest change in seasonal variability arises from the change in the oceanic q-fluxes, which is visible in the sunorbmq scenario (black dashed line). For this scenario the highest temperatures occur at an earlier time around May or June. Hence, the ocean heats up faster, if monthly mean q-fluxes are applied. For the sunorbmq scenarios, overall the 2m temperature is higher, as has also been discussed in Chapter 8.

Nevertheless, highest temperatures occur around spring and summer time in the northern hemisphere which also holds for the planets around other stars, probably because the continental setup was not changed.

For the planets around the F-type star a change in lengths of period is clearly visible in dashed and solid line compared to dotted line with 1 Earth year orbit. Note that the same

seasons do not occur at the same time due to the different lengths of the year. Northern hemispheric summer temperatures are always at maximum. The temperature difference between global mean maximum and minimum slightly increases for a larger orbital period. While for the fmlo scenario the 2m temperature varies by about 3 K over an orbital period, it varies by about 4–5 K for a longer orbital period.

For the planet around the K-type star the variation of the 2m temperature is much larger, which is due to the high amount of water vapor which varies strongly over time (see Fig. 10.2). A slight overall increase in the 2m temperature can be inferred for the korbmq scenario, hence for monthly mean q-fluxes. This was also shown for the planet around the Sun (see Chapter 8).

The overall effect of introducing another orbital period is small. However, this may be different for other oceanic q-fluxes or for including the effect of photochemistry.

10.2 Water vapor column

The amount of water vapor in an atmosphere influences planetary climate via the greenhouse effect and absorption of NIR radiation and latent heat release during condensation. Therefore, here the change in the integrated water vapor column over the orbital period for the planets around the different types of stars is discussed.

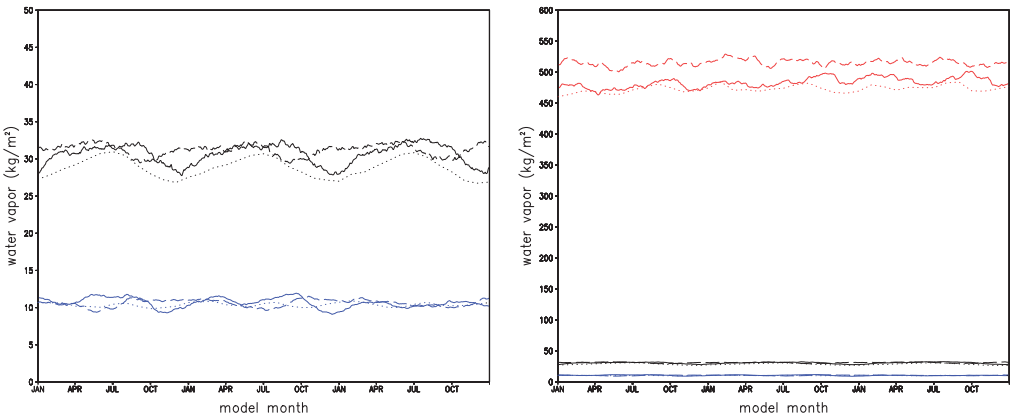

Figure 10.2: Orbital variation of the global mean integrated water vapor for planets around different stars. Left: only Sun and F-type star, right: all scenarios. Sun: black, K-type star: red, F-type star: blue. Scenarios with a change in orbital period are shown in solid lines: sunorb, korb, forb scenarios and dashed lines: sunorbmq, korbmq, forbmq. Dotted lines show scenarios with Earth orbit: sunmlo, kmloalb, fmlo.

Fig. 10.2 shows the integrated water vapor column for the different scenarios.
For the scenarios with solar radiation (see black lines in left panel of Fig. 10.2) highest water vapor columns corresponds to the highest 2m temperatures. Hence for the sunmlo and the sunorb scenario highest water vapor columns are found during northern hemispheric summer and lower amounts are obtained for northern hemispheric winter. For the sunorbmq scenario the maximum in 2m temperatures was shifted to May/June, hence for this scenario also the maximum and minimum amount of water vapor occur at an earlier

time during one orbital period. This is caused by the monthly mean q-flux assumed. Due to the small increase in temperatures for the sunorbmq scenario, also the water vapor column is slightly larger.

For the scenarios with F-type stellar radiation (blue lines in the left panel of Fig. 10.2) the water vapor column amount is less variable than for the planets around the Sun. This is due to the lower temperatures in these scenarios, which lead to less evaporation of water vapor. Even for similarly varying 2m temperatures for the planets around the F-type star and the Sun, less variability of the water vapor column arises due to less seasonally varying evaporation.

For the planets around the K-type star (red lines in the right panel of Fig. 10.2) a larger variability of the vertically integrated water vapor amount is found in comparison to the planets around the Sun or the F-type star. Seasons are not well identifiable, since water vapor concentrations are similar at all latitudes as has been shown in Chapter 9. Therefore, it can be expected that the influence of the q-fluxes is small. To verify this, however, a detailed parameter study is needed (see Chapter 13), but this is beyond the scope of this thesis.

10.3 Surface albedo and sea ice

The surface albedo determines how much stellar light is reflected or absorbed at the planetary surface, therefore it is an important surface property determining the habitability of a planet. For the Earth its variation is mainly determined by build up and melting of sea ice.

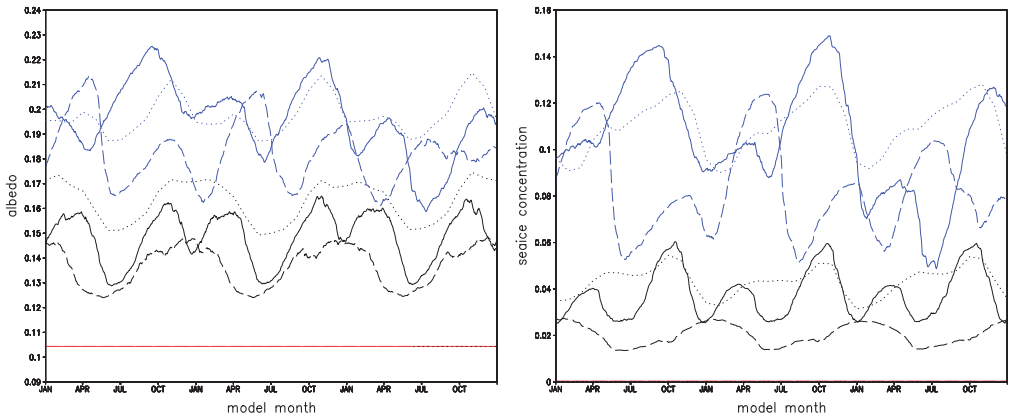

Figure 10.3: Orbital variation of the global mean surface albedo (left) and sea ice concentration relative to ocean (right) for planets around different stars. Sun: black, K-type star: red, F-type star: blue. Scenarios with a change in orbital period are shown in solid lines: sunorb, korb, forb scenarios and dashed lines: sunorbmq, korbmq, forbmq. Dotted lines show scenarios with Earth orbit: sunmlo, kmloalb, fmlo.

In Fig. 10.3 the global mean surface albedo (left) and the sea ice concentrations (right) are shown for the different scenarios.

For the planets around the Sun (black lines) the highest global mean albedo is found for the sunmlo scenario, since here the high albedo map is used. Lowest surface albedos are found for northern hemispheric summer, despite the build up of sea ice in the southern hemispheric winter. Highest surface albedos are obtained for northern hemispheric winter due to build up of snow over the Arctic ice cover. The lowest global mean sea ice concentrations are obtained for north hemispheric winter, where the global mean surface albedo is highest.

For the sunorb scenario a double peak in surface albedo occurs in north hemispheric winter due to a lower albedo of Antarctica. This is caused by the low albedo map and subsequent higher temperatures in this region, which lead to melting of sea ice and snow. This can be inferred from the little lower sea ice concentrations in northern hemispheric winter compared to the sunmlo scenario (see right panel of Fig. 10.3). For the sunorb scenario lower sea ice concentrations are obtained in northern hemispheric summer, which suggests that large parts of the north polar ice cap melt during polar summer.

For the sunorbmq scenario the highest albedo is again obtained for northern hemispheric winter. The seasonality of the surface albedo is similar to that of the sunmlo scenario, however the global mean albedo and its variations are generally lower. The highest sea ice concentrations now occur for north hemispheric winter, suggesting that less sea ice builds up in the southern hemisphere during winter. This can be understood from the generally higher temperatures globally and in this region, as was shown in Chapter 8.
For the planets around the F-type star (shown in blue) the variation of the global surface albedo increases for changing the orbital periods. Since winter and summer periods are longer for a 450 day orbit sea ice build up effectively. The largest global mean surface albedo is obtained for northern hemispheric winter as for solar radiation, which corresponds to build up of sea ice in the north polar region, since snow fall is only weak due to the low amounts of water in the atmosphere. The model results for the Earth-like extrasolar planet around the F-type star may be different when applying other q-fluxes, since they influence the build-up of sea ice.

For the planets around the K-type star since no sea ice nor snow is present at these high temperatures, no change in albedo occurs.

10.4 Summary

In this chapter the influence of the orbital period on the climatic response has been shortly discussed. The change in orbital period and model setup generally shows only a small impact on the temperatures near the surface. This may be different for other q-fluxes and should be investigated in detail by a future parameter study (see Chapter 13). Especially for the K-type star the influence of the orbital period and lower boundary is small, since the atmosphere is dominated by water vapor. For the scenarios of planets around the Sun and the F-type star the seasonality of the temperature stays the same, despite the fact that the seasonality in sea ice concentrations and albedo change. From an observational point of view it would be interesting to study the variability, especially of the surface albedo and the water vapor column in more detail. Note, however, that these results depend on the q-flux chosen for the MLO model. There influence may be inferred by a parameter study or by coupling an ocean circulation model.

CHAPTER 11

Comparison of 3D and 1D model results: Influence of dynamical processes

To further evaluate which influences dynamical processes have on the climate and whether their impact on the global mean state of the atmosphere can be captured with a 1D model, this chapter compares the results of the 3D model to those of the 1D model described in Chapter 5.
In the first section differences between the global mean temperature profile of the 3D model with fixed sea surface conditions and the 1D model are discussed for K-type stellar radiation (sec. 11.1). In Section 11.2 the the global mean temperature and water profiles for the planets around different stars, which were analyzed in detail in Chapter 9 are compared to results of the 1D model. Section 11.3 analyzes the influence of the relative humidity profile which is an input for the 1D model. 1D model results in this section were provided by Dr. B. Stracke and have been published in Stracke (2012).

11.1 Comparison of 3D and 1D model results for fixed sea surface conditions

In this section the results of the 3D and 1D model, described in Chapter 5, for an Earth-like planet irradiated with a normalized K-type stellar spectrum and a solar spectrum are compared for fixed sea surface conditions in the 3D model, in contrast to the model results shown in the previous Chapters, which included interactively calculated sea surface temperatures and sea ice. This has been done prior to the model calculations presented in the last Chapter to evaluate, whether the dynamical response is already large for fixed surface conditions. The Earth-like planet around the K-type star has been chosen, since for K-type stellar radiation 1D model studies revealed the largest change in the stratospheric temperature structure, such as a very weak stratospheric temperature inversion.

In this study the sea surface temperatures, sea ice concentrations and sea ice depth were prescribed from the AMIP II climatology (Taylor et al., 2000). The concentrations of the radiative gases are the same in both models, except for ozone and water. The 1D model uses a global annual mean ozone profile, while for the 3D model the climatology of Fortuin and Kelder (1998) is used, see also sec. 5.5. The concentrations of water vapor are

Scenario	Model	Stellar spectrum	bands in the sw radiation scheme
sunsst	3D	solar	52
k4sst	K-type star	solar	4
k52sst	3D	K-type star	52
Sun1D	1D	solar	38
K1D	1D	K-Star	38

Table 11.1: Model setups used for the 1D–3D model comparison for Earth-like planets around the Sun and the K-type star with fixed sea surface conditions.

calculated by both models. For the 1D model it is calculated from the temperature profile using a relative humidity profile of Manabe and Wetherald (1967), and in the 3D model by solving the continuity equation for water compounds. In the 1D model the surface albedo is fixed to 0.21, in order to obtain the global annual mean temperature of the Earth (288.1 K) under solar irradiation.

In addition, the impact of the resolution of the shortwave radiative transfer scheme in the 3D model was evaluated by using the two different shortwave radiation schemes available in EMAC (see sec. 5.3.2.1). For the 3D model scenario k4sst (see also Table 11.1) the standard radiation scheme with four bands covering a wavelength regime from 250 nm to 4 μm was utilized. For the other 3D model scenarios, with K-type stellar irradiation (k52sst) and solar irradiation (sunsst) the FUBRAD radiation scheme was applied, which calculated the shortwave heating rates for pressures smaller than 70 hPa in 52 bands ranging from 121.4 nm to 4 μm.

11.1.1 Comparison of the global annual mean temperature profiles

Fig. 11.1 shows the global annual mean temperature profiles for the 1D and 3D model calculations.
The model results obtained with the solar spectrum are shown in black (solid: 3D model, dash-dotted: 1D model), whereas the profiles for the K-type stellar spectrum are displayed in green. The 1D model result is indicted by the dashed line, the solid line shows 3D profiles for the K52sst, scenario and the dotted line the 3D model result for the K4sst scenario, respectively.

For the K-type stellar radiation the temperature profile changes drastically (compared to the result for solar irradiation) without showing any significant stratospheric temperature inversion for the 1D model result (green dash-dotted) and 3D model scenario with high spectral resolution in the shortwave radiative transfer (k52sst, solid green line). This is caused by the reduced stellar UV flux and has been found in previous 1D model calculations, e.g. by Segura et al. (2003).

In the case of solar radiation the differences between the 1D and 3D model results are smaller, yet discernible, such as different tropospheric lapse rates resulting from different treatments of convection, and therefore also different inversion heights. Nevertheless, stratospheric profiles agree well for pressures larger than 1 hPa, where the 1D model also re-

sembles the US-Standard-Atmosphere from 1976. The deviations for pressures smaller than 1 hPa originate from different vertical domains of the models and corresponding boundary conditions, such as the neglected downward infrared radiation at the top of the atmosphere, as well as from the missing absorption of far UV radiation by O_2 in the 1D model.

For both stellar flux distributions the stratospheric temperature profiles computed with the 1D model (dash-dotted) and the 3D model with the high resolution radiative scheme (solid) agree well up to about 1 hPa. The comparison of the standard radiation scheme in EMAC and FUBRAD for solar irradiation was presented in Nissen et al. (2007).

For the K-type stellar radiation, significant differences become obvious in the stratospheric temperature profiles for the 3D model calculations using different spectral resolutions. Since in the low resolution scheme (dotted), the UV and visible wavelength regime is represented by one band only, the stellar radiation is integrated over the whole band (see Fig. 7.2 in the scenario description). Therefore, spectral differences at wavelengths where ozone heating is important are not resolved and the low resolution scheme fails to produce realistic heating rates.

This clearly demonstrates that a radiation scheme with a sufficiently high spectral resolution is needed for investigations of the influence of the stellar spectral type upon atmospheric properties.

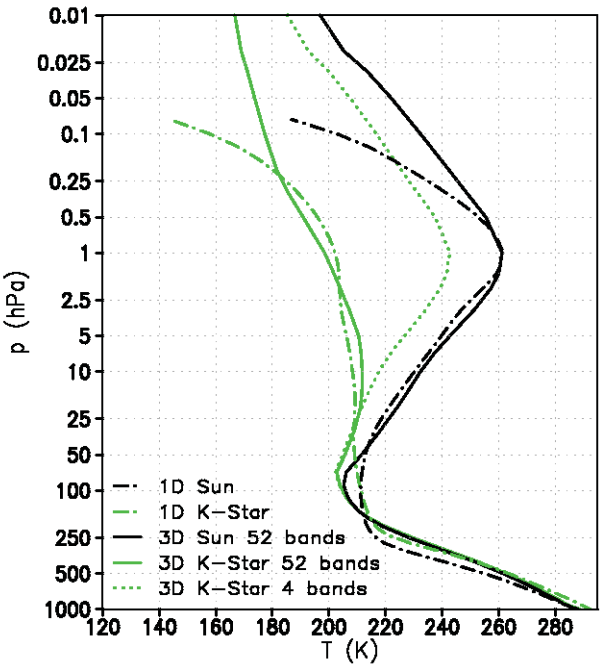

Figure 11.1: Global annual mean temperature profiles for an Earth-like exoplanet around a K-type star (green) in comparison to a planet around the Sun (black).

11.1.2 3D model results

Global annual mean temperature profiles of the 3D model agree well with these of the 1D model for a sufficiently high spectral resolution, despite the fact that the temperature structure and the stratospheric dynamics change for the K-type stellar spectrum as will be shown in this section.
Fig. 11.2 show the temperature structure (upper panels) and the corresponding zonal wind (middle panels) in January and the stratospheric mass stream function in northern hemispheric winter (lower panels) for the sunsst and the k52sst scenario.

Due to the prescribed sea surface conditions tropospheric temperatures do not show any noteworthy response to the changed stellar spectrum. However, the stratospheric temperature structure is strongly influenced. Comparing the summer temperature structures for the solar (upper left panel of Fig. 11.2) and the K-type radiation (upper right panel of Fig. 11.2) suggests that the stratopause is located at lower altitudes for the K-type radiation (at 10 hPa instead of 1 hPa). This region is about 50 K colder than in the solar case, which leads to an overall sinking of the atmosphere in the vertical.
The stratospheric temperature inversion in the winter hemisphere, which is a consequence of the Brewer-Dobson circulation is weak for the k52sst scenario, suggesting a weakening in meridional circulation.
Temperatures typical of Earth's lower stratosphere now appear nearly in the entire winter stratosphere for the K-type stellar irradiation.
The temperature in the lower winter stratosphere appears to be mostly similar for both scenarios, a result which has been found also in the 3D model results with interactive ocean (Chapter 9). It is a consequence of the missing stellar radiation during polar night.

In addition to overall decreasing stratospheric temperatures, the stratospheric meridional temperature gradient weakens for the K-type radiation, e.g. the temperature gradient between the stratospheric temperature maximum in summer and the equator is about 10 K smaller. This leads to reduced zonal wind speeds, as shown in the middle panels of Fig. 11.2.

For solar radiation (see left middle panel of Fig. 11.2) stratospheric jet streams in the winter hemisphere are usually westerly (denoted by positive values) and easterly in the summer hemisphere (denoted by negative wind speeds). Furthermore, the southern hemispheric jet stream is stronger compared to the northern hemisphere due to less deceleration by planetary waves, since the southern hemisphere has orography than the northern hemisphere.

For K-type radiation (Fig. 11.2 right middle panel) the stratospheric jet streams in the southern hemisphere decrease by approximately $30\,\frac{m}{s}$ and about $20\,\frac{m}{s}$ in the northern hemisphere compared to the sunsst scenario.
The maximum wind speeds in the summer hemispheres appear at nearly the same pressures around 0.1 hPa as for solar radiation, whereas in the winter hemisphere the wind maximum occurs at larger pressures for the K-type radiation. Additionally, due to the lower stratospheric temperatures for the K-type radiation, the atmosphere sinks in the vertical and zonal wind features similar to Earth's thermosphere appear at the upper model lid. For more reliable results in this region a model including processes relevant in the thermosphere would be required.

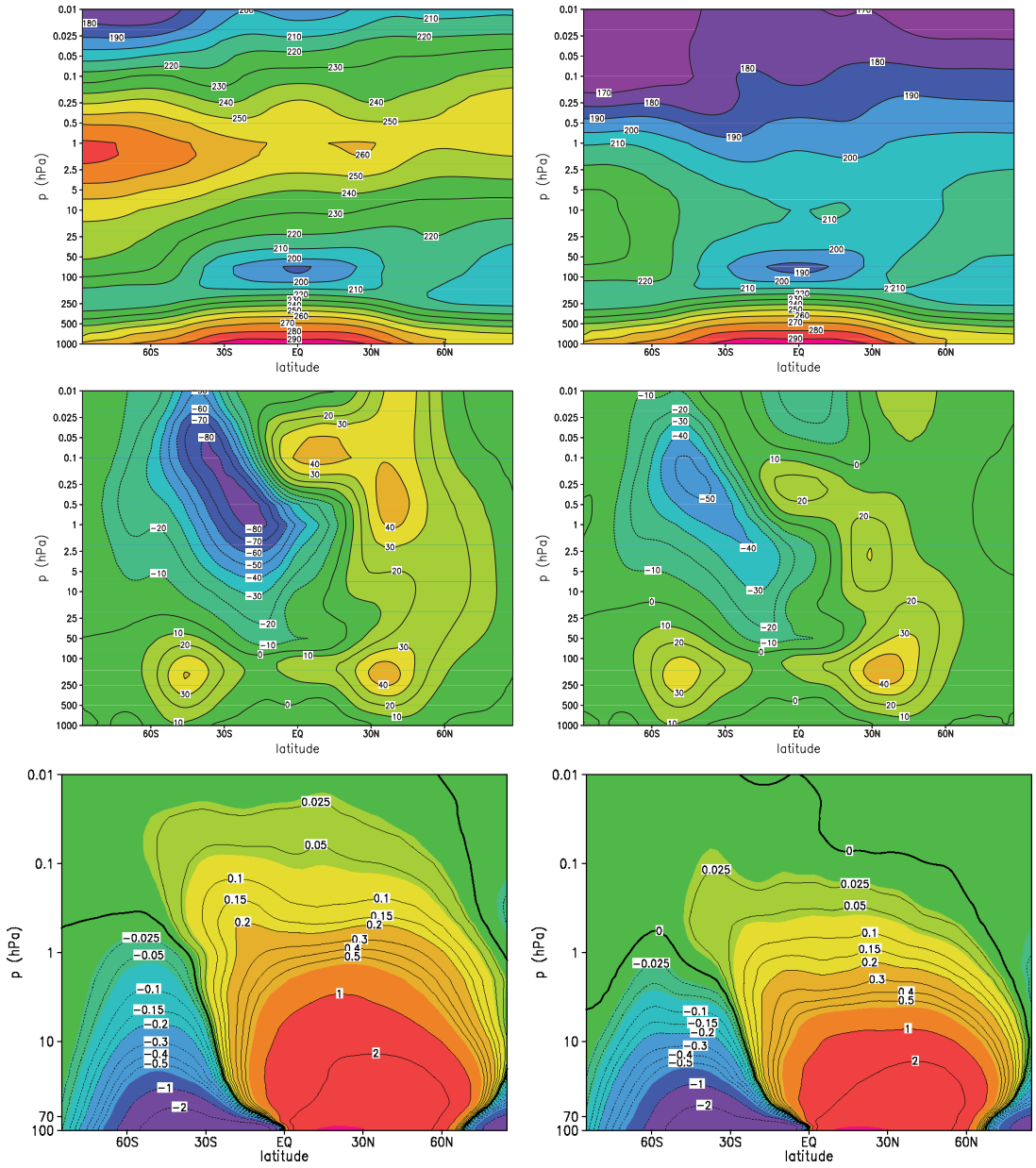

Figure 11.2: Zonal mean January temperatures in K (upper panels), and zonal wind in m/s (middle panels) for the sunsst (left) and the k52sst (right) scenario. Lower panels show the stratospheric mass stream function Ψ^* in $10^9 \frac{kg}{s}$ for northern hemispheric winter. For the zonal wind positive values indicate westerly winds. For the mass stream function positive values indicate clockwise circulation.

The stratospheric meridional circulation is presented in terms of the mass stream function in the lower panels of Fig. 11.2. The left panel shows again the result for solar radiation, where positive (negative) values correspond to clockwise (anti-clockwise) circulation. The stratospheric meridional circulation transports air from the summer to the winter hemisphere. The rising air in the summer hemisphere cools adiabatically and leads to a cold summer mesosphere, whereas the descending air in the winter hemisphere heats adiabatically causing the winter stratospheric temperature maximum, which is evident in the upper

left panel of Fig. 11.2.

For K-type radiation (right lower panel of Fig. 11.2) the strength of the mass stream function is approximately half of that of the sunsst scenario at pressures lower than 1 hPa compared to the solar radiation scenario. Hence, mass transport occurs at larger pressures and over a smaller vertical domain for the K-type radiation. Therefore, the descending air causes less adiabatic heating in the winter hemisphere, since temperature and pressure differences between descending and surrounding air are smaller (see upper right panel). Otherwise, the overall shape of the stratospheric circulation patterns for the K-type radiation is similar to that for solar radiation.

11.1.3 Summary of results for fixed sea surface conditions

A comparison of the global mean vertical temperature-pressure profiles of the 3D model calculations with the results of a 1D radiative-convective model suggests that global mean stratospheric profiles can indeed be approximated by a 1D model (see Fig. 11.2), although the analysis of the dynamical response revealed a weakening in zonal winds and in the meridional circulation in the case of the K-type stellar radiation.

Also, it has been shown that a sufficiently high spectral resolution in the UV and visible wavelengths range is required to resolve differences in the stellar radiation, hence, for calculating realistic heating rates for different types of stars. Consequently, high resolution radiative transfer schemes have to be applied whenever investigating responses to changes in stellar radiation.
The resulting temperature structure indicates that for K-type stellar radiation the stratospheric temperatures are lower compared to those for solar radiation due to lower radiation fluxes by the K-type star at wavelengths where ozone absorbs. The stellar energy distribution critically affects atmospheric temperatures, hence also atmospheric dynamics (hence possibly chemistry), and thereby planetary spectra.

This study was performed prior to the climate modeling with a mixed layer ocean also to verify that the effect of the different stellar flux distributions can be resolved by the 3D model. As a consequence all other model scenarios were carried out with the high resolution radiative transfer scheme FUBRAD.

11.2 Comparison of 1D and 3D climate modeling for planets around different types of stars with interactive ocean

In this section the global annual mean temperature and water vapor profiles for the Earth-like planets around different types of stars, which have been presented in detail in Chapter 9 are compared to those of the 1D radiative convective model. A summary of the model setups are found in Table 11.2.

The major differences in the models and the model setups are that in the 1D model, firstly, the surface albedo is fixed to a value of 0.21, in order to obtain the mean surface temperature of the Earth (288 K), while it is calculated interactively in the 3D model, by accounting for melting or build up of sea ice and snow.

Scenario	Model	Stellar spectrum	albedo	water profile
sunorb	3D	solar	calculated (0.15)	calculated
Sun1D	1D	solar	fixed 0.21	calculated with RH profile
korb	3D	K-Star	calculated (0.10)	calculated
K1D	1D	K-Star	fixed 0.21	calculated with RH profile
forb	3D	F-Star	calculated (0.19)	calculated
F1D	1D	F-Star	fixed 0.21	calculated with RH profile

Table 11.2: Model setups used for the 1D–3D model comparison for Earth-like planets around different stars.

Secondly, the water profile in the 1D model is calculated from the pressure, the saturation water vapor pressure and a vertical relative humidity profile from Manabe and Wetherald (1967) by $c_{H_2O}=\frac{p}{p_{sat}}RH$, whereas in the 3D model the water profile is calculated by the continuity equation for the specific humidity, which accounts e.g. for transport processes as well as phase changes.
Thirdly, in the 3D model radiative effects of cloud are included, but not in the 1D model. The reflectance of clouds is indirectly included in the 1D model by assuming a higher surface albedo. This however assumes that clouds around different planets will scatter the same amount of energy as they do for a planet around the Sun. A last mentionable point is that in the 1D model, the near surface temperature (at 1000 hPa) is calculated via convective adjustment of the lower atmosphere, while in the 3D model it is calculated from the balance of radiative, convective and sensible heat fluxes.

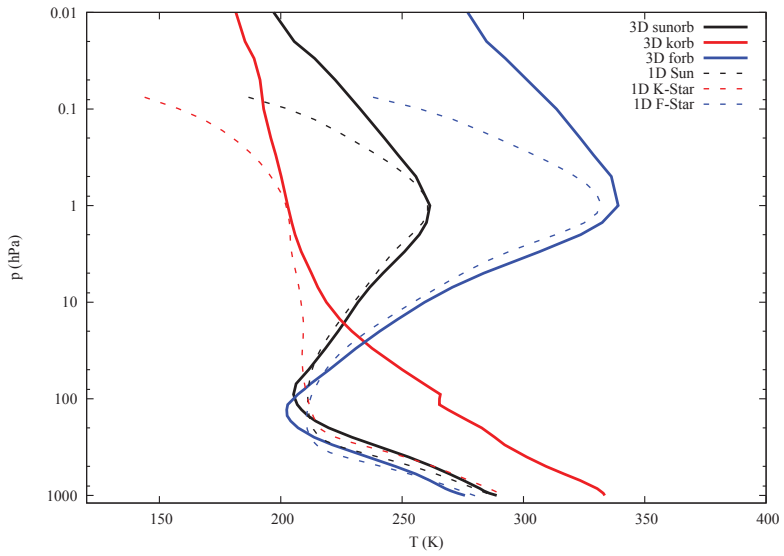

Figure 11.3: Mean temperature-pressure profiles for Earth-like planets around different types of stars. Global annual mean results from the 3D model in solid, temperature profile from the 1D model in dashed lines. Results for solar radiation in black, for the planet around the K-type star in red, and the planet around the F-type star in blue.

Fig. 11.3 shows the temperature-pressure profiles from the 1D and 3D model calculations for Earth-like planets around different types of stars. For the planet around the Sun the

temperature profiles agree well for pressures larger than 1 hPa, as has been discussed in Chapter 6. The differences for pressures smaller than 1 hPa result from different boundary conditions, pressures at top of the atmosphere, and the missing absorption of shortwave radiation by molecular oxygen in the 1D model.

Both, 1D and 3D model results show lower temperatures for the planet around the F-type star and higher temperatures for the planet around the K-type star. However, the absolute change in temperature is different.

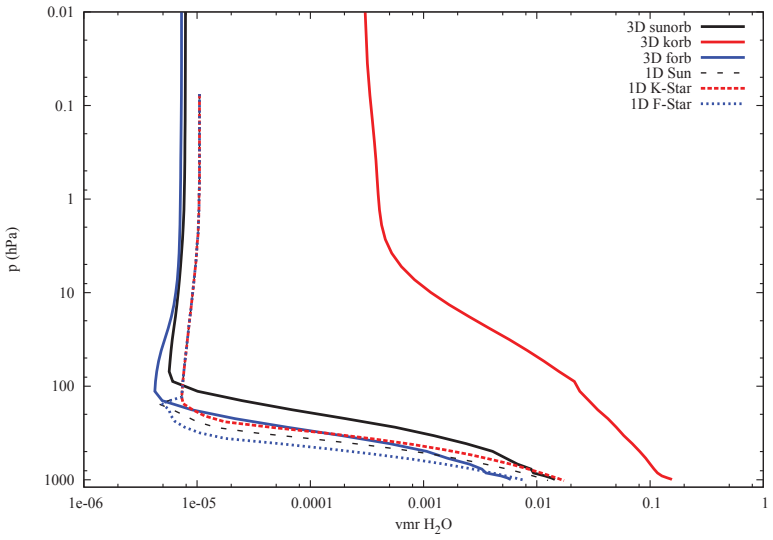

Figure 11.4: Mean water vapor profiles for Earth-like planets orbiting different types of central stars. Global annual mean results from the 3D model in solid, water profile from the 1D model in discontinuous lines. Results for solar radiation in black, for the planet around the K-type star in red, and the planet around the F-type star in blue.

Table 11.3: 1D and 3D global mean temperature and water vapor vmr at 1000 hPa for planets around different stars.

Scenario	temperature at 1000 hPa (K)	water vapor vmr (%)
sunorb	289	1.4
Sun1D	288	1.3
korb	334	15.6
K1D	293	1.7
forb (3D)	276	0.6
F1D	280	0.8

Fig. 11.4 shows the corresponding water vapor profiles in volume mixing ratio. For all three stellar irradiations the water profiles of the 1D and the 3D model show some differences. Generally, in the troposphere water concentrations are lower in the 1D model results than those calculated by the 3D model, except for the lowermost layers, see Table 11.3 for exact values. In the upper atmosphere the water profiles computed by the 1D model are all very

similar and slightly higher for the planet around the Sun and the F-type star than those resulting from the 3D model. For the planet around the K-type star, water concentrations from the 3D model are much higher, which is also the reason for the stronger temperature response in the 3D model for this scenario.

The different model results are now discussed in detail.

11.2.1 Planet around the F-type star

For the planet around the F-type star minor differences between the 1D and 3D model results occur in the troposphere and in the stratosphere. Near the surface and at the tropopause the temperatures obtained with the 1D model are slightly higher, while in the upper troposphere and in the stratosphere the temperatures are lower than those resulting from the 3D model. The deviation of the near surface temperatures can be explained by the assumption of a fixed albedo in the 1D model.

Since in the 1D model the same surface albedo is assumed for the planet around the F-type star as for the planet around the Sun, the impact of the albedo feedback, which leads to higher albedos for lower temperatures, hence even lower temperatures, is neglected. In the 3D model, however, the build up of sea ice is included, hence also the albedo feedback. By this the temperature difference of 4 K can be explained.

In the upper troposphere temperatures obtained with the 1D model are lower than those of the 3D model. This results from different water vapor concentrations in the lower atmosphere (see Fig. 11.4). Water concentrations are lower in the 1D model, which causes a smaller greenhouse effect, and results in lower tropospheric temperatures.

The water vapor profile in the 3D model is calculated using the continuity equation for water compounds (see sec. 5.3.1). Hence, the gaseous phase as well as the condensed phases of water are taken into account, as well as phase changes, the transport by atmospheric dynamics or convection, and precipitation. In the 1D model the water profile is calculated, as stated above, from the saturation water vapor pressure and a predefined relative humidity profile which resembles observations of the Earth. Furthermore, in the stratosphere, above the cold trap, the water vapor profile is set to a constant value as that of the cold trap and relative humidities may not fall below 0.08.

While the water vapor concentrations in the lower atmosphere are smaller in the 1D model than in the 3D model results, they are higher in the stratosphere. This leads to more effective cooling of the upper atmosphere by long wave radiation and thereby explains at least partly the lower stratospheric temperatures in the 1D model. Furthermore, it has been argued that the stratospheric temperatures for the planet around the F-type star may be overestimated due to the use of unadjusted stellar fluxes in the Chappuis band (see sec. 6.2.2 of the validation chapter). Since the stellar flux at these wavelengths (from 407 to 682.5 nm) is higher for an F-type star than for the Sun the influence of this model shortcoming may have a stronger impact for this scenario.

In summary, the different tropopause temperatures are caused by the different treatments

of convection. While in the 3D model convection is calculated with a mass-flux scheme, which evaluates the buoyancy, hence the density difference, of a disturbed air parcel and includes the release of latent heat during ascent (see sec. 5.3.3), the 1D model evaluates the difference in temperature of an atmospheric layer calculated by convective adjustment and radiative transfer. Therefore, in the 3D model convection stops if the buoyancy of an air parcel vanishes. In the 1D model convection stops when the adiabatic temperature is lower than the temperature calculated from radiative transfer. This difference results in different tropopause heights between the models.

11.2.2 Planet around the K-type star

For the planet around the K-type star, differences in the temperature and water profiles between the 1D and the 3D model are large. In the lowermost atmospheric layer, near the surface the temperature difference is about 40 K, see table 11.3. The largest temperature difference can be found at approximately 200 hPa with about 60 K. Also the water profiles deviate largely. Whereas near the surface the difference in water volume mixing ratio is about one order of magnitude, in the upper atmosphere the water concentrations resulting from the 3D model are about two orders of magnitude larger than those of the 1D model. However, in the stratosphere at around 1 hPa, the temperatures of the 1D and the 3D model agree very well.

The higher temperatures resulting from the 3D model calculations for the planet around the K-type star may partly be explained by the decrease in albedo in the 3D model due to complete melting of ice in comparison to the fixed surface albedo in the 1D model. More importantly however is the difference in the water profile, hence the water vapor feedback.

An increase in water vapor and temperature results from both models for the planet around the K-type star. However, the response is much smaller in the 1D model, since the water profile is calculated from a predefined relative humidity profile (see also sec. 11.3). Therefore, a change in the gradient of the relative humidity cannot be taken into account, which may however result from an increase in upwards motion of water compounds e.g. by convection. As has been shown in Chapter 9, discussing the 3D model results, the hydrological cycle strongly changes for the planet around the K-type star. An increase in the water vapor concentrations leads to an increase in temperature, hence even more evaporation of water from the surface, which increases the buoyancy and thereby convective mass transport. The resulting water profiles are therefore very different.

A test with the 1D model has been performed, in which the water vapor profile in the 1D model was kept fixed to the values of the korb model results (not shown). Similar temperatures near the surface and in the lower atmosphere for pressures larger than about 100 hPa were found. In the upper atmosphere the temperature profiles of the 1D and 3D model showed again deviations, resulting from radiative heating by molecular oxygen and ice clouds in the upper atmosphere in the 3D model. The influence of different relative humidity profiles in the 1D model for the planet around the K-type star is discussed in 11.3.

11.2.3 Summary of results with mixed layer ocean

The comparison of the 1D and 3D model results for Earth-like planets around different types of stars showed that processes, such as the albedo feedback and the water vapor feedback, including the upwards transport of water compounds, have an impact on the temperature and water profile. For the planet around the F-type star this leads to minor differences in temperature and water. For the planet around the K-type star the effect is higher.
For the planet around the K-type star the influence of different relative humidity profiles will be addressed in sec. 11.3.

11.3 Effect of the relative humidity for the planet around the K-type star

In this section it is evaluated whether the 3D model results for the planet around the K-type star can be approximated by the 1D model when using a different relative humidity profile. To do this, 1D model results which were provided by Barbara Stracke (Stracke, 2012) are used and compared to the 3D model result.

The 1D model results were obtained for another atmospheric composition. Only the major greenhouse gases carbon dioxide and water vapor are included, and nitrogen as a filling gas. Carbon dioxide is set to a constant volume mixing ratio of 355 ppm, as for the 3D model scenarios. Water vapor is calculated from the relative humidity profile and the saturation water vapor pressure. In addition in the 1D model an increase of the surface pressure due to evaporation of water is taken into account, as well as Rayleigh scattering of all three atmospheric constituents.

The water vapor profile in the 1D model is calculated by:

$$c_{H_2O}(p) = \frac{p_{sat}(T(p))}{p} RH(p), \tag{11.1}$$

where $c_{H_2O}(p)$ is the volume mixing ratio of water vapor at a certain pressure level, $p_{sat}(T)$ is the saturation water vapor pressure for the temperature at this pressure, p the pressure and RH the relative humidity (see also sec. 5.2.2). This is applied in the lower atmosphere for pressure levels, where the ratio of the saturation water vapor pressure to the pressure ($f_{sat} = \frac{p_{sat}(T(p))}{p}$) of the layer decreases with height. At the point where f_{sat} increases with height, at the model cold trap, the water vapor concentration is fixed to that value and kept constant throughout the above atmosphere.
For the kRH100 scenario (see table 11.4), the relative humidity is set to 100%, hence the air is assumed to be saturated. For the kRHMW scenario the relative humidity profile is calculated according to Manabe and Wetherald (1967):

$$RH(p) = 0.77 \frac{\frac{p}{p_{surf}} - 0.02}{0.98}, \tag{11.2}$$

hence the relative humidity decreases with decreasing pressure.

Scenario	Model	albedo	RH	atmospheric composition
korb	3D	calculated (0.10)	calculated	Earth-like
kRHMW	1D	fixed 0.22	Manabe and Wetherald (1967)	N_2, CO_2, H_2O
kRH100	1D	fixed 0.22	100%	N_2, CO_2, H_2O

Table 11.4: Model setups used for the 1D–3D model comparison for the planet around the K-type star with different relative humidity profiles in the 1D model.

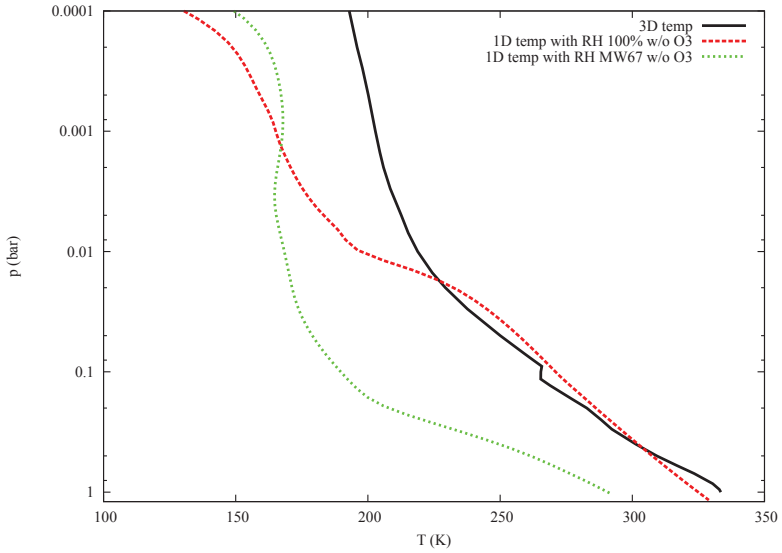

Figure 11.5: Comparison of the global annual mean temperature profile of the 3D korb scenario (black) with 1D model results including different RH profiles, RH profile by Manabe and Wetherald (1967) in green, RH profile with saturated lower atmosphere in red.

In section 11.2 it has been shown that for the planet around the K-type star the 1D model does not agree with the 3D model result when assuming the relative humidity profile of Manabe and Wetherald (1967). This is also shown in Fig. 11.5, where the korb scenario is depicted in black and the kRHMW scenario in green. Additionally the kRH100 scenario is shown in red.

When assuming a relative humidity of 100% (shown in red) the lower atmospheric temperature profile are more comparable and near surface temperatures are also similar (see table 11.5).

In the upper atmosphere the temperature profile deviate strongly, which is due to the fact that ozone absorption is not considered in the 1D model.

In the 1D model the change in surface pressure due to evaporation of surface water is taken into account, which may alter the atmospheric optical depth. For water dominated atmospheres the increase in the Rayleigh scattering optical depth is important. However, was found that this effect is only important when the partial pressure of water vapor exceeds 1 bar at the surface (Selsis et al. (2007) and B. Stracke private communication). For the kRH100 scenario the surface pressure is increased to 1.16 bar, hence this effect is

negligible.

Table 11.5: 1D and 3D global mean temperature and water vapor vmr at 1000 hPa for planet around the K-type star with different relative humidities

Scenario	temperature at 1000 hPa (K)	water vapor vmr (%)
korb	334	15.6
kRHMW	292	1.7
kRH100	329	14.1

Fig. 11.6 shows the water vapor profiles for the different scenarios. The water vapor concentration are lowest for the kRHMW, showing a strong decrease with decreasing pressure. For the other two scenarios the water vapor profiles still show some difference but agree better. The kRH100 scenario shows larger water vapor concentrations in the lower atmosphere and smaller concentrations in the upper atmosphere compared to the 3D korb scenario. In the lower atmosphere the difference results from the assumption that the atmosphere is completely saturated in the kRH100 scenario, which is not the case in the korb scenario. In the upper atmosphere, the lower water vapor concentrations result from the lower temperatures for the kRH100 scenario compared to korb, due to the lack of ozone absorption.

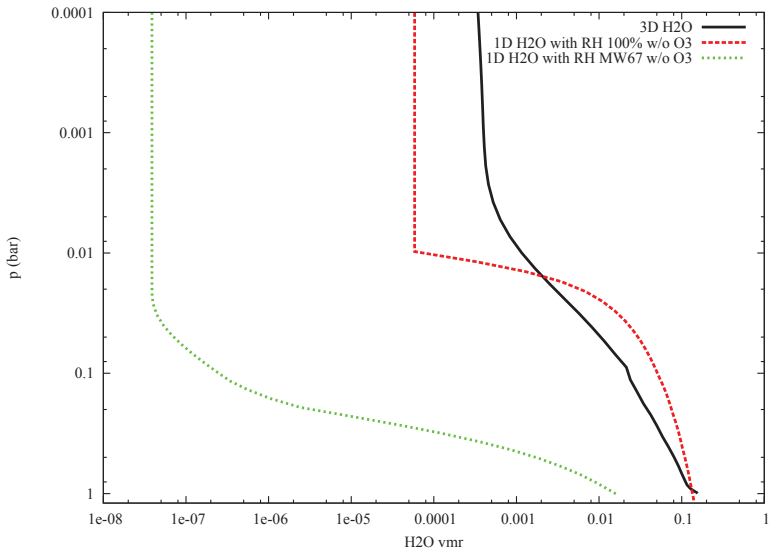

Figure 11.6: Comparison of the global annual mean water vapor profile (vmr) of the 3D korb scenario (black) with 1D model results including different RH profiles, RH profile by Manabe and Wetherald (1967) in green, RH profile with saturated lower atmosphere in red.

These results lead to the conclusion that one may find a relative humidity profile which allows a good agreement between the 1D and 3D model results also for the planet around the K-type star. There are other relative humidity profiles in use in the literature (e.g. Kasting and Ackerman, 1986), which aim to capture the change in relative humidity with increasing water vapor content or surface temperature. Those should be evaluated more carefully and compared to 3D model results for warm climates.

11.4 Summary

In this chapter it was evaluated which dynamical processes play an important role for the mean climate state of an Earth-like planet around different types of stars. This was done by comparing 3D model results to those of a 1D radiative convective climate model. In section 11.1 it has been shown that global annual mean stratospheric temperatures for a planet around a K-type star can be approximated by a 1D model when prescribing the sea surface conditions in the 3D model scenario, despite the fact that the atmospheric circulation decreases.

When including an interactive ocean in the 3D model, the global mean temperature may also be approximated by the 1D model. The 1D model results however strongly depend on the relative humidity profile chosen.

Which relative humidity profile needs to be chosen as input for 1D modeling studies depends strongly on the scenario investigated. For the Earth-like planet around an F-type star an Earth-like relative humidity profile seems to be adequate, while it underestimates the climatic response for the planet around the K-type star. Hence, a parameter study with the 3D model for different scenarios would be needed before deciding on a suitable relative humidity parametrization in the 1D model.

Part IV

Summary & Outlook

CHAPTER 12

Summary

This chapter summarizes the most important results of this thesis. The main goal of this thesis was to determine the influence of atmospheric dynamical processes upon the habitability of planets around different stellar types.
In this work the climatic response of Earth-like extrasolar planets around the Sun, a K and an F-type star has been studied by applying an adapted state-of-the-art 3D climate model of the Earth. The influence of the dynamical processes, such as atmospheric dynamics, the hydrological cycle and the albedo feedback on the climate of these planets has been evaluated. The planets have been placed at an orbital distance where the total energy input by the star is equal to the total solar irradiance of the present Earth. The influence of adapting the orbital period has also been evaluated.

The 3D model results have been compared to those of a steady state 1D radiative convective atmosphere model, to determine whether such a rather simplified model allows for the approximation of the global mean climate state, which is the combined result of complex, non-linear processes.

12.1 Adaptation of the 3D climate model

To evaluate the interaction of different stellar irradiations and dynamical processes for Earth-like extrasolar planets around K- and F-type stars, the state-of-the-art 3D climate chemistry model EMAC-FUB has been applied. To allow for the calculation of the climatic response of an Earth-like planet to different stellar radiation, the model has been adapted as follows.

- A mixed layer ocean model, provided by S. Dietmüller and M. Ponater (DLR, Oberpfaffenhofen), has been implemented into EMAC, which calculates the sea surface temperatures, the sea ice concentrations and thickness. This mixed layer ocean model was needed to determine the near surface and lower atmospheric temperatures, hence the habitability of the planet.
- To calculate the climate of Earth-like planets around different types of stars, high resolution stellar spectra had to be converted into binned stellar input spectra needed by the shortwave radiative transfer modules of EMAC. The influence of the use of an unadjusted stellar energy flux in the Chappuis band has been evaluated for a solar input spectrum.

- The implemented expression for the calculation of the saturation water vapor pressure with respect to liquid water was replaced by the expression given by Wagner and Pruß (2002). This was done to allow for the calculation of the saturation water vapor pressure for temperatures above 400 K until the critical point of water (647 K), which temporarily and locally occurred during the evolution into a new equilibrium climate state for the planet around the K-type star.

- In the long wavelengths radiative transfer scheme RRTM, the calculation of unphysical negative optical depths was suppressed in the 3D model as suggested by M. Ponater (private communication).

The impact of the adaptations to the model has been evaluated for the Earth around the Sun, see Chapter 6 and 8. Furthermore, for the planets around the different types of stars the orbital period was changed, to account for the different orbital distances.

12.2 Aim of this thesis

12.2.1 What is the influence of atmospheric dynamical processes on the habitability of terrestrial planets?

The influence of atmospheric dynamical processes upon the habitability of terrestrial planets has been studied for Earth-like planets around a K-type, an F-type star and the Sun, which receive the same amount of total energy as the Earth from the Sun.

For all scenarios studied the planet stays habitable in terms of allowing for liquid water on the planetary surface.

For the scenarios studied the largest impact of dynamical processes upon the climate has been found for the planet around the K-type star. The change in the stellar spectral energy distribution leads to an increase in lower atmospheric and near surface temperatures, as has also been found by 1D model studies, e.g. Kasting et al. (1993), Kitzmann et al. (2010). This increase in temperature leads to a massive build up of water vapor in the atmosphere due to enhanced evaporation of water from the surface. This in turn leads to a further increase in surface temperatures, due to increased absorption of radiation.
The resulting high temperatures in the lower atmosphere lead to a change in the hydrological cycle. Rain and snow formation takes place at higher altitudes than for the Earth around the Sun. Cycling of water compounds between the atmosphere and the surface is less effective due to the high atmospheric temperatures. A large amount of the precipitation flux undergoes sublimation, melting and evaporation before it reaches the surface. This leads to large concentrations of water vapor at high altitudes. These high water vapor concentrations may be photolysed by the stellar radiation, and could subsequently be lost to space by atmospheric escape of hydrogen compounds, which should be investigated in future work.

The strong increase in water vapor concentrations can only be captured by the 1D model applied here, when assuming a saturated lower atmosphere, which clearly overestimates the water vapor concentrations, since under such conditions strong cloud formation is expected, which reduces the relative humidity.

For the Earth-like planet around the F-type star no large impact of the dynamical processes on the climate is found. Despite the fact that the surface albedo increases due to build up of sea ice global mean surface temperatures only decrease by about 10 K. For this scenario the atmospheric temperatures and water vapor concentrations resulting from 1D and 3D calculations are comparable, since the relative humidity profile utilized in the 1D model is more appropriate for this scenario.

12.2.2 What is the influence of different stellar types on climate feedback cycles and how do they affect the habitability of a planet?

For the scenarios studied it was evaluated whether climate feedback cycles are influenced by the different stellar spectra.

For the Earth-like planet around the F-type star only little changes due to climate feedback cycles have been found. The lower temperatures near the surface lead to the onset of the water vapor and the albedo feedback cycle, which lead to low atmospheric water vapor concentrations and an increase in albedo. However, this leads only to a small decrease in lower atmospheric and near surface temperatures. This is a result of the sufficiently high amount of incident stellar energy and the presence of other greenhouse gases such as carbon dioxide.

For the Earth-like planet around the K-type star an interaction of the incident stellar irradiation and the water vapor feedback cycle has been found. The increase in lower atmospheric and near surface temperatures lead to an increase in evaporation of water, which enhances the optical depth of the atmosphere. This leads to an increase in the greenhouse effect, hence atmospheric and surface temperatures. For the planet around the K-type star in addition to the heating by absorption of thermal radiation emitted by the planet, near infrared radiation by the star is effectively absorbed by the increased amounts of water vapor. This leads to a further increase in atmospheric and thereby also surface temperatures. For this scenario the high lower atmospheric temperatures resulted in a completely ice and snow free surface, hence the albedo feedback was no longer present.

For the scenarios studied the 3D model results suggest that clouds may introduce a positive climate feedback. Especially for the planet around the K-type star a massive build up of ice clouds in the upper atmosphere has been found, which lead to additional heating of the atmosphere. This response is in contrast to previous assumptions, that water droplet clouds will form and lead to a cooling of the atmosphere for such warm climate states (Kasting et al., 1993).

CHAPTER 13

Outlook

In this work the 3D climate chemistry model EMAC-FUB has been adapted to calculate the climatic response of Earth-like extrasolar planets around K and F-type stars. Model improvements would be required to answer additional scientific question of interest regarding the habitability of extrasolar planets.

13.1 Future model improvements

13.1.1 EMAC-FUB

Shortwave radiative transfer

- The use of unadjusted stellar radiative fluxes in the Chappuis band in the FUBRAD scheme caused a non-negligible change in the upper atmospheric temperature structure for the Earth around the Sun. To obtain realistic heating rates in the upper atmosphere for other stellar irradiations absorption of the stellar flux in the Chappuis band has to be treated consistently. This is work in progress by M. Kunze (Freie Universität Berlin).

- Rayleigh scattering by atmospheric constituents is considered by a fixed optical depth in the 3D Model. For larger differences in the atmospheric composition, e.g. due to a further increase of water vapor or higher atmospheric concentrations of carbon dioxide, the composition of the atmosphere and its impact on scattering properties have to be taken into account.

Longwave radiative transfer

- In the longwave radiative transfer scheme RRTM an update has been implemented which suppresses the use of negative optical depths resulting from the extrapolation of absorption coefficients. A set of absorption coefficients calculated for a larger temperature and pressure range are needed to overcome this shortcoming of the model, and to allow for the calculation of extrasolar planetary climates which are less similar to that of present Earth.

Pressure changes due to evaporation

- For high surface temperatures surface water evaporates. This causes an increase in surface pressure, which is neglected in the 3D model. To allow for the simulation of

hot extrasolar planets, close to the inner boundary of the habitable zone, the pressure increase due to evaporation has to be taken into account, since for such scenarios, water is the main atmospheric constituent.

Sea surface conditions

- The mixed layer ocean model used in this work requires the input of so-called q-fluxes, which aim for considering the influence of the oceanic heat transport. These fluxes are not known for extrasolar planetary scenarios, and thereby introduce a major uncertainty. To estimate this uncertainty a parameter study with the mixed layer ocean model is needed . A more sophisticated approach would be coupling of a three-dimensional ocean circulation model to the 3D atmosphere model.

13.1.2 1D model

Relative humidity profile

- For the 1D radiative convective climate model, an improvement of the parametrization for the relative humidity profile is needed to account for the change in the atmospheric water vapor concentration profile with increasing surface temperatures, or saturation water vapor pressure.

13.2 Further model scenarios

With the adapted 3D model the climatic response of Earth-like extrasolar planets around K and F-type stars has been investigated. Further model scenarios could now be investigated with this model.

The climatic response of terrestrial extrasolar planets with Earth-like atmospheric composition for different surface properties

- The climate state of a planet depends on surface properties such as the land-sea mask and the water reservoir. The influence of different surface properties could be investigated with the existing model. It would be of interest to study the most extreme cases, a land and an ocean planet to infer the possible range of climate states and the dependence of the water vapor feedback on the water reservoir of the planet. A parameter study for the oceanic q-fluxes would further allow for an estimate of their impact upon the climate state.

The climatic response of Earth-like extrasolar planets with Earth-like atmospheric for different obliquities

- The obliquity of the present Earth leads to seasonal variations of stellar insolation. For an obliquity of 0° the polar regions of an Earth-like planet would not receive such high amounts of energy e.g. during polar summer as for a larger obliquity. This may lead to different cooling of the planetary atmosphere and change the climatic response as has been discussed in the literature (Abe et al., 2011, Williams and Pollard, 2003). Therefore it would be of interest to study the impact of different obliquities for the model scenarios studied in this thesis.

With further adaptations of the 3D model other scientific questions could be addressed.

The influence of dynamical processes on the photochemistry of Earth-like planets around different types of stars

- It has been shown that the atmospheric dynamics change for the Earth-like planets around different types of central stars. This will have an impact on the transport of chemical species in these atmospheres. It has been furthermore shown in the literature, that the chemical composition changes for different stellar irradiations (Segura et al., 2003, Grenfell et al., 2007). It would be of interest to investigate the interaction of photochemistry and atmospheric dynamics upon planetary habitability. Furthermore, a change in the transport of chemical species may alter the spectral appearance of a planet, which is of interest in the search for atmospheric biosignatures. For the scenario of the planet around the K-type star, it would be interesting to study whether the photodissociation of water in the upper atmosphere would be efficient enough to result in substantial photolytic loss of water vapor and atmospheric escape of hydrogen compounds.

The climatic response of Earth-like planets around M-type stars

- For the Earth-like planet around the K-type star a strong climatic response has been found due to the interaction of the stellar irradiation at near infrared wavelengths with the water vapor feedback. This interaction is expected to lead to an even stronger amplification of the water vapor feedback for Earth-like planets around M-type stars, since these stars emit more radiation in the near infrared than K-type stars. This may influence the width of the habitable zone for planets around M-type stars.

The climatic response of Earth-like extrasolar planets for different total stellar insolations

- In this work the climatic response of Earth-like extrasolar planets, which receive the same total amount of energy from their different host stars has been investigated. It would be of interest to study the influence of different total stellar insolations for different types of stars to evaluate the impact of dynamical processes on the width of the habitable zone around different types of stars.

Bibliography

U.S. standard atmosphere, 1976. Technical report, October 1976.

Annual Report of the World Meteorological Organization 1986. WMO, 1987.

Y. Abe, A. Abe-Ouchi, N. H. Sleep, and K. J. Zahnle. Habitable Zone Limits for Dry Planets. *Astrobiology*, 11:443–460, June 2011. doi: 10.1089/ast.2010.0545.

D.G. Andrews, J.R. Holten, and C.B. Leovy. *Middle Atmosphere Dynamics*, volume 40 of *International Geophysics Series*. Academic Press, Hartcourt Brace Jovanovich, 1987.

J. L. Bean, J.-M. Désert, P. Kabath, B. Stalder, S. Seager, E. Miller-Ricci Kempton, Z. K. Berta, D. Homeier, S. Walsh, and A. Seifahrt. The Optical and Near-infrared Transmission Spectrum of the Super-Earth GJ 1214b: Further Evidence for a Metal-rich Atmosphere. *ApJ*, 743:92, December 2011. doi: 10.1088/0004-637X/743/1/92.

P. Bechtold, J.-P. Chaboureau, A. Beljaars, A. K. Betts, M. Köhler, M. Miller, and J.-L. Redelsperger. The simulation of the diurnal cycle of convective precipitation over land in a global model. *Q. J. R. Meteorol. Soc.*, 130:3119?3137, 2004.

P. Bretagnon and G. Francou. Planetary theories in rectangular and spherical variables - VSOP 87 solutions. *A&A*, 202:309–315, August 1988.

A. J. Cenarro, R. F. Peletier, P. Sanchez-Blazquez, S. O. Selam, E. Toloba, N. Cardiel, J. Falcon-Barroso, J. Gorgas, J. Jimenez-Vicente, and A. Vazdekis. Stellar atmospheric parameters in MILES library (Cenarro+, 2007). *VizieR Online Data Catalog*, 837:40664–+, September 2007.

S. Chabrillat and G. Kockarts. Simple parameterization of the absorption of the solar Lyman-alpha line. *Geophys. Res. Lett.*, 24:2659–2662, November 1997. doi: 10.1029/97GL52690.

D. Charbonneau, H. A. Knutson, T. Barman, L. E. Allen, M. Mayor, S. T. Megeath, D. Queloz, and S. Udry. The Broadband Infrared Emission Spectrum of the Exoplanet HD 189733b. *ApJ*, 686:1341–1348, October 2008. doi: 10.1086/591635.

A. C. M. Correia, B. Levrard, and J. Laskar. On the equilibrium rotation of Earth-like extra-solar planets. *A&A*, 488:L63–L66, September 2008. doi: 10.1051/0004-6361:200810388.

A. N. Cox. *Allen's astrophysical quantities*. 2000.

B. Croll, L. Albert, R. Jayawardhana, E. Miller-Ricci Kempton, J. J. Fortney, N. Murray, and H. Neilson. Broadband Transmission Spectroscopy of the Super-Earth GJ 1214b Suggests a Low Mean Molecular Weight Atmosphere. *ApJ*, 736:78, August 2011. doi: 10.1088/0004-637X/736/2/78.

I. J. M. Crossfield, H. Knutson, J. Fortney, A. P. Showman, N. B. Cowan, and D. Deming. Spitzer/MIPS 24 μm Observations of HD 209458b: Three Eclipses, Two and a Half Transits, and a Phase Curve Corrupted by Instrumental Sensitivity Variations. *ApJ*, 752:81, June 2012. doi: 10.1088/0004-637X/752/2/81.

P. M. de F. Forster, M. Blackburn, R. Glover, and K. P. Shine. An examination of climate sensitivity for idealised climate change experiments in an intermediate general circulation model. *Climate Dynamics*, 16:833–849, 2000. doi: 10.1007/s003820000083.

J.-P. de Vera, D. Möhlmann, F. Butina, A. Lorek, R. Wernecke, and S. Ott. Survival Potential and Photosynthetic Activity of Lichens Under Mars-Like Conditions: A Laboratory Study. *Astrobiology*, 10:215–227, March 2010. doi: 10.1089/ast.2009.0362.

A. D. del Genio and R. J. Suozzo. A comparative study of rapidly and slowly rotating dynamical regimes in a terrestrial general circulation model. *Journal of Atmospheric Sciences*, 44:973–986, March 1987. doi: 10.1175/1520-0469(1987)044.

B.-O. Demory, M. Gillon, S. Seager, B. Benneke, D. Deming, and B. Jackson. Detection of Thermal Emission from a Super-Earth. *ApJ*, 751:L28, June 2012. doi: 10.1088/2041-8205/751/2/L28.

Modellbetreuungsgruppe Deutsches Klimarechenzentrum (DKRZ). The echam3 atmospheric general circulation model. Technical report, Deutsches Klimarechenzentrum, Hamburg, Germany, 1992.

C. D. Dressing, D. S. Spiegel, C. A. Scharf, K. Menou, and S. N. Raymond. Habitable Climates: The Influence of Eccentricity. *The Astrophysical Journal*, 721:1295–1307, October 2010. doi: 10.1088/0004-637X/721/2/1295.

F. Forget, F. Hourdin, R. Fournier, C. Hourdin, O. Talagrand, M. Collins, S. R. Lewis, P. L. Read, and J.-P. Huot. Improved general circulation models of the Martian atmosphere from the surface to above 80 km. *J. Geophys. Res.*, 104:24155–24176, October 1999. doi: 10.1029/1999JE001025.

J.P.F. Fortuin and H. Kelder. An ozone climatology based on ozonesonde and satellite measurements. *Journal of Geophysics Research*, 103:31709–31734, December 1998. doi: 10.1029/1998JD200008.

Y. Fouquart and B. Bonnel. Computations of solar heating of the earth's atmosphere: A new parameterization. *Beiträge zur Physik der Atmosphäre*, 53:35–62, 1980.

K. Fraedrich, A. Kleidon, and F. Lunkeit. A Green Planet versus a Desert World: Estimating the Effect of Vegetation Extremes on the Atmosphere. *Journal of Climate*, 12: 3156–3163, October 1999. doi: 10.1175/1520-0442(1999)012.

K. Fraedrich, H. Jansen, E. Kirk, U. Luksch, and F. Lunkeit. The Planet Simulator: Towards a user friendly model. *Meteorologische Zeitschrift*, 14:299–304, June 2005a. doi: 10.1127/0941-2948/2005/0043.

K. Fraedrich, H. Jansen, E. Kirk, and F. Lunkeit. The Planet Simulator: Green planet and desert world. *Meteorologische Zeitschrift*, 14:305–314, June 2005b. doi: 10.1127/0941-2948/2005/0044.

N. P. Gibson, F. Pont, and S. Aigrain. A new look at nicmos transmission spectroscopy of hd 189733, gj-436 and xo-1: no conclusive evidence for molecular features. *Monthly Notices of the Royal Astronomical Society*, 411(4):2199–2213, 2011. ISSN 1365-2966. doi: 10.1111/j.1365-2966.2010.17837.x. URL `http://dx.doi.org/10.1111/j.1365-2966.2010.17837.x`.

R. Goody, R. West, L. Chen, and D. Crisp. The correlated-k method for radiation calculations in nonhomogeneous atmospheres. *J. Quant. Spec. Radiat. Transf.*, 42:539–550, December 1989. doi: 10.1016/0022-4073(89)90044-7.

D. O. Gough. Solar interior structure and luminosity variations. *Sol. Phys.*, 74:21–34, November 1981. doi: 10.1007/BF00151270.

J. L. Grenfell, B. Stracke, P. von Paris, B. Patzer, R. Titz, A. Segura, and H. Rauer. The response of atmospheric chemistry on earthlike planets around F, G and K stars to small variations in orbital distance. *Planetary and Space Science*, 55(5):661–671, 2007.

E. W. Guenther, J. Cabrera, A. Erikson, M. Fridlund, H. Lammer, A. Mura, H. Rauer, J. Schneider, M. Tulej, P. von Paris, and P. Wurz. Constraints on the exosphere of CoRoT-7b. *A&A*, 525:A24, January 2011. doi: 10.1051/0004-6361/201014868.

Christian A. Gueymard. The sun's total and spectral irradiance for solar energy applications and solar radiation models. *Solar Energy*, 76(4):423–453, April 2004.

H. J. Habing, C. Dominik, M. Jourdain de Muizon, R. J. Laureijs, M. F. Kessler, K. Leech, L. Metcalfe, A. Salama, R. Siebenmorgen, N. Trams, and P. Bouchet. Incidence and survival of remnant disks around main-sequence stars. *A&A*, 365:545–561, January 2001. doi: 10.1051/0004-6361:20000075.

J. Hansen, G. Russell, D. Rind, P. Stone, A. Lacis, S. Lebedeff, R. Ruedy, and L. Travis. Efficient Three-Dimensional Global Models for Climate Studies: Models I and II. *Monthly Weather Review*, 111:609–+, 1983. doi: 10.1175/1520-0493(1983)111.

M. H. Hart. The evolution of the atmosphere of the earth. *ICARUS*, 33:23–39, January 1978. doi: 10.1016/0019-1035(78)90021-0.

M. H. Hart. Habitable Zones about Main Sequence Stars. *ICARUS*, 37:351–357, January 1979. doi: 10.1016/0019-1035(79)90141-6.

P. H. Hauschildt, F. Allard, J. Ferguson, E. Baron, and D. R. Alexander. The NEXTGEN Model Atmosphere Grid. II. Spherically Symmetric Model Atmospheres for Giant Stars with Effective Temperatures between 3000 and 6800 K. *ApJ*, 525:871–880, November 1999. doi: 10.1086/307954.

J. R. Holton, P. H. Haynes, M. E. McIntyre, A. R. Douglass, R. B. Rood, and L. Pfister. Stratosphere-troposphere exchange. *Reviews of Geophysics*, 33:403–439, November 1995. doi: 10.1029/95RG02097.

J. T. Houghton, Y. Ding, D.J. Griggs, M. Noguer, P. J. van der Linden, and D. Xiaosu, editors. *Climate Change 2001: The Scientific Basis*. Cambridge University Press, UK, 2001.

A. P. Ingersoll. The runaway greenhouse: A history of water on venus. *ournal of Atmospheric Sciences*, 1969.

M. Joshi. Climate Model Studies of Synchronously Rotating Planets. *Astrobiology*, 3: 415–427, June 2003. doi: 10.1089/153110703769016488.

M. M. Joshi, S. R. Lewis, P. L. Read, and D. C. Catling. Western boundary currents in the Martian atmosphere: Numerical simulations and observational evidence. *J. Geophys. Res.*, 100:5485–5500, March 1995. doi: 10.1029/94JE02716.

M. M. Joshi, R. M. Haberle, and R. T. Reynolds. Simulations of the Atmospheres of Synchronously Rotating Terrestrial Planets Orbiting M Dwarfs: Conditions for Atmospheric Collapse and the Implications for Habitability. *Icarus*, 129:450–465, October 1997. doi: 10.1006/icar.1997.5793.

P. Jöckel, H. Tost, A. Pozzer, C. Brühl, J. Buchholz, L. Ganzeveld, P. Hoor, A. Kerkweg, M.G. Lawrence, R. Sander, B. Steil, G. Stiller, M. Tanarhte, D. Taraborrelli, J. van Aardenne, and J. Lelieveld. The atmospheric chemistry general circulation model echam5/messy1: consistent simulation of ozone from the surface to the mesosphere. *Atmospheric Chemistry and Physics*, 6(12):5067–5104, 2006. ISSN 1680-7316. URL `http://www.atmos-chem-phys.net/6/5067/2006/`.

J. F. Kasting. Runaway and moist greenhouse atmospheres and the evolution of earth and Venus. *ICARUS*, 74:472–494, June 1988. doi: 10.1016/0019-1035(88)90116-9.

J. F. Kasting and T. P. Ackerman. Climatic consequences of very high carbon dioxide levels in the earth's early atmosphere. *Science*, 234:1383–1385, December 1986. doi: 10.1126/science.234.4782.1383.

J. F. Kasting, J. B. Pollack, and D. Crisp. Effects of high CO2 levels on surface temperature and atmospheric oxidation state of the early earth. *Journal of Atmospheric Chemistry*, pages 403–428, 1984.

J. F. Kasting, D. P. Whitmire, and R. T. Reynolds. Habitable Zones around Main Sequence Stars. *Icarus*, 101:108–128, January 1993. doi: 10.1006/icar.1993.1010.

D. Kitzmann, A. B. C. Patzer, P. von Paris, M. Godolt, B. Stracke, S. Gebauer, J. L. Grenfell, and H. Rauer. Clouds in the atmospheres of extrasolar planets. I. Climatic effects of multi-layered clouds for Earth-like planets and implications for habitable zones. *Astronomy and Astrophysics*, 511:A66+, February 2010. doi: 10.1051/0004-6361/200913491.

A. Kleidon, K. Fraedrich, and M. Heimann. A green planet versus a desert world: estimating the maximum effect of vegetation on the land surface climate. *Climate Change*, 44(4):471–493, March 2000.

H. A. Knutson, D. Charbonneau, L. E. Allen, A. Burrows, and S. T. Megeath. The 3.6-8.0 μm Broadband Emission Spectrum of HD 209458b: Evidence for an Atmospheric Temperature Inversion. *ApJ*, 673:526–531, January 2008. doi: 10.1086/523894.

Lee R. Kump. The rise of atmospheric oxygen. *Nature*, 451:277–278, jan 2008.

R. L. Kurucz. Model atmospheres for G, F, A, B, and O stars. *ApJS*, 40:1–340, May 1979. doi: 10.1086/190589.

D. W. Latham, R. P. Stefanik, T. Mazeh, M. Mayor, and G. Burki. The unseen companion of HD114762 - A probable brown dwarf. *Nature*, 339:38–40, May 1989. doi: 10.1038/339038a0.

J. Lean and C. Frohlich. Solar Total Irradiance Variations. In K. S. Balasubramaniam, J. Harvey, & D. Rabin, editor, *Synoptic Solar Physics*, volume 140 of *Astronomical Society of the Pacific Conference Series*, pages 281–+, 1998.

U. Lohmann and E. Roeckner. Design and performance of a new cloud microphysics scheme developed for the ECHAM general circulation model. *Climate Dynamics*, 12:557–572, June 1996. doi: 10.1007/BF00207939.

S. Manabe and R. T. Wetherald. Thermal Equilibrium of the Atmosphere with a Given Distribution of Relative Humidity. *Journal of Atmospheric Sciences*, 24:241–259, May 1967. doi: 10.1175/1520-0469(1967)024.

J. Marotzke and M. Botzet. Present-day and ice-covered equilibrium states in a comprehensive climate model. *Geophys. Res. Lett.*, 34:L16704, August 2007. doi: 10.1029/2006GL028880.

S. Marsland. The Max-Planck-Institute global ocean/sea ice model with orthogonal curvilinear coordinates. *Ocean Modelling*, 5:91–127, 2003. doi: 10.1016/S1463-5003(02)00015-X.

M. Mayor and D. Queloz. A Jupiter-mass companion to a solar-type star. *Nature*, 378:355–359, November 1995. doi: 10.1038/378355a0.

C. P. McKay. *How to search for life on other worlds.* In Sullivan, W.T. and Baross, J.A., editor, Planets and Life. Cambridge University Press, 2007.

W. E. Meador and W. R. Weaver. Two-stream approximations to radiative transfer in planetary atmospheres - A unified description of existing methods and a new improvement. *Journal of Atmospheric Sciences*, 37:630–643, March 1980. doi: 10.1175/1520-0469(1980)037<0630:TSATRT>2.0.CO;2.

E. J. Mlawer, S. J. Taubman, P. D. Brown, M. J. Iacono, and S. A. Clough. Radiative transfer for inhomogeneous atmospheres: RRTM, a validated correlated-k model for the longwave. *Journal of Geophysical Research*, 102:16663–16682, July 1997. doi: 10.1029/97JD00237.

L. T. Molina and M. J. Molina. Absolute absorption cross sections of ozone in the 185- to 350-nm wavelength range. *J. Geophys. Res.*, 91:14501–14508, December 1986. doi: 10.1029/JD091iD13p14501.

J.-J. Morcrette. Impact of Changes to the Radiation Transfer Parameterizations Plus Cloud Optical. Properties in the ECMWF Model. *Monthly Weather Review*, 118:847–+, 1990. doi: 10.1175/1520-0493(1990)118.

K. M. Nissen, K. Matthes, U. Langematz, and B. Mayer. Towards a better representation of the solar cycle in general circulation models. *Atmospheric Chemistry and Physics*, 7(20):5391–5400, 2007. ISSN 1680-7316. URL `http://www.atmos-chem-phys.net/7/5391/2007/`.

L. Noack, D. Breuer, and T. Spohn. Coupling the atmosphere with interior dynamics: Implications for the resurfacing of Venus. *ICARUS*, 217:484–498, February 2012. doi: 10.1016/j.icarus.2011.08.026.

W. Randel, P. Udelhofen, E. Fleming, M. Geller, M. Gelman, K. Hamilton, D. Karoly, D. Ortland, S. Pawson, R. Swinbank, F. Wu, M. Baldwin, M.-L. Chanin, P. Keckhut, K. Labitzke, E. Remsberg, A. Simmons, and D. Wu. The SPARC Intercomparison of Middle-Atmosphere Climatologies. *Journal of Climate*, 17:986–1003, March 2004. doi: 10.1175/1520-0442(2004)017<0986:TSIOMC>2.0.CO;2.

H. Rauer, S. Gebauer, P. von Paris, J. Cabrera, M. Godolt, J. L. Grenfell, A. Belu, F. Selsis, P. Hedelt, and F. Schreier. Potential biosignatures in super-Earth atmospheres. I. Spectral appearance of super-Earths around M dwarfs. *A&A*, 529:A8+, May 2011. doi: 10.1051/0004-6361/201014368.

S. Redfield, M. Endl, W. D. Cochran, and L. Koesterke. Sodium Absorption from the Exoplanetary Atmosphere of HD 189733b Detected in the Optical Transmission Spectrum. *ApJ*, 673:L87–L90, January 2008. doi: 10.1086/527475.

E. Roeckner, T Siebert, and J. Feichter. Climatic response to anthropogenic sulfate forcing simulated with a general circulation model. *Aerosol Forcing of Climate*, 1995.

E. Roeckner, K. Arpe, L. Bengtsson, M. Christoph, M. Claussen, L. Dümenil, M. Esch, M. Giorgetta, U. Schlese, and U. Schulzweida. The atmospheric general circulation model echam-4: model description and simulation of present-day climate. Technical report, Max-Planck Institute for Meteorology, Hamburg, Germany, 1996.

E. Roeckner, G. Bäuml, L. Bonaventura, R. Brokopf, M. Esch, M. Giorgetta, S. Hagemann, I. Kirchner, L. Kornblueh, E. Manzini, A. Rhodin, U. Schlese, U. Schulzweida, and A. Tompkins. "the atmospheric general circulation model echam5, parti, report no.349". Technical report, Max-Planck-Institut für Meteorologie, November 2003.

E. Roeckner, R. Brokopf, M. Esch, M. Giorgetta, S. Hagemann, L. Kornblueh, E. Manzini, U. Schlese, and U. Schulzweida. Sensitivity of Simulated Climate to Horizontal and Vertical Resolution in the ECHAM5 Atmosphere Model. *Journal of Climate*, 19:3771, 2006. doi: 10.1175/JCLI3824.1.

E. A. Saad, A. A. El-Dimerdash, and M. S. Abdel Krim. Pade approximant calculations for dispersive, isotropic scattering, homogeneous media. *Ap&SS*, 149:187–195, November 1988. doi: 10.1007/BF00639789.

N. C. Santos, G. Israelian, and M. Mayor. Spectroscopic [Fe/H] for 98 extra-solar planet-host stars. Exploring the probability of planet formation. *A&A*, 415:1153–1166, March 2004. doi: 10.1051/0004-6361:20034469.

D. D. Sasselov. Astronomy: Extrasolar planets. *Nature*, 451:29–31, January 2008. doi: 10.1038/451029a.

Masaki Satoh. *Atmospheric Circulation Dynamics and General circulation Models*. Springer, Praxis Publishing Ltd, 2004.

J. W. Schopf and B. M. Packer. Early Archean (3.3-Billion to 3.5-Billion-Year-Old) Microfossils from Warrawoona Group, Australia. *Science*, 237:70–73, July 1987. doi: 10.1126/science.11539686.

A. Segura, K. Krelove, J. F. Kasting, D. Sommerlatt, V. Meadows, D. Crisp, M. Cohen, and E. Mlawer. Ozone Concentrations and Ultraviolet Fluxes on Earth-Like Planets Around Other Stars. *Astrobiology*, 3:689–708, December 2003. doi: 10.1089/153110703322736024.

A. Segura, J. F. Kasting, V. Meadows, M. Cohen, J. Scalo, D. Crisp, R. A. H. Butler, and G. Tinetti. Biosignatures from Earth-Like Planets Around M Dwarfs. *Astrobiology*, 5: 706–725, December 2005. doi: 10.1089/ast.2005.5.706.

F. Selsis, J. F. Kasting, B. Levrard, J. Paillet, I. Ribas, and X. Delfosse. Habitable planets around the star Gliese 581? *A&A*, 476:1373–1387, December 2007. doi: 10.1051/0004-6361:20078091.

K. P. Shine and J. A. Rickaby. Solar radiative heating due to absorption by ozone. In R. D. Bojkov & P. Fabian, editor, *Ozone in the Atmosphere*, pages 597–+, 1989.

D. K. Sing, F. Pont, S. Aigrain, D. Charbonneau, J.-M. Désert, N. Gibson, R. Gilliland, W. Hayek, G. Henry, H. Knutson, A. Lecavelier des Etangs, T. Mazeh, and A. Shporer. Hubble space telescope transmission spectroscopy of the exoplanet hd 189733b: high-altitude atmospheric haze in the optical and near-ultraviolet with stis. *Monthly Notices of the Royal Astronomical Society*, 416(2): 1443–1455, 2011. ISSN 1365-2966. doi: 10.1111/j.1365-2966.2011.19142.x. URL `http://dx.doi.org/10.1111/j.1365-2966.2011.19142.x`.

D. Sonntag. Advancements in the field of hygrometry. *Meteorologische Zeitschrift*, 3:51–66, April 1994.

D. S. Spiegel, K. Menou, and C. A. Scharf. Habitable Climates: The Influence of Obliquity. *The Astrophysical Journal*, 691:596–610, January 2009. doi: 10.1088/0004-637X/691/1/596.

Barbara Stracke. *Modeling of terrestrial extrasolar planetary atmospheres in view of habitability*. PhD thesis, Technische Universität Berlin, 2012.

D. F. Strobel. Parameterization of the atmospheric heating rate from 15 to 120 km due to O2 and O3 absorption of solar radiation. *J. Geophys. Res.*, 83:6225–6230, December 1978. doi: 10.1029/JC083iC12p06225.

H. Sundqvist. A parameterization scheme for non-convective condensation including prediction of cloud water content. *Quart. J. R. Met. Soc.*, 104:677–690, 1978.

G. Takeda, E. B. Ford, A. Sills, F. A. Rasio, D. A. Fischer, and J. A. Valenti. Structure and Evolution of Nearby Stars with Planets. II. Physical Properties of ˜1000 Cool Stars from the SPOCS Catalog. *ApJS*, 168:297–318, February 2007. doi: 10.1086/509763.

D. Tanré, J-F. Geleyn, and J. M. Slingo. First results of the introduction of an advanced aerosol?radiation interaction in the ecmwf low resolution global model. Aerosols and Their Climatic Effects, H. Gerber and A. Deepak, Eds., A. Deepak, 1984.

K.E. Taylor, D. Williamson, and F. Zwiers. The sea surface temperature and sea-ice concentration boundary conditions for amip ii simulations. *PCMDI Report No. 60, Program for Climate Model Diagnosis and Intercomparison*, page 25 pp., 2000.

S. L. Thompson and D. Pollard. Greenland and Antarctic Mass Balances for Present and Doubled Atmospheric CO_2 from the GENESIS Version-2 Global Climate Model. *Journal of Climate*, 10:871–900, May 1997. doi: 10.1175/1520-0442(1997)010.

Adrian M. Tompkins. A prognostic parameterization for the subgrid-scale variability of water vapor and clouds in large-scale models and its use to diagnose cloud cover. *Journal of the Atmospheric Sciences*, 59(12):1917–1942, 2002.

O. B. Toon, C. P. McKay, T. P. Ackerman, and K. Santhanam. Rapid calculation of radiative heating rates and photodissociation rates in inhomogeneous multiple scattering atmospheres. *Jornal of Geophysical Research*, 94:16287–16301, November 1989. doi: 10.1029/JD094iD13p16287.

H. Tost, P. Jöckel, and J. Lelieveld. Influence of different convection parameterisations in a gcm. *Atmospheric Chemistry and Physics*, 6(12):5475–5493, 2006. ISSN 1680-7316. URL `http://www.atmos-chem-phys.net/6/5475/2006/`.

S. Udry, X. Bonfils, X. Delfosse, T. Forveille, M. Mayor, C. Perrier, F. Bouchy, C. Lovis, F. Pepe, D. Queloz, and J.-L. Bertaux. The HARPS search for southern extra-solar planets. XI. Super-Earths (5 and 8 $M_\oplus$) in a 3-planet system. *A&A*, 469:L43–L47, July 2007. doi: 10.1051/0004-6361:20077612.

D. Valencia, R. J. O'Connell, and D. D. Sasselov. Inevitability of Plate Tectonics on Super-Earths. *ApJ*, 670:L45–L48, November 2007. doi: 10.1086/524012.

P. von Paris, H. Rauer, J. Lee Grenfell, B. Patzer, P. Hedelt, B. Stracke, T. Trautmann, and F. Schreier. Warming the early earth – CO_2 reconsidered. *Planet. Space Science*, 56:1244–1259, July 2008. doi: 10.1016/j.pss.2008.04.008.

P. von Paris, S. Gebauer, M. Godolt, J. L. Grenfell, P. Hedelt, D. Kitzmann, A. B. C. Patzer, H. Rauer, and B. Stracke. The extrasolar planet Gliese 581d: a potentially habitable planet? *A&A*, 522:A23+, November 2010. doi: 10.1051/0004-6361/201015329.

Philip von Paris. *The atmospheres of Super-Earths.* PhD thesis, TU Berlin, 2010.

W. Wagner and A. Pruß. The IAPWS Formulation 1995 for the Thermodynamic Properties of Ordinary Water Substance for General and Scientific Use. *Journal of Physical and Chemical Reference Data*, 31:387–+, June 2002.

J. C. G. Walker, P. B. Hays, and J. F. Kasting. A negative feedback mechanism for the long-term stabilization of the earth's surface temperature. *J. Geophys. Res.*, 86: 9776–9782, October 1981. doi: 10.1029/JC086iC10p09776.

D. M. Williams and D. Pollard. Earth-like worlds on eccentric orbits: excursions beyond the habitable zone. *International Journal of Astrobiology*, 1:61–69, January 2002. doi: 10.1017/S1473550402001064.

D. M. Williams and D. Pollard. Extraordinary climates of Earth-like planets: three-dimensional climate simulations at extreme obliquity. *International Journal of Astrobiology*, 2:1–19, January 2003. doi: 10.1017/S1473550403001356.

D. M. Williams, J. F. Kasting, and R. A. Wade. Habitable moons around extrasolar giant planets. *Nature*, 385:234–236, January 1997. doi: 10.1038/385234a0.

G. E. Williams. History of the earth's obliquity. *Earth Science Reviews*, 34:1–45, March 1993. doi: 10.1016/0012-8252(93)90004-Q.

A. Wolszczan and D. A. Frail. A planetary system around the millisecond pulsar PSR1257 + 12. *Nature*, 355:145–147, January 1992. doi: 10.1038/355145a0.

R. Wordsworth, F. Forget, F. Selsis, J. -. Madeleine, E. Millour, and V. Eymet. Is Gliese 581d habitable? Some constraints from radiative-convective climate modeling. *ArXiv e-prints*, May 2010.

R. D. Wordsworth, F. Forget, F. Selsis, E. Millour, B. Charnay, and J.-B. Madeleine. Gliese 581d is the First Discovered Terrestrial-mass Exoplanet in the Habitable Zone. *ApJ*, 733:L48+, June 2011. doi: 10.1088/2041-8205/733/2/L48.

Yuk Ling Yung and William B. DeMore. *Photochemistry of planetary atmospheres*. Oxford University Press, 1998.

Acknowledgements

This work has been supported by the Forschungsallianz *Planetary Evolution and Life* of the Helmholtz Gemeinschaft (HGF).
The 3D model calculations have been performed on the North-German Supercomputing Alliance (HLRN) parallel supercomputing system.
Furthermore, I would like to thank S. Dietmüller and M. Ponater for providing and helping with the mixed layer ocean.

Danksagung

Bei Frau Prof. Heike Rauer möchte ich für Aufnahme in der Arbeitsgruppe und die Betreuung dieser Arbeit bedanken. Ich habe durch die Anfertigung dieser Arbeit in der Arbeitsgruppe *Extrasolare Planeten und Atmosphären* und im Rahmen der *Helmholtz-Forschungsallianz Planetenentwicklung und Leben* viele neue interessante Fachgebiete kennengelernt und meinen Wissenshorizont stetig erweitern können.

Großer Dank gebührt auch Frau Prof. Ulrike Langematz, dafür dass Sie sich die Zeit genommen hat, diese Arbeit zu Begutachten und mir die atmosphärische Dynamik der Erdatmosphäre näher gebracht hat.

Ganz herzlich möchte ich mich auch bei Lee Grenfell bedanken, der immer ein offenes Ohr und Zeit für Fragen hatte, und seine Urlaubstage für das Korrekturlesen geopfert hat.

Auch Markus Kunze möchte ich danken, ohne dessen Hilfestellung ich das 3D Modell so schnell nicht hätte benutzen können.

Der Atmosphärengruppe, Barbara, Beate, Steffi, Daniel, Joachim, Lee und Philip möchte ich für die teils hitzigen Diskussionen im Atmosmeeting und außerhalb danken. Ich habe viel Spaß daran gemeinsam mit euch die physikalischen (und chemischen) Prozesse in der Atmosphäre besser zu verstehen.

Vielen Dank an Beate Patzer, die mir in schwierigen Momenten immer wieder gezeigt hat, dass es noch ganz viele spannende Prozesse zu entdecken gilt.

Ganz herzlich möchte ich mich bei Barbara bedanken für die große Unterstützung in den letzten Wochen aber auf für die großartige Zeit bei unseren montaglichen Arbeitstreffen. Ich hoffe das können wir auch ohne unsere Doktorarbeiten weiter beibehalten.

Bei Claudia und Daniel möchte ich mich ganz herzlich für die schnellen Korrekturen in den letzten Tagen bedanken und natürlich für die vielen, vielen Balzac-Kaffeepausen.

Meinen Freunden und meiner Familie danke ich, dass sie es mir nicht übel nehmen, dass sie mich in der letzten Zeit so selten gehört und gesehen haben und natürlich dafür, dass sie trotzdem immer da waren.

Ganz ganz herzlich danke ich Philipp, ohne den die letzten Monate sicherlich nicht so schön und entspannt gewesen wären.